AFIT/GAE/ENY/96M-03

COMPRESSIBLE TURBULENCE MEASUREMENTS IN A SUPERSONIC BOUNDARY LAYER WITH IMPINGING SHOCK WAVE INTERACTION

THESIS

Michael J. Meyer
First Lieutenant, USAF

AFIT/GAE/ENY/96M-03

Approved for public release; distribution unlimited

CASE NO. T1002

Modal deformation

Fig.3-7 モード形(SYM.)

cons. No. 11002

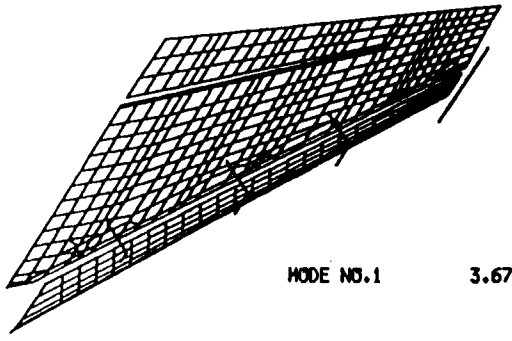

内舷Roll
Inboard Roll

MODE NO.1 3.67(HZ)

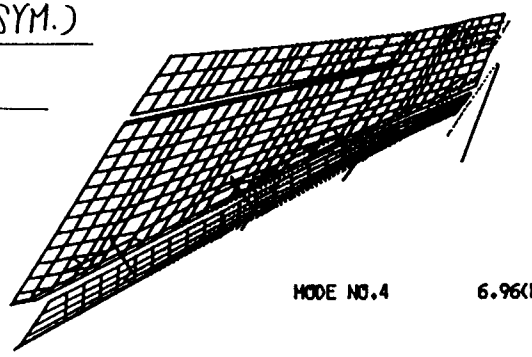

翼端Pitch
Tip Pitch

MODE NO.4 6.96(HZ)

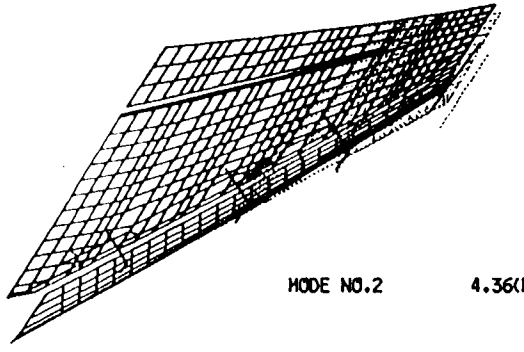

WB1

MODE NO.2 4.36(HZ)

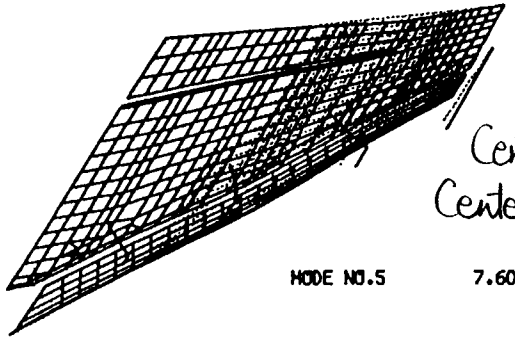

中内舷Roll
中外舷Roll
Center Inboard Roll
Center Outboard Roll

MODE NO.5 7.60(HZ)

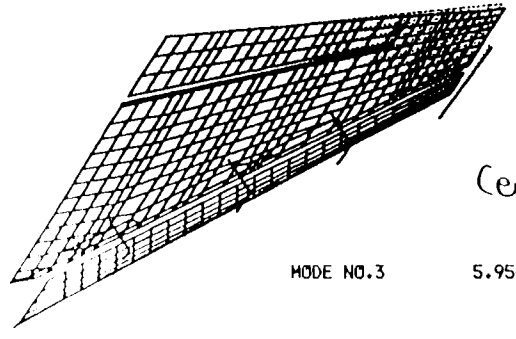

翼端Pitch
中外舷Pitch
Tip Pitch
Center Outboard Pitch

MODE NO.3 5.95(HZ)

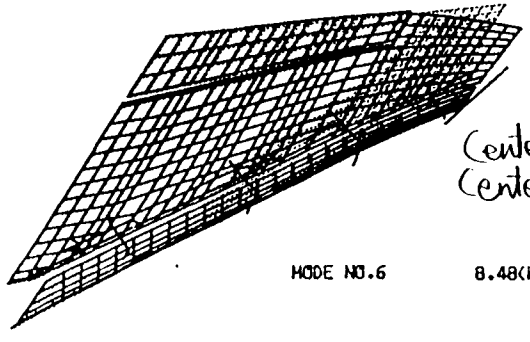

中外舷Roll
中内舷Roll
Center Outboard Roll
Center Inboard Roll

MODE NO.6 8.48(HZ)

NAF02861

193

March 1996 Master's Thesis

COMPRESSIBLE TURBULENCE MEASUREMENTS IN A SUPERSONIC BOUNDARY LAYER WITH IMPINGING SHOCK WAVE INTERACTION

Michael J. Meyer

Air Force Institute of Technology, WPAFB OH 45433-6583

AFIT/GAE/ENY/96M-03

Dr. James McMichael
AFOSR/NA, BOLLING AFB, MD

This study used laser Doppler velocimetry techniques to measure the turbulence intensities and Reynolds shear stresses in a Mach 2.9 turbulent flat plate with an impinging shock wave. The shock strength was varied, using three wedge shock generators with turning angles of 5^o, 7^o, and 10^o. Each flow field was studied at four locations, $X = -1.32\delta_o, 0\delta_o, 1.32\delta_o, 2.64\delta_o$, relative to the shock wave/boundary layer interaction. An additional streamwise profile, parallel to the wall at a height of $\frac{Y}{\delta_o} = 0.66$. This study showed that the velocity fluctuations ($\frac{<u'>}{U}$, $\frac{<v'>}{U}$) were energized by the shock wave/boundary layer interaction, and while remaining at a higher value than the upstream stations, decreased in value with distance downstream of the interaction. The Reynolds shear stress $-\overline{\rho u'v'}$ followed a similar pattern, sharply increasing immediately after the interaction and dissipating with distance downstream of the interaction.

Shock Waves, Supersonic, Wind Tunnel, Turbulence, Laser Doppler Velocimetry, Shock Wave/Boundary Layer Interaction 150

UNCLASSIFIED UNCLASSIFIED UNCLASSIFIED UL

The views expressed in this thesis are those of the author and do not reflect the official policy or position of the Department of Defense or the U. S. Government.

AFIT/GAE/ENY/96M-03

COMPRESSIBLE TURBULENCE MEASUREMENTS IN A SUPERSONIC BOUNDARY LAYER WITH IMPINGING SHOCK WAVE INTERACTION

THESIS

Presented to the Faculty of the Graduate School of Engineering

of the Air Force Institute of Technology

Air University

In Partial Fulfillment of the

Requirements for the Degree of

Master of Science in Aeronautical Engineering

Michael J. Meyer, B.S.E., Aerospace Engineering

First Lieutenant, USAF

March, 1996

Acknowledgements

I am deeply indepted to my thesis advisor, Major Thomas A. Buter. His guidance and knowledge were critical to this research. His example and motivation greatly inspired me to finish this project. I would not be here if it was not for him. Also, Dr Rodney Bowersox has provided invaluable expertise and encouragement throughout this project. In addition, I am grateful to Lt Joel Luker and Lt Chad Hale for allowing me to learn the laboratory systems while they were trying to finish their own thesis. I will not forget their help and friendship. I am also thankful to my supervisor at Wright Laboratory, Mr. Edward O. Roberts. He generously allowed me the time to pursue this project and always encouraged me throughout my Master's Degree. Finally, I would like to thank my wife Laura for her patience and understanding. I have lost count of the times she has rebuilt my determination through her love and encouragement.

Michael J. Meyer

Table of Contents

List of Figures

List of Tables

Abstract

This study used laser Doppler velocimetry techniques to measure the turbulence intensities and Reynolds shear stresses in a Mach 2.9 turbulent flat plate with an impinging shock wave. The shock strength was varied, using three wedge shock generators with turning angles of 5^o, 7^o, and 10^o. Each flow field was studied at four locations, $X = -1.32\delta_o, 0\delta_o, 1.32\delta_o, 2.64\delta_o$, relative to the shock wave/boundary layer interaction. An additional streamwise profile, parallel to the wall at a height of $\frac{Y}{\delta_o} = 0.66$. This study showed that the velocity fluctuations ($\frac{<u'>}{U}$, $\frac{<v'>}{U}$) were energized by the shock wave/boundary layer interaction, and while remaining at a higher value than the upstream stations, decreased in value with distance downstream of the interaction. The Reynolds shear stress $-\overline{\rho u'v'}$ followed a similar pattern, sharply increasing immediately after the interaction and dissipating with distance downstream of the interaction.

COMPRESSIBLE TURBULENCE MEASUREMENTS IN A SUPERSONIC BOUNDARY LAYER WITH IMPINGING SHOCK WAVE INTERACTION

I. Introduction

1.1 Introduction

The interaction between supersonic boundary layers and impinging shock waves represents a significant problem for the designers of high-speed air vehicles. Impinging shock waves appear frequently in engine inlets and compression systems. The abrupt pressure rise caused by the impinging shock wave complicates the vehicle structural design. If the shock is strong enough, the boundary layer may separate, causing higher heat transfer rates and burdening the designer with the additional problem of thermal protection (19).

This problem appeared with a vengeance on October 3, 1967 when an X-15 high-speed research aircraft, piloted by Pete Knight, reached a Mach Number of 6.72 at an altitude just over 100,000 feet. The aircraft carried a dummy ramjet connected to the lower surface of the X-15 by a pylon. During the flight, a shock wave from the nacelle of the ramjet impinged on the pylon, burning a hole through the surface. In addition, the pylon itself created a bow shock that impinged on the lower surface of the X-15, causing local heating damage. The dummy ramjet was completely burned off the pylon and, during separation from the aircraft, punched a hole in the X-15 that allowed heated external air into the internal aircraft structure. Knight was able to land the damaged X-15 but this was the worst case of aerodynamic heating damage experienced during the X-15 Program (10).

Flight testing or wind tunnel testing of hypersonic and supersonic air vehicle configurations to identify these impinging-shock-wave problems can be cost-prohibitive and possibly hazardous. Using Computational Fluid Dynamics (CFD), the designer will have ample opportunity to test and

refine the design on the ground at a much lower cost. However, before this is possible, advanced CFD techniques must be developed to handle the different flow structures expected in high-speed flight (19).

Directly solving the Navier-Stokes Equations for high Reynolds number flow is impractical. Luker (13) shows that for the present test section (6.35cm by 6.35 cm by 80cm, M = 2.9, Re_δ roughly 1.6 X 10^6, boundary layer thickness delta roughly = 0.009 m) the Kolmogoroff turbulent length scale is roughly 2 X 10^{-7} m. To resolve this flow we would need 4 X 10^{17} grid points, 4 X 10^{28} calculations, and, at an optimistic one nanosecond per calculation, 1.2 X 10^{12} years to complete the numerical solution to the Navier-Stokes solutions. The most advanced computers of the day can not make this calculation and most would not wait for it. This is a relatively simple flowfield. Direct calculation of low Reynolds number flows have been completed but for most practical flows aerodynamicists must resort to approximate methods. These approximate methods usually involve averaging the Navier-Stokes equations and writing the dependent variables in terms of a mean and fluctuation about that mean. However, when the non-linear Navier-Stokes equations are cast in this form, cross correlation fluctuation terms appear, leading to fewer equations than unknowns. These terms cause the problem of turbulent closure. To achieve closure is the role of the turbulence model.

The development of these advanced CFD techniques and turbulence models is greatly aided by careful experiments performed to provide validation cases and verifying the accuracy of the computational techniques. These experiments not only increase the basic understanding of the flow structure and fluid motions but can also provide input for modeling and precise checks on computational output. For research codes and initial trials of turbulence models, building block experiments, providing phenomenological modeling information, are needed (14).

To achieve closure, simplified turbulence models are used. However, these models are not rigorously correct and are not adequate for general predictions of flowfields around high-speed vehicles.

Compressible, supersonic flows have drastically different properties from the simple, low-speed flows initially studied and used to build turbulence models. Yet, many incompressible turbulence models are applied to compressible, high-speed flow with little or no theoretical justification. This method has been reasonably successful for flat plate flow but turbulent quantities change greatly for complex geometries and large pressure gradients(18). The complexity of turbulence modeling demands great expertise and large quantities of intellectual energy and must be guided by careful experiments. Upon the introduction of a new turbulence model, it must be tested and validated against quality data. To adequately test these turbulence models, a broad range of flow field experiments with careful measurement of the turbulent quantities is needed (17).

This research will attempt to meet the eight necessary criteria for a CFD validation case as spelled out by Settles and Dodson (17):

Baseline Applicability : Each experiment must involve Mach 3 or higher turbulent flow with a shock wave-boundary layer interaction.

Simplicity : Each experiment must involve a simple "building-block" geometry which can be sufficiently modeled by CFD methods without great difficulty.

Specific Applicability : Each experiment must provide a useful test of a turbulence model.

Well-defined Experimental Boundary Conditions : This condition requires that all incoming boundary conditions be known including the state of the incoming boundary layer. Also, a claim of two-dimensional flow must show experimental data to verify the extent of spanwise flow.

Well-defined Experimental Error Bounds : Each experiment must be accompanied by an analysis of the accuracy and repeatability of the data to ensure proper code validation can be conducted.

Consistency Criterion : No mutually inconsistent results can appear in the experiment.

Adequate Documentation of Data : The data from the experiment must be tabulated and in a machine-readable form.

Adequate Spatial Resolution of Data : Each experiment must have adequate spatial resolution to resolve the key features of the flow.

Using these eight criteria to review of the literature, Settles and Dodson did not find an accepted experiment for impinging shock wave - boundary layer interaction. Secondary criteria include turbulence data, realistic test conditions, nonintrusive instrumentation, and redundant measurements (17).

The only source found that measured impinging shock wave - boundary layer interaction with nonintrusive instrumentation was Rose and Johnson's 1975 study. In this study, Rose and Johnson only report on the shock wave - boundary layer interaction for one shock system caused by a 7 degree ramp. However, the study does compare Laser Doppler Velocimetry (LDV) data with hot-wire anemometry data for this flow field (16).

1.2 Thesis Objective

The objective of this thesis is to determine the effect of impinging shock wave with varied strengths on the turbulence characteristics of a boundary layer in Mach 2.9 flow. A secondary objective of this thesis is to provide quality validation data for turbulence model developers that meets the eight criteria outlined by Settles and Dodson.

1.3 Document Roadmap

As a basis for the determination of the necessary validation measurements for turbulence modeling, the approximate form of the governing equations of compressible, turbulent flow are presented in Chapter Two, showing the importance of the velocity cross-correlation term, $\overline{u'v'}$. An explanation of the experimental apparatus and test methodology used are presented in Chapter Three. The data reduction techniques used to determine the turbulent properties of shock wave-boundary layer interactions are addressed in Chapter Four. The results of this study are presented and discussed in Chapter Five culminating in a series of conclusions provided in Chapter Six, along with a series of recommendations for further research.

II. Governing Equations

2.1 Forms of the Governing Equations

Computational study of turbulent flow is primarily conducted by numerically solving the time-averaged Navier-Stokes equations. This system of equations is derived by breaking the dependent variables into mean and fluctuating components and time-averaging the entire equation set. This process leads to new terms which appear as stress gradients and heat-flux quantities which involve products of the fluctuating quantities. To accurately account for these terms, the system must be closed with functions of mean flow variables. This is done through a turbulence model. Two types of averaging are used and will be discussed, the classical Reynolds averaging and Favré mass-weighted averaging. The two forms become identical when the density fluctuations are neglected (4).

2.2 Compressible Navier-Stokes Equations

The governing equations for continuum fluid flow are the Navier-Stokes equations presented here in compressible form(4).

Continuity:

$$\frac{D\rho}{Dt} + \rho(\nabla \cdot \mathbf{V}) = 0 \tag{2.1}$$

Momentum:

$$\rho\frac{D\mathbf{V}}{\mathrm{Dt}} = \rho\mathbf{f} + \nabla \cdot \pi_{\mathrm{ij}} \tag{2.2}$$

Energy:

$$\rho\frac{Dh}{Dt} = \frac{DP}{Dt} + \frac{\partial Q}{\partial t} - \nabla\cdot\mathbf{q} + \Phi \tag{2.3}$$

where **f** represents the body forces acting on the fluid and

$$\pi_{ij} = -p\delta_{ij} + \tau_{ij} \tag{2.4}$$

$$\tau_{ij} = \mu\left[\left(\frac{\partial u_i}{\partial x_j} + \frac{\partial u_j}{\partial x_i}\right) - \frac{2}{3}\delta_{ij}\frac{\partial u_k}{\partial x_k}\right] \tag{2.5}$$

$$\Phi = \tau_{ij}\frac{\partial u_i}{\partial x_j} \tag{2.6}$$

In turbulent flow, rapid fluctuations in the important flow variables leads to very small time scales associated with the flowfield. Averaging schemes, such as the Reynolds or Favré averaging, were developed to lower the computational work involved in solving flows with small time scales. This way only large mean flow variations (compared to the turbulence time scales) are captured using the time-dependent Navier-Stokes equations. This leads to a dramatic decrease in the computational burden.

In both averaging schemes, the flow variables are broken into a mean component and a fluctuating component. The instantaneous variable, h, consists of the time averaged component, $\overline{h}$, and the fluctuation from that value, h'.

$$h(x,y,z,t) = \overline{h}(x,y,z) + h'(x,y,z,t) \tag{2.7}$$

It should be noted that in equation 2.7 $\overline{h}$ is allowed to vary with time, thus the averaging process admits time-dependent behavior. This process requires that the time-averaging period must be long compared to the turbulence time scales but relatively short compared to the overall flowfield time (4).

2.3 Reynolds-Averaged Navier-Stokes Equations

When using Reynolds averaging, any given primitive flow quantity, ϕ, is expressed as the sum of a time-averaged component, $\overline{\phi}$ and a fluctuating component, ϕ', as follows (4):

$$\rho = \overline{\rho} + \rho' \qquad u_i = \overline{u}_i + u'_i$$

$$p = \overline{p} + p' \qquad T = \overline{T} + T'$$

$$E = \overline{E} + E' \qquad H = \overline{H} + H'$$

$$\mu = \overline{\mu} + \mu' \qquad \mu^* = \overline{\mu^*} + \mu^{*'}$$

$$C_v = \overline{C_v} + C'_v \qquad C_p = \overline{C_p} + C'_p$$

The time average is defined by

$$\overline{\phi} = \frac{1}{T}\int_{t_0}^{t_0+T} \phi \, dt \tag{2.8}$$

where the characteristic time T is long in comparison to the cycle times of the fluctuating component, but still permits gradual time-dependent fluid motion for non-stationary flows.

To obtain the mean flow equations, these expressions for the decomposed variables are substituted into the governing equations. These instantaneous equations are then time averaged, expanded, and simplified using the rules given in (19). The results are the Reynolds-averaged Navier-Stokes equations given below (4)

Continuity:

$$\frac{\partial \overline{\rho}}{\partial t} + \frac{\partial(\overline{\rho u_i} + \overline{\rho' u_i'})}{\partial x_i} = 0 \tag{2.9}$$

Momentum:

$$\frac{\partial \overline{\rho u_i} + \overline{\rho' u'_i}}{\partial t} + \frac{\partial \overline{\rho u_i u_j}}{\partial x_j} = -\frac{\partial \overline{p}}{\partial x_i} + \frac{\partial(\overline{\tau_{ij}} + \tau_{ij}^T)}{\partial x_j} \tag{2.10}$$

Energy:

$$\frac{\partial(\overline{\rho e_o} + \overline{\rho' h_o'})}{\partial t} + \frac{\partial(\overline{\rho} \overline{h_o} \overline{u_j})}{\partial x_j} = \frac{\partial(\overline{u_i \tau_{ij}} + \overline{u_i' \tau_{ij}'} - \overline{q_j} - q_j^T)}{\partial x_j} \tag{2.11}$$

In addition,

$$\overline{\tau_{ij}} = \mu \left[\left(\frac{\partial \overline{u_i}}{\partial x_j} + \frac{\partial \overline{u_j}}{\partial x_i} \right) - \frac{2}{3} \delta_{ij} \frac{\partial \overline{u_k}}{\partial x_k} \right] \tag{2.12}$$

$$\tau_{ij}' = \mu \left[\left(\frac{\partial u_i'}{\partial x_j} + \frac{\partial u_j'}{\partial x_i} \right) - \frac{2}{3} \delta_{ij} \frac{\partial u_k'}{\partial x_k} \right] \tag{2.13}$$

$$\tau_{ij}^T = -\overline{\rho} \overline{u_i' u_j'} - \overline{u_i} \overline{\rho' u_j'} - \overline{u_j} \overline{\rho' u_i'} - \overline{\rho' u_i' u_j'} \tag{2.14}$$

$$\overline{q_i} = -k \frac{\partial \overline{T}}{\partial x_i} \tag{2.15}$$

$$q_i^T = -\overline{\rho} \overline{h_o' u_i'} + \overline{h_o \rho' u_i'} + \overline{u_i} \overline{\rho' h_o'} - \overline{\rho' h_o' u_i'} \tag{2.16}$$

In the above equations, e_o and h_o are stagnation reference quantities.

2.4 Favré-Averaged Navier-Stokes Equations

When employing Favré averaging, any given primitive flow quantity, ϕ, is expressed as the sum of a mass-weighted-averaged mean value (Favré averaged), $\tilde{\phi}$, and a fluctuating component, ϕ''. The Favré averaged quantity and the Favré turbulent fluctuation of the quantity are defined as (4):

$$\tilde{\phi} = \frac{\overline{\rho\phi}}{\overline{\rho}} \quad \text{and} \quad \phi'' = \phi - \tilde{\phi} \tag{2.17}$$

It should be noted that although

$$\overline{\phi''} \neq 0$$

$\overline{\rho\phi}$ becomes

$$\begin{aligned}
\overline{\rho\phi} &= \overline{\rho(\tilde{\phi} + \phi'')} \\
&= \overline{\rho\tilde{\phi}} + \overline{\rho\phi''} \\
&= \overline{\rho}\tilde{\phi} + \overline{\rho\phi''} \\
&= \overline{\rho}\frac{\overline{\rho\phi}}{\overline{\rho}} + \overline{\rho\phi''} \\
&= \overline{\rho\phi} + \overline{\rho\phi''}
\end{aligned}$$

forcing

$$\overline{\rho\phi''} = 0$$

Also, the following relationships can be derived

$$\overline{\phi} - \tilde{\phi} = \phi'' - \phi' = \overline{\phi''} = -\frac{\overline{\rho'\phi''}}{\overline{\rho}} = -\frac{\overline{\rho'\phi'}}{\overline{\rho}}$$

The Favré averaged equations, as presented by Marvin (14) (and corrected here), are

Continuity:

$$\frac{\partial\overline{\rho}}{\partial t} + \frac{\partial(\overline{\rho}\tilde{u}_i)}{\partial x_i} = 0 \tag{2.18}$$

Momentum:

$$\frac{\partial(\overline{\rho}\tilde{u}_i)}{\partial t} + \frac{\partial(\overline{\rho}\tilde{u}_i\tilde{u}_j)}{\partial x_j} = -\frac{\partial \tilde{p}}{\partial x_i} + \frac{\partial(\overline{\tau}_{ij} - \overline{\rho u_i'' u_j''})}{\partial x_j} \tag{2.19}$$

Energy:

$$\frac{\partial \overline{\rho}\tilde{h}}{\partial t} + \frac{\partial(\overline{\rho}\tilde{h}\tilde{u}_j)}{\partial x_j} = \frac{\partial \tilde{p}}{\partial t} + \tilde{u}_j\frac{\partial \tilde{p}}{\partial x_j} + \overline{u_j''\frac{\partial p}{\partial x_j}} + \frac{\partial(-\overline{q}_j - \overline{\rho h'' u_j''})}{\partial x_j} + \overline{\tau_{ij}\frac{\partial u_i''}{\partial x_j}} \tag{2.20}$$

These governing equations *may* be supplemented by the following transport equations.

Turbulent Kinetic Energy:

$$\frac{\partial(\rho k)}{\partial t} + \frac{\partial(\rho\tilde{u}_j k)}{\partial x_j} = -\overline{\rho u_i'' u_k''}\frac{\partial \tilde{u}_k}{\partial x_k} - \frac{\partial(\overline{\rho u_k'' k})}{\partial x_j} - \frac{\partial(\overline{u_i'' p})}{\partial x_i} + p\overline{\frac{\partial u_i''}{\partial x_i}} + \frac{\partial(\overline{u_i''\tau_{ik}})}{\partial x_k} - \overline{\tau_{ik}\frac{\partial(u_i'')}{\partial x_k}} \tag{2.21}$$

Reynolds stress transport:

$$\begin{aligned}\frac{\partial(\overline{\rho u_i'' u_j''})}{\partial t} + \frac{\partial(\tilde{u}_j\overline{\rho u_i'' u_k''})}{\partial x_j} = \; & (\overline{\rho u_i'' u_j''})\frac{\partial(\tilde{u}_k)}{\partial x_j} - (\overline{\rho u_k'' u_j''})\frac{\partial(\tilde{u}_i)}{\partial x_j} \\ & - \frac{\partial(\overline{\rho u_i'' u_k'' u_j''})}{\partial x_j} - \frac{\partial(\overline{u_i'' p})}{\partial x_j} - \frac{\partial(\overline{u_j'' p})}{\partial x_k} + \overline{p\frac{\partial(u_k'')}{\partial x_i}} + \overline{\frac{\partial(u_k'')}{\partial x_k}} + \frac{\partial(\overline{u_k''\tau_{ij}})}{\partial x_j} \\ & + \frac{\partial(\overline{u_i''\tau_{ki}})}{\partial x_j} - \overline{\tau_{ij}\frac{\partial(u_k'')}{\partial x_j}} - \overline{\tau_{ki}\frac{\partial(u_i'')}{\partial x_j}}\end{aligned} \tag{2.22}$$

These equations have the same form as the *incompressible* Reynolds averaged equations, except that the Reynolds stresses $\overline{\rho u_i'' u_j''}$ include the density fluctuations, which must be accounted for in some way. Compressibility is generally included by replacing the density with the mean density neglecting the terms which involve additional correlations arising from compressibility. Researchers using the Favré forms of the governing equations cite that avoiding some of the fluctuating density-generated terms simplifies closure of the system. However since much of the experimental data provides RANS-type information, modeling the effects of compressibility presents a problem. The lack of an explicit fluctuating density component in the turbulent shear stresses is one of the specific shortcomings of this model.

The compressible FANS turbulence terms are expressed as

$$m_i^T = 0 \qquad \tau_{ij}^T = -\overline{\rho u_i'' u_j''} \qquad q_i^T = \overline{\rho h_o'' u_i''} \tag{2.23}$$

It can be seen that the conservation and supplemental equations have a greater number of unknowns than equations. This is the problem of closure and must be remedied through turbulence modeling. A detailed discussion of turbulence modeling is beyond the scope of this thesis. The reader is referred to Marvin for an excellent overview of the direction of modeling efforts (14).

III. Experimental Apparatus and Procedures

3.1 Facility Description

The experimental work presented here was performed in the AFIT Supersonic Wind Tunnel Facility. A schematic of the facility is shown in Figure 3.1 and Figure 3.2.

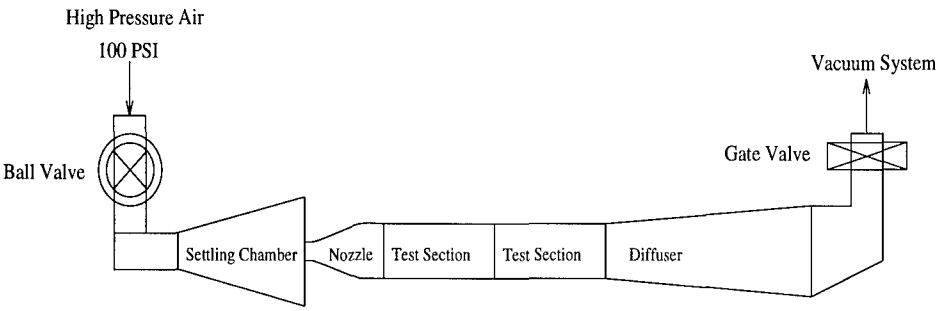

Figure 3.1 Tunnel Schematic

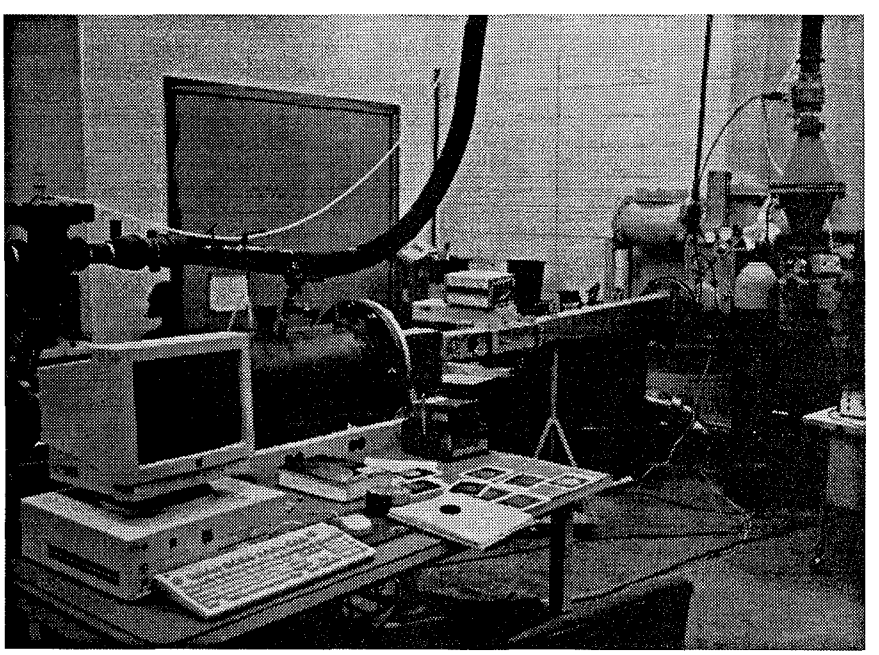

Figure 3.2 AFIT Mach 3 Wind Tunnel

3.2 Description of Wind Tunnel

The wind tunnel used for this research is a Mach 2.9 combination blowdown-drawdown tunnel, shown in Figure 3.2 supplied by 100 psi high pressure shop air exhausting into a vacuum system. The high pressure air is supplied by an Atlas Compco compressor facility with an approximate mass flow capacity of 0.45 kg/sec. The system air is then passed through two Pioneer Air Systems Inc. Model R500A refrigeration dryers and into a centrifugal particle and moisture separator. Finally, the air passes through a fiber-reinforced paper filter before entering the settling chamber. The compressed air is released into the tunnel using an El-o-Matic ED10 Ball Valve. In the settling chamber, Bertoli brand extra virgin olive oil from a TSI Six Jet Atomizer Model 9306 feeds a custom built seeder rake designed and constructed by Luker (13) and Hale (9) and modified for this thesis (See Figure 3.3). According to the Atomizer Manual (1), the average particle size for olive oil is 0.6 μm.

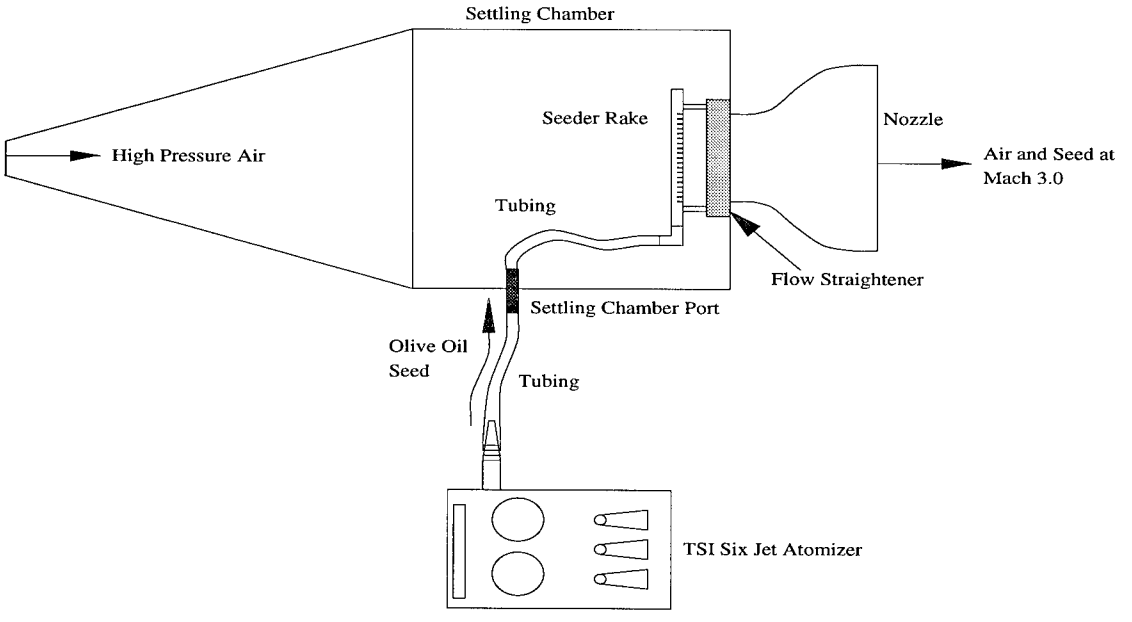

Figure 3.3 Seeder System Schematic

The air, carrying the olive oil seed, is accelerated through the nozzle and into two square test sections each measuring 6.35 cm by 6.35 cm by 33.02 cm. The nozzle, test section, and diffuser are

each constructed from 1.905cm thick aluminum alloy. The test section is modular in design (Figure 3.4), allowing different components to be mixed and matched. Two different side walls were used in this research. To allow for photographic analysis of the flow field, a sidewall was constructed from 1.905 cm thick optical grade Plexiglass. An alternate sidewall, used with the Laser Doppler Velocimeter, consists of an aluminum housing protecting two 3 inch diameter optical pure glass windows. The test section floors, ceilings, and sidewalls are sealed with rubber gaskets to prevent leakage. Room temperature vulcanizer was also used for any remaining test section leakage.

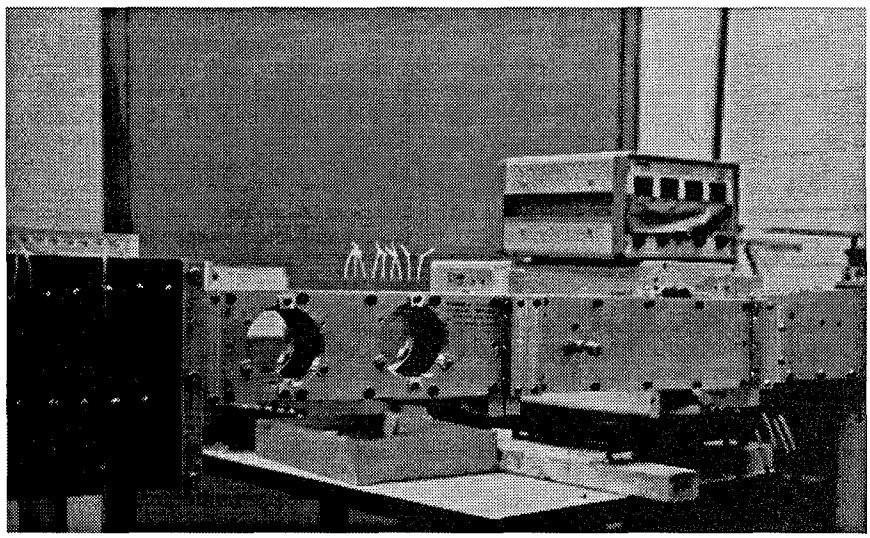

Figure 3.4 Photograph of Test Section in AFIT Mach 3 Wind Tunnel

The tunnel air exhausts through a Kinney Corporation GP-8 gate valve into the vacuum system with a tank capacity of 20 cubic meters, providing an approximate run time of 35 seconds. The tunnel takes approximately 8 seconds to reach steady state, providing usable steady-state flow for roughly 25 seconds. The vacuum is provided by three Model 212-11 MicoVac vacuum pumps manufactured by Stokes Penwalt, Figure 3.5. Each vacuum pump is powered by a 7.6 metric horsepower Reliance electric motor.

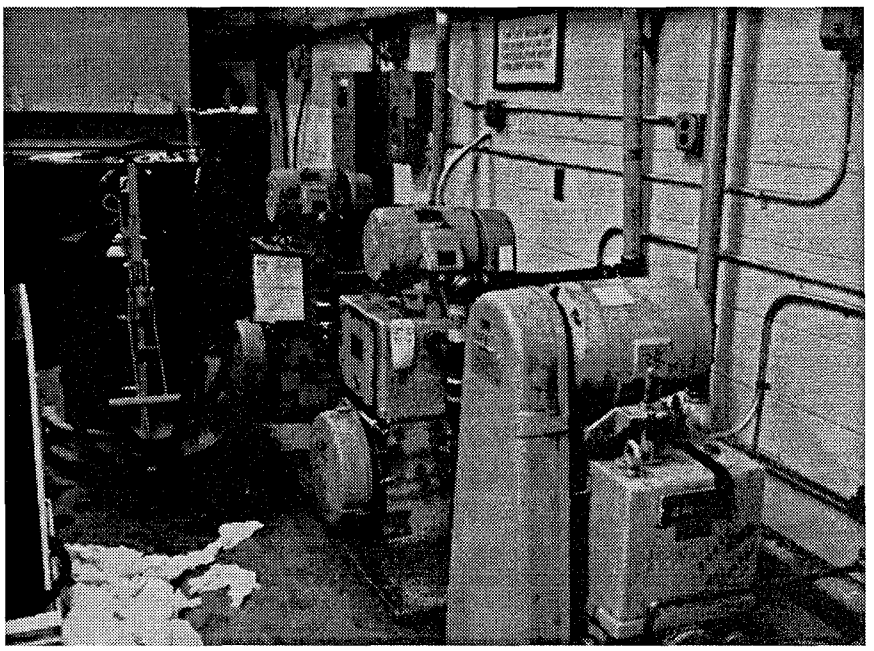

Figure 3.5 Vacuum Pumps for AFIT Mach 3 Wind Tunnel

3.3 Laser Doppler Velocimeter

The Laser Doppler Velocimeter used in this research is a Dantec Laser Doppler Anemometer with the Dantec 60X series fiber flow optics system, shown in Figure 3.6. The optical system consists of a laser, routing transmitter, transmitting optics, receiving optics and photomultiplier tubes. The system uses a Ion Laser Technology Model 5500A laser with a maximum of 300 mW of power and operates in the frequency range from 457 nanometers to 514.5 nanometers. Luker (13) showed the laser has degraded in efficiency and has a maximum output power of 275mW. This laser is powered by a 210V and 20A Laser Technology Model 5405A power supply running off 220 VAC power. The laser $\frac{1}{e^2}$ beam diameter was 0.82 mm and the laser was operated in the TEM_{oo} mode, allowing the beam to be centered around the optical axis with maximum power in the center of the beam.

A Fiber Flow 60X41 transmitter was used with a 40 Mhz Bragg cell that split the laser into 514.5 nm (green), 488.0 nm (blue), and 476.5 nm (violet). Each wavelength was also split into

two independent beams and the Bragg cell supplied the necessary 40 Mhz frequency shift as noted in Luker (13). The use of DANTEC 60X24 fiber manipulators allowed the fiberoptic cables to be precisely aligned with the beam, ensuring maximum power and efficiency. These cables carried the beam to the transmitting and recieving optics.

The collection optical probe was a DANTEC model 60X60 and the transmitting probe was a DANTEC model 60X61. Each probe contains transmitting and collecting fibers, an optical transducer, and a distribution unit. The model 60X61 transmitting probe was a two-component, four-beam probe using 488 nm and 514.5 nm beams. The model 60X60 was a one-component, two-beam, 476.5 nm probe. The transmitting optics were mounted on the traverse mounting bench using DANTEC Model 60X3611 probe support that allowed gross angular adjustments and the receiving optics were mounted on a DANTEC Model 60X3631 probe support with micrometer adjustments for precise, three-dimensional alignment.

The control volume generated by the laser beams was 9.0 mm across the tunnel and 0.276 mm in diameter. Both probes used a 600 mm focal length lens and the collection optics also used a DANTEC Model 55X12 beam expander, allowing additional reflected light to be collected. The collected light was channeled through the fiberoptic cables to a DANTEC Model 55X35 color separator. This device split incoming laser energy into the 514.5 nm and the 488.0 nm wavelengths and routed each color to a DANTEC Model 55X35 Photomultiplier tube. These tubes converted the incoming light into electrical signals for processing by a Burst Spectrum Analyzer (BSA).

The DANTEC 3D Traverse System held the optics and was used to position the lasers for precise control. The traverse was powered by three Cleveland Machine Controls stepper motors regulated by Dynapar encoders Model M20100003331 that converted 1000 pulses into a 2mm displacement of the traverse through one revolution of the screw. The entire system accuracy was rated at ± 80 μm over 600 mm range of travel and could support a maximum load of 445 N. A 1.83m

DANTEC laser mounting bench replaced the traverse mounting bench to obtain more favorable optical characteristics. This can be seen in figure 3.7.

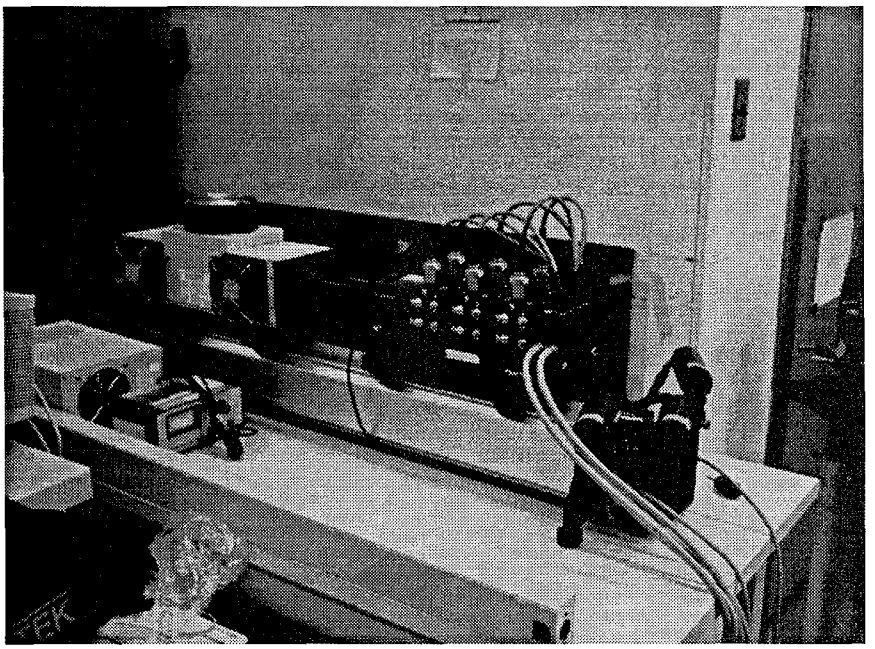

Figure 3.6 Laser and Photomultiplier Tubes

The data are processed by a Dantec Burst Spectrum Analyzer Model 57N20 Enhanced (u component of velocity) for the 514.5nm (green) laser and a Dantec Burst Spectrum Analyzer Model 57N35 (v component of velocity) for the 488.0 nm (violet) laser. The 57N20 is the master BSA for coincidence filtering. The data collection is performed on a Gateway 2000 486DX/33Mhz computer with a 92032 IEEE data collection card feeding the Burstware Version 3.00 data acquisition software system. The Burst Spectrum Analyzers and data acquisition computer are shown in figure 3.8.

For an excellent description of the principles of Laser Doppler Velocimetry, the reader is encouraged to see Chapter 3 of Luker (13) or Chapter 3 of Hale (9).

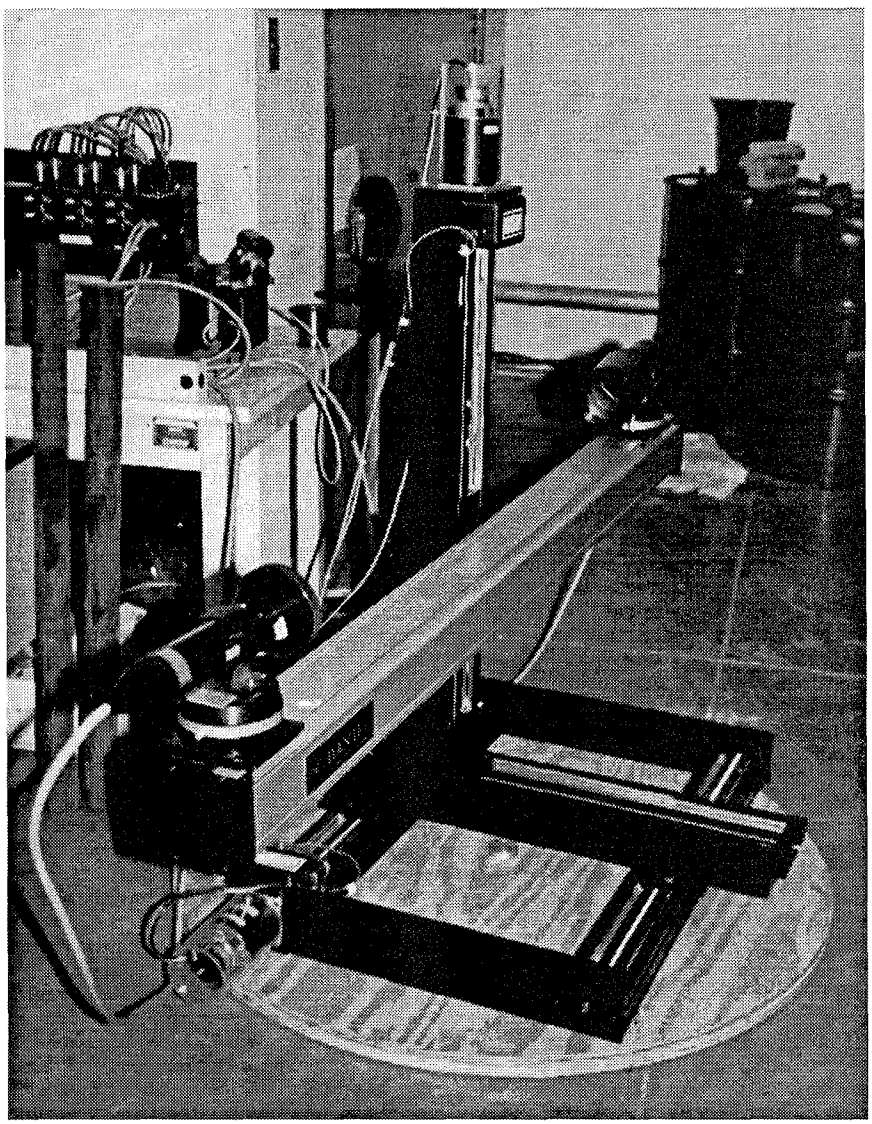

Figure 3.7 Laser Optics and Traverse

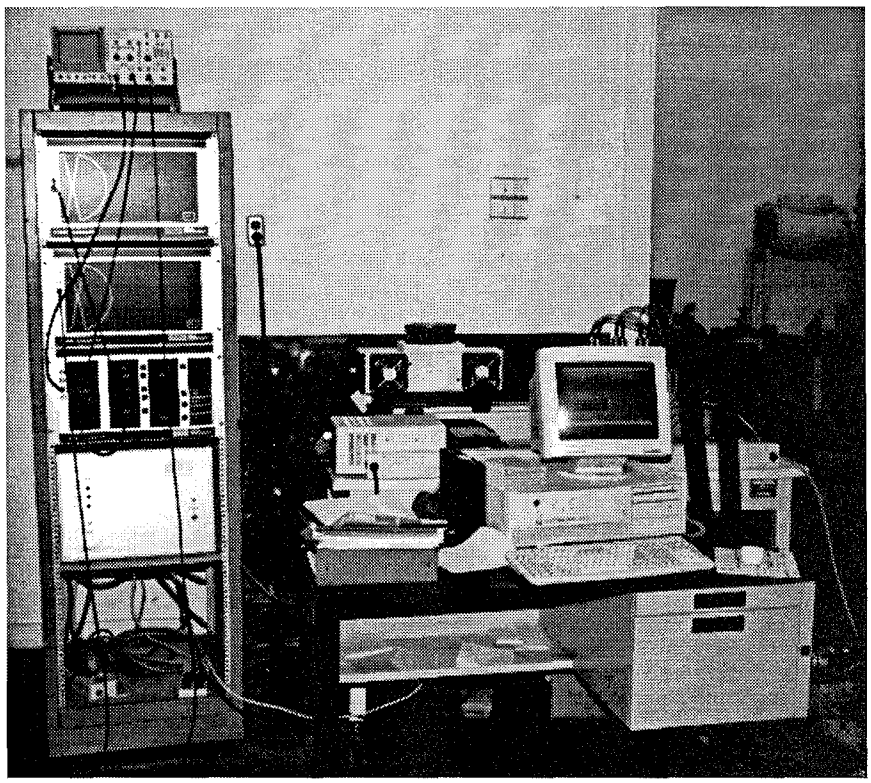

Figure 3.8 Data Acquisition Computer and Burst Spectrum Analyzers

3.4 Photographic Analysis Apparatus

A Xenon Corporation 437B Nanopulser fed a DeLeone N-787B Broad Spectrum spark generator providing light to obtain the shadowgraphs (See Figure 3.9) by reflecting the light from a 152.4 cm focal length/14.4 cm diameter mirror and using type 57 ISO 3000/36° Polaroid film and a Polaroid 545i camera to capture the image. Using an additional mirror and a light-splitting knife edge, the schlieren images were obtained using the same light source and an additional 11.2 cm diameter focusing lens. This is shown in Figure 3.10.

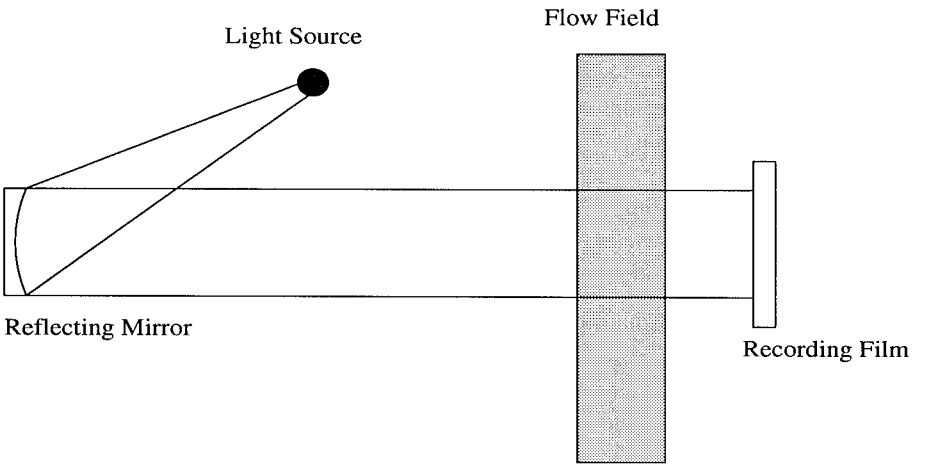

Figure 3.9 Shadowgraph Setup

3.5 Pressure and Temperature Measurement

The total pressure measurements were taken with an Endevco brand 0-0.69 MPa pressure transducer set at 2.13 X $10^5 \pm$ 690 Pa. The total temperature was measured using an Omega Engineering Type K thermocouple.

3.6 Model Description

The model used to generate the shock-boundary layer interaction was a machined aluminum wedge rigidly mounted to the wind tunnel floor. The flow deflection angles for the three wedges were $5°, 7°$, and 10^0. Each wedge measured 7.21 cm in the streamwise direction and 6.35 cm across

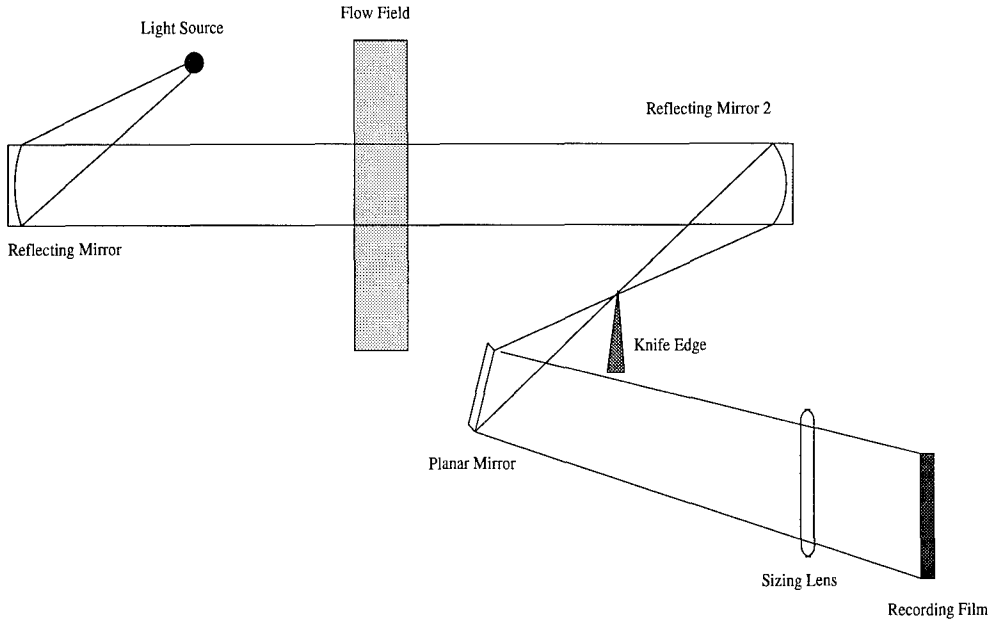

Figure 3.10 Schlieren Setup

the wind tunnel test section. The shock-generating wedges were set at 6.99 cm downstream of the upstream test section edge so that the shock wave/boundary layer interaction would appear in the available LDV windows. The wedges were secured to the tunnel floor with four screws and sealed with a rubber gasket as seen in Figure 3.11. This designed allowed rapid changeout of the wedge without removing the test section from the wind tunnel.

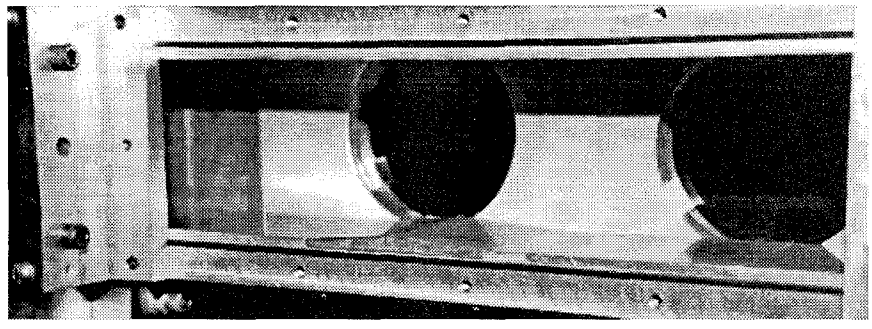

Figure 3.11 Photograph of Shock-Generating Wedge and Tunnel Floor

Each wedge had three pressure taps equally spaced on the upstream face. The tunnel floor also had a pressure tap 1.27 cm upstream of the wedge leading edge. The tunnel ceiling had nine

pressure taps spaced 1.0 cm apart, beginning at 16.18 cm from the upstream edge of the test section, to locate the shock wave reflection from the ceiling. The pressure ports were also designed to address the pressure gradient variations between shock wave angles (See Figure 3.12).

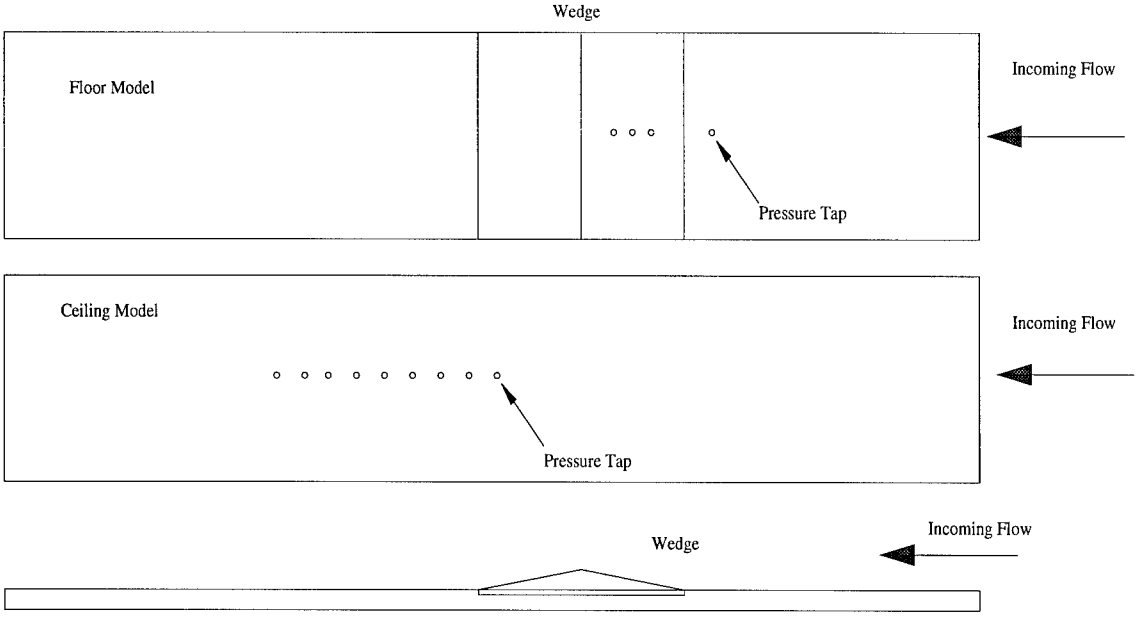

Figure 3.12 Pressure Tap Locations

3.7 Wind Tunnel Test Procedure

When the vacuum tanks were below 10 mmHg the tunnel was ready for operation. The first step was to release the gate valve and expose the test section to the vacuum system. Then, the high pressure air was released through the ball valve to begin high-speed airflow. The tunnel took approximately 8 seconds to reach steady-state. During this time, two jets of the six-jet seeder system were activated, injecting the seed into the test section. Once steady-state flow was achieved, the Burstware software was activated to collect data for 12 seconds, sampling as much data as possible. After this was complete, the tunnel was shut down by first closing the ball valve, stopping the high pressure air. It was then safe to close the gate valve and begin to drawdown the vacuum system again. The vacuum system could recharge in approximately 6 minutes.

3.8 Traverse and Laser Alignment

To simplify LDV operation and coordinate transforms, the traverse bench was set perpendicular to the test section. The alignment was by accomplished by aligning the lasers parallel to the traverse bench. The probe supports were marked at 1^o increments, allowing accurate alignment with the bench. The traverse assembly was then rotated until the lasers reflected back on themselves, ensuring an accurate alignment. Then, the lasers were rotated 3.5^o off axis of the bench, allowing the lasers to point downstream and operate in the forward-scatter mode. This also protected the sensitive photomultiplier tubes from direct laser light from the transmitting lasers. This alignment does cause a small bias in the data but it was considered small enough to be neglected (See Figure 3.13). Notice that ϕ is 7^o. Luker shows that a 7^o angle provides the maximum laser scattering intensity(13).

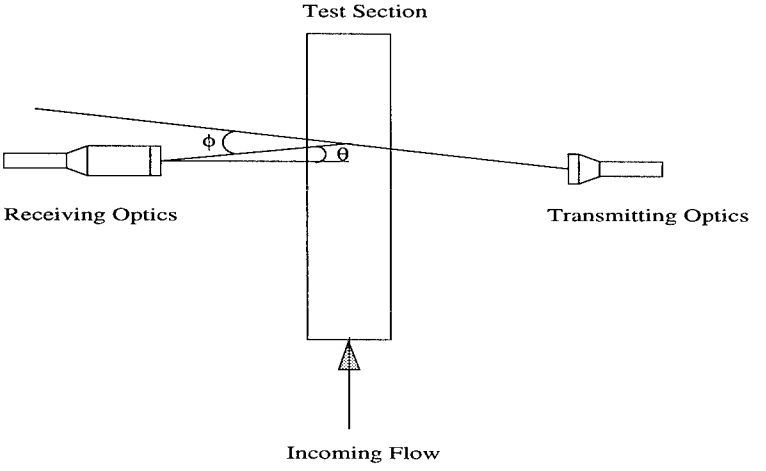

Figure 3.13 Laser and Traverse Alignment Relative to Test Section

Since the shock wave/boundary layer interaction occurred on a flat plate, the problems of LDV angular bias were minimized. However, to place the origin of the traverse it was necessary to align the lasers with the test section floor. Using a set of Argon-ion laser protective goggles, the laser reflection points appeared as small dots. These small dots were located at the point of maximum laser intensity. These dots were placed by moving the traverse such that the two 514.5

nm (green) beams were bisected by the tunnel floor. This location was set as the traverse origin point.

With the transmitting optics aligned with the wind tunnel, the receiving optics were aligned with the control volume. Using the lasers from the transmitting optics, the two control volumes could be aligned with a rough degree of accuracy. The lasers were then raised to the freestream of the test section and fine-tuned by injecting a small amount of seed into the test section. With the tunnel not operating and using the on-line display feature of the Burstware software, it was possible to complete the alignment process. The on-line display feature constantly updates the validity and the data acquisition rates as the receiving optics were adjusted. This allowed the receiving optics to be adjusted very accurately for the maximum data acquisition and validity rates. The goal for this process was both BSA's over 90% validity and data acquisition rates over 24 KHz. It was important to maximize both BSA's simultaneously as it was possible to achieve high rates on one BSA while the other BSA's rates were very low.

3.9 Burst Spectrum Analyzer Settings

The fixed software settings for the Burstware Data Acquisition Software are presented in Tables 3.1 to 3.3. These settings were kept constant throughout the experiment.

Table 3.1 **Quick** Menu Constant Settings

Category	**BSA 1 Setting**	**BSA 2 Setting**
Bandwidth (m/s)	325.12	246.7
Shifter Mode	Norm	Norm
Signal Gain (dB)	42	42
High Voltage (V)	1304	1504
Max. Anode Current (mA)	1.6	1.6
Pedestal Attenuation (dB)	6	6
Duty Cycle (%)	100	100
Dead Time	0	0

Table 3.2 **Soft** Menu Constant Settings

Category	BSA 1 Setting	BSA 2 Setting
Timer Clock	Master	Slave
Coincidence Mode	Master	Slave
Arrival Time Base	Internal	Internal
Burst Detection	Both	Both
Oversize Rejection	1	1
Buffer Mode	FIFO	FIFO
Max. Anode Current (mA)	1.6	1.6
Quality Factor (%)	50	50
Collection Mode	Burst	Burst

Table 3.3 **BSA Program** Menu Constant Settings

Category	BSA 1 Setting	BSA 2 Setting
Timeout (Sec)	12.0	12.0
Number of Bursts	150000	150000
Velocity	Yes	Yes
Transit Time	Yes	Yes
Arrival Time	Yes	Yes

In addition to the constant settings above, the record length was kept constant at 16 samples. The variable settings adjusted during the experiment were the center frequency on BSA 1 (u-component of velocity), and the size of the FIFO Buffer. The center frequency was kept as close as possible to the average velocity at any given point. This value needed to be adjusted as the point of interest moved from the wall to the freestream. The size of the FIFO buffer determined how many bursts were stored on the BSA's before transfer to memory. If the buffer size was set at 2000, the BSA's would collect 2000 bursts before sending them to memory. The problem with this buffer was the last group of bursts would not be sent to memory. If 2500 bursts were collected, the last 500 bursts would be lost. In order to keep as many bursts as possible, the FIFO buffer needed to be reduced. However, a balance was sought because if the FIFO buffer was too small the BSA's spent too much time transfering data and not collecting it.

Coincidence filtering was performed on the data by the BSA's based on a user-input value. According to the Burstware Manual (5), best results are achieved when the coincidence window is set at twice the record interval. Realizing that at 650 m/s, a particle will transit the 0.276mm long

control volume in roughly 0.4 μs, following this advice would limit the record length to 8 samples. When the record length was set to 16 samples, the record interval was 0.333μs, slightly below the minimum transit time. The effects of record length are discussed in Luker where it was shown that the 16 sample record length was well-behaved while the 8 sample record length showed enormous scatter (13). Therefore, for this experiment, the coincidence window value was set to 0.333μs and the record length was set to 16 samples.

IV. Data Reduction Techniques

4.1 Velocity Calculation

The Dantec Burst Spectrum Analyzer used a Fast Fourier Transform (FFT) to determine the Doppler frequency of the scattered laser light. This frequency was converted to velocity using the frequency-velocity calibration factor, C_{fv}. During this project, the calibration factors for the u and v components were

$$C_{fv,u} = 8.128\frac{m/s}{MHz}, C_{fv,v} = 7.709\frac{m/s}{MHz} \tag{4.1}$$

The total velocity can be shown to be (13)

$$\overline{Q} = \sqrt{\overline{u}^2 + \overline{v}^2 + \overline{(v')^2}} \tag{4.2}$$

and the Root Mean Square (RMS) value of the velocity components becomes, with the assumption of $\frac{\overline{u}}{\overline{Q}} \simeq 1$ and $\frac{\overline{v}}{\overline{Q}} \ll 1$,

$$\overline{(Q')^2} = \overline{(u')^2} \tag{4.3}$$

4.2 Separation of Mean and Turbulent Mach Numbers

As previously noted, the turbulent characteristics of the flow greatly complicate the calculation of the flow variables. The Mach number is no different. Generally, the Mach number is given by

$$M = \frac{Q}{a} = \frac{Q}{\sqrt{\gamma RT}} \tag{4.4}$$

Expanding the Mach number into mean and fluctuating components and solving for M' gives, after manipulation (13), the fluctuating Mach number RMS value

$$\overline{(M')^2} = \overline{M}\frac{\overline{(Q')^2}}{\overline{Q}}\left[1 + \frac{1}{2}(\gamma - 1)\overline{M^2}\right] \tag{4.5}$$

4.3 Mach Number Calculation

The local Mach number was calculated using the measured LDV velocity and the total temperature measured in the plenum along with the assumptions of adiabatic flow and a calorically perfect gas. The adiabatic energy equation was developed for turbulent flow by expanding the adiabatic relationship between temperature, stagnation temperature, and Mach number (13). The final mean Mach number expression is

$$\overline{M} = \left[\frac{2\overline{Q}^2}{2\gamma R\overline{T_o} - \overline{Q}^2(\gamma - 1)}\right] \tag{4.6}$$

It is important to remember that this Mach number expression was developed assuming adiabatic flow (constant total temperature) throughout the boundary layer. Kistler (12) verified this assumption by measurement on a flat plate.

4.4 Density and Temperature Calculation

Calculation of the density and temperature profiles were complicated by the fact that the only measurements taken in the test section were the wall pressure and temperature. The density and temperature in the boundary layer were estimated based on certain assumptions. If the validity of these assumptions breaks down, the reported values of the temperature, density, and, of course, incompressible Reynold's shear stress will be incorrect.

4.4.1 Flat Plate. On the flat plate, the density was calculated assuming that the pressure normal to the surface was constant. Using this assumption, the modified Crocco-Busemann approximation produces (6)

$$\frac{\rho_w}{\overline{\rho}} = \frac{\overline{T}}{T_w} = 1 + B'\left(\frac{\overline{u}}{u_e}\right) - (A')^2\left(\frac{\overline{u}}{u_e}\right)^2 \tag{4.7}$$

where ρ_w and T_w are the density and temperature at the wall and A' and B' are given by

$$(A')^2 = \frac{\frac{\gamma-1}{2} r M_e^2}{\frac{T_w}{T_e}} \tag{4.8}$$

$$B' = \frac{1 + \frac{(\gamma-1)}{2} r M_e^2}{\frac{T_w}{T_e}} - 1 \tag{4.9}$$

The density at the wall, ρ_w, was calculated using the measured wall temperature and pressure and the perfect gas relation:

$$\rho_w = \frac{p_w}{R_u T_w} \tag{4.10}$$

4.5 Boundary Layer, Displacement and Momentum Thickness Calculations

The boundary layer thicknesses, based on velocity (δ_u), was calculated for the flat plate. The boundary layer thicknesses were calculated by choosing the largest velocity from a given traverse as the edge value, non-dimensionalizing the profile by the edge value, and searching outward from the wall until the value of $\frac{u}{U_e} \geq 0.995$ was attained. The value of δ was then calculated by linear interpolation between the data points just above and below the boundary layer edge. The displacement and momentum thicknesses were calculated using the equations in White (19) and implemented by Luker (13).

4.6 Turbulence Statistics

Turbulence statistics are needed for two reasons. First, statistical variables appear directly in the time-averaged form of the Navier-Stokes equations. In addition, the turbulence statistics help to understand features of the fluctuating flowfield. For an additional discussion of turbulence statistics, see Luker (13).

The fluctuation from the mean, $x' = x - \overline{x}$, is the variable around which the turbulent statistics are built. Here, the variable x was used to show that turbulent statistics were generated for both the u and v components of velocity. One problem appears, though. By definition, the average of x' is zero. Therefore, in order to get an estimate of the average size of the fluctuations, the Root Mean Square (RMS) value of x' was used. The RMS value of x' is defined as

$$X_{RMS} = \sigma_x = \sqrt{\frac{\sum (x')^2}{(n-1)}} \tag{4.11}$$

Here the summation is performed using the n samples collected. Notice that the denominator is $n-1$ samples. The Burstware software, however, calculates the RMS value over n samples. See Appendix B for a more complete discussion of the effect of this error on the results.

The Burstware software also performs calculations to determine the skewness (Sk_x) and flatness (Fl_x). These are shown below.

$$Sk_x \equiv \frac{\sum (x')^3}{\sigma_x^3 n} \tag{4.12}$$

$$Fl_x \equiv \frac{\sum (x')^4}{\sigma_x^4 n} \tag{4.13}$$

The skewness is important when using LDV because it helps determine if the results are affected by seeding problems. On the other hand, the flatness is used to calculate the intermittency

factor, γ_u. This factor is the ratio of the flatness of the Gaussian curve (3.0) and the flatness of the measurements:

$$\gamma_u = \frac{3.0}{Fl_u} \tag{4.14}$$

The most important statistical variable is the velocity correlation $\overline{u'v'}$. This appears directly in the Reynold's Averaged Navier-Stokes equations and, along with density, are the building blocks of the incompressible Reynolds shear stress. The correlation was calculated using

$$\overline{u'v'} = \frac{\sum(u'v')}{n} \tag{4.15}$$

Notice that while the averages of u' and v' are zero, the average of the product $u'v'$ may not be zero.

The final statistical value calculated was the velocity correlation coefficient, R_{uv}, which is calculated by

$$R_{uv} = \frac{\overline{u'v'}}{\sigma_u \sigma_v} \tag{4.16}$$

R_{uv} was used to provide insight in the nature of the turbulence. As an example, if the turbulence was isotropic (no preferred direction of turbulent structures), R_{uv} shold have had a value of 1.0. Usually, for low speed flat plate flow shows that the magnitude of R_{uv} is approximately 0.4 to 0.5. (3)

4.7 Wall Shear Stress

The wall shear stress was interatively calculated using the bisection method to solve the skin-friction equation developed by Van Driest (6) and implemented by Luker (13).

$$\frac{0.242}{A'\sqrt{C_f(\frac{T_w}{T_e})}}\left[\sin^{-1}\left(\frac{2(A')^2-B'}{\sqrt{4(A')^2+(B')^2}}\right)+\sin^{-1}\left(\frac{B'}{\sqrt{4(A')^2+(B')^2}}\right)\right]=\kappa+\log(Re_xC_f)-\omega\log(\frac{T_w}{T_e}) \tag{4.17}$$

where $\kappa = 0.41$ and $\omega = 0.68$. It should be noted that this equation was developed for turbulent flow over a flat plate. Re_x is the Reynolds number based on the distance from the leading edge of a flat plate immersed in a uniform flowfield. The wind tunnel is modeled as a flat plate with the leading edge at the nozzle throat.

For a discussion of the Van Driest velocity profile as implemented in this study, see Chapter 4 of Luker (13).

4.8 Turbulent Kinetic Energy

The Turbulent Kinetic Energy (TKE) is a measure of the energy contained in the turbulent motion of a flowfield. The TKE is defined as

$$TKE \equiv \frac{(u')^2+(v')^2+(w')^2}{2} \tag{4.18}$$

Even in a two-dimensional flowfield, where $\overline{w} = 0$, the lateral fluctuation, w', is not necessarily zero. With the current experimental setup it was not possible to measure w'. Therefore, in order to calculate TKE, it was assumed that the size of w' is the same order as v', and the estimated TKE relationship becomes

$$TKE \equiv \frac{(u')^2+(v')^2+(v')^2}{2} \approx \frac{(u')^2}{2}+(v')^2 \tag{4.19}$$

V. Results and Discussion

5.1 Roadmap

This discussion of the results for this study will begin with an explanation of the coordinate systems used followed by a summary of the test conditions. Schlieren and shadowgraph photographs for each flow field are then presented in the section on flow visualization. The flat plate Laser Doppler Velocimetry (LDV) results are presented and compared to Luker (13), Hale (9), and Elena and LaCharme (7). The shock wave/boundary layer interaction discussion begins with a comparison to the data from Rose and Johnson (16) for a similar shock wave/boundary layer interaction flowfield. The present study results for the flowfield induced by a wall-mounted 5^o wedge are then presented, to illustrate the effects of a shock wave/boundary layer interaction. Finally, the effects of shock strength on the properties of the flowfield are examined.

5.2 Comments on Coordinate Systems

Throughout this report, two different coordinate axes are used. In order to avoid confusion during the discussion, each will be developed.

The wind tunnel coordinate scheme is a Cartesian system with the tunnel nozzle at $x = 0$. The y-coordinate is pointed vertically with the positive direction down. The z-coordinate completes the axis system using the right-hand rule.

The shock wave/boundary layer interaction coordinate system, denoted by the capital letters (X, Y, Z), are used to describe variables in relation to the shock wave/boundary layer interaction. The X-coordinate is pointed down the tunnel with positive in the downstream direction. The Y-coordinate is pointed positive down and the Z-coordinate completes the system using the right-hand rule (see Figure 5.1).

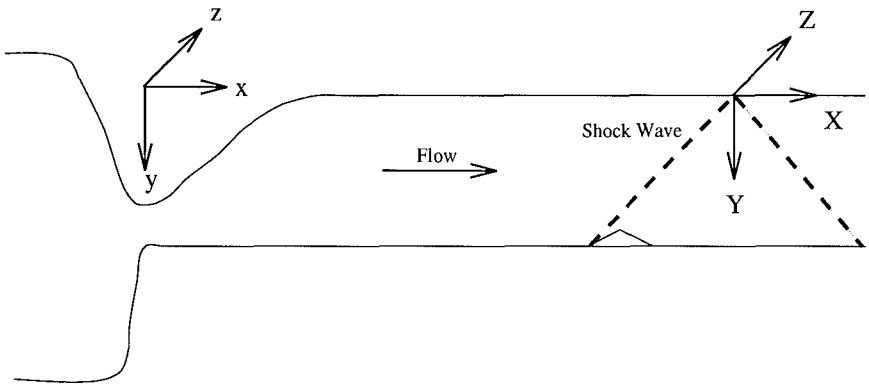

Figure 5.1 Wind Tunnel and Shock Wave/Boundary Layer Interaction Coordinate Systems

5.3 Test Conditions

The pressure transducer located in the settling chamber showed that the wind tunnel was operating with a stagnation pressure of $2.18\text{X}10^5 \pm 3.4\text{X}10^3$ Pa. The stagnation temperature measured in the settling chamber was 297K $\pm$ 2.1K. This variation was averaged between traverses. The stagnation temperature climbed throughout a single traverse but the variation was usually less than 1K. The temperature climb was attributed to the operation of the compressors. The mean temperature never rose above 300K. Because of this temperature rise, the stagnation pressure and temperature were recorded during each data point and used during data reduction accordingly. The Mach number of the flow was approximately 2.9 with $Re_x = 8.423\text{X}10^6$ and $Re_{\delta_o} = 1.332\text{X}10^5$.

5.4 Flow Visualization

Flow visualization photographs, both Schlieren and shadowgraphs, were taken of each flowfield using the setup described in Chapter 4. The flow for each photo is left to right.

5.4.1 Flat Plate. The flat plate Schlieren photograph is shown in Figure 5.2. The waves crossing the tunnel in an "X" pattern are shocks caused by slight misalignments of the tunnel test sections.

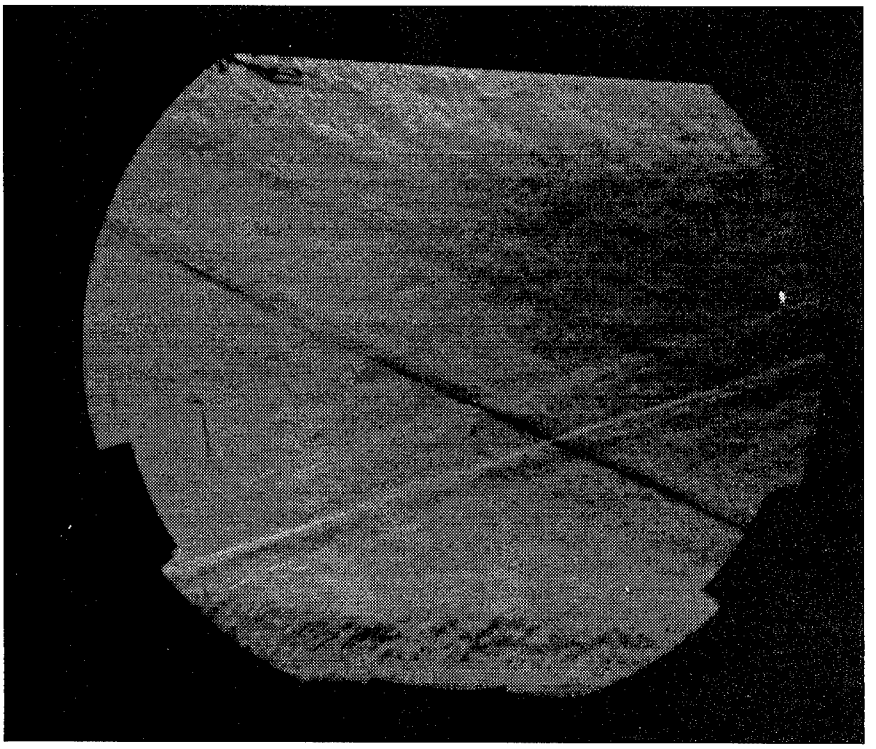

Figure 5.2 Schlieren of Flat Plate Using Horizontal Knife Edge

The flat plate shadowgraph photo, shown in Figure 5.3, clearly shows that the seam shocks are very weak and have little effect on the flow.

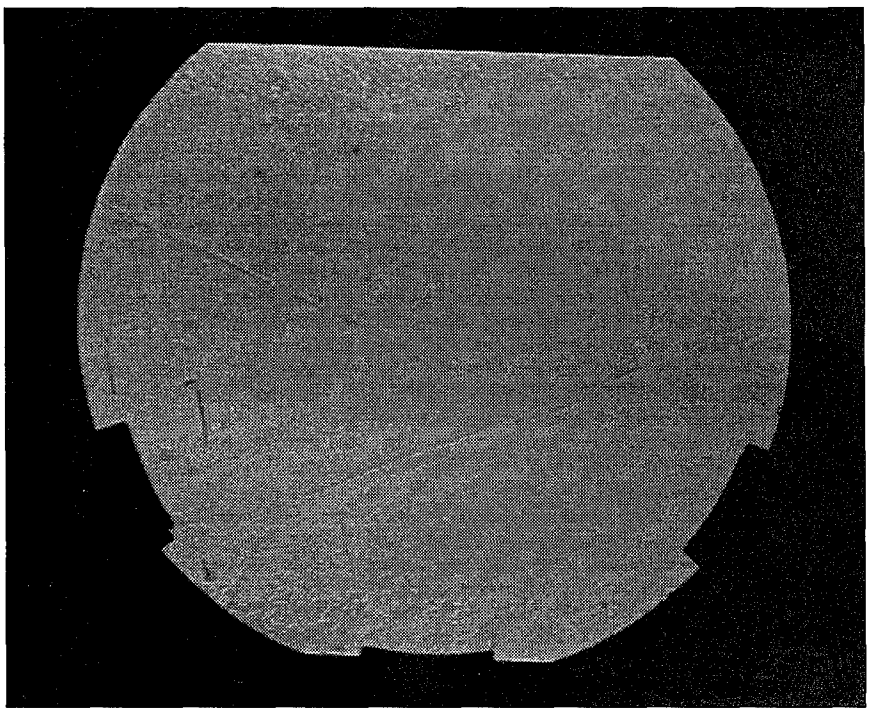

Figure 5.3 Shadowgraph of Flat Plate Flowfield

5.5 Effective Flow Turning Angle

During initial model checkout runs of the wind tunnel, it was observed that the shock wave interaction was occurring significantly upstream of the location expected by inviscid shock wave theory. As this moved the interaction outside of the available LDV viewing area, this was of great concern. The shock wave generators were designed assuming inviscid, M = 2.90, uniform flow. However, from initial shadowgraph photographs, the shock wave angle for the 5^o, 7^o, and 10^o were 26.5^o, 28.5^o, and 31.5^o with an error of $\pm 0.5^o$. Initally, the Mach Number of the tunnel was considered the suspect value. However, after examination of the tunnel and comparing the present configuration with other work performed in this facility, the Mach Number was ruled out. After careful consideration, the suspect value is the assumption of inviscid flow. It appears the boundary

layer, on the same order as the shock generating wedge, causes the flow to turn more sharply for a given wedge angle. Using the θ-β-Mach relationship (2) and holding the Mach Number at 2.90 and using the above values for the shock wave angle, the effective turning angles, denoted by θ_{eff}, became 8.17^o, 10.40^o, and 13.52^o, respectively. It appears that the boundary layer constricts the flow into a smaller area, producing a greater turning angle. Even though the effective turning angle is greater than the wedge angle, for clarity, the wedge angle will be continue to be used to identify each flowfield.

5.5.1 Shock Wave/Boundary Layer Interaction. The shock wave/boundary layer interaction for the shock wave induced by the 5^o wedge is shown Figure 5.4. The 5^o wedge flow, because of the low shock wave angle, needed two window views in order to visualize the entire interaction region. Figure 5.4 shows the interaction in the upper right corner of the photo. The accompanying shadowgraph is shown in Figure 5.5. The shock wave in the lower half of the photos is the shock wave off the trailing edge of the wedge, after which the flow is again aligned with the tunnel walls.

The downstream section of the 5^o wedge flow is shown in Figures 5.6 and 5.7. The interaction is in the extreme upper left corner of the photos.

The shock wave/boundary layer interaction for the 7^o wedge flowfield is shown in Figures 5.8 and 5.9. The larger shock wave angle of the 7^o wedge flowfield have allowed the entire interaction region to be viewed in one photo. Note the additional waves emanating from the boundary layer after the interaction in Figure 5.9. Also, note the clear intermittency at the top of the boundary layer at the lower edge of Figure 5.8. At the vertex of the shock wave reflection, note the small lambda shock developing. From this photo, it can be seen that the 7^o wedge flow may have a small separated region at the interaction. However, for the 5^o wedge flow there is no evidence of a lambda shock wave, allowing the conclusion to be drawn that the 5^o wedge flow is not separated at the interaction.

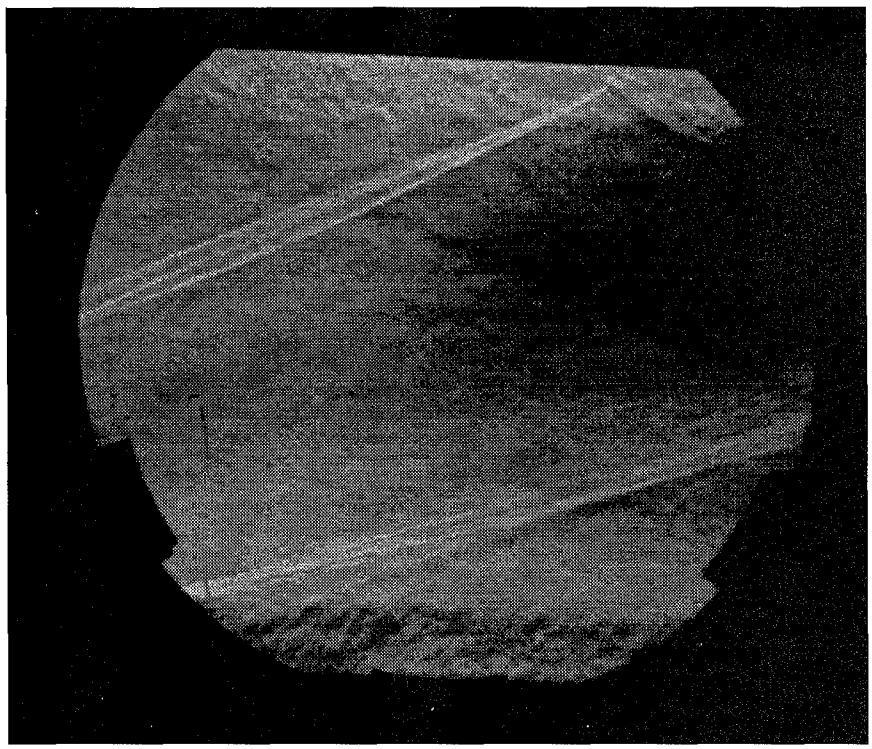

Figure 5.4 Schlieren of 5^o Wedge Flow Interaction Using Horizontal Knife Edge (Forward Window)

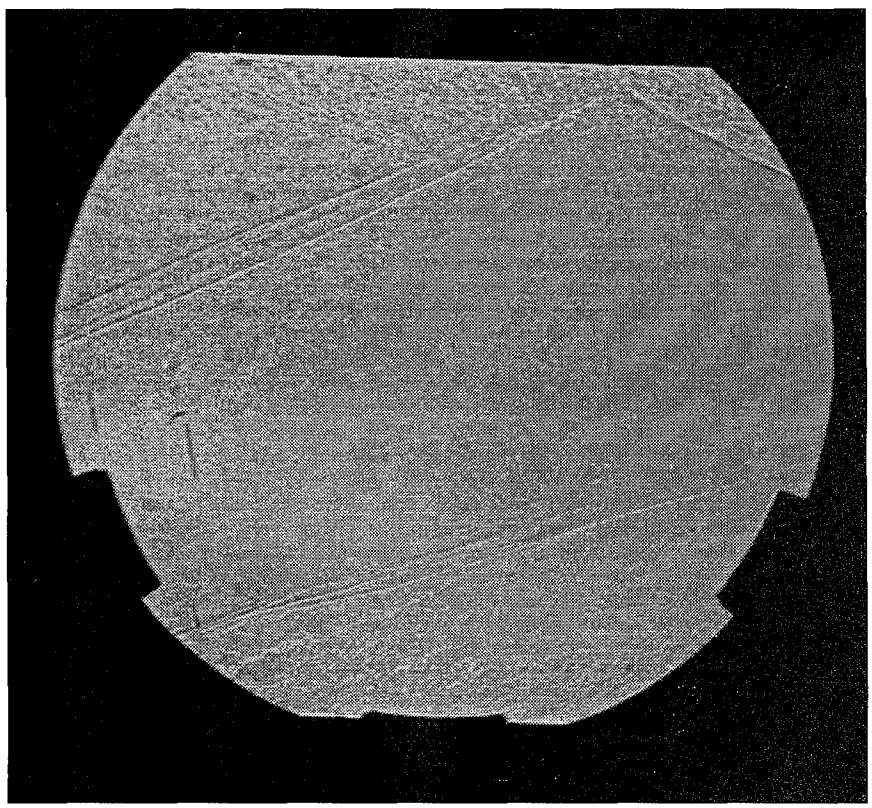

Figure 5.5 Shadowgraph of 5^o Wedge Flow Interaction Flowfield (Forward Window)

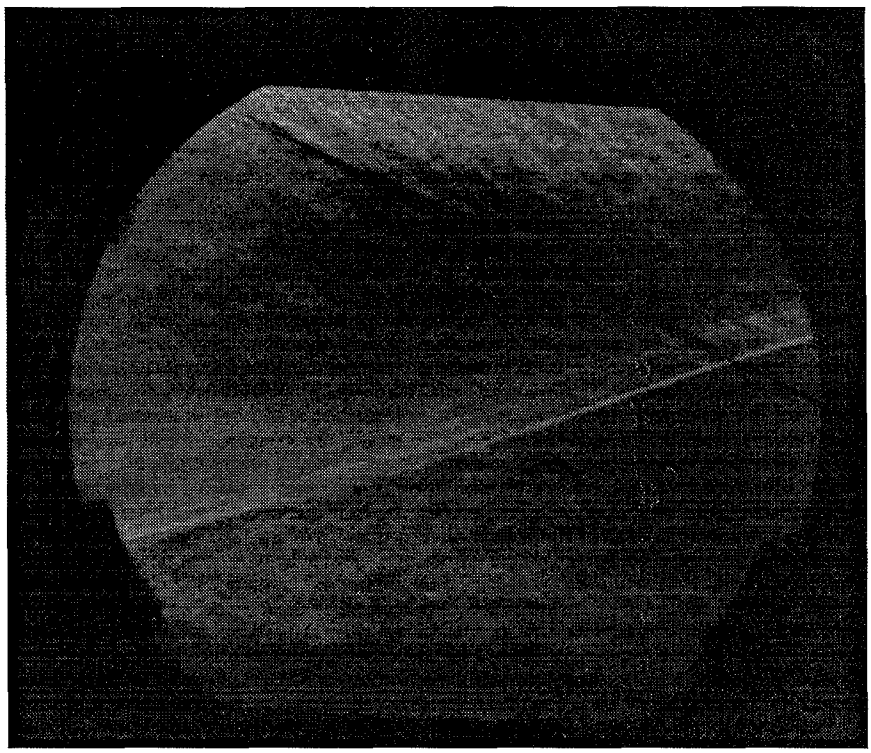

Figure 5.6 Schlieren of 5° Wedge Flow Interaction Using Horizontal Knife Edge (Rear Window)

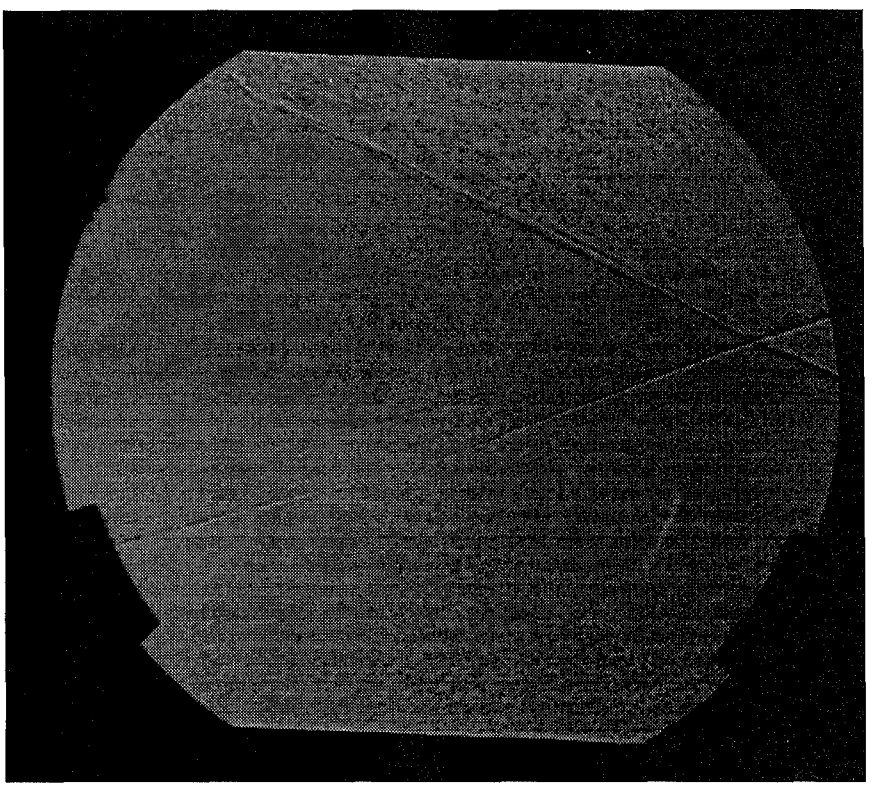

Figure 5.7 Shadowgraph of 5° Wedge Flow Interaction Flowfield (Rear Window)

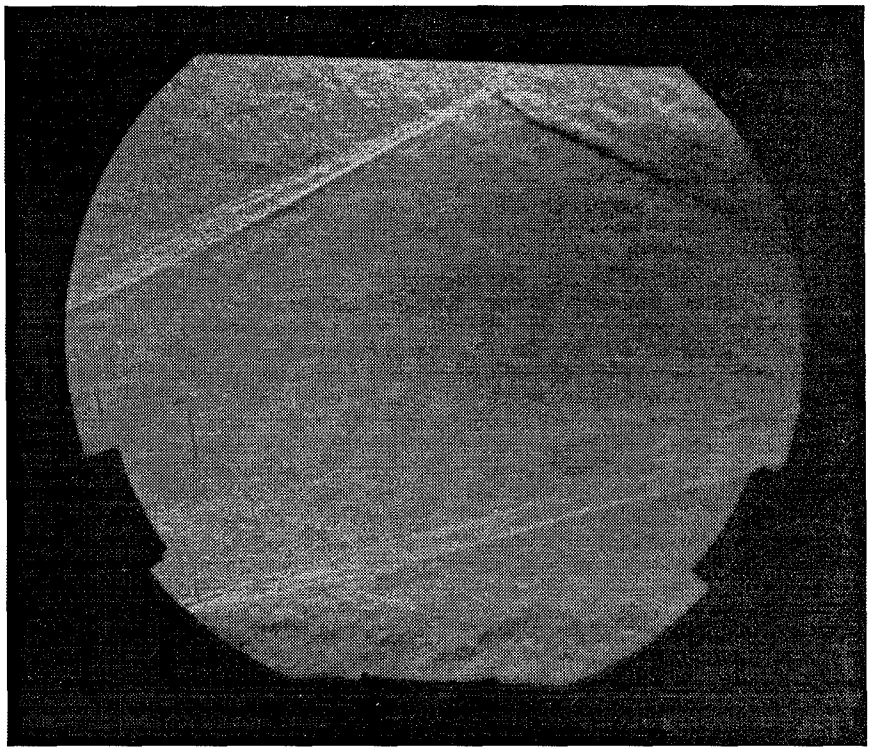

Figure 5.8 Schlieren of 7° Wedge Flow Interaction Using Horizontal Knife Edge

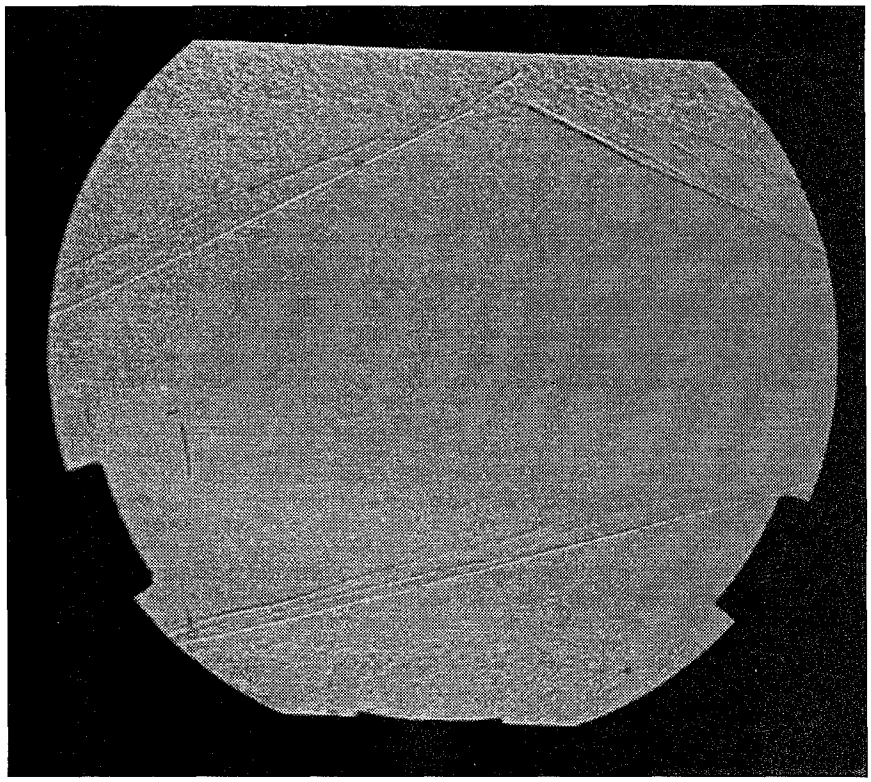

Figure 5.9 Shadowgraph of 7° Wedge Flow Interaction Flowfield

Figures 5.10 and 5.11 show the shock wave/boundary layer interaction for the 10^o wedge flowfield. Both of these figures show a small lambda shock forming at the interaction. Again, note the additional waves emanating from the boundary layer after the shock wave reflection. In these figures, the lambda shock pattern at the vertex of the shock waves is sharper and larger. The 10^o wedge flow has a larger separated region than the 7^o wedge flow.

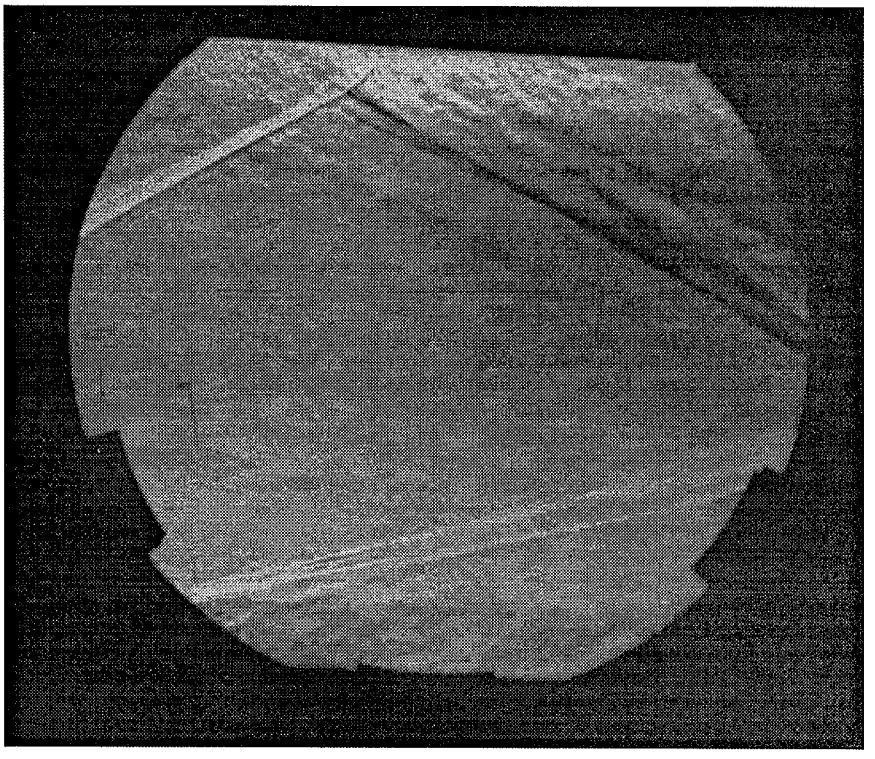

Figure 5.10 Schlieren of 10^o Wedge Flow Interaction Using Horizontal Knife Edge

5.6 Pressure and Temperature Measurements

The pressure distribution over the flat plate with the impinging shock wave is shown in Figure 5.12. Notice the sharp rise in pressure where the shock wave impinges on the flat plate. The flat plate pressure distribution is also presented for comparison. Downstream of the boundary layer/shock wave interaction, the pressure again drops towards the freestream value after the shock wave reflects off the boundary layer. As expected, the pressure rise increases with increasing wedge

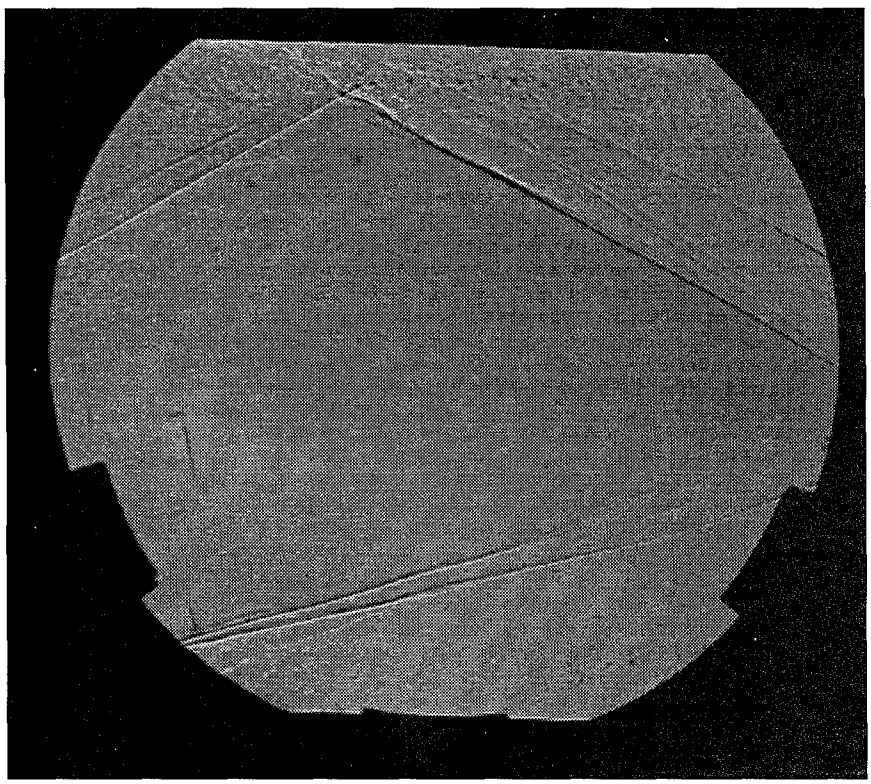

Figure 5.11 Shadowgraph of 10° Wedge Flow Interaction Flowfield

angle and is greatest for the 10^o wedge flowfield. The pressure rise from the shock waves generated by the 7^o and the 5^o wedges are less severe as shown in Figure 5.12. The pressure rise normalized by the first pressure measurement is presented in Table 5.1.

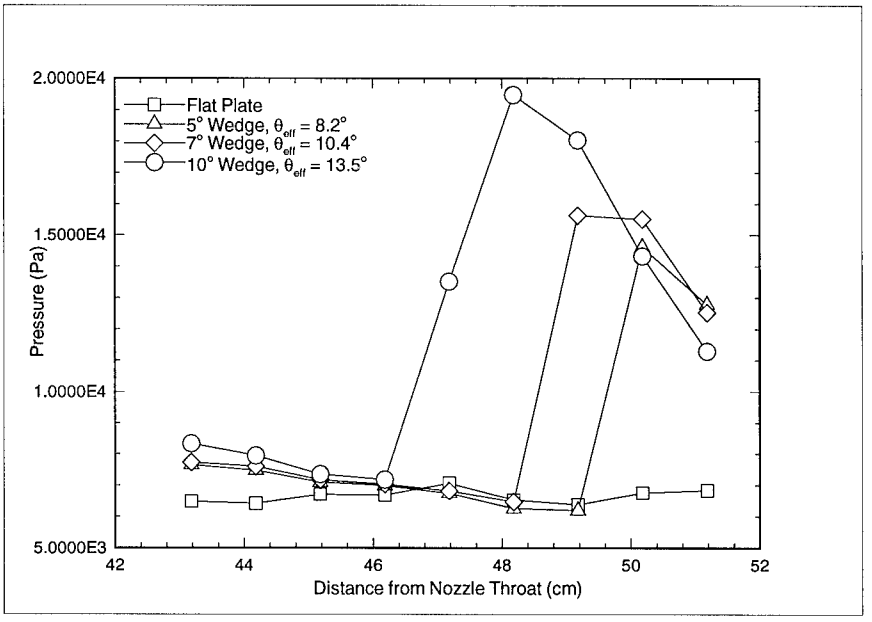

Figure 5.12 Pressure Distribution over Flat Plate with Impinging Shock Wave

10^o	7^o	5^o
2.34	2.02	1.91

Table 5.1 Normalized Shock Wave Interaction Pressure Increase

The pressure distribution on the shock-generating wedge is shown in Figure 5.13. As expected, the 10^o wedge had the highest pressure followed, respectively, by the 7^o and the 5^o wedges.

5.7 Flat Plate LDV Results

In order to ensure that the LDV system and wind tunnel were working correctly, it was important to compare to earlier studies. The works of Luker (13) and Hale (9) were chosen for a number of reasons. The author assisted on the data collection for Luker and Hale while learning the tunnel and LDV systems, and the data were readily available. Both Luker and Hale did exhaustive

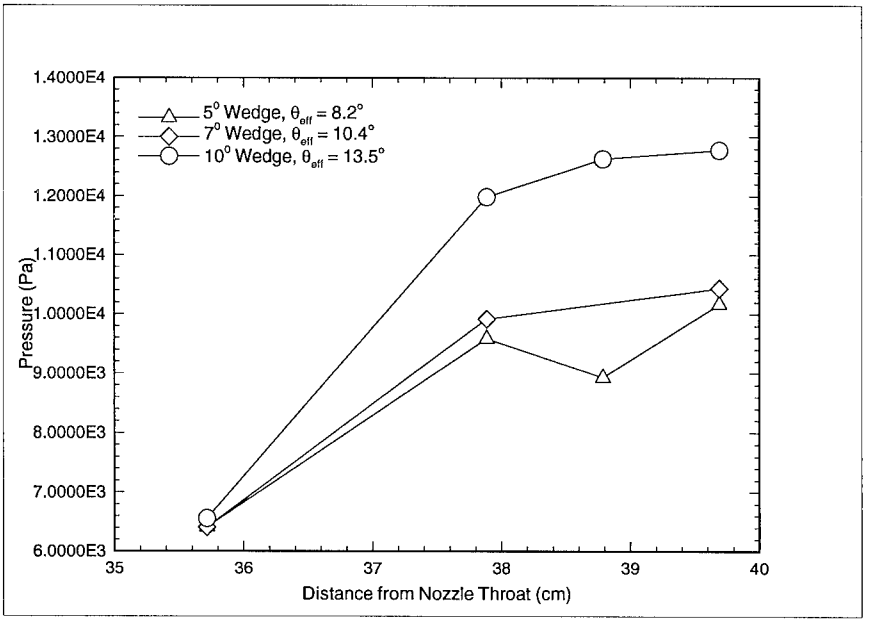

Figure 5.13 Pressure Distribution over Shock Generating Wedges

studies of the flat plate characteristics of the AFIT Mach 3 Wind Tunnel and this data are used to show the accuracy of the present system. The data are also compared to Elena and LaCharme 1988 flat plate experiments (7). In addition, the flat plate flowfield serves as a baseline against which the effects of the shock wave/boundary layer interaction may be ascertained.

5.7.1 Flat Plate Mean Flow Characteristics. Mean flow properties are compared to Luker's (13) and Hale's (9) data in the form of normalized velocity profiles $\frac{\overline{u}}{U_e}$, and Mach number profiles.

5.7.1.1 Flat Plate Velocity Profiles. To determine the flat plate boundary layer thickness, the streamwise mean velocity was scaled by the edge value (603.16 m/s at $x = 48$ cm) and plotted versus normalized distance from the wall (Figure 5.14). It is important to scale the velocity data by the edge value to eliminate any variations in test conditions between test traverses across the boundary layer. The boundary layer thickness was taken as the distance from the wall where $\frac{\overline{u}}{U_e} = 0.995$. The flat plate boundary layer thickness for this experiment was found to be

roughly 7.6 mm. The agreement with Luker's (13) and Hale's (9) measurements, seen in Figure 5.14, is excellent.

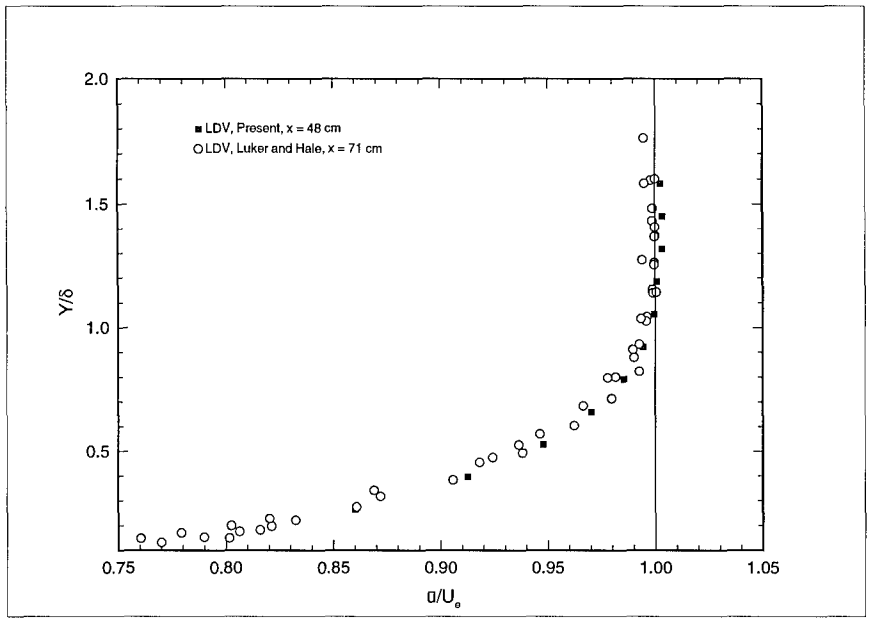

Figure 5.14 Normalized Flat Plate Velocity Profile

5.7.1.2 Flat Plate Mach Number. The Mach number was calculated as described in Chapter 4 and is shown in Figure 5.15. The data presented here is for $x = 48$ cm, equating to approximately 63.25 boundary layer thicknesses (δ_{fp}) downstream of the wind tunnel nozzle throat. The comparison data from Luker and Hale was taken at $x = 71$ cm (94.67 δ_{fp} downstream of the nozzle throat). Luker commented on the Mach number decay with downstream distance. This is seen in Figure 5.15. The present study is 23 cm upstream of Luker's (13) and Hale's (9) and the Mach number is 0.1 higher.

The fluctuating profile comparison is presented in Figure 5.16. In general, there is good agreement. The present data tends toward a higher fluctuating Mach number but it never approaches M = 1.0, eliminating any tendency to produce shocklets (18). In addition, Morkovin's hypothesis can be stated as "the dynamics of a compressible boundary layer will follow the incompressible pattern

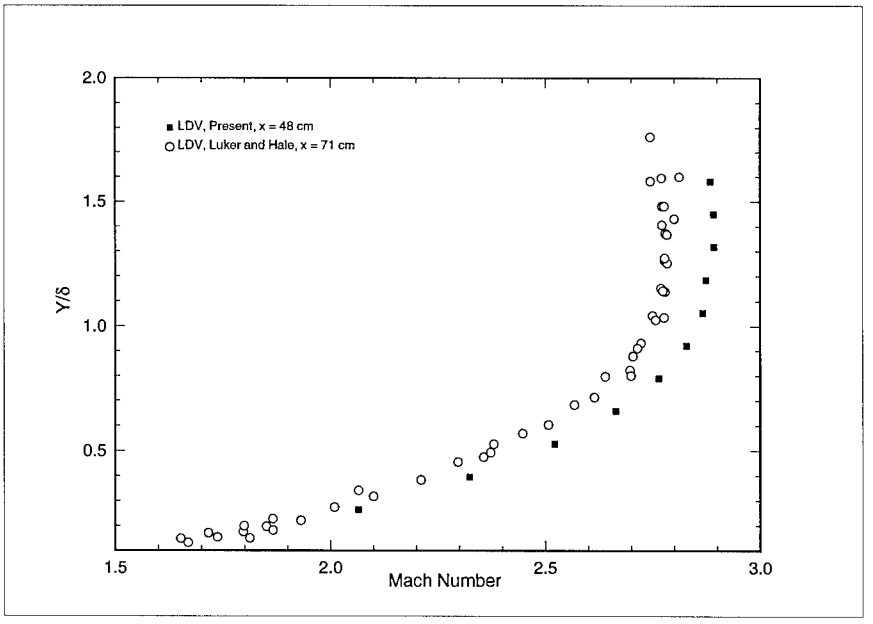

Figure 5.15 Flat Plate Mach Number Profile

closely, as long as the fluctuating Mach number, M', remains small." (18) Since the M' for the flat plate in the present study never exceeds 0.35, Morkovin's hypothesis should hold.

5.7.2 Flat Plate Velocity Fluctuations. The streamwise velocity fluctuations, scaled versus both local and edge velocities, are presented in Figures 5.17 and 5.18. Note, in Figure 5.17, the excellent agreement with both Luker and Hale (13) (9)and Elena and LaCharme (7). Although the comparison to Robinson, et al., (15) was not as good, it was still reasonable.

The cross-stream velocity fluctuation is presented in Figures 5.19 and 5.20, again scaled by local velocity and edge velocity, respectively. When scaled against the local velocity, the agreement appears excellent. However, when compared to the data of Robinson, et al., (15), the agreement noticeably worsens. The present data, along with Luker's (13) and Hale's (9) cross-stream velocity fluctuation, appear to fall much lower closer to the wall. However, in general, the agreement with the literature is considered acceptable.

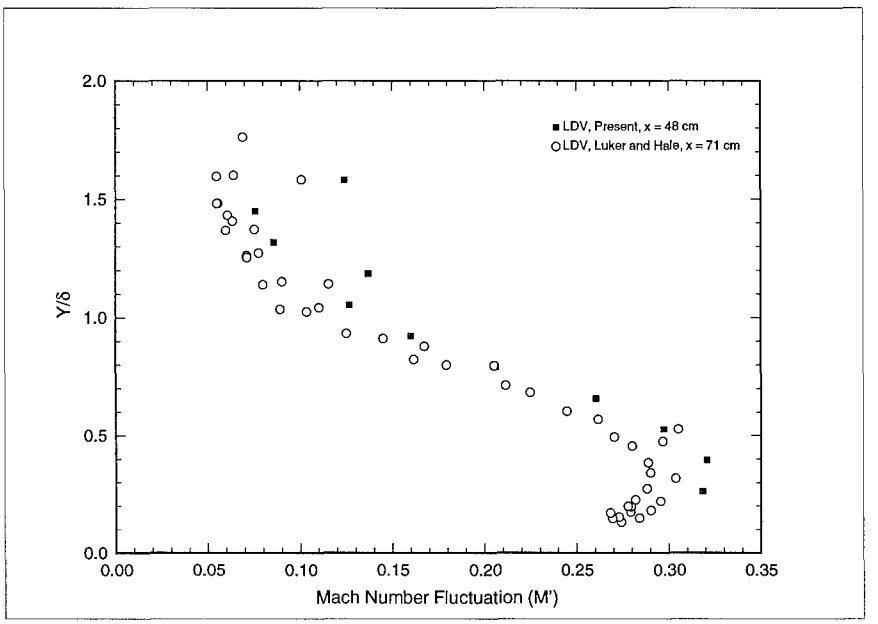

Figure 5.16 Flat Plate Fluctuating Mach Number Profile

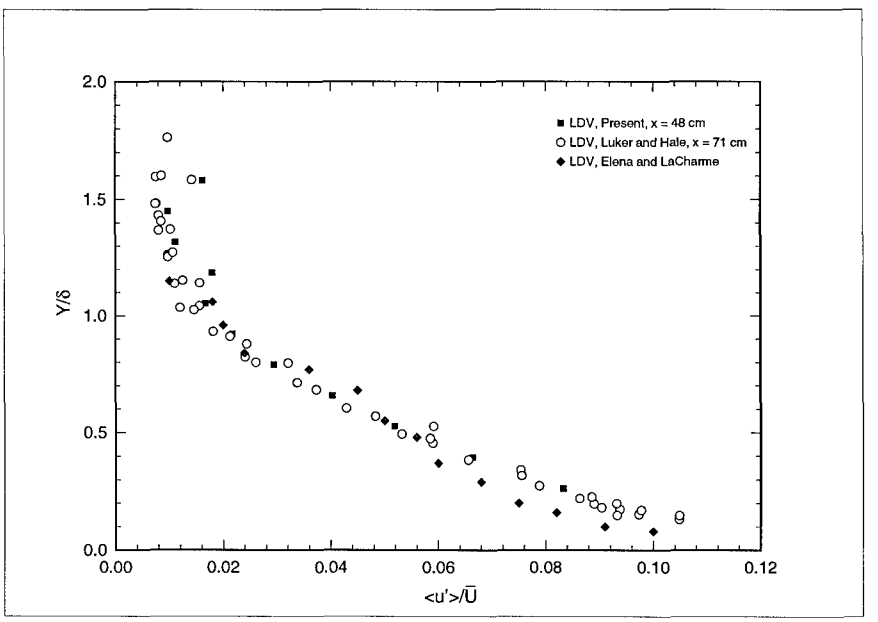

Figure 5.17 Flat Plate Streamwise Velocity Fluctuations Scaled by Local Velocity

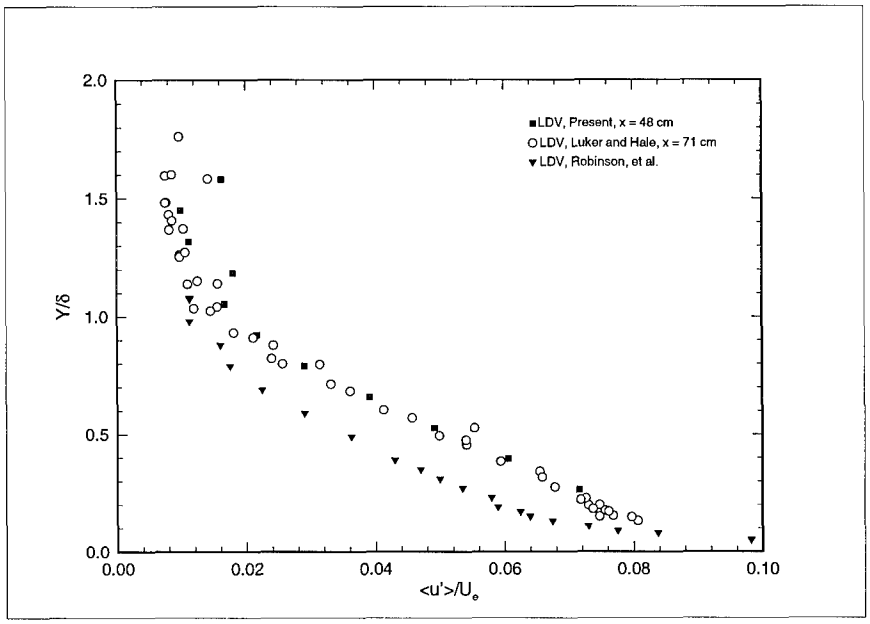

Figure 5.18 Flat Plate Streamwise Velocity Fluctuations Scaled by Edge Velocity

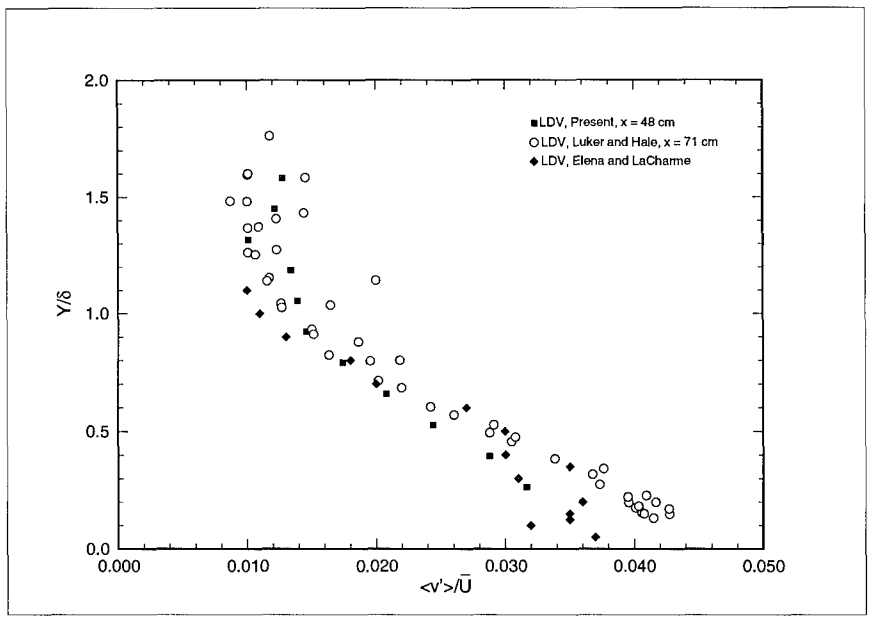

Figure 5.19 Flat Plate Cross-stream Velocity Fluctuation Scaled by Local Velocity

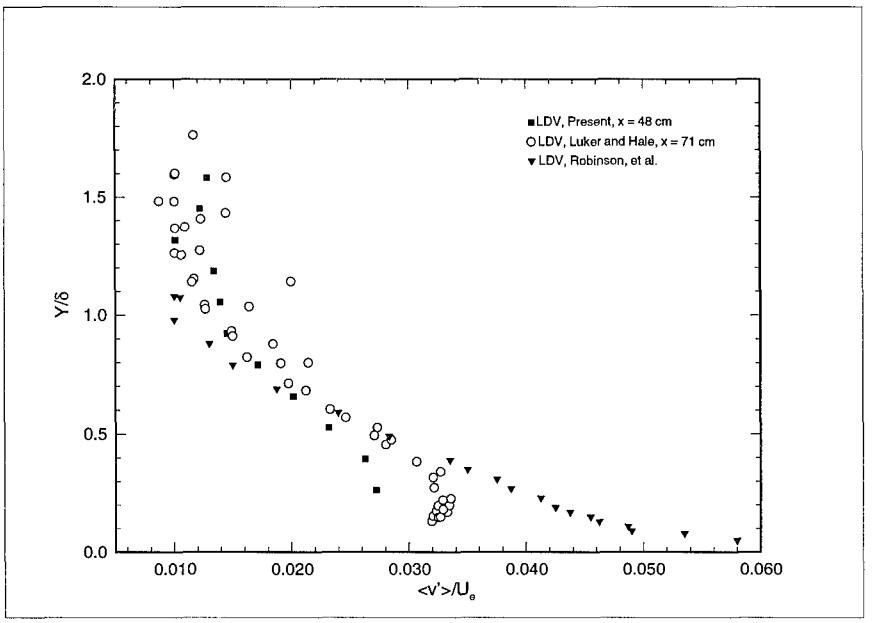

Figure 5.20 Flat Plate Cross-stream Velocity Fluctuation Scaled by Edge Velocity

5.7.3 "Incompressible" Reynolds Shear Stress. The incompressible Reynolds shear stress is defined as $-\overline{\rho u'v'}$. To facilitate comparison with other studies, it is important to represent the shear stress in a non-dimensional fashion. By noting that $\frac{\overline{-u'v'}}{\overline{u}^2}$ is equivalent to the incompressible Reynold's Shear, $-\overline{\rho u'v'}$, divided by $\overline{\rho u}^2$, a convenient and accurate scaling is obtained. This scaling is important for three reasons. First, this method of scaling eliminates any linear biasing which may influence the measurements (see Appendix B of Luker (13)). Also, this scaling allows easier comparison to CFD results, because turbulence models cannot resolve $\overline{u'v'}$ but can resolve, $\tau_{xy}^T \approx -\overline{\rho u'v'}$. More importantly, however, this scaling allowed the presentation of the incompressible turbulent shear stress profile using only directly measured information. This eliminates errors occurring from inaccurate calculations of other scaling properties. Figure 5.21 shows excellent agreement between Luker's (13) and Hale's (9) data and the present study for the "incompressible" shear stress.

The flat plate results presented above are considered acceptable and allow consideration of the primary flowfield of interest, the shock wave/boundary layer interaction.

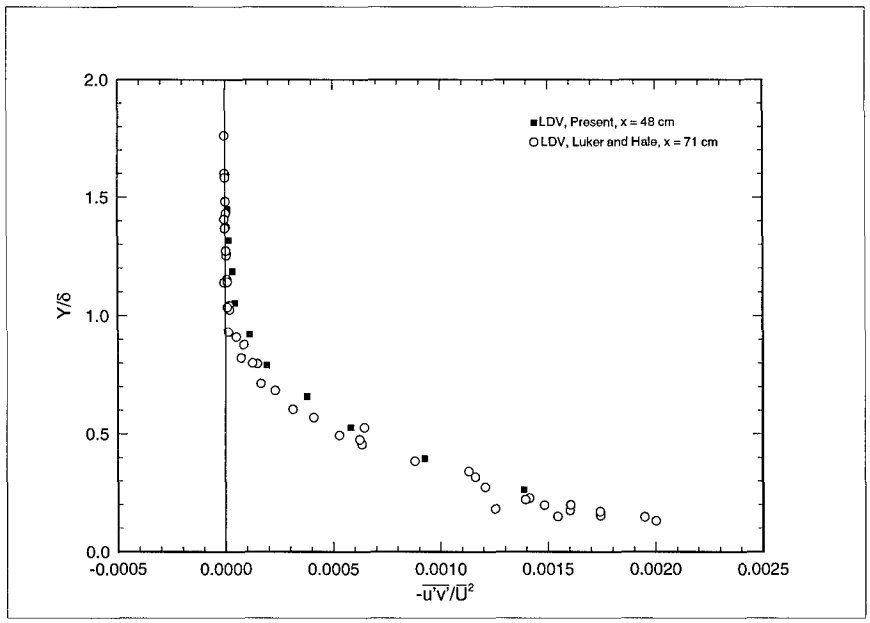

Figure 5.21 Incompressible Reynolds Shear Stress Scaled by Local Velocity

5.8 Shock Wave/Boundary Layer Interaction LDV Results

5.8.1 Scaling Factors. During the present study it was noted that the boundary layer thickness at each location would be extremely difficult to obtain for a number of reasons. Most importantly, the shock wave itself interferes with the boundary layer at the upstream measurement stations. In addition, the velocity profiles at the downstream stations did not have a classic boundary layer profile. Therefore, it was decided to scale the data by a universal set of scale factors. In addition, to facilitate comparison, a similar set of scale factors was developed for the data of Rose and Johnson (16). These values are shown in Table 5.2.

Present δ_o (mm)	Present U_o (m/s)	M_e	ρ_e $\frac{kg}{m^3}$
7.59	608.0	2.87	0.224
Rose and Johnson δ_o (mm)	Rose and Johnson U_o (m/s)		
22.9	613.0		

Table 5.2 Scaling Factors for Present Study and Rose and Johnson

5.8.2 Comparison to Rose and Johnson Shock Wave/Boundary Layer Interaction. The work of Rose and Johnson (16) was chosen for comparison because of the experimental similarity.

Their experiment turned the flow 7^o, creating a shock wave that impinged on a flat plate, and studied the turbulence properties both upstream and downstream of the interaction using both LDV and hot-wire anemometry.

As seen in Figure 5.22, there is good agreement with the velocity profile data of Rose and Johnson (16) at the upstream station. See Section 5.5 for a discussion on the effective turning angle, θ_{eff}. It is important to note that Rose and Johnson's upstream measurement station was at 13.7 cm or $X = 1.66\delta_o$ upstream of the shock wave/boundary layer interaction while the present study's upstream location was 1.0 cm or $X = 1.32\delta_o$ upstream of the vertex of the shock wave reflection.

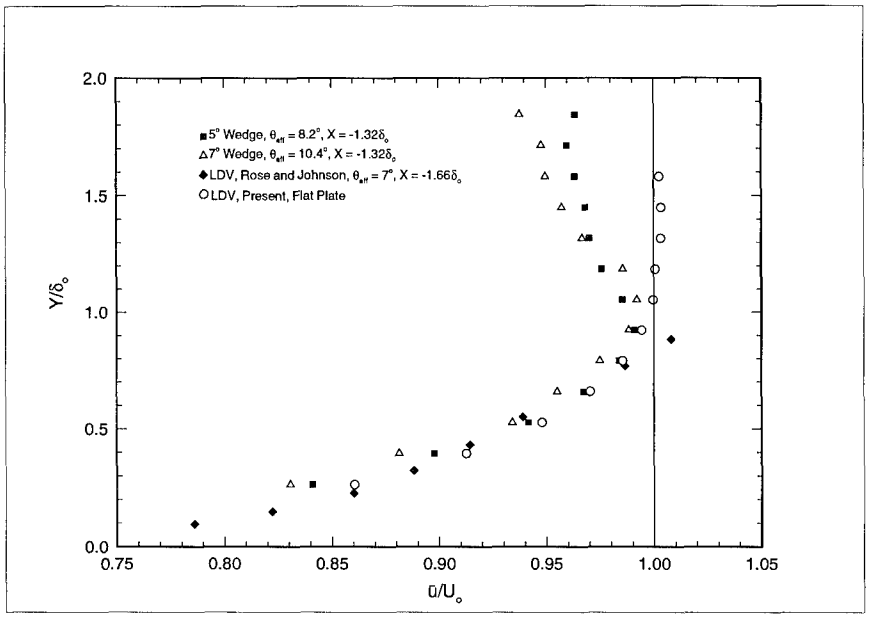

Figure 5.22 Normalized Velocity Profile Comparison at Upstream Stations

1^{st} Station	2^{nd} Station	1_{st} Rose and Johnson Station	2^{nd} Rose and Johnson Station
$1.32\delta_o$	$2.64\delta_o$	$1.66\delta_o$	$2.75\delta_o$

Table 5.3 Downstream Measurement Stations in Boundary Layer Thicknesses from Interaction

The velocity profile agreement between the present study and Rose and Johnson experiment is good. The measurements from Rose and Johnson at 21.3 cm or $X = 1.66\delta_o$ downstream of the

interaction follow the present data for the 5^o and 7^o wedges quite closely. Both the 5^o and 7^o flowfield values are compared because of the effective turning angle phenomenon discussed earlier.

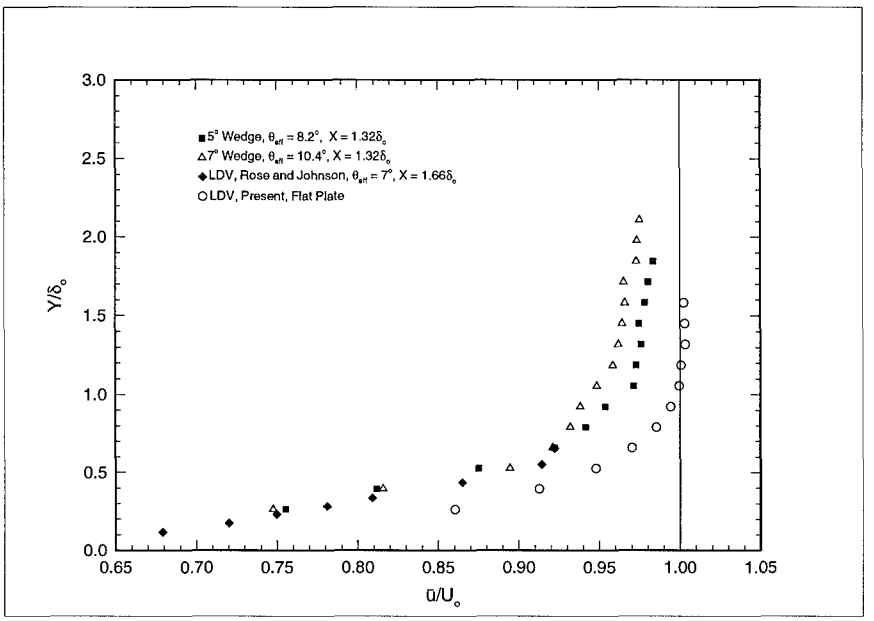

Figure 5.23 Normalized Velocity Profile Comparison at First Downstream Stations

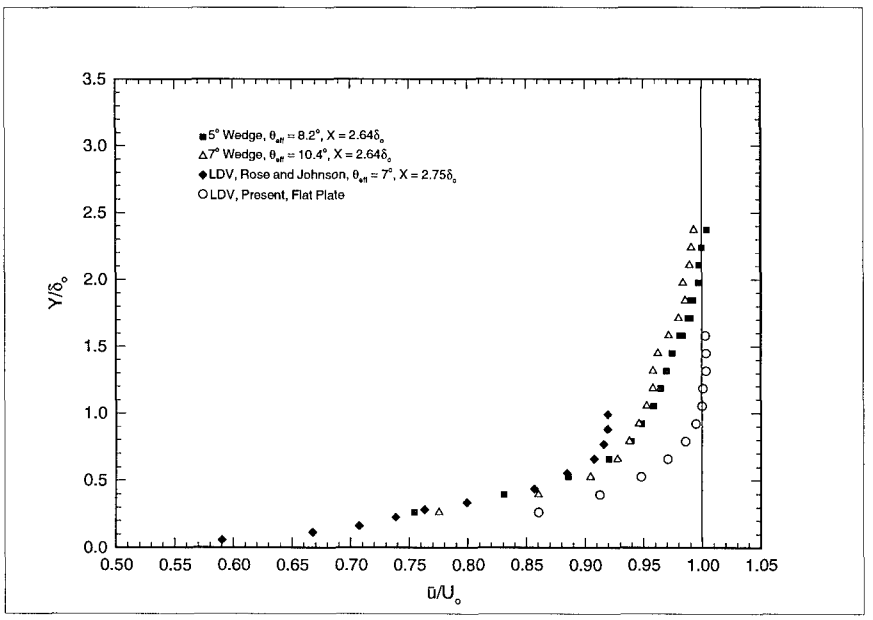

Figure 5.24 Normalized Velocity Profile Comparison at Second Downstream Stations

The agreement for the streamwise velocity fluctuations at the upstream location between the present study and Rose and Johnson is fair. Rose and Johnson's streamwise velocity fluctuation data is consistently lower than the present study but does follow the same trend. In Figure 5.25, note the three data points of Rose and Johnson near the value of $\frac{Y}{\delta_o} = 1.0$. At similar locations, all the data traces are abruptly shifted towards zero. This is an indication of shock passage through the data traces.

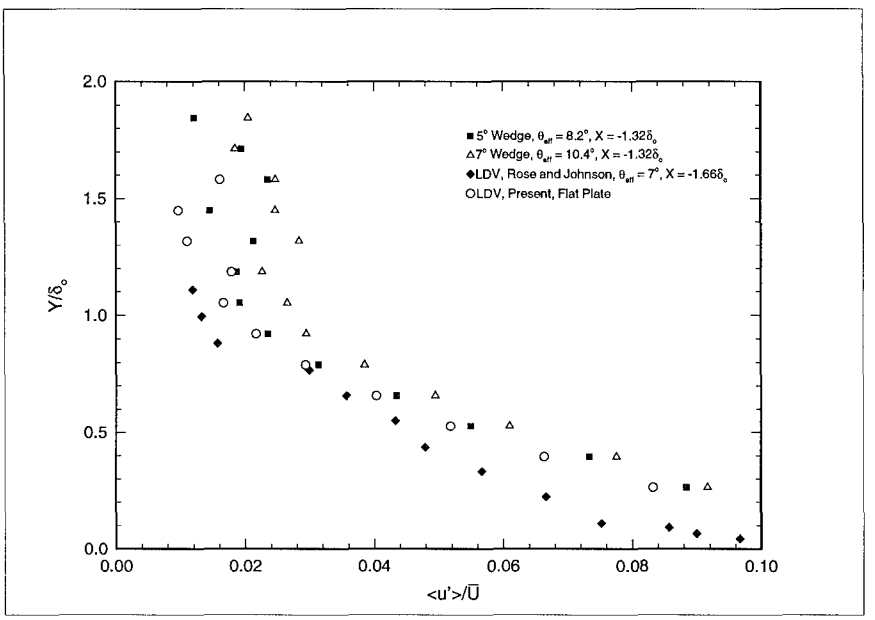

Figure 5.25 Streamwise Velocity Fluctuation Comparison at the Upstream Station

On the other hand, the downstream streamwise turbulence intensity profiles, in Figures 5.26 and 5.27, show excellent agreement within an acceptable scatter. Both studies have similar measurement distances downstream of the shock wave/boundary layer interaction and this fact bears out in the data.

The cross-stream velocity fluctuations at the upstream measurement stations, shown in Figure 5.28, also shows excellent agreement. Rose and Johnson's data follows the pattern for the 7° wedge closely and all data points from the present study are clustered around Rose and Johnson's data.

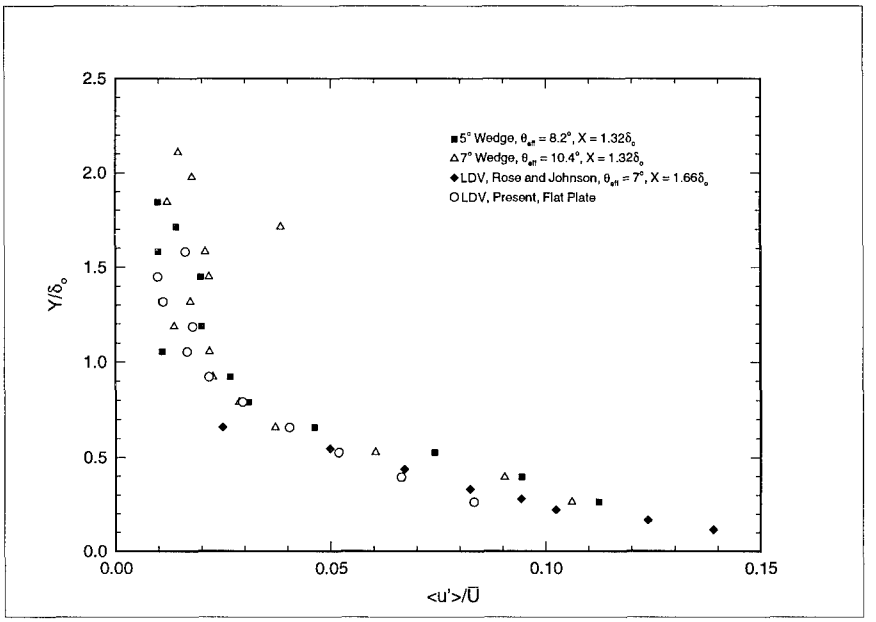

Figure 5.26 Streamwise Velocity Fluctuation Comparison at 1^{st} Downstream Stations

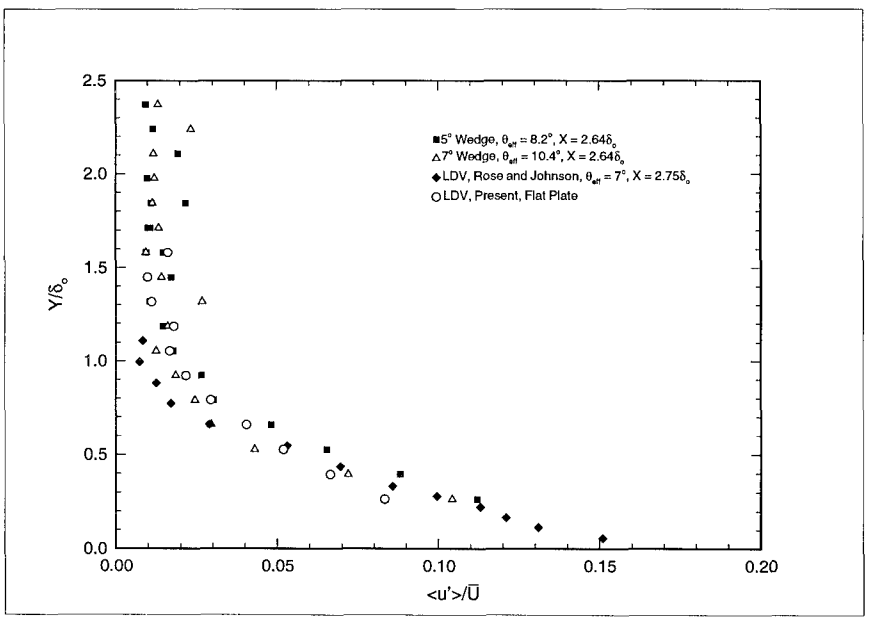

Figure 5.27 Streamwise Velocity Fluctuation Comparison at the 2^{nd} Downstream Stations

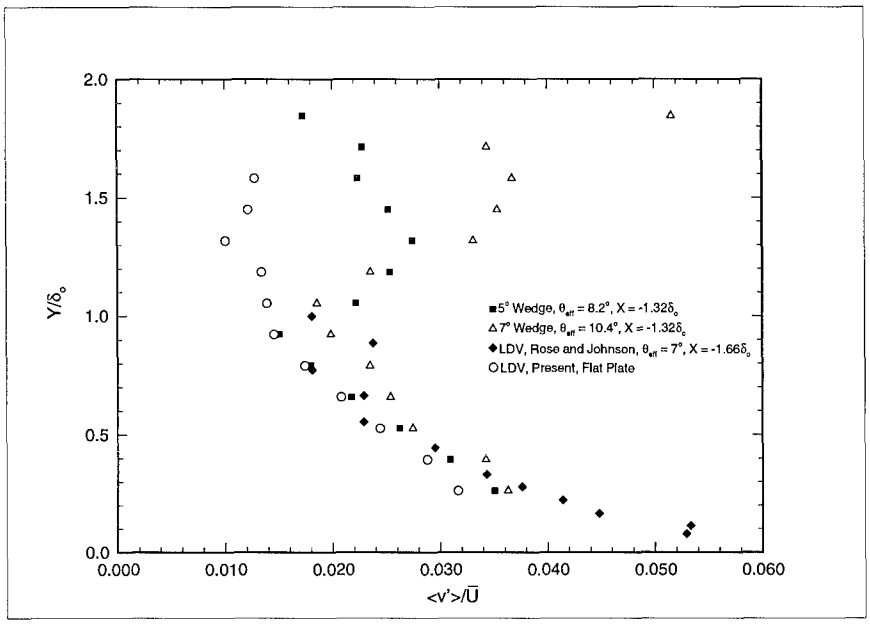

Figure 5.28 Cross-stream Velocity Fluctuations Comparison at the Upstream Station

On the other hand, the downstream agreement, shown in Figures 5.29 and 5.30, is only fair. The present study's magnitude is greater but roughly equal in scatter.

For the Reynolds shear stress profiles, Rose and Johnson's data are scaled by the wall shear stress value reported in reference (16). These values are 157 $\frac{N}{m^2}$ for the $X = -1.66\delta_o$ station and 221 $\frac{N}{m^2}$ at the $X = 2.75\delta_o$ station. The Reynolds shear stress upstream station comparison is shown in Figure 5.31. The agreement at the upstream stations is excellent between Rose and Johnson's data and the present study. The calculation of τ_w used for this comparison is discussed later in this chapter (Section 5.9.2).

However, the Reynolds shear stress agreement at the downstream stations is poor. The present data for Reynold's shear stress are scaled by the wall shear stress, τ_w. The calculation of τ_w downstream of the interaction in this study is considered suspect and is a poor choice as a scaling factor but Rose and Johnson do not report any other adequate scaling factor in (16), choosing instead to leave the Reynolds shear stress in dimensional form. It appears that the assumption of

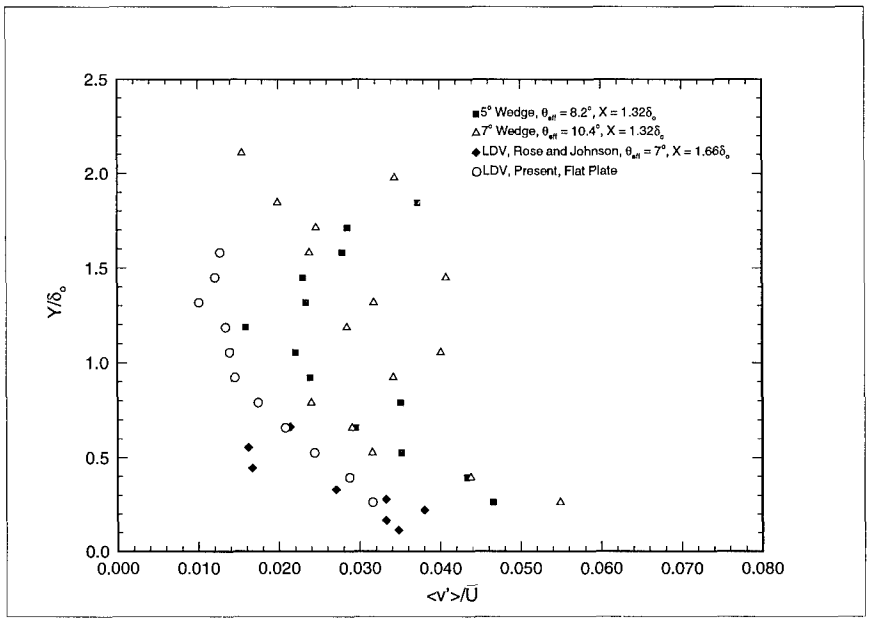

Figure 5.29 Cross-stream Velocity Fluctuation Comparison at 1^{st} Downstream Station

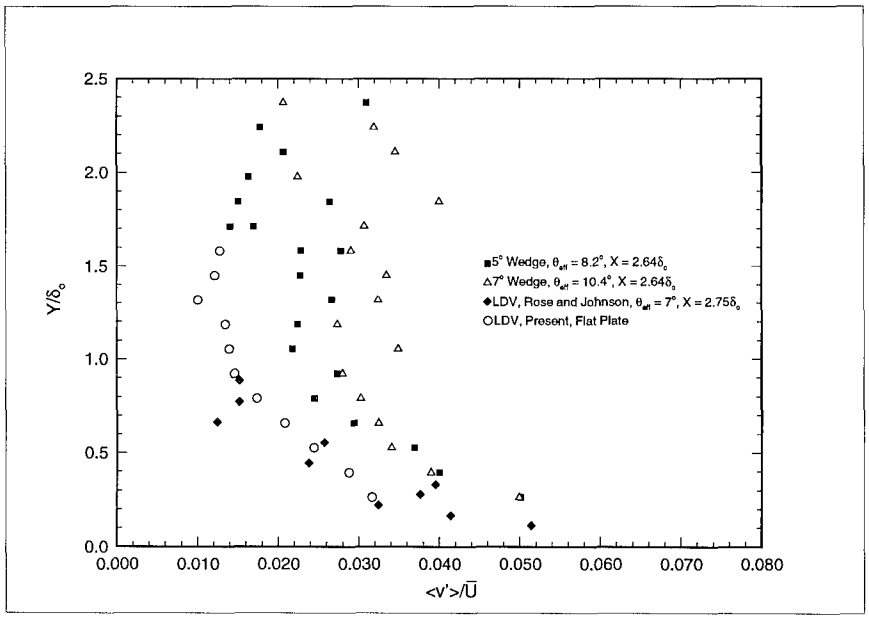

Figure 5.30 Cross-stream Velocity Fluctuation Comparison at 2^{nd} Downstream Station

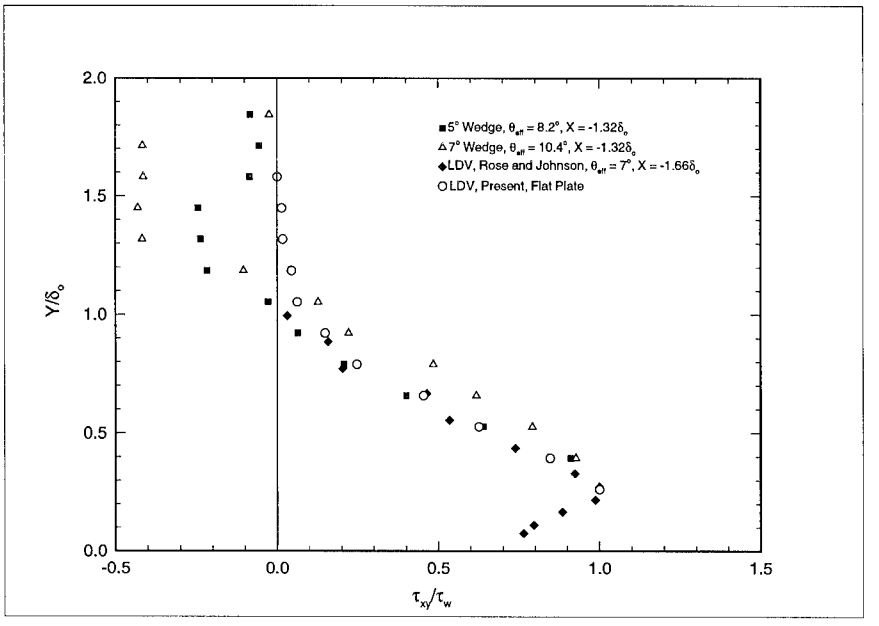

Figure 5.31 Reynolds Shear Stress Scaled by Wall Shear Stress for the Upstream Station

Couette flow may fail at this measurement station. The calculation of τ_w is explained in Section 5.9.2.

The agreement with Rose and Johnson's (16) data is good and the studies do not blatantly disagree or contradict each other, with the possible exception of the downstream Reynolds shear stress scaled by the wall shear stress. This has provided a sound foundation for the discussion of the effects of shock strength and measurement location on the turbulence properties of a boundary layer subject to a shock wave interaction.

5.8.3 Shock Wave Boundary Layer Results. This section will cover the shock wave/boundary layer results for the 5^o wedge flow to illustrate the effects of a shock wave impingement on a turbulent supersonic boundary layer. Initially, the mean flow characteristics are discussed, followed by an explanation of the turbulent properties.

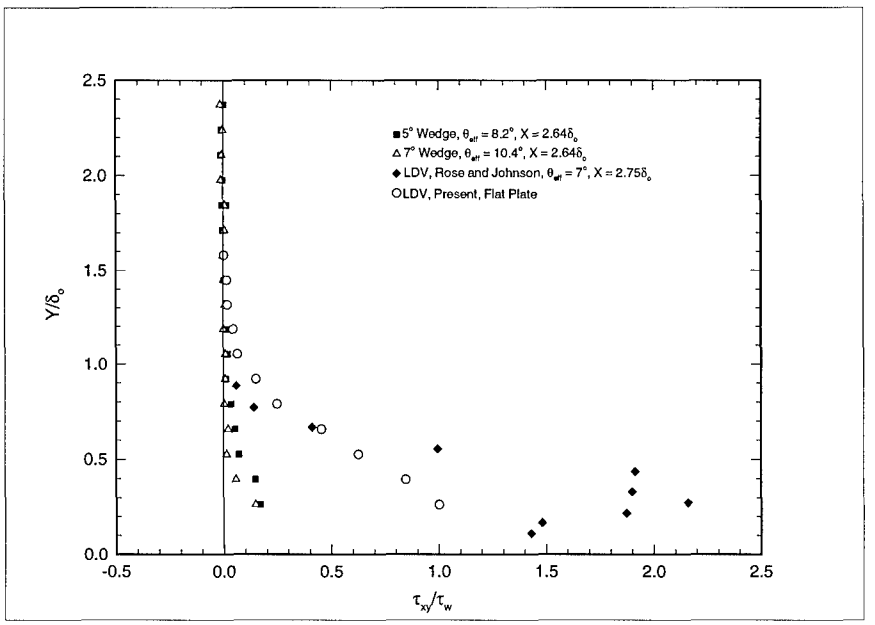

Figure 5.32 Reynolds Shear Stress Scaled by Wall Shear Stress for 2^{nd} Downstream Station

The velocity profiles were obtained by dividing the streamwise mean velocity by the velocity reference value, U_o. These results are shown plotted versus $\frac{Y}{\delta_o}$ to facilitate comparison and greatly simplify the data reduction process.

The effects of measurement location on the velocity profiles for the 5^o wedge flowfield is shown in Figure 5.33. The upstream station, at $X = -1.32\delta_o$, follows the flat plate data closely. The profiles at $X = 0\delta_o$, $X = 1.32\delta_o$, and $X = 2.64\delta_o$ match each other closely, showing the effect of the shock wave on the velocity downstream. It appears that the velocity profiles remain relatively unchanged downstream of the interaction, considering each profile is scaled by a reference quantity and not an edge value. Notice the profile at $X = -1.32\delta_o$ rapidly slows above $\frac{Y}{\delta_o} \approx 1.0$, where the shock wave passed through the traverse profile.

The Mach number profiles for the 5^o wedge flow are shown in Figure 5.34. The downstream Mach numbers are roughly 0.2 lower than the flat plate or the upstream values. The stations at $0\delta_o$, $1.32\delta_o$, and $2.64\delta_o$ are closely matched and show similar trends to the velocity profiles.

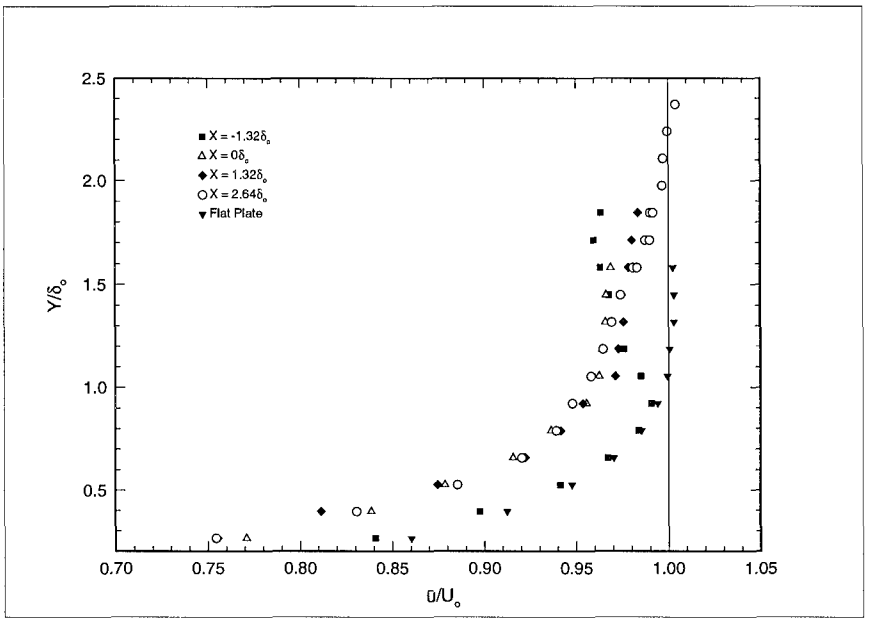

Figure 5.33 5^o Wedge ($\theta_{eff} = 8.2^o$) Velocity Profiles at Each Measurement Station

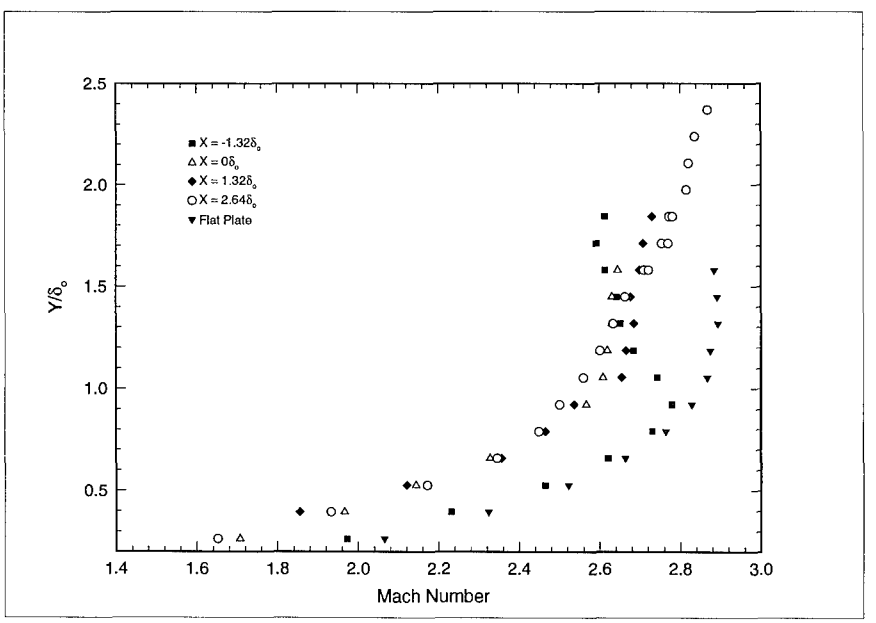

Figure 5.34 5^o Wedge ($\theta_{eff} = 8.2^o$) Mach Number Profiles at each Measurement Station

As seen in Figure 5.35, the streamwise velocity fluctuations are increased by the shock wave interaction. Near the wall, the increase is approximately 29%. Further from the wall the increase is smaller but still distinct. There is also some upstream influence near the wall where the $X = -1.32\delta_o$ station streamwise velocity fluctuations are larger than the flat plate.

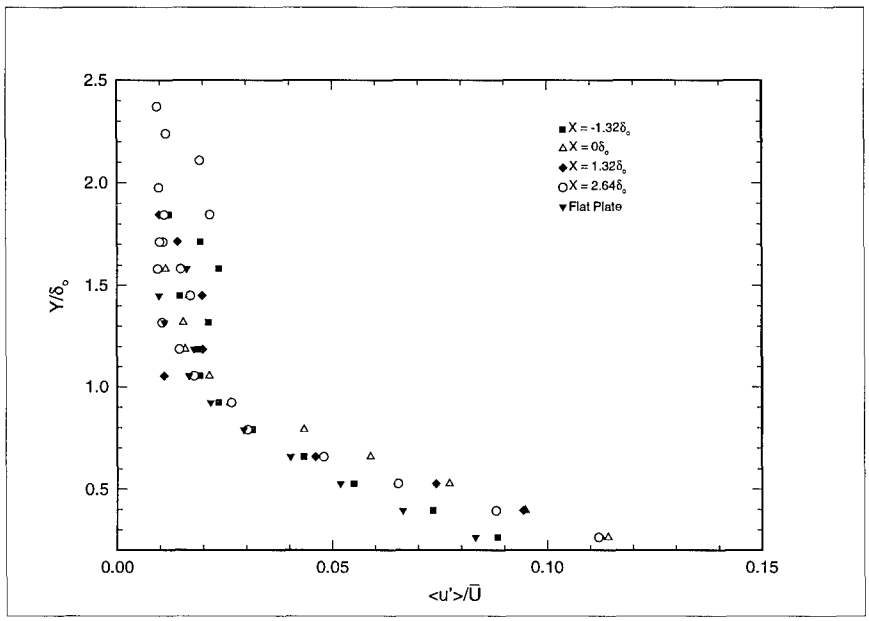

Figure 5.35 5^o Wedge ($\theta_{eff} = 8.2^o$) Streamwise Velocity Fluctuations

Like the streamwise fluctuations, the cross-stream velocity fluctuations, as seen in Figure 5.36, are energized by the shock wave interaction and remain elevated through the $X = 2.64\delta_o$ measurement station. However, no distinct trend based on downstream location can be discerned from these data. Note that the upstream profile is intersected by the shock at roughly $X = 0.9\delta_o$ and values above this should not be considered when comparing the upstream to downstream stations.

Along the same lines, the shock wave/boundary layer interaction has a distinct effect on the Reynolds shear stress. The downstream measurement locations have a much higher shear stress near the wall than the upstream station. The increase for the 5^o wedge flow, as shown in Figure 5.37, equates to nearly a 56% rise in shear stress downstream of the interaction over the upstream

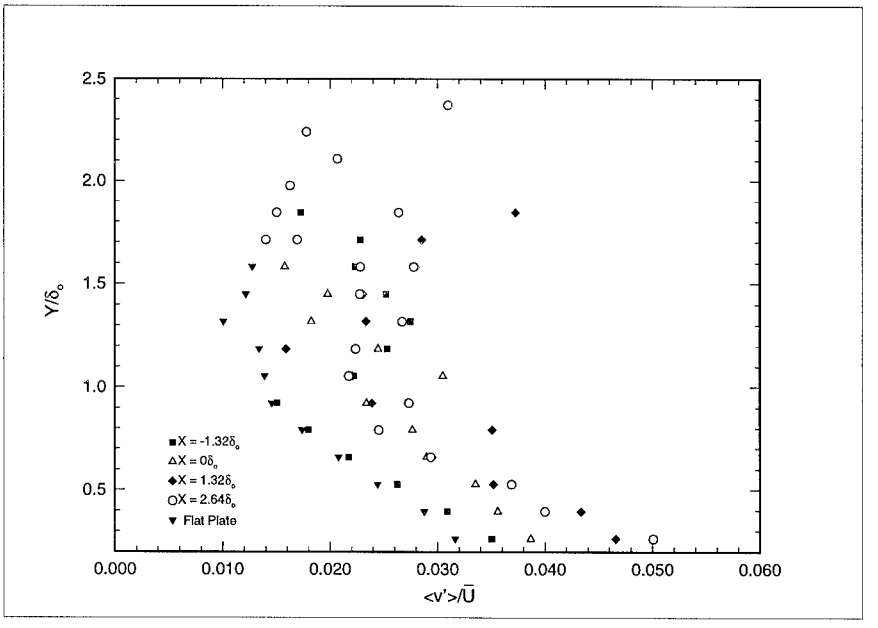

Figure 5.36 5^o Wedge ($\theta_{eff} = 8.2^o$) Cross-stream Velocity Fluctuations

values. The shear stress gradients perpendicular to the wall are much higher downstream of the interaction, allowing the profiles to return to upstream values by a height of $Y = 0.5\delta_o$.

Concluding the examination of the effect of the shock wave/boundary layer interaction on the 5^o wedge flow, the TKE profiles are presented in Figure 5.38. The interaction has energized the energy in the flow downstream, increasing the TKE at all downstream locations. The TKE near the wall increases with downstream distance, reaching a maximum value at $X = 2.64\delta_o$, the final measurement station.

5.9 Effect of Shock Strength

To examine the effect of shock strength on the turbulent properties of a shock wave/boundary layer interaction, three wedge angles were used: 5^o, 7^o, and 10^o. Streamwise profiles were obtained at a constant height above the wall of $Y = 0.66\delta_o$ will be used. This profile orientation facilitated the analysis of shock strength, along with the effect of downstream distrance, on the evolving boundary layer.

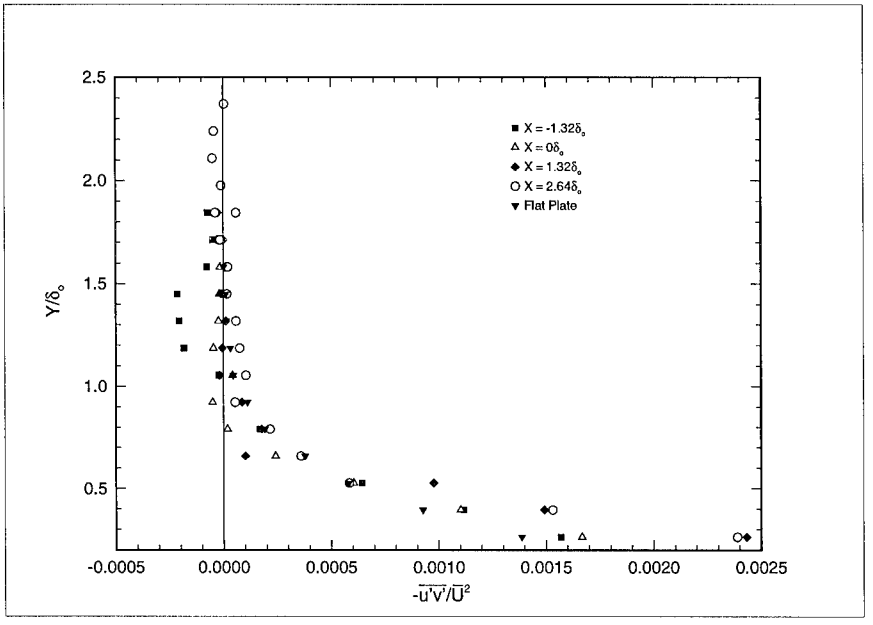

Figure 5.37 5^o Wedge ($\theta_{eff} = 8.2^o$) Incompressible Reynolds Shear Stress Scaled by Local Velocity

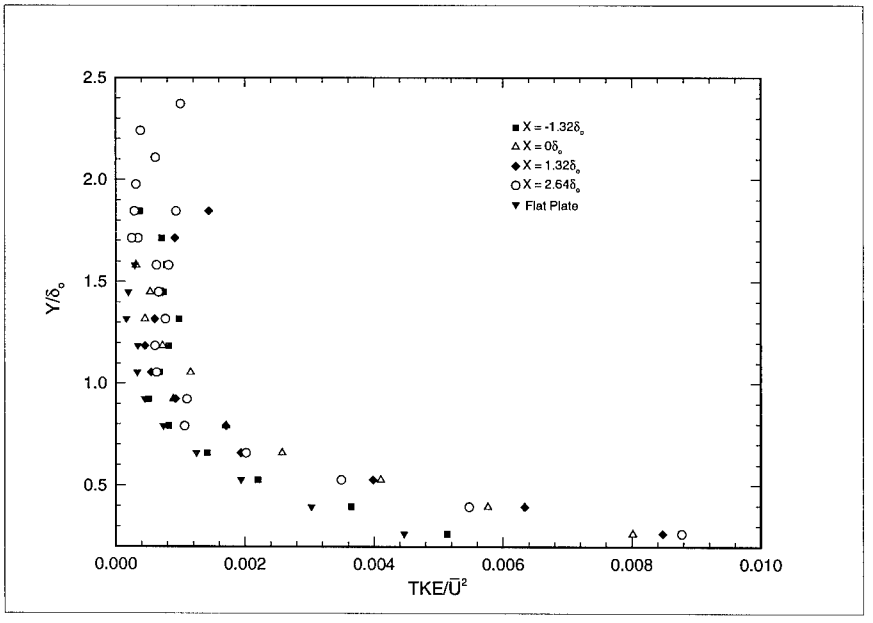

Figure 5.38 5^o Wedge ($\theta_{eff} = 8.2^o$) Turbulent Kinetic Energy

The velocity defect through the shock wave/boundary layer interaction is dependent on shock strength, as seen in Figure 5.39. The velocity drop occurs slightly upstream of the interaction and continues downstream roughly $0.4\delta_o$. Note that the 10^o wedge profile never reachs a steady state velocity, continuing to accelerate through the last measurement at $X = 4.0\delta_o$.

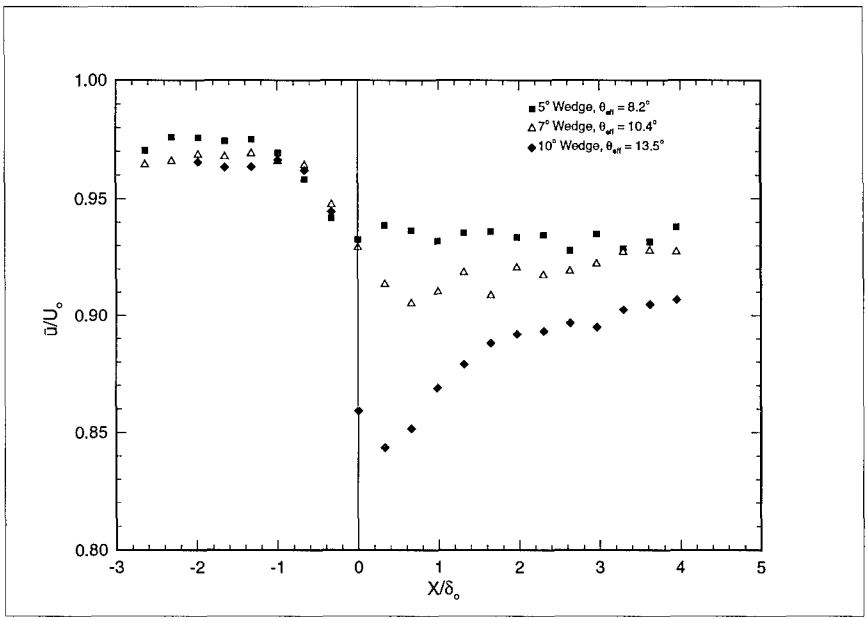

Figure 5.39 Streamwise Velocity Profile at Height from Wall $Y = 0.66\delta_o$

Figure 5.40 shows the Mach number profile versus distance from the shock wave/boundary layer interaction at a height from the wall of $Y = 0.66\delta_o$. This figure clearly shows the effect of increasing shock strength on the Mach number as the flow moves through the interaction. The Mach number gradient is greater for increasing shock strength. Figure 5.40 also shows that, in the 10^o wedge case, the Mach number has recovered from the interaction and is approaching a new equilibrium value by roughly $2.0\delta_o$ downstream.

The streamwise velocity fluctuations for the different shock strengths at a height from wall of $0.66\delta_o$ is seen in Figure 5.41. These data support the conclusion that increasing shock strength causes an increase in the streamwise velocity fluctuations. The nature of the 10^o wedge curve also

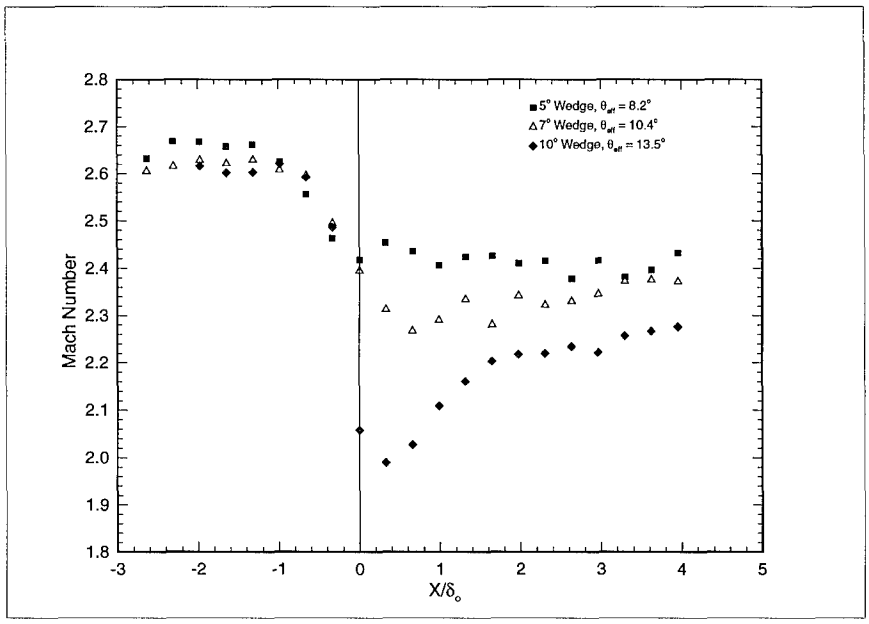

Figure 5.40 Streamwise Mach Number Profiles at Height from Wall $Y = 0.66\delta_o$

supports the conclusion that this flow is fundamentally different than either the 5^o or the 7^o wedge flows. The evidence supports that the 10^o flow has separated at the interaction.

Similar to the streamwise velocity fluctuations (Figure 5.42), the cross-stream velocity fluctuations increase as a function of shock strength near the interaction. Farther downstream, however, this conclusion no longer seems valid. However, the downstream values for cross-stream velocity fluctuations remain elevated over the upstream values through the last measurement location, $X = 4.0\delta_o$.

The incompressible Reynolds shear stress is defined as $-\overline{\rho}\overline{u'v'}$. However, to facilitate comparison with other studies, it is important to represent the shear stress in a non-dimensional fashion. The correlation $\frac{-\overline{u'v'}}{\overline{U}^2}$ is presented below for each shock strength thoughout the shock wave/boundary layer interaction. It is hoped that this representation of the incompressible Reynolds shear stress will allow easy comparison to CFD results. Other reasons for this scaling are outlined in flat plate Reynolds shear stress discussion in Section 5.7.3.

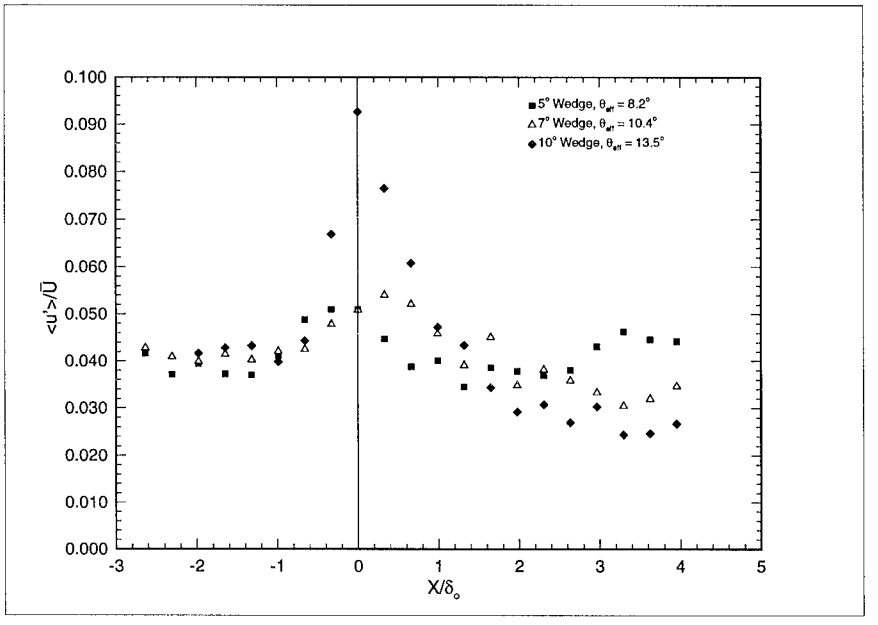

Figure 5.41 Streamwise Velocity Fluctuations at Height from Wall $Y = 0.66\delta_o$

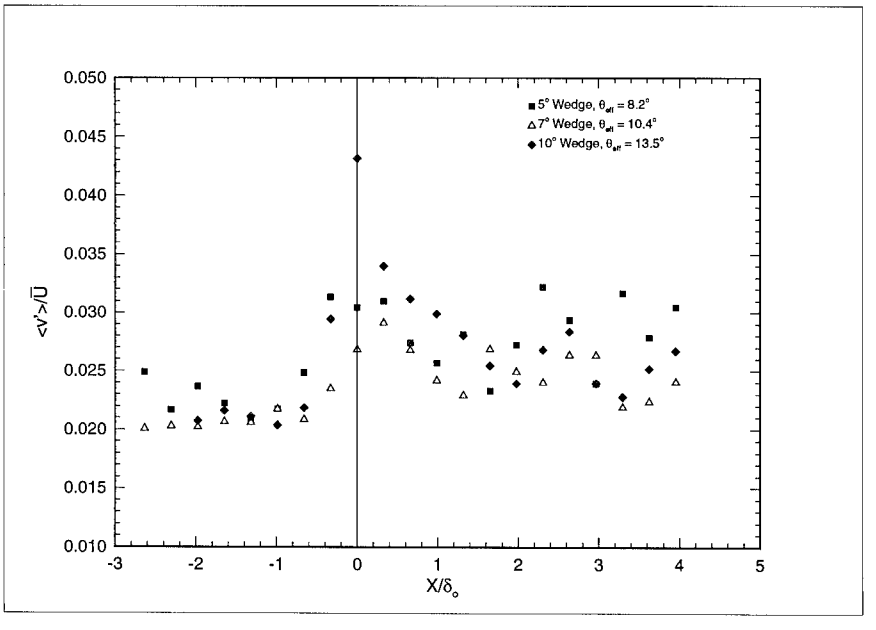

Figure 5.42 Cross-stream Velocity Fluctuations at Height from Wall $Y = 0.66\delta_o$

Examining the incompressible Reynolds shear stress streamwise profile at $Y = 0.66\delta_o$ (see Figure 5.43), the profiles for the 5^o and the 7^o wedge drop just before the interaction and return to near upstream values downstream of the interaction. The 10^o wedge flow, however, rises sharply just before the interaction and drops below the upstream values downstream of the interaction. Thus, it appears the character of the flow may have changed with the higher shock strength. The 10^o wedge flow may have separation near the interaction, as suggested by the Schlieren and shadowgraph photos in Figures 5.10 and 5.11.

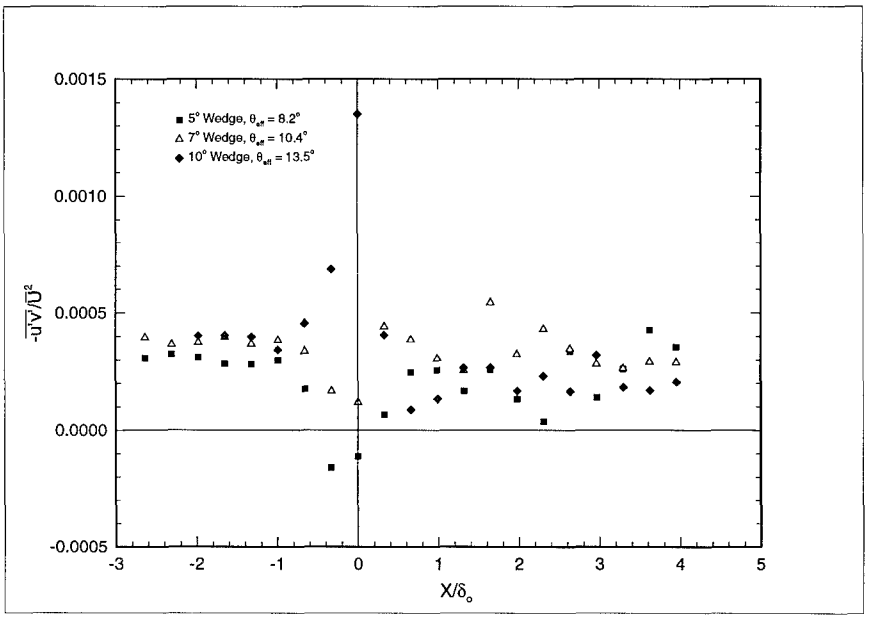

Figure 5.43 Incompressible Reynolds Shear Stess Scaled by Local Velocity at Height from Wall $Y = 0.66\delta_o$

Turbulent kinetic energy (TKE) was calculated as described in Chapter 4, using the relationship $v' \approx w'$ to compensate for the inability to measure w' with the present test setup. In Figure 5.44, the TKE for each wedge flow rises upon nearing the interaction and quickly returns to near upstream values in roughly $1.5\delta_o$ at the measurement height $Y = 0.66\delta_o$. The value at the interaction for both the 5^o and 7^o wedge flows are nearly equal but the 10^o wedge flow has a significant rise at the interaction. This, again, supports the conclusion that the 10^o wedge flow is fundamentally different and may be separated. However, there is no LDV evidence to support the

conclusion that the 7^o wedge flow is separated. Note that the order of increasing TKE upstream of the interaction is reversed downstream of the interaction with the 5^o wedge flow retaining the highest TKE after the interaction.

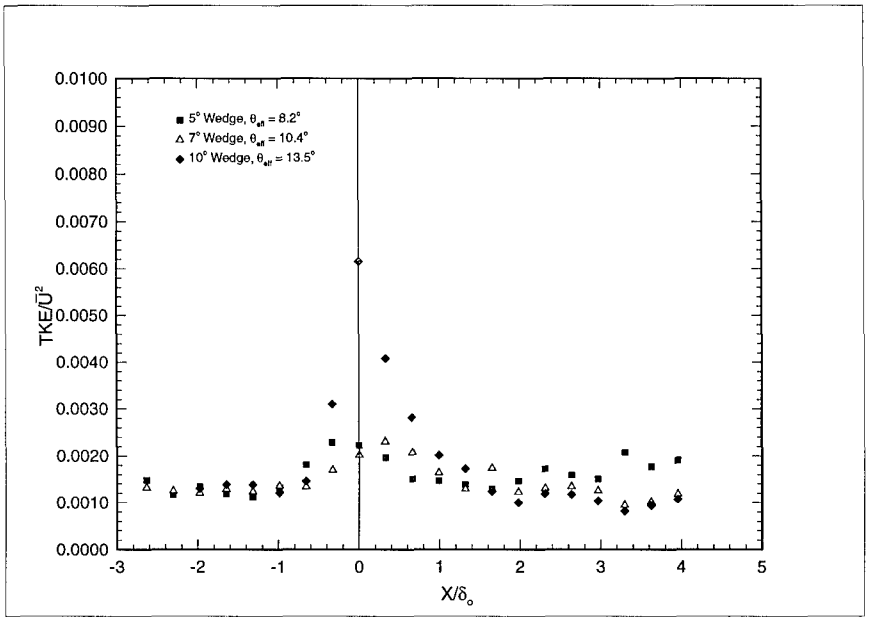

Figure 5.44 Turbulent Kinetic Energy at Height from Wall $Y = 0.66\delta_o$

5.9.1 Fluctuating Mach Number. As stated in the discussion on the flat plate results, the fluctuating Mach number is a measure of the validity of Morkovin's hypothesis. The fluctuating Mach number was calculated from the data and examined to ensure that the value never approached $M' = 1.0$. In all cases the maximum values of M' never exceeded 0.40. Caution, however, should be exercised using these data near the incoming and reflecting shock waves.

5.9.2 Wall Shear Stress. By integrating the boundary layer momentum equation from the wall to a point in the boundary layer a distance y from the wall (where y must be within in the boundary layer), it can be shown that the boundary layer shear stress should tend towards the wall shear stress (11). With the assumption that $\rho\overline{u}\frac{\partial\overline{u}}{\partial x} = 0$ and no blowing or suction, the boundary layer momentum equation becomes

$$\tau_{xy}^{T} = \tau_w + \frac{\partial \overline{P}}{\partial x} y \tag{5.1}$$

Solving for τ_w gives

$$\tau_w = \tau_{xy}^{T} - \frac{\partial \overline{P}}{\partial x} y \tag{5.2}$$

This is called the Couette Flow assumption and is valid at values of $y^+ < 500$. Couette flow also assumes the flow is unseparated. The pressure gradients used for this study in Equation 5.2 were obtained by assuming a linear distribution of pressure between the static pressure measurements. The pressure gradients used are then the slopes of the linear segments between the static pressure measurements. All upstream pressure gradients were assumed to be zero, in order to avoid differentiating possible sensor noise between two upstream static pressure measurement points. The pressure gradient used for the downstream values are shown in Table 5.4.

	$10^o Wedge$	$7^o Wedge$	$5^o Wedge$
$-1.32\delta_o$	0	0	0
$1.32\delta_o$	596121	-11368	-183461
$2.64\delta_o$	-144284	-298307	-183461

Table 5.4 Pressure Gradients in Pa/m Used in Calculation of Wall Shear Stress

At the $X = 1.32\delta_o$ station for the 10^o wedge flow, the Couette flow assumption breaks down, giving a nonsensical value of τ_w. Therefore, that data point has been discarded. The remaining wall shear stress points are plotted in Figure 5.45. This figure shows a 700% increase in the wall shear stress over the upstream values (solid and dashed lines in Figure 5.45) for the 5^o wedge case. The 7^o wedge flow does not show an increase in the wall shear stress at the $X = 1.32\delta_o$ location because of the small pressure gradient measured there. However, at the $X = 2.64\delta_o$ station, the wall shear stress is 1000% larger than the upstream value. Along the same lines, the 10^o wedge flowfield experienced a 670% increase in wall shear stress. The wall shear stress dramatically increases due

to the shock wave interaction and has not returned to the upstream value at the last measurement station. The measured y^+ for the lowest measurement from the wall for this study was 315 ± 5.0.

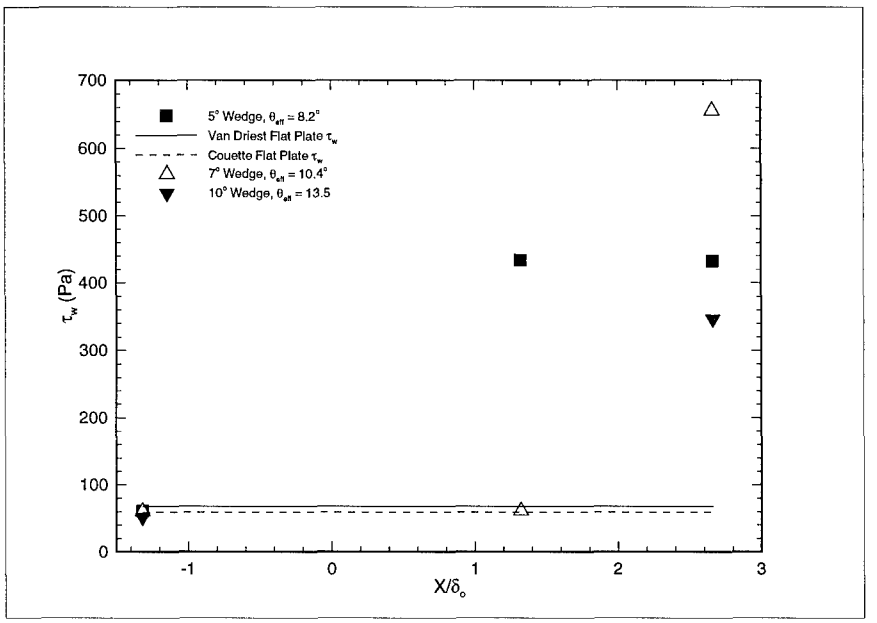

Figure 5.45 Comparisons of Wall Shear Stress

The corresponding skin friction coefficient chart is shown in Figure 5.46. The skin friction coefficient was calculated using Equation 5.3 and the values of τ_w shown in Figure 5.45. ρ_o and U_o are the reference quantities defined in Table 5.2. The skin friction coefficient follows similar trends as the wall shear stress, showing a dramatic increase due to the shock wave interaction.

$$\frac{C_f}{2} = \frac{\tau_w}{\frac{1}{2}\rho_o U_o^2} \tag{5.3}$$

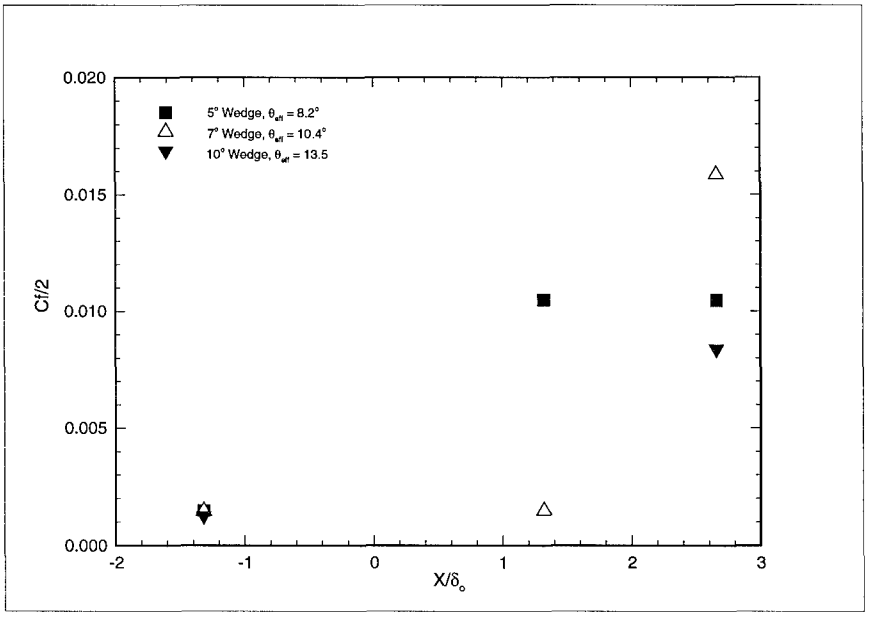

Figure 5.46 Skin Friction Coefficients for the Shock Wave/Boundary Layer Interaction

VI. Conclusions and Recommendations

6.1 Summary and Conclusions

This study had two goals, to increase the understanding of a shock wave/boundary layer interaction on a flat plate and to provide information to increase the turbulence database for compressible flows. To this end, static surface pressures were measured through the shock wave/boundary layer interaction and Laser Doppler Velocimetry (LDV) was used to measure the mean and fluctuating flow characteristics of the shock wave/boundary layer interaction. The flow properties derived from these measurements included velocity and Mach number profiles, the velocity fluctuations, Reynolds shear stress, turbulent kinetic energy, wall shear stress, and the skin friction coefficient.

The results from Chapter 5 allow some general conclusions to be drawn. The flat plate results from the present study match well with the data from Luker (13) and Hale (9) and, also, with Elena and LaCharme (7). Additionally, the present shock wave/boundary layer interaction data match with Rose and Johnson (16) with the exception of the cross-stream velocity fluctuation. The cross-stream velocity measurements, throughout the present experiment, may not be valid over $\frac{Y}{\delta_o} \approx 1.0$. This is caused by shock waves passing through the traverse profiles leading to a consistently lower number of coincident samples farther from the wall. Examination of the downstream velocity profiles reveals that velocity does not change appreciably in the streamwise direction for a particular shock strength. However, the wall shear stress and skin friction coefficient increase over 500% across the interaction.

The shock wave/boundary layer interaction causes significant changes in the downstream flow structure. The velocity fluctuations have increased, particularly near the wall. The streamwise velocity fluctuations increased, for example, 29% for the 5^o wedge flow near the wall. The one exception to this was the 10^o wedge flow which showed a lower streamwise velocity fluctuation downstream of the interaction. It is believed that the favorable pressure gradient off of the interaction-induced separation region dampens out these fluctuations. The cross-stream velocity

fluctuations also increased across the interaction. The 5^o wedge flow showed an approximate 37% increase near the wall when comparing upstream and downstream measurements. The Reynolds shear stress increased by 60% near the wall for the 5^o wedge flow. The turbulent kinetic energy increased by as much as 29% across the interaction for the 5^o wedge flow.

The strength of the impinging shock also has significant effects on the properties downstream of the interaction. The mean velocity and Mach number defects caused by the impinging shock wave increased with shock strength, as expected from inviscid theory. Most of the turbulence properties also increased with shock strength near the interaction with the exception of the cross-stream velocity fluctuation. The streamwise velocity fluctuations increased with increasing shock strength but recovered to upstream values quickly with the exception of the 10^o wedge flow as discussed above. In addition, the Reynolds shear stress and the turbulent kinetic energy increased with increasing shock strength near the interaction. However, the cross-stream velocity fluctuations do not appear to depend on shock strength for the range of shock strength considered. One exception to this, however, was the 10^o wedge flow very near the interaction, which showed a significant increase.

The lower number of collected coincident bursts increased the error bounds of this experiment over the studies of Luker (13) and Hale (9). However, the error increase was small and the study is still considered acceptable with the error bounds stated in Appendix B.

6.2 Recommendations

These data should be compared to CFD solutions using established turbulence models, similar to the study done by Fick (8). However, several aspects of this experiment could be improved to make the data more useful.

The first recommendation is to use a different shock generating scheme, instead of the wedge shock generator. The wedge, roughly the same height as the incoming boundary layer, caused an unexpectedly large flow turning angle, complicating comparison to numerical analysis.

To increase the turbulence data base, additional streamwise profiles should be taken closer to the wall to confirm the effects near the wall of the shock wave/boundary layer interaction. Streamwise profiles are an excellent method of determining the effect of both shock strength and location in a shock wave/boundary layer interaction.

The olive oil seeder mechanism should be redesigned to give a more even distribution of seed through the boundary layer. It appeared during the experiment that the seeder holes as presently designed created dead zones in the boundary layer which had very little seed. This caused the number of coincident bursts collected to drop. A seeder with a continuous vertical slit may solve this problem.

The final recommendation is to take accurate wall shear stress measurements over the shock wave/boundary layer interaction. The wall shear stress is the determining factor in the magnitude of the friction drag and heat transfer to the surface. The current LDV setup was limited in how close it could get to the wall, making it difficult, if not impossible, to accurately determine the wall shear stress. The Couette flow assumption gives an idea of the magnitude but this assumption breaks down as the shock strength is increased. Obtaining accurate wall shear stress measurements would aid in the analysis of the data presented here and would also be useful for further research performed in this facility.

Appendix A. Rose and Johnson 1975 Data

A.1 Rose and Johnson 1975 Tabular Data

Table A.1 Mean Velocity Profiles

X = 13.7 cm		X = 21.3 cm		X = 23.8 cm	
y (cm)	$\overline{U}(m/s)$	y(cm)	$\overline{U}$ (m/s)	y(cm)	$\overline{U}(m/s)$
0.22	478	0.27	413	0.13	359
0.34	500	0.40	438	0.26	406
0.52	523	0.53	456	0.37	430
0.74	540	0.65	475	0.52	449
0.99	556	0.77	492	0.65	464
1.26	571	1.00	526	0.77	486
1.50	590	1.26	556	1.00	521
1.76	600	1.50	561	1.27	538
2.02	613			1.51	552
				1.76	557
				2.02	559
				2.27	559

Table A.2 Streamwise Velocity Fluctuations

X = 13.7 cm		X = 21.3 cm		X = 23.8 cm	
y (cm)	$\frac{<u'>}{\overline{U}}$	y (cm)	$\frac{<u'>}{\overline{U}}$	y(cm)	$\frac{<u'>}{\overline{U}}$
0.10	0.0967	0.26	0.1390	0.13	0.1510
0.15	0.0900	0.38	0.1238	0.26	0.1310
0.21	0.0857	0.51	0.1024	0.38	0.1210
0.25	0.0752	0.64	0.0943	0.51	0.1130
0.50	0.0667	0.76	0.0824	0.64	0.0995
0.76	0.0567	1.00	0.0671	0.76	0.0857
1.00	0.0479	1.25	0.0498	1.00	0.0695
1.26	0.0433	1.51	0.0248	1.25	0.0530
1.51	0.0357			1.51	0.0288
1.76	0.0300			1.77	0.0172
2.02	0.0158			2.02	0.0126
2.28	0.0133			2.28	0.0074
2.54	0.0119			2.54	0.0083

Table A.3 Crosswise Velocity Fluctuations

X = 13.7 cm		X = 21.3 cm		X = 23.8 cm	
y (cm)	$\frac{<v'>}{\overline{U}}$	y (cm)	$\frac{<v'>}{\overline{U}}$	y (cm)	$\frac{<v'>}{\overline{U}}$
0.18	0.0529	0.26	0.0348	0.26	0.0514
0.26	0.0533	0.38	0.0333	0.38	0.0414
0.38	0.0448	0.51	0.0381	0.51	0.0324
0.51	0.0414	0.64	0.0333	0.64	0.0376
0.64	0.0376	0.76	0.0271	0.76	0.0395
0.76	0.0343	1.02	0.0167	1.02	0.0238
1.02	0.0295	1.27	0.0162	1.27	0.0257
1.27	0.0229	1.52	0.0214	1.52	0.0124
1.52	0.0229			1.77	0.0152
1.77	0.0181			2.03	0.0152
2.03	0.0238				
2.29	0.0181				

Table A.4 Reynold's Normal Stress

X = 13.7 cm		X = 21.3 cm		X = 23.8 cm	
y (cm)	$\overline{\rho U'^2}(N/m^2)$	y (cm)	$\overline{\rho U'^2}(N/m^2)$	y (cm)	$\overline{\rho U'^2}(N/m^2)$
0.104	857	0.253	3000	0.123	2637
0.142	810	0.383	2812	0.253	2693
0.204	810	0.500	2376	0.383	2743
0.259	676	0.628	2168	0.500	2713
0.500	648	0.756	1853	0.628	2366
0.756	543	1.00	1608	0.756	2000
1.000	438	1.27	1000	1.00	1582
1.27	390	1.53	276	1.27	1087
1.53	371			1.53	352
1.77	190			1.77	133
2.03	57				
2.28	38				

Table A.5 Reynold's Shear Stress

X = 13.7 cm		X = 23.8 cm	
y (cm)	$\rho\overline{u'v'}(N/m^2)$	y (cm)	$\rho\overline{u'v'}(N/m^2)$
0.174	120	0.253	316
0.253	125	0.383	327
0.383	139	0.500	414
0.500	155	0.628	477
0.628	157	0.756	420
0.756	145	1.00	423
1.00	116	1.27	220
1.27	84	1.53	91
1.53	73	1.77	31
1.77	32	2.03	13
2.03	25		
2.28	5		

A.2 Rose and Johnson 1975 Graphical Data

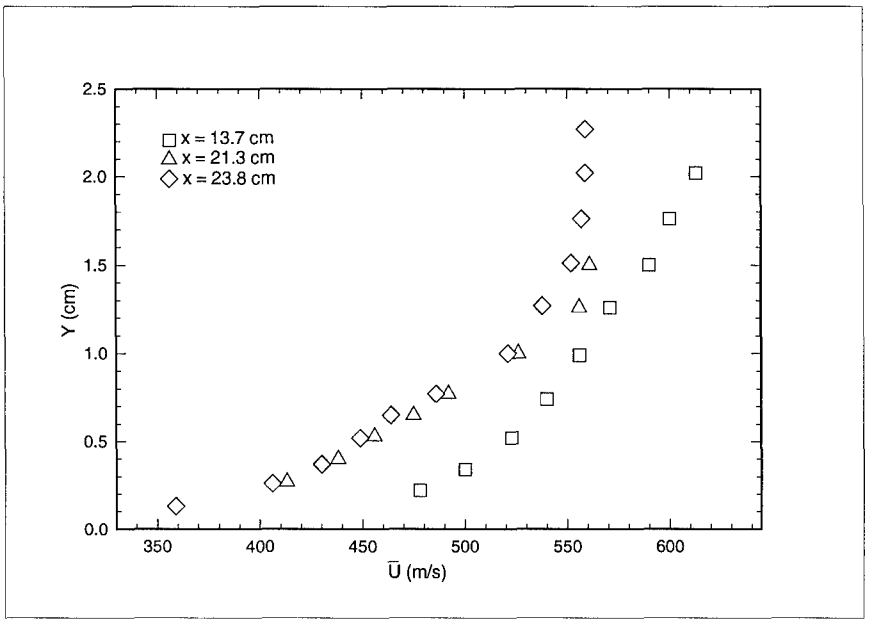

Figure A.1 Mean Velocity Profiles

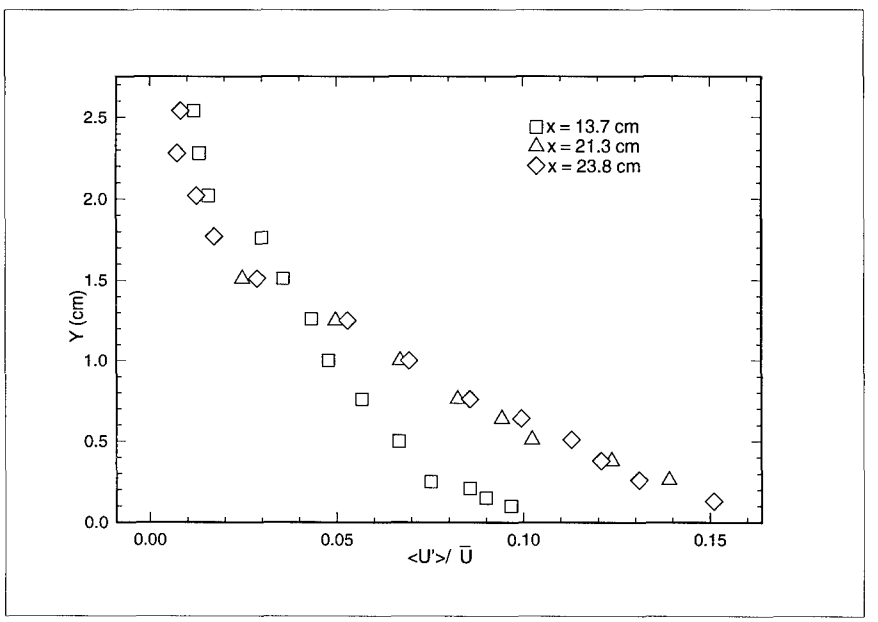

Figure A.2 Streamwise Velocity Fluctuations

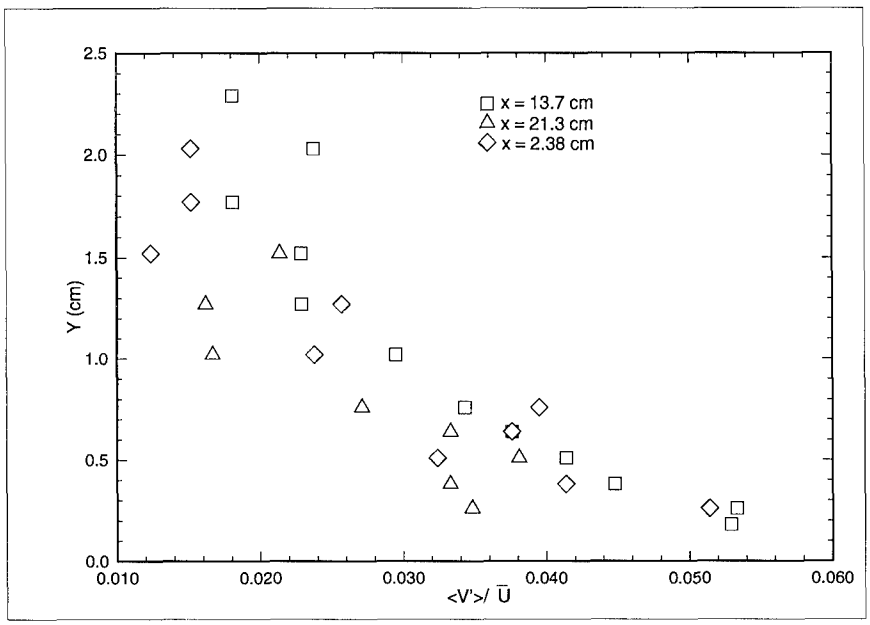

Figure A.3 Crosswise Velocity Fluctuations

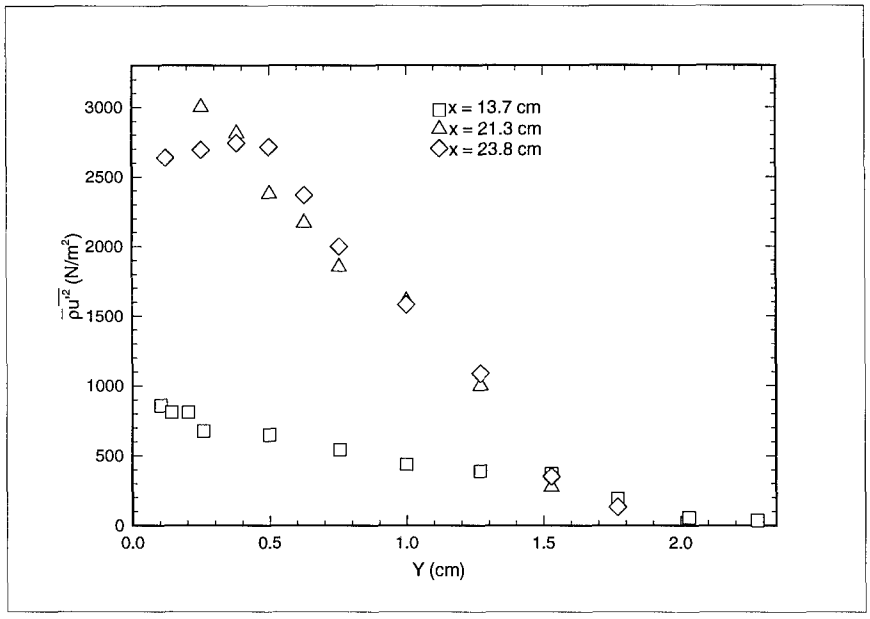

Figure A.4 Reynolds Normal Stress

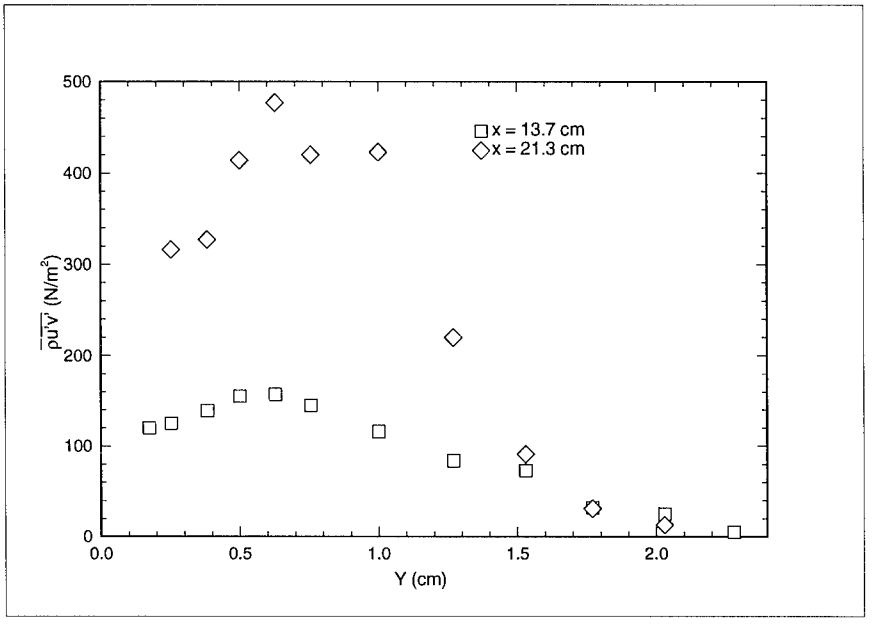

Figure A.5 Reynolds Shear Stress

Appendix B. Error Analysis

The error analysis for this experiment follows Luker's Appendix B "Error Analysis" (13) closely, as that reference calculated all the required error statistics for the present test setup and wind tunnel combination. The only error values that have changed are the turbulence statistics values. These values have changed due to the difference in the number of coincident bursts collected. The lowest number of bursts collected during the experiment was 121. This value will be used to determine the effect on the error in the turbulence statistics, to highlight the worst case . All other variables continue to have the same error values as presented in Luker.

Define the error from the low number of bursts as ε_B and the number of bursts collected as N_B. Then the error in the Root Mean Square (RMS) values is given by

$$\varepsilon_B = \frac{100|N_B - 1 - N_B|}{N_B} = \frac{100}{N_B} = 0.833\% \tag{B.1}$$

This error is then combined with the errors found by Luker using the Euclidian norm of the independent error terms. For example, the total error $\varepsilon_{u'_{Total}}$ is given by

$$\varepsilon_{u'_{Total}} = \sqrt{\varepsilon_B^2 + \varepsilon_{u'}^2} \tag{B.2}$$

Using equation B.2, $\varepsilon_{u'_{Total}} = 1.89\%$. The remaining error terms, both Luker's error calculations and the present study's, are shown in table B.1. The different values for this study are marked with an asterisk.

Variable	% Error	Variable	% Error	Variable	% Error
$\overline{U}$	8.8	Flat Plate U_e	1.3	σ_u	1.89*
$\overline{v}$	8.5	Q_e	1.5	σ_v	7.94*
u'	1.89*	T_e	1.8	Sk_u	8.01*
v'	7.94*	p_e	6.4	Sk_v	33.68*
$\overline{u'v'}$	8.16*	ρ_e	6.6	Fl_u	10.69*
$\overline{Q}$	8.8	T_w	0.1	Fl_v	44.91*
$\overline{M}$	9.0	p_w	0.6	γ_u	10.69*
$\overline{p_o}$	0.6	ρ_w	0.6	R_{uv}	11.54*
$\overline{T_{o,\infty}}$	4.0	$\overline{T}$	11.7	$\overline{T_o}$	4.0
$\overline{p}$	6.6	Flat Plate δ	28.0	$\overline{\rho}$	13.5
M_e	1.5	u_{eff}	18.9	τ_w	7.1
u^*	3.5	$\frac{u_{eff}}{u^*}$	19.2		

Table B.1 Error Summary: Values marked by * represent changes from Luker (13)

Appendix C. Turbulence Statistics

C.1 Skewness

The skewness was computed using the method described in Chapter 4 and is presented below in figures C.1 through C.16. The error bounds for these data are presented in appendix B and the data is tabulated in appendix D.

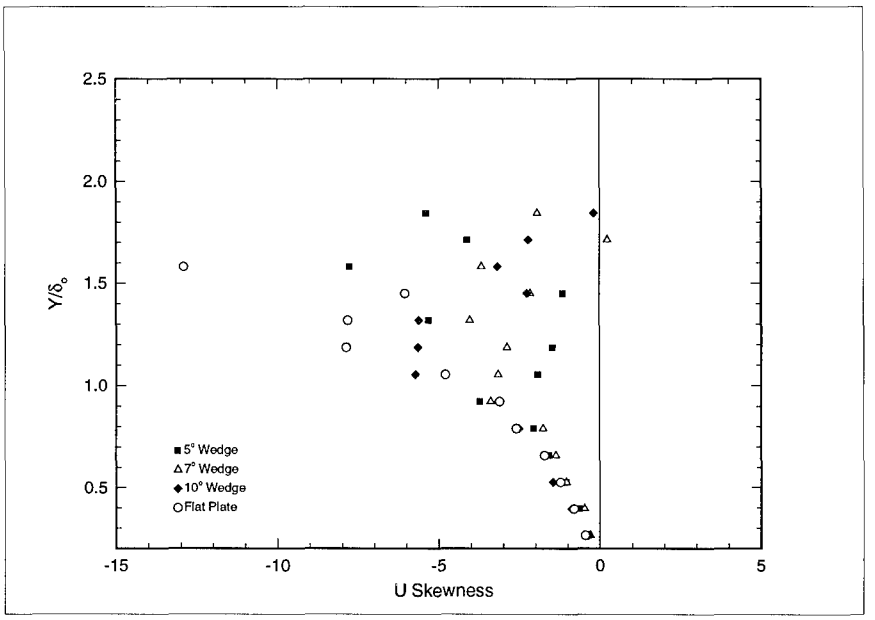

Figure C.1 $X = -1.32\delta_o$ Streamwise Skewness

C.2 Flatness

The flatness was computed using the method described in Chapter 4 and is presented below in figures C.17 through C.32. The error bounds for these data are presented in appendix B and the data is tabulated in appendix D.

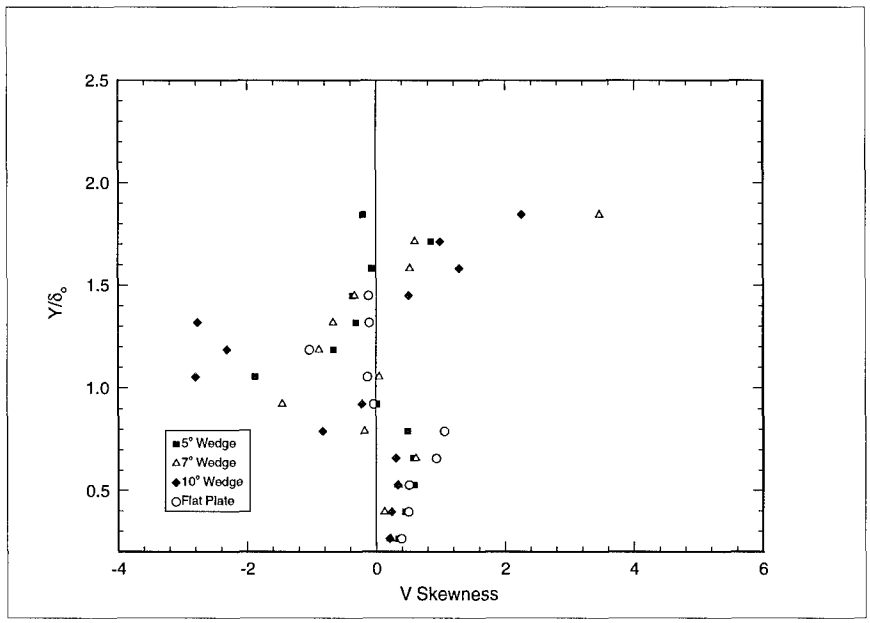

Figure C.2 $X = -1.32\delta_o$ Cross-stream Skewness

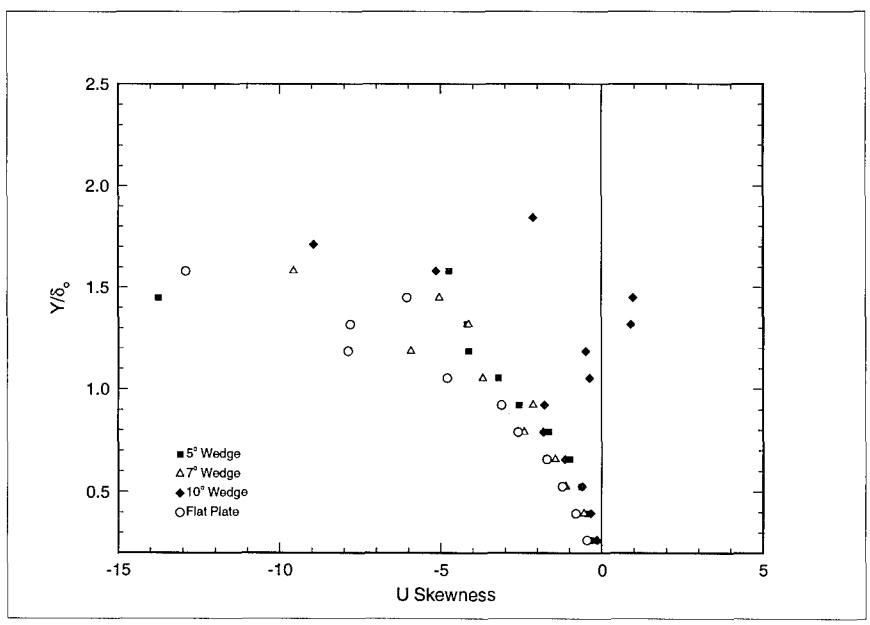

Figure C.3 $X = 0\delta_o$ Streamwise Skewness

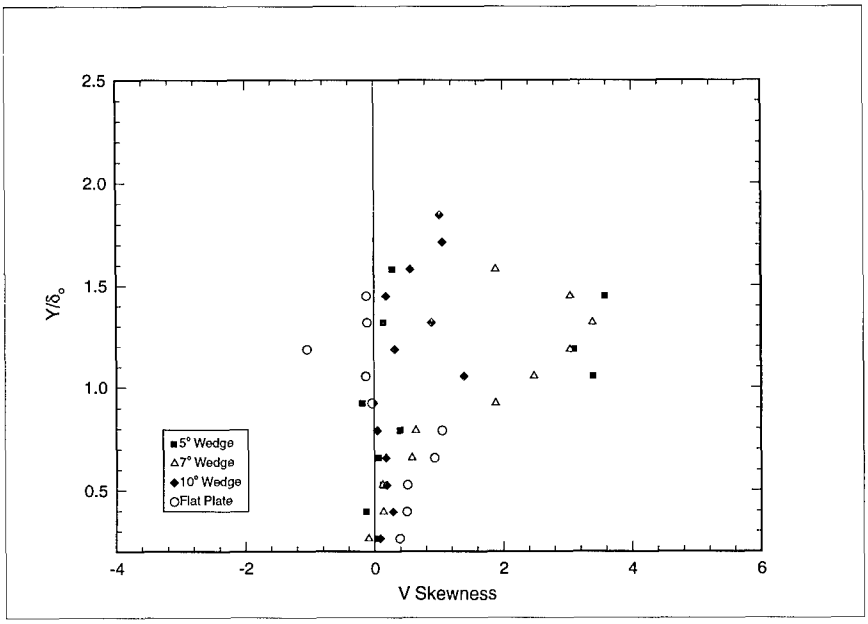

Figure C.4 $X = 0\delta_o$ Cross-stream Skewness

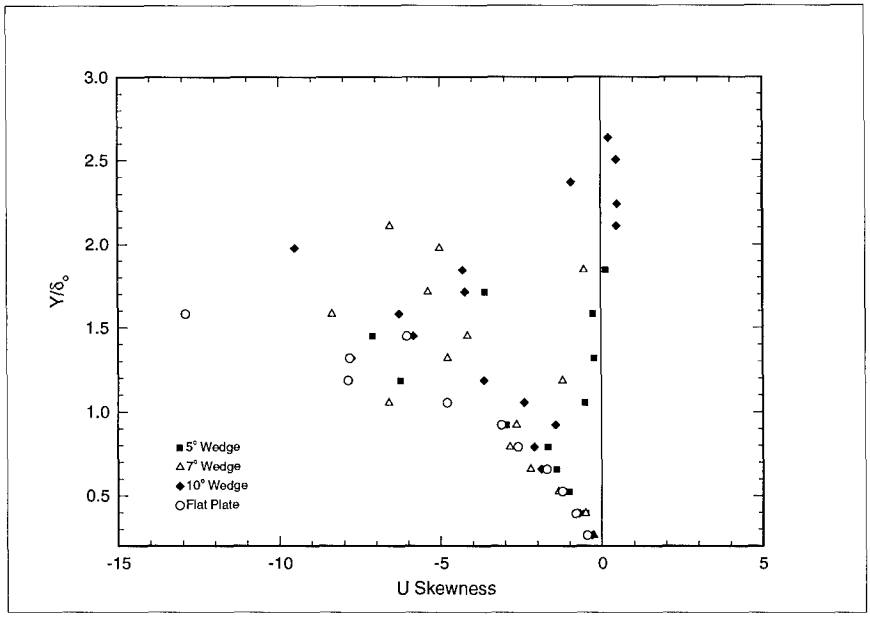

Figure C.5 $X = 1.32\delta_o$ Streamwise Skewness

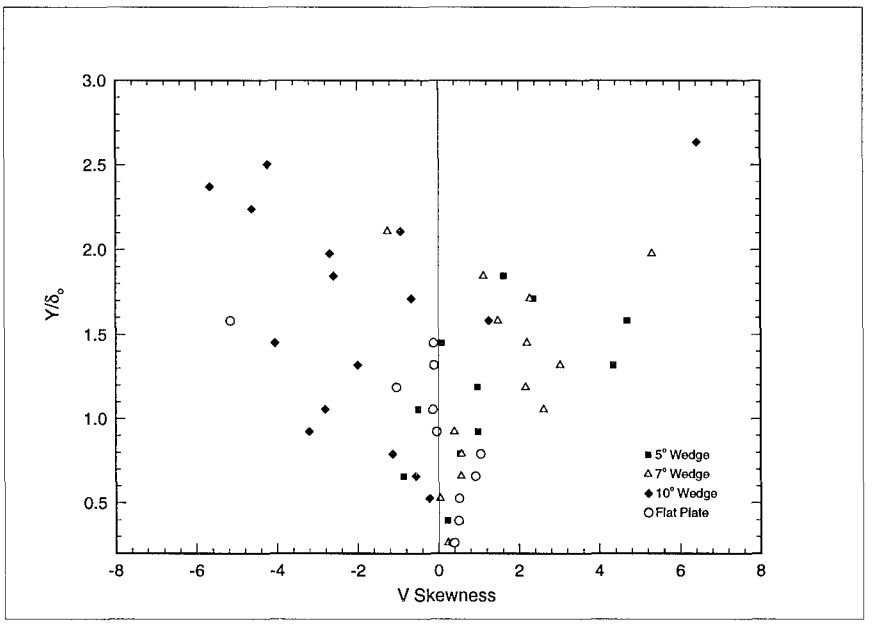

Figure C.6 $X = 1.32\delta_o$ Cross-stream Skewness

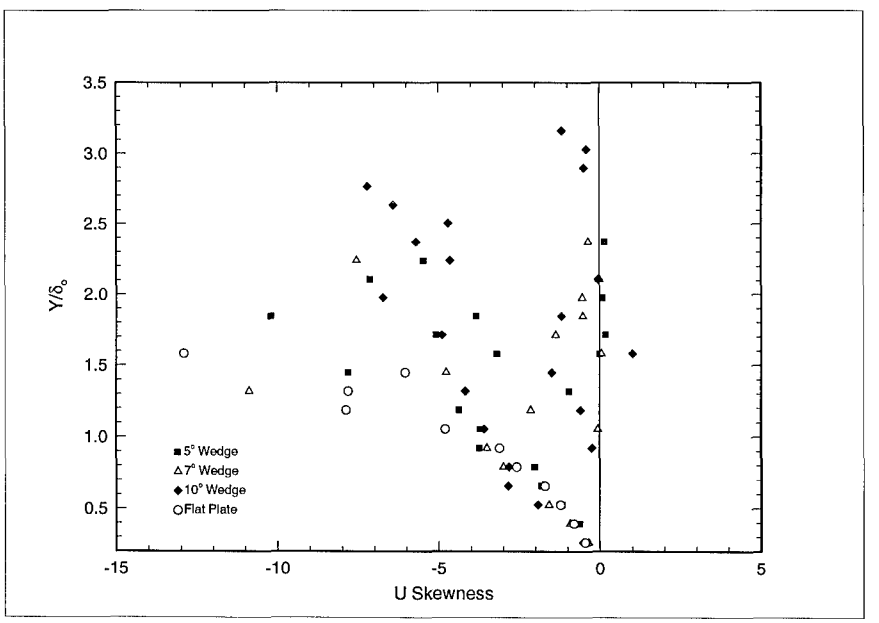

Figure C.7 $X = 2.64\delta_o$ Streamwise Skewness

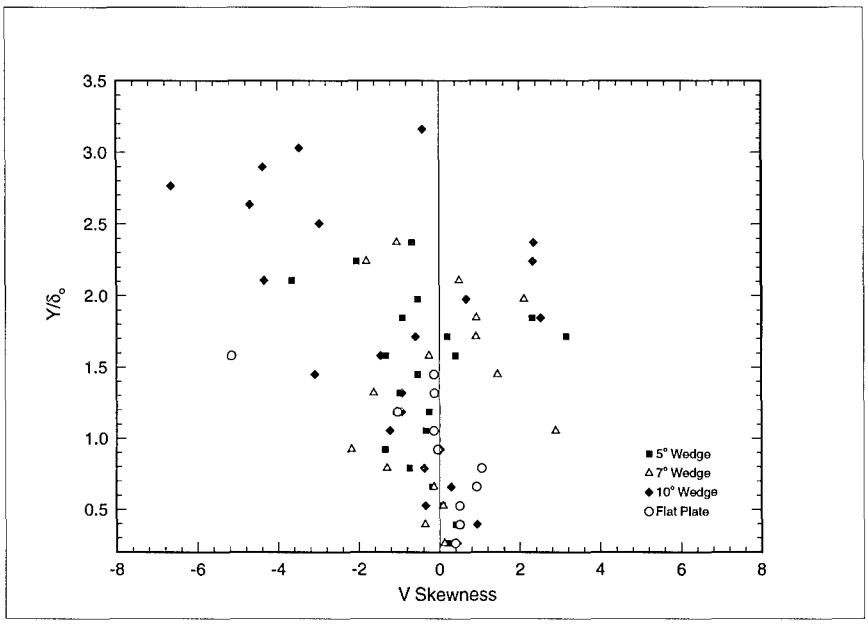

Figure C.8 $X = 2.64\delta_o$ Cross-stream Skewness

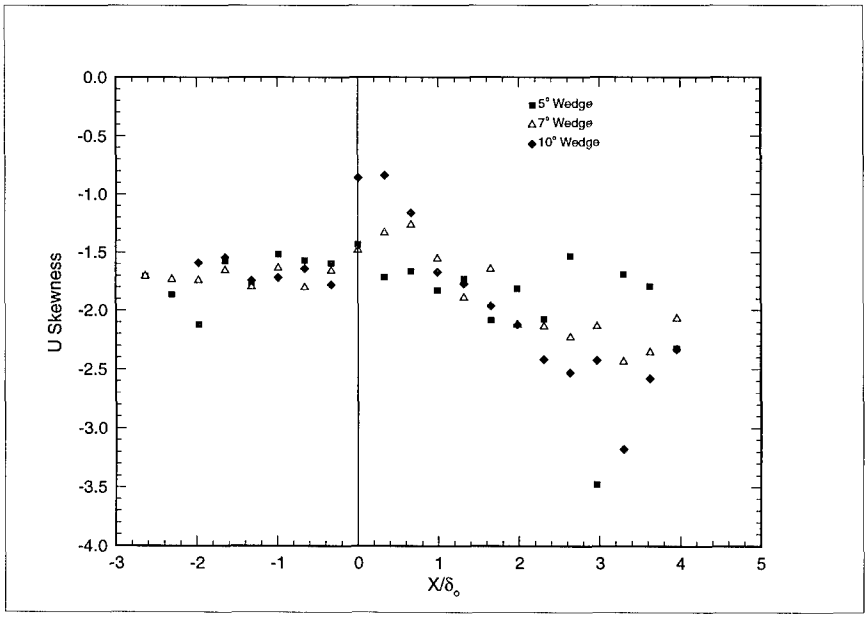

Figure C.9 Streamwise Skewness at a Height from Wall $Y = 0.66\delta_o$

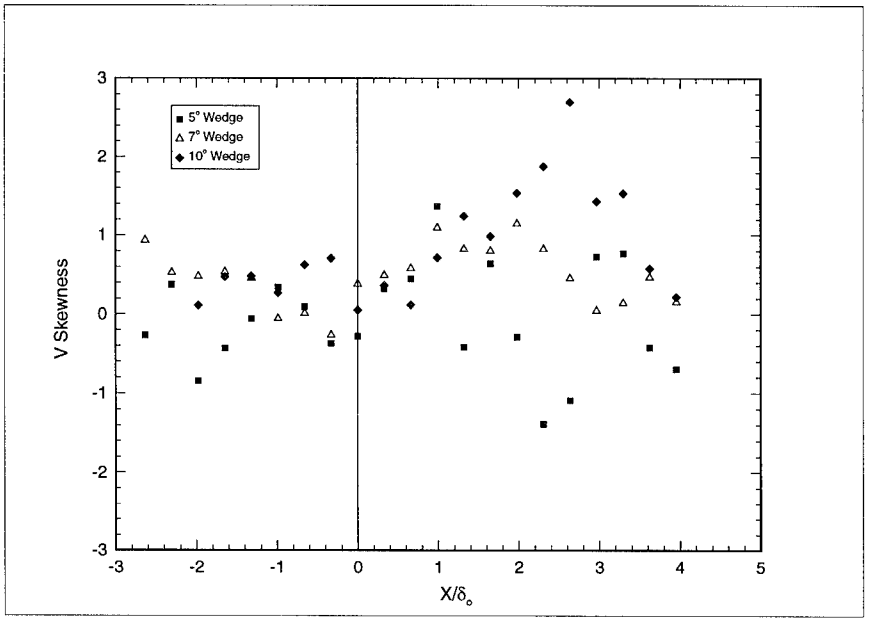

Figure C.10 Cross-stream Skewness at a Height from Wall $Y = 0.66\delta_o$

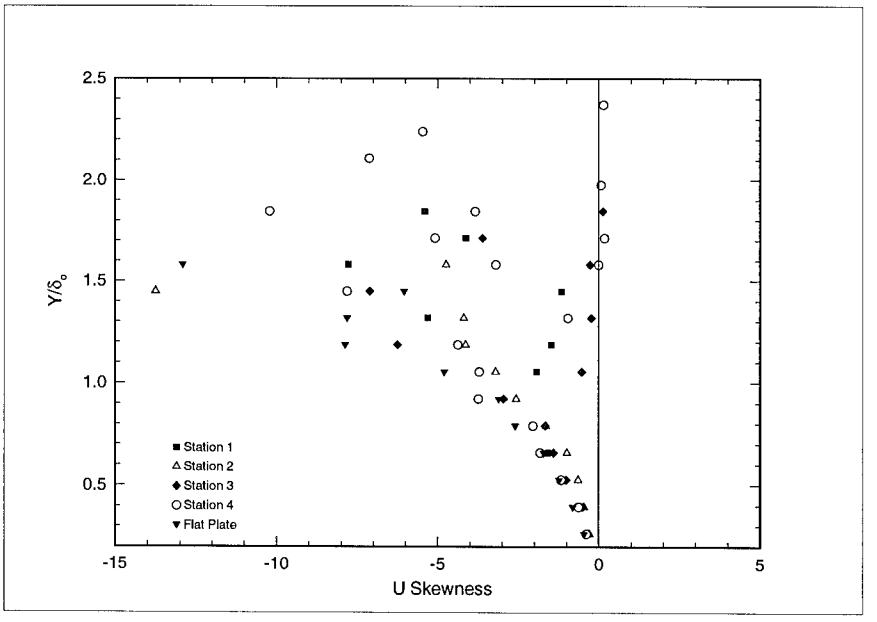

Figure C.11 5^o Wedge Streamwise Skewness at each Station

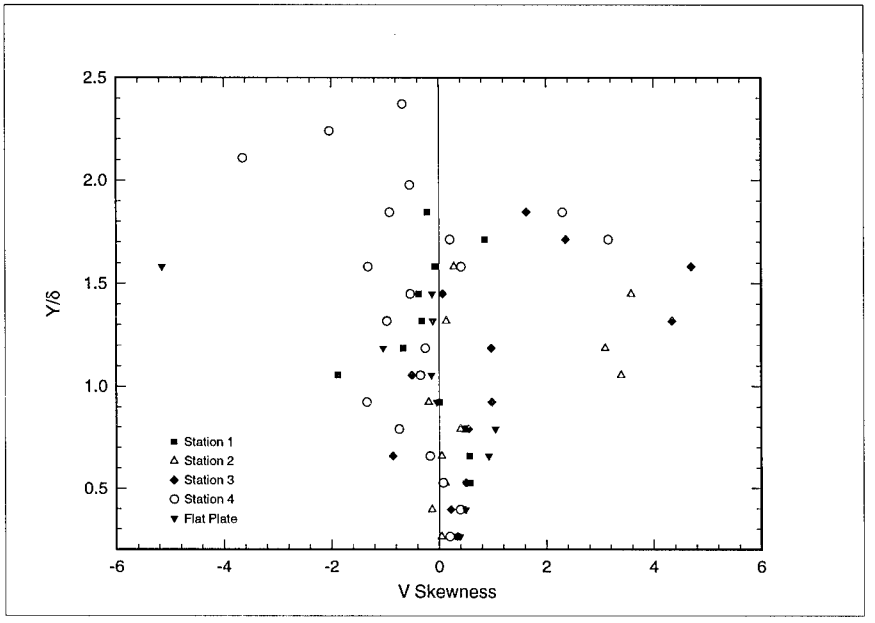

Figure C.12 5^o Wedge Cross-stream Skewness at each Station

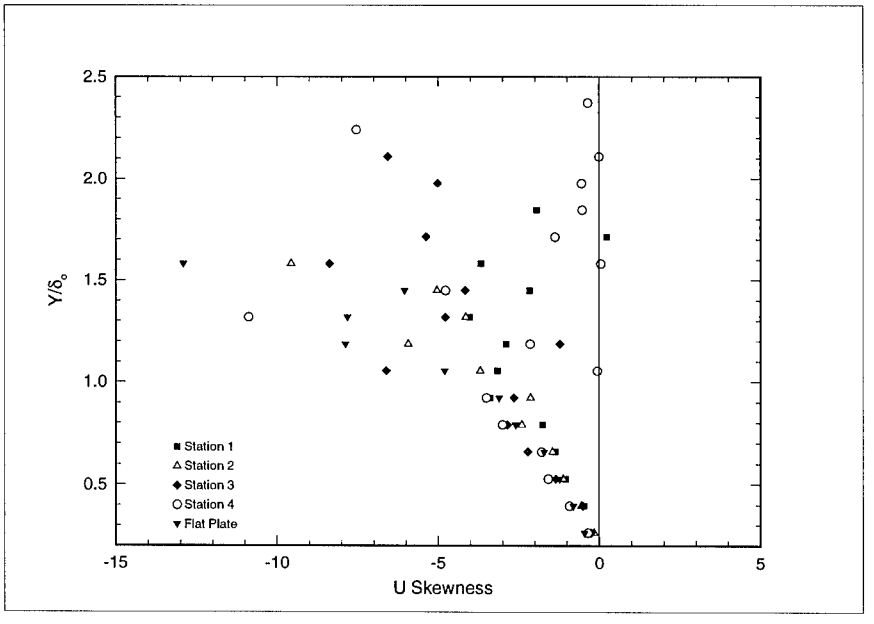

Figure C.13 7^o Wedge Streamwise Skewness at each Station

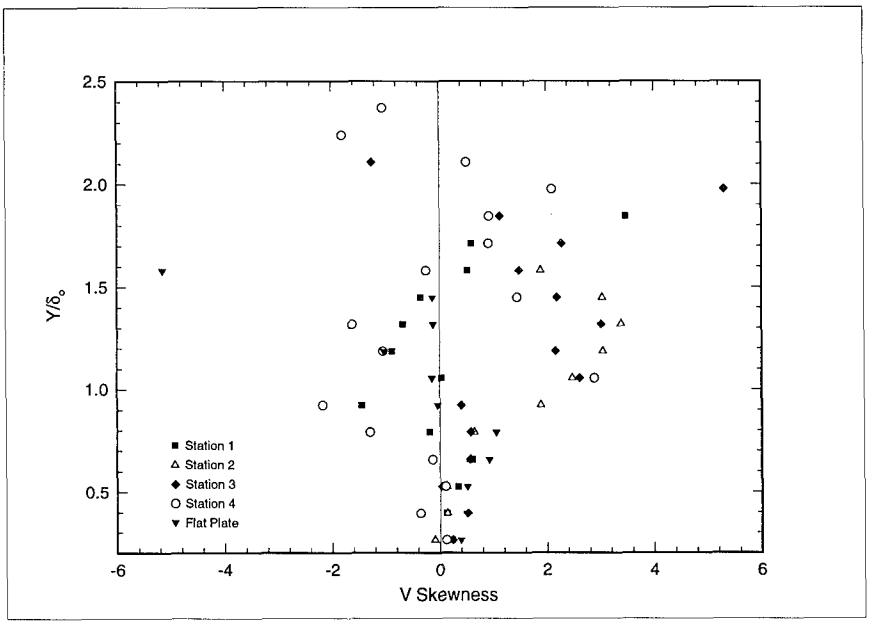

Figure C.14 7^o Wedge Cross-stream Skewness at each Station

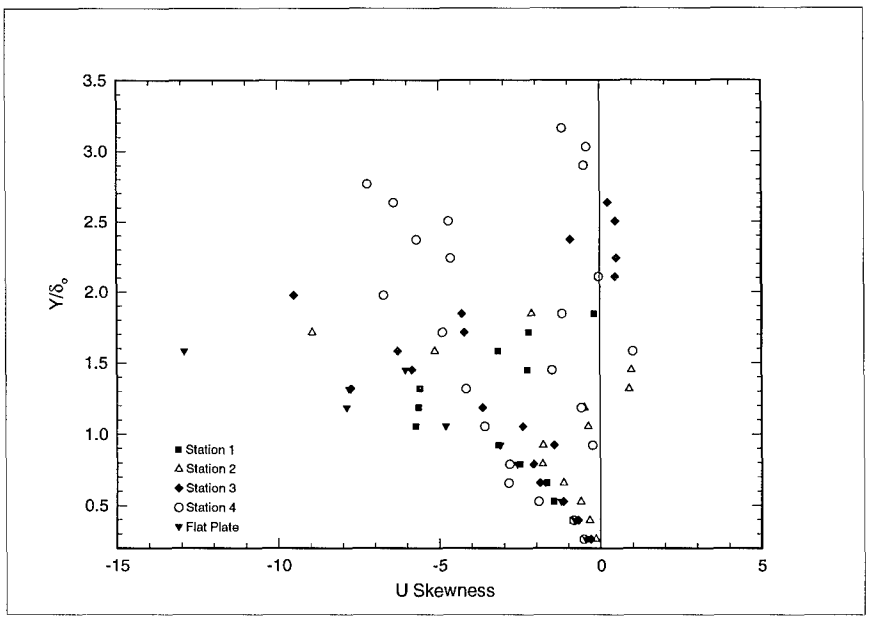

Figure C.15 10^o Wedge Streamwise Skewness at each Station

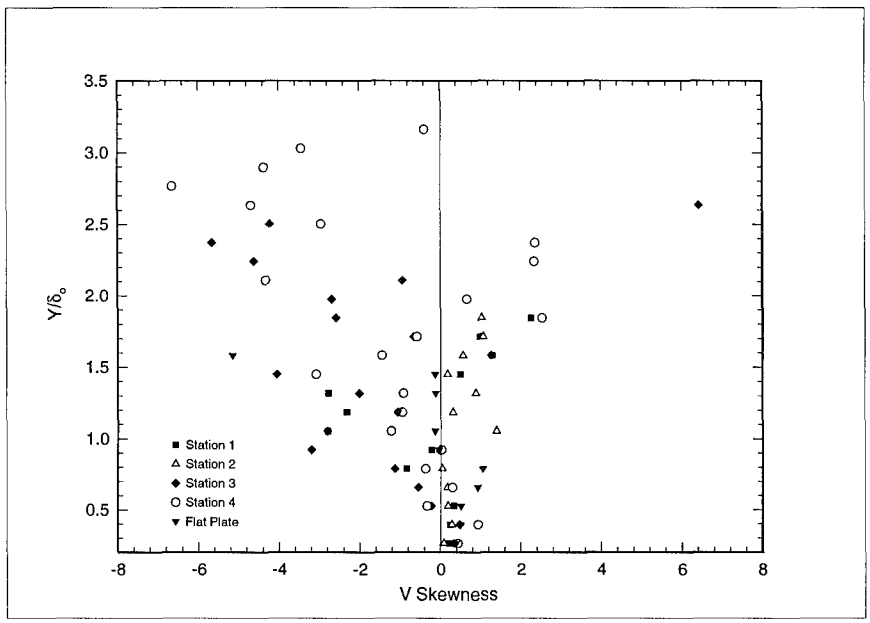

Figure C.16 10^o Wedge Cross-stream Skewness at each Station

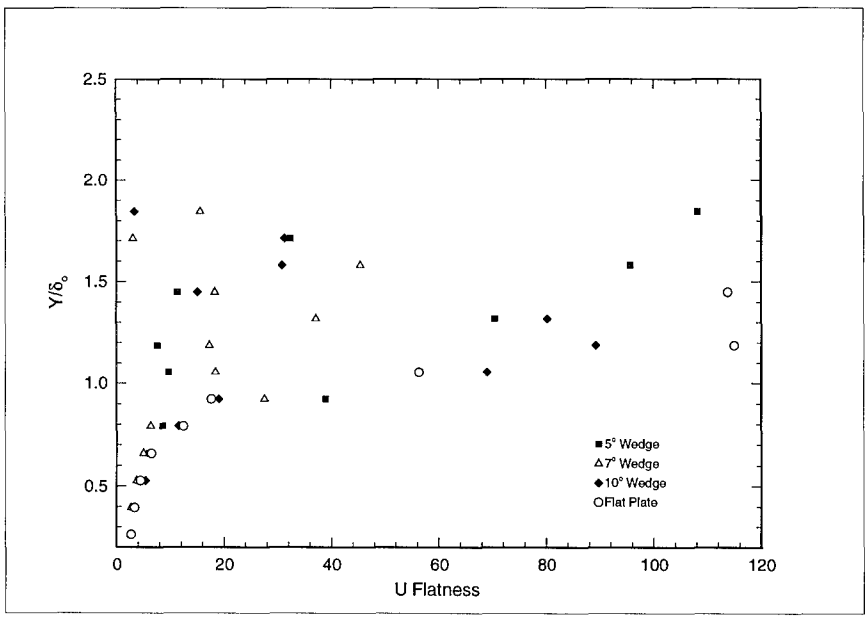

Figure C.17 $X = -1.32\delta_o$ Streamwise Flatness

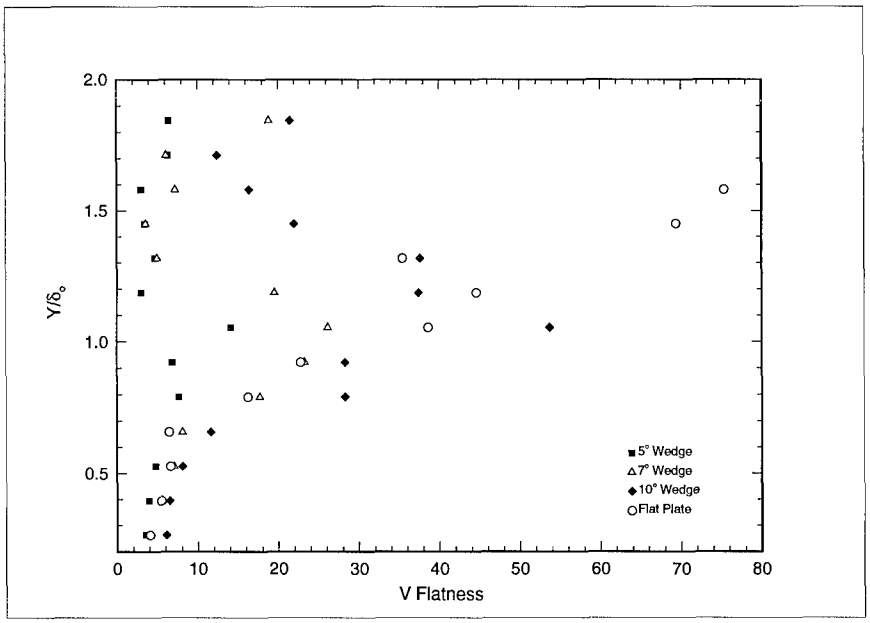

Figure C.18 $X = -1.32\delta_o$ Cross-stream Flatness

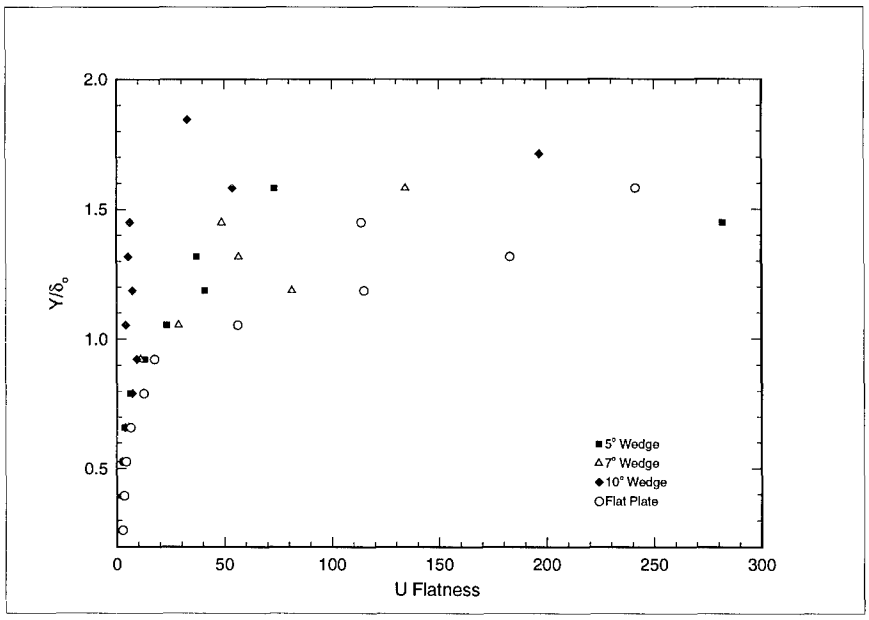

Figure C.19 $X = 0\delta_o$ Streamwise Flatness

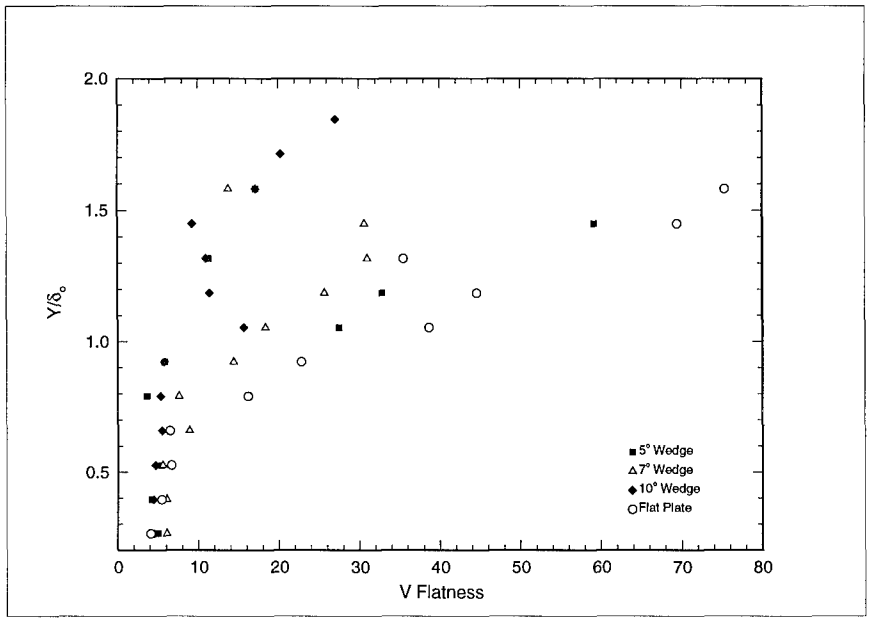

Figure C.20 $X = 0\delta_o$ Cross-stream Flatness

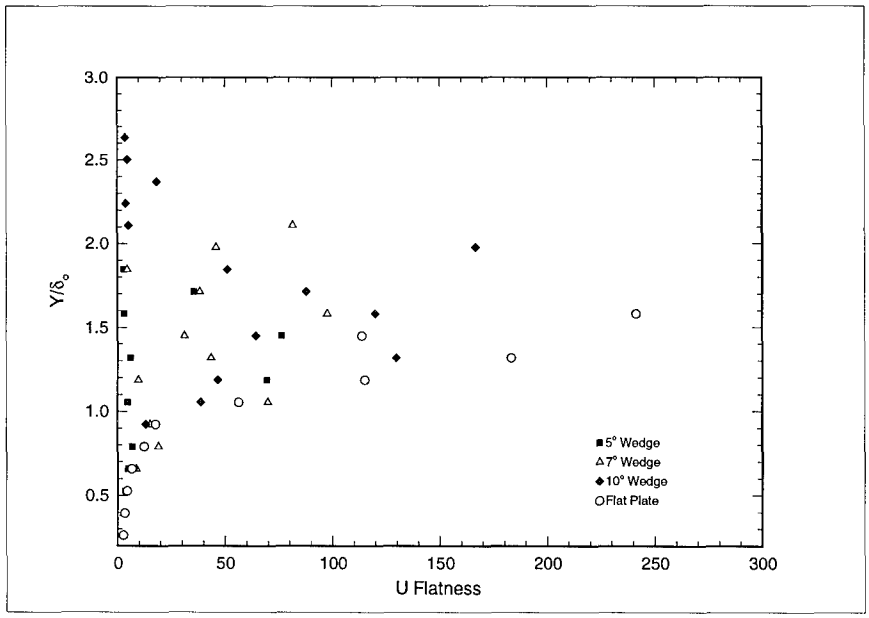

Figure C.21 $X = 1.32\delta_o$ Streamwise Flatness

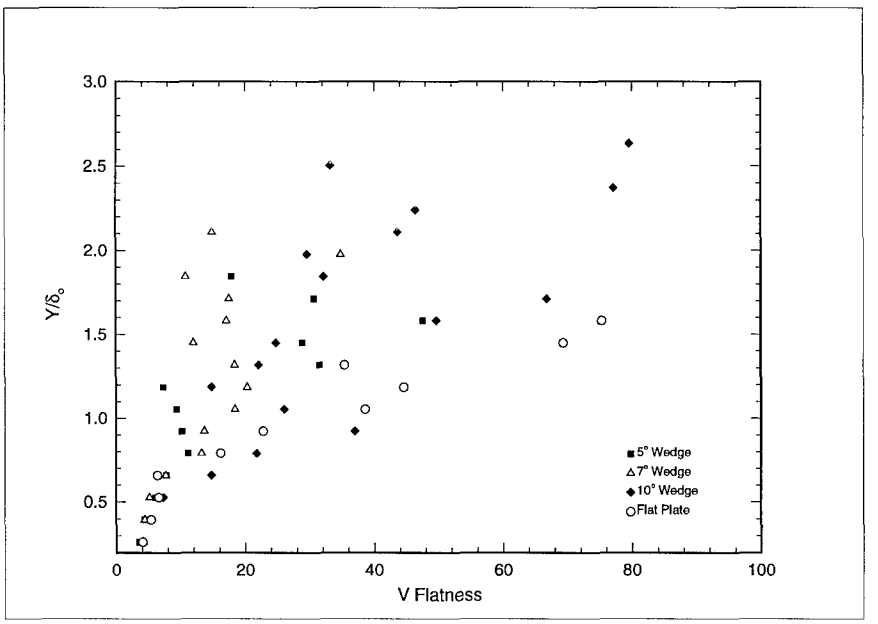

Figure C.22 $X = 1.32\delta_o$ Cross-stream Flatness

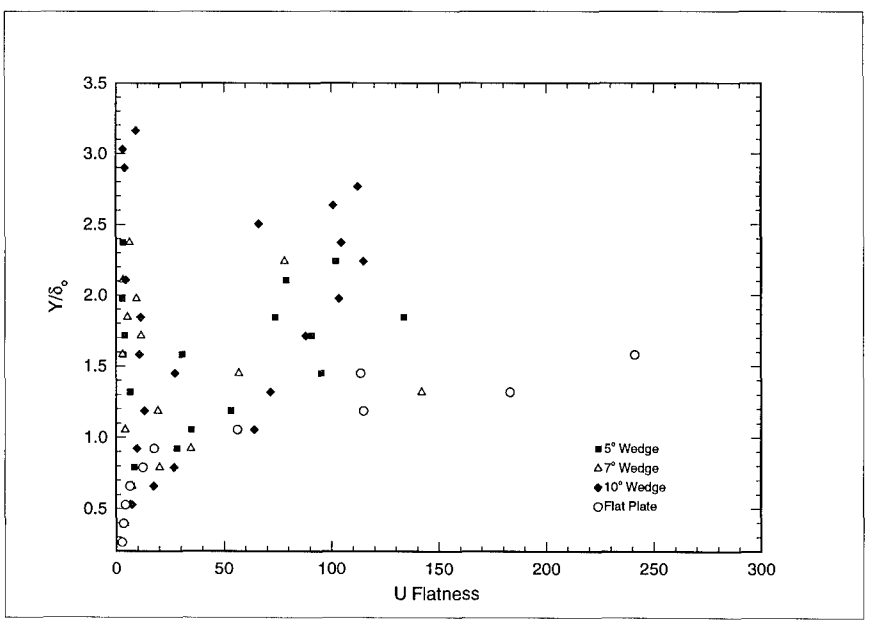

Figure C.23 $X = 2.64\delta_o$ Streamwise Flatness

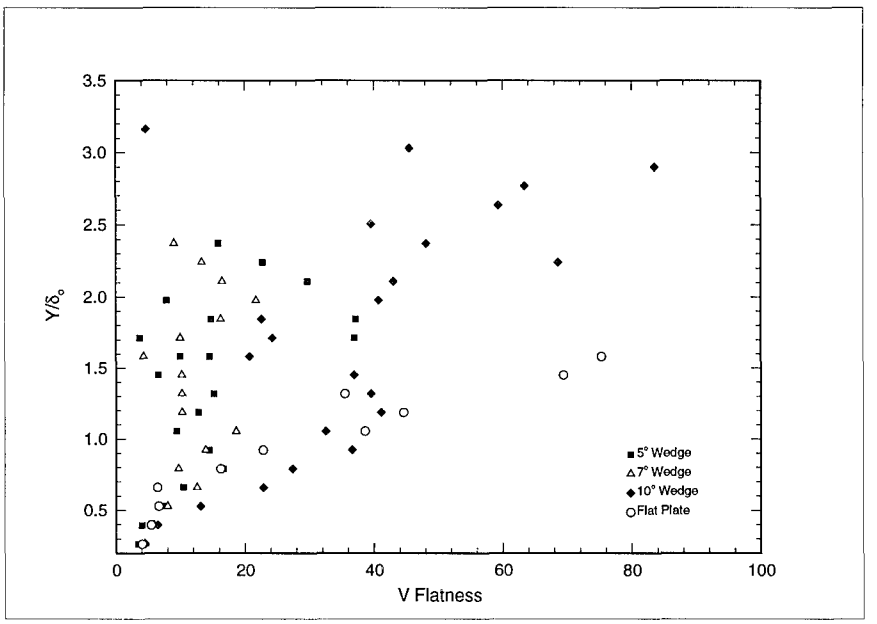

Figure C.24 $X = 2.64\delta_o$ Cross-stream Flatness

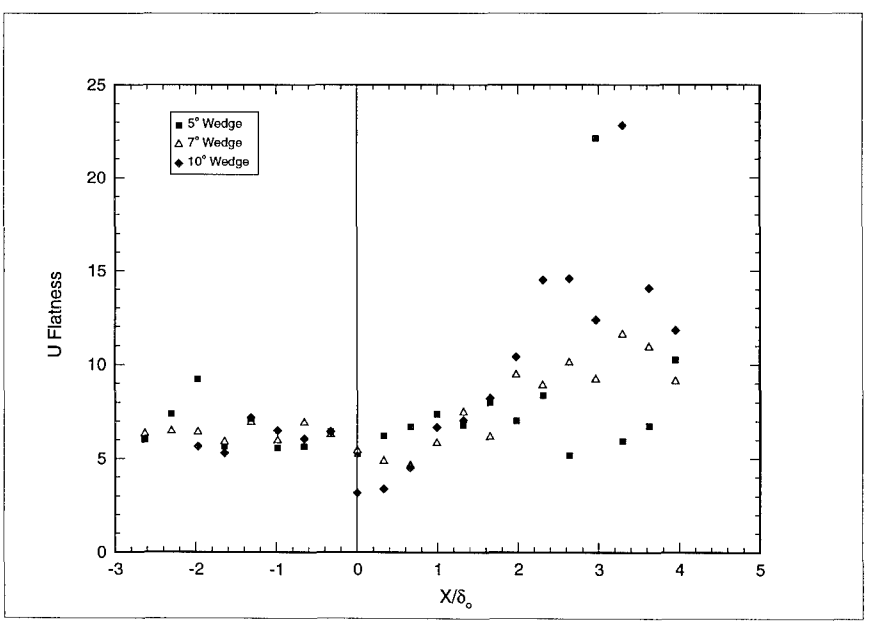

Figure C.25 Streamwise Flatness at a Height from Wall $Y = 0.66\delta_o$

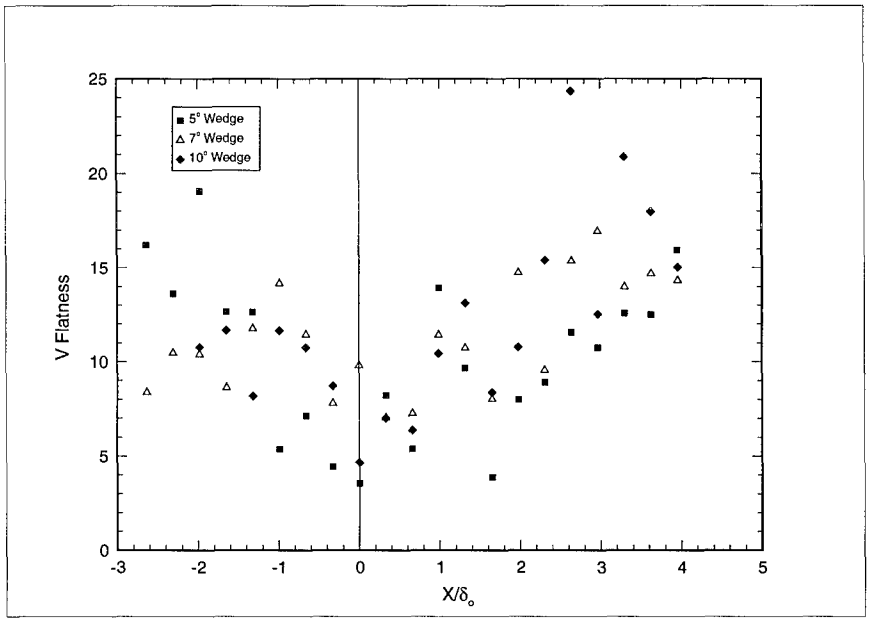

Figure C.26 Cross-stream Flatness at a Height from Wall $Y = 0.66\delta_o$

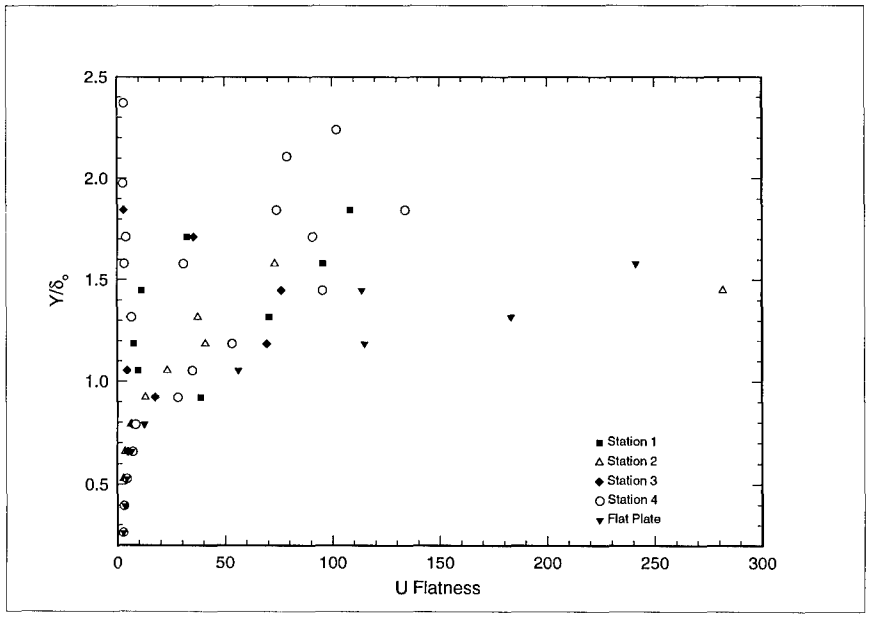

Figure C.27 5^o Wedge Streamwise Flatness at each Station

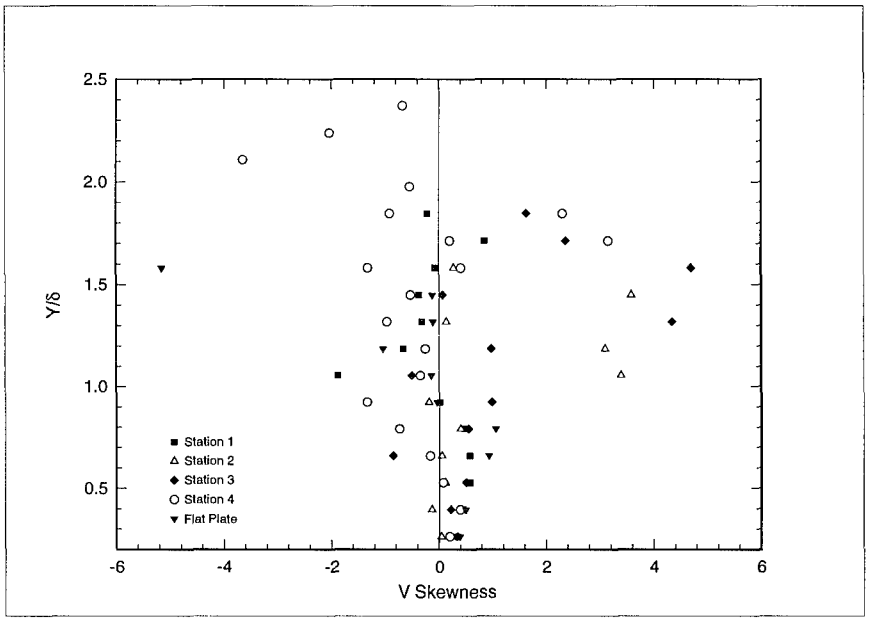

Figure C.28 5° Wedge Cross-stream Skewness at each Station

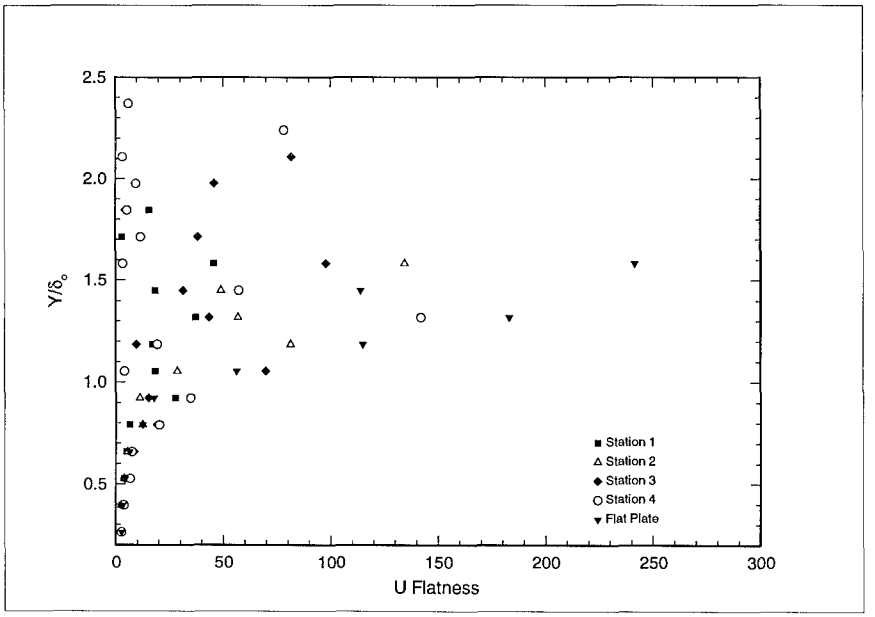

Figure C.29 7° Wedge Streamwise Flatness at each Station

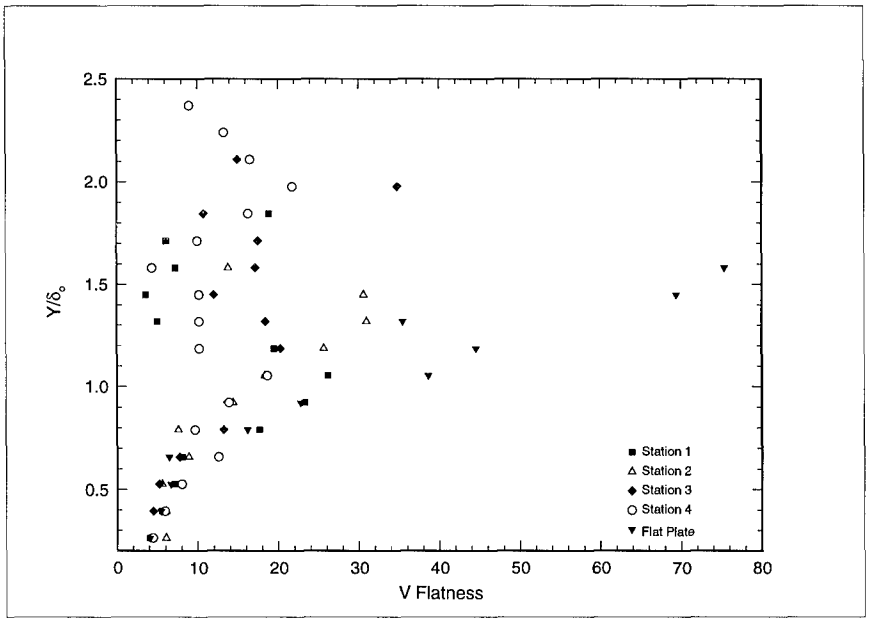

Figure C.30 7^o Wedge Cross-stream Flatness at each Station

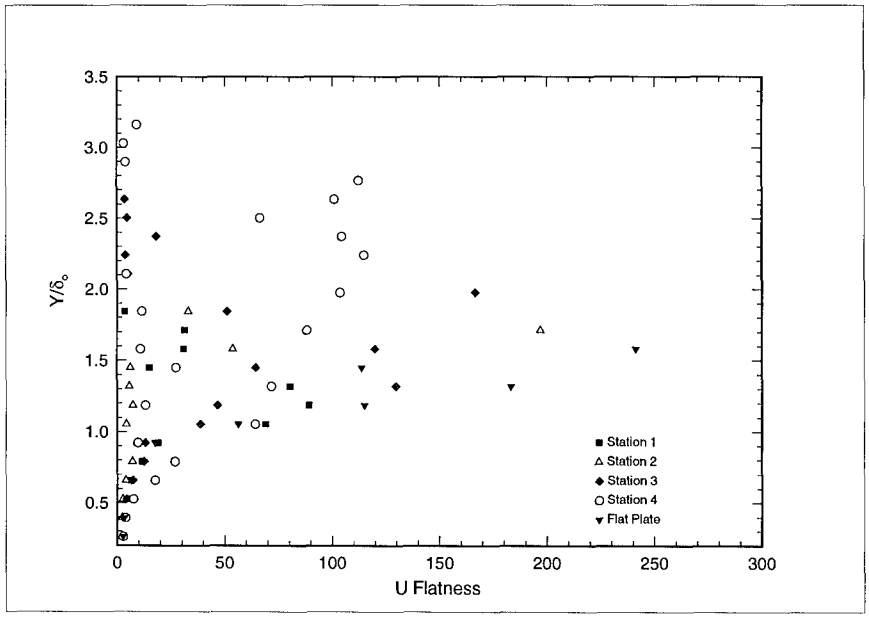

Figure C.31 10^o Wedge Streamwise Flatness at each Station

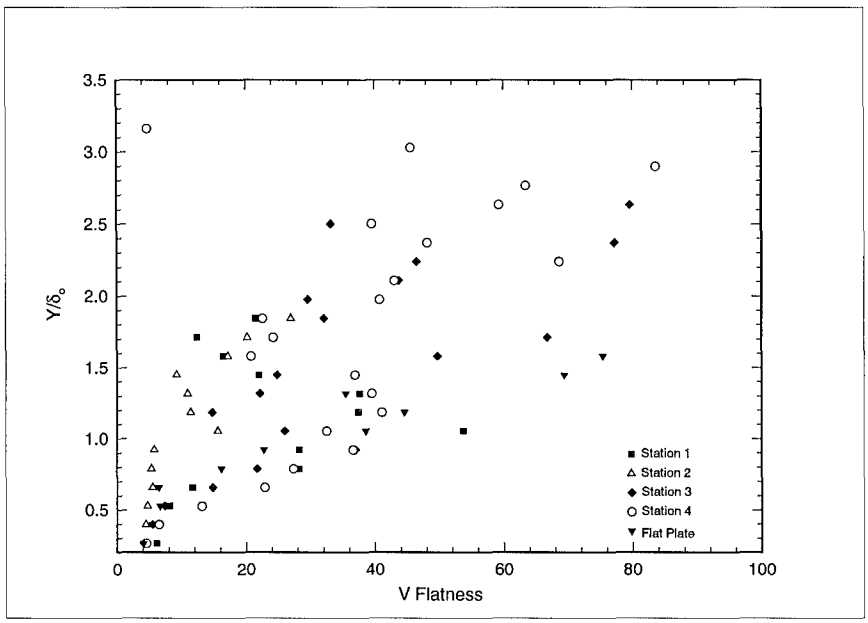

Figure C.32 10^o Wedge Cross-stream Flatness at each Station

C.3 Intermittency

The intermittency was computed from the flatness using the method described in Chapter 4 and is presented below in figures C.33 through C.39. The error bounds for these data are presented in appendix B and the data is tabulated in appendix D.

C.4 Velocity Correlation Coefficient

The velocity correlation coefficient was computed using the method described in Chapter 4 and is presented below in figures C.40 through C.46. The error bounds for these data are presented in appendix B and the data is tabulated in appendix D.

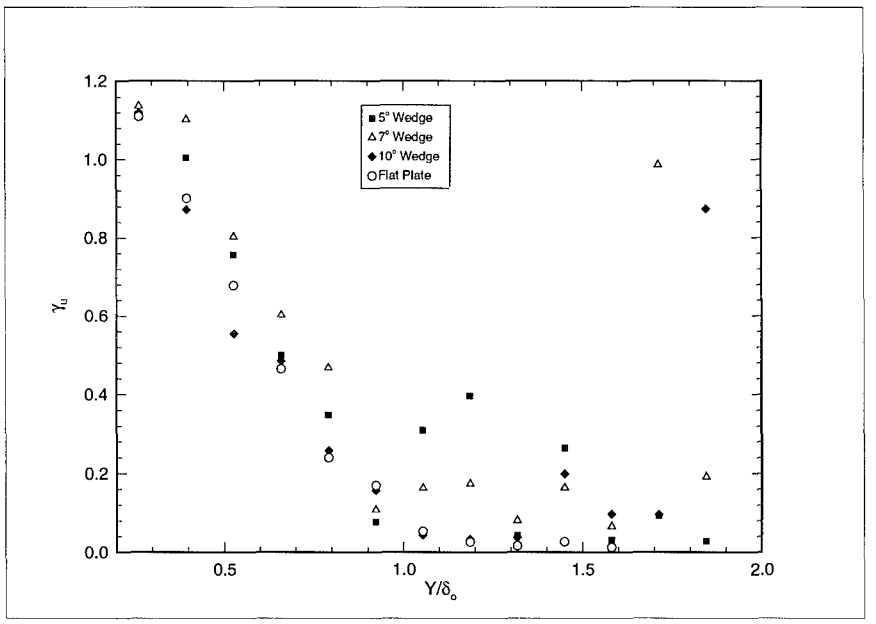

Figure C.33 $X = -1.32\delta_o$ Intermittency Function

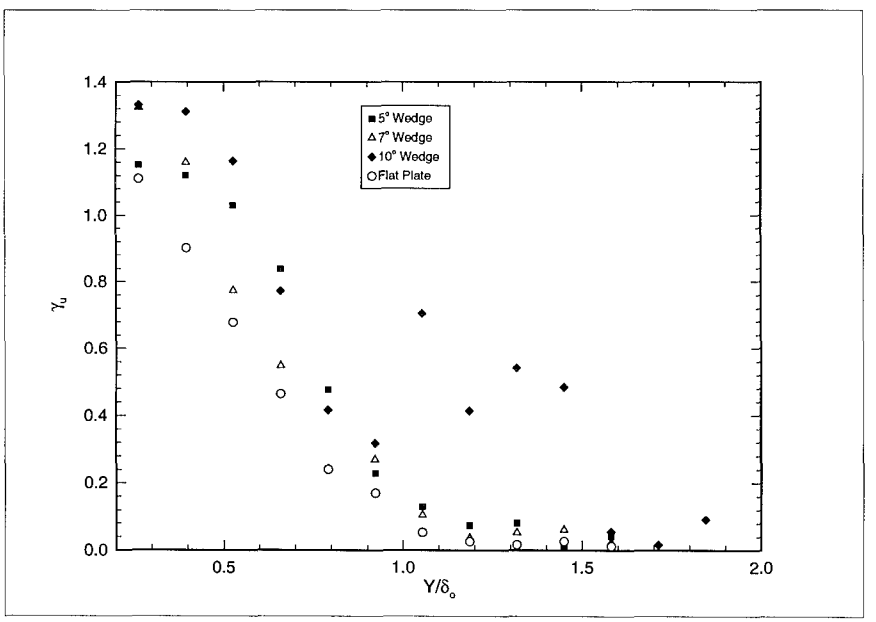

Figure C.34 $X = 0\delta_o$ Intermittency Function

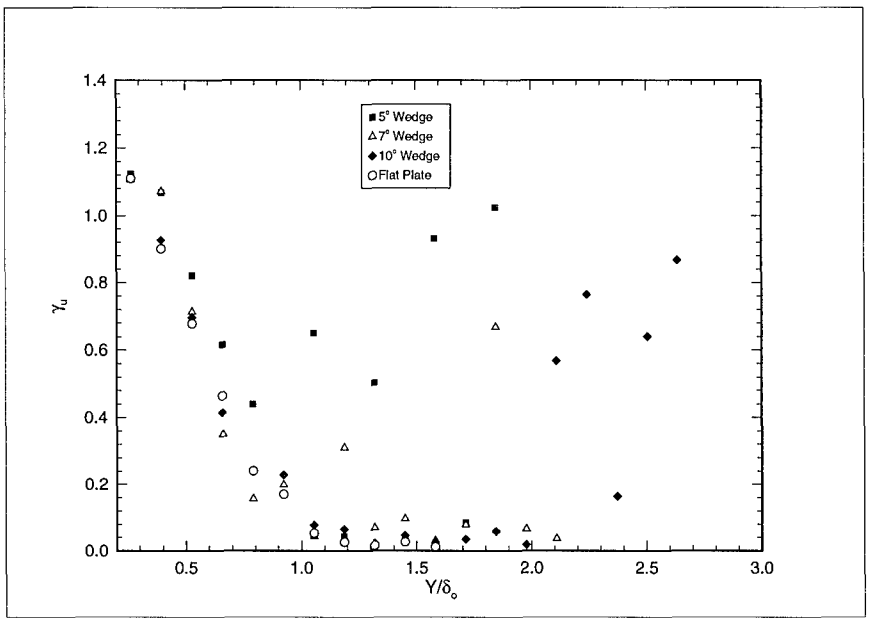

Figure C.35 $X = 1.32\delta_o$ Intermittency Function

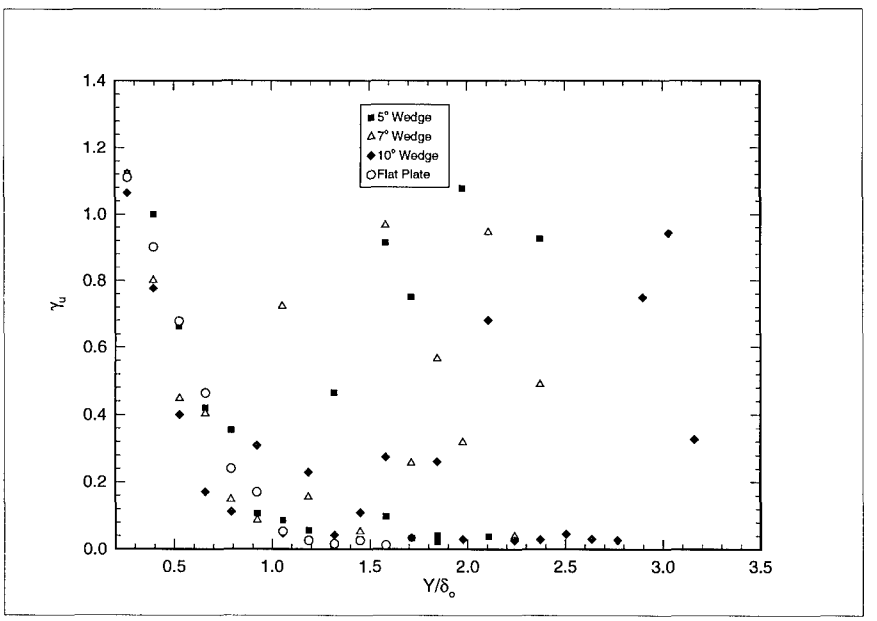

Figure C.36 $X = 2.64\delta_o$ Intermittency Function

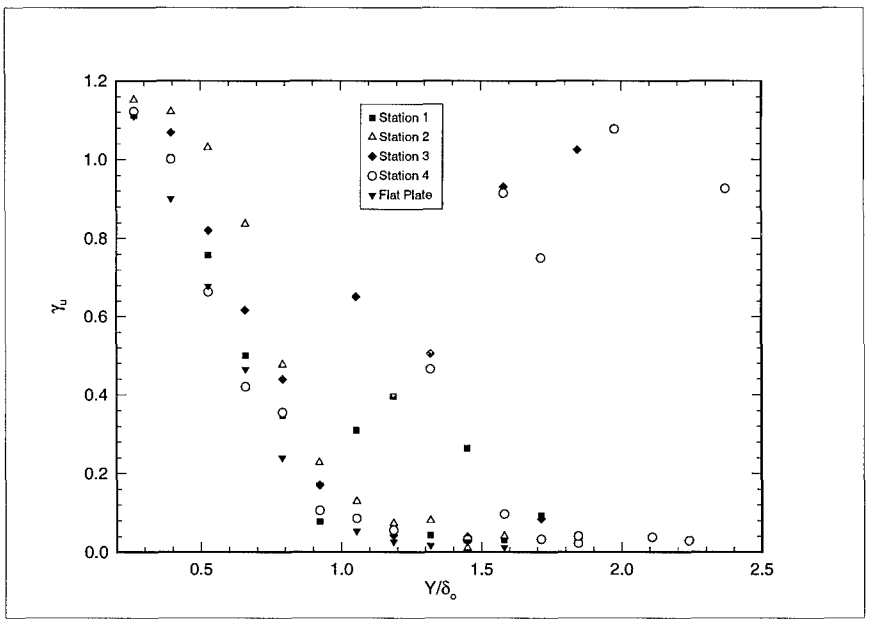

Figure C.37 5^o Wedge Intermittency Function

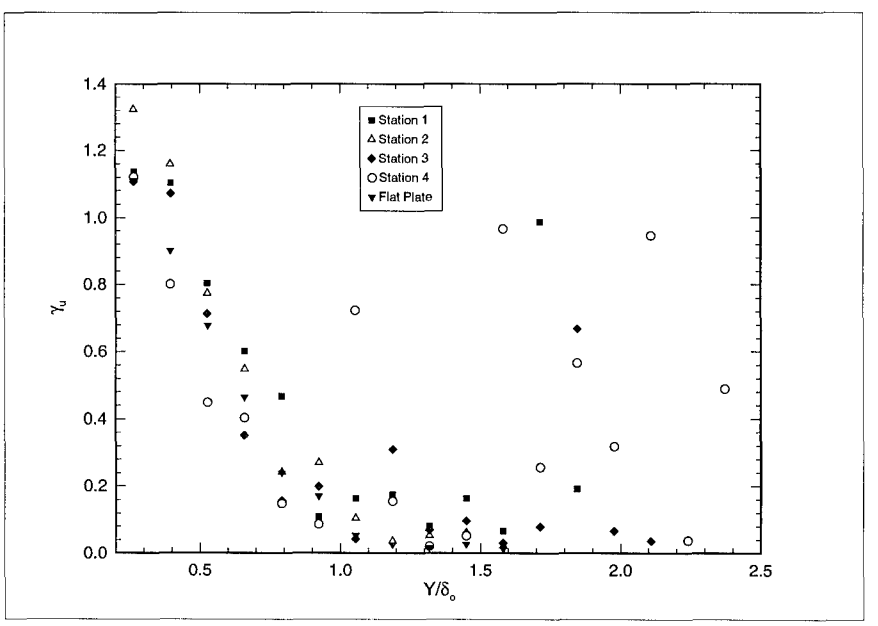

Figure C.38 7^o Wedge Intermittency Function

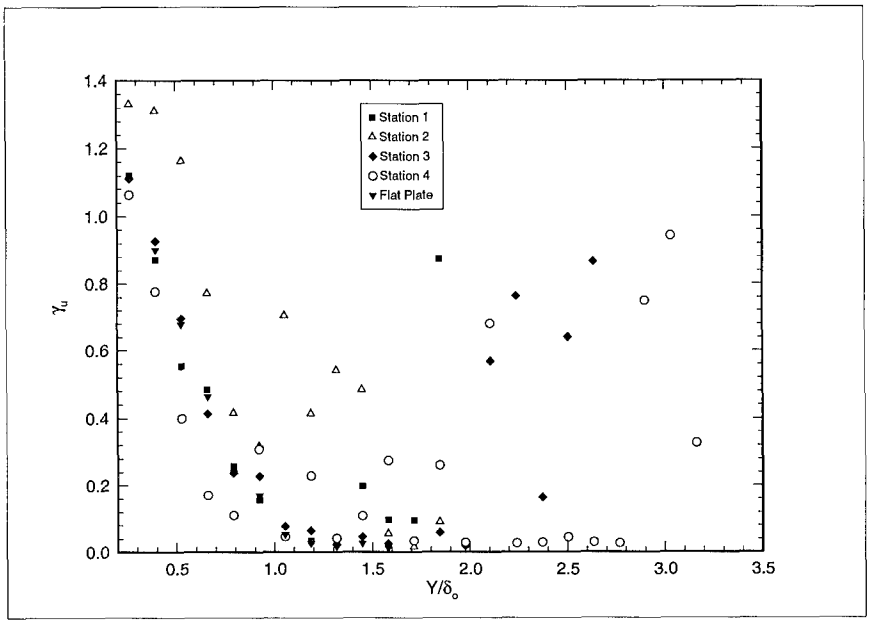

Figure C.39 10^o Wedge Intermittency Function

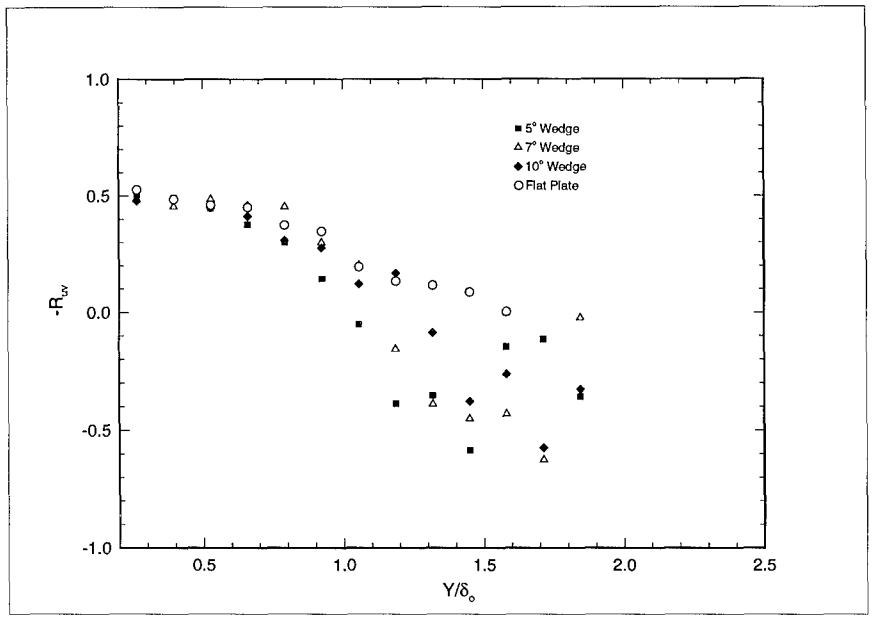

Figure C.40 Velocity Correlation Coefficient at $X = -1.32\delta_o$

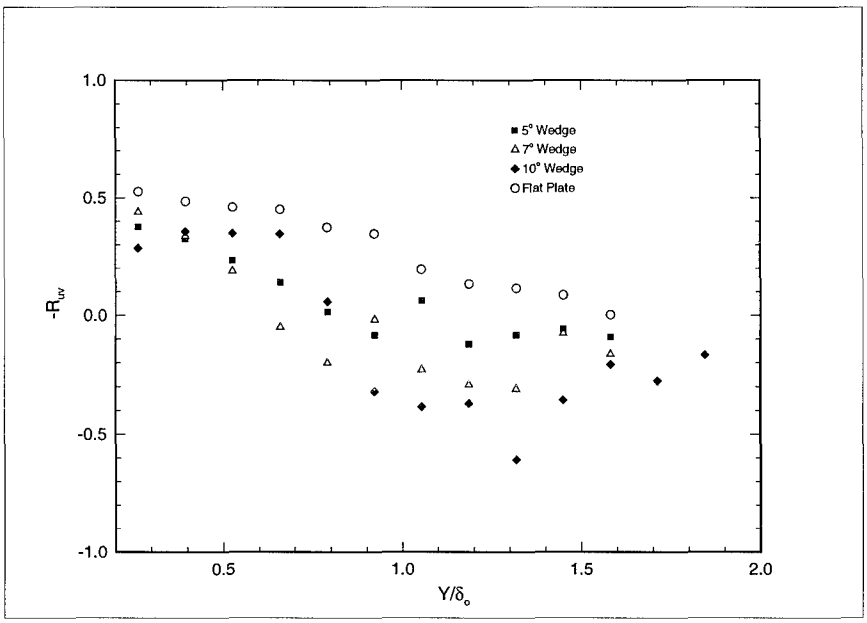

Figure C.41 Velocity Correlation Coefficient at $X = 0\delta_o$

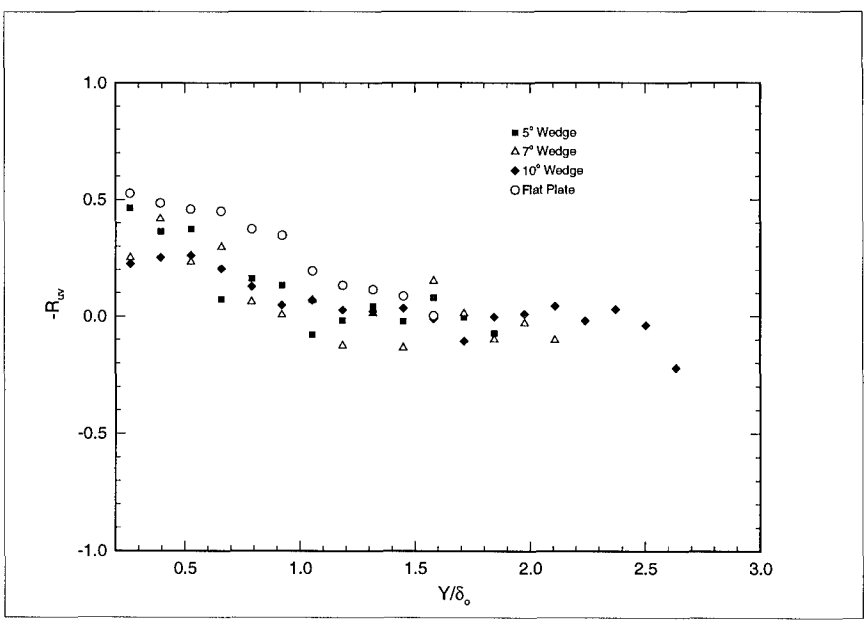

Figure C.42 Velocity Correlation Coefficient at $X = 1.32\delta_o$

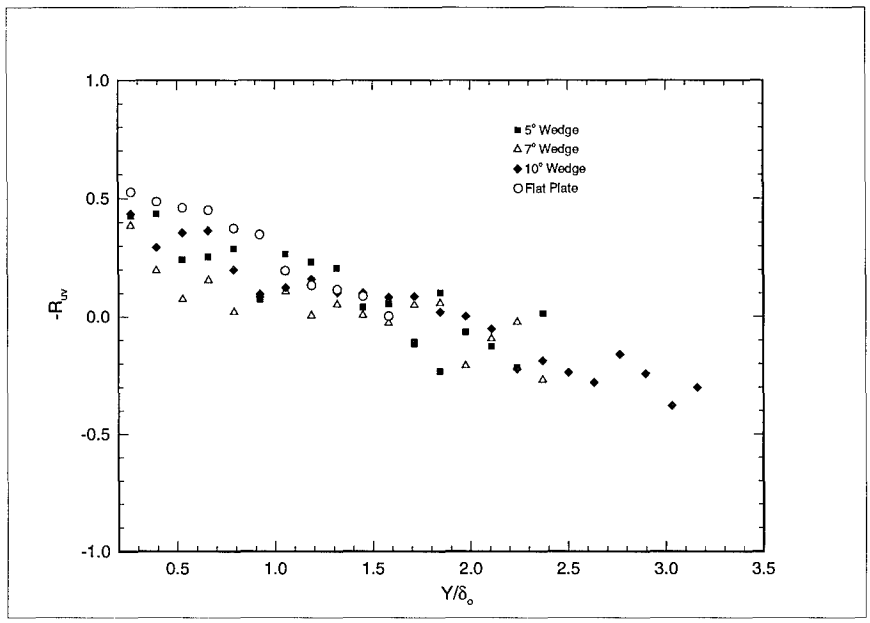

Figure C.43 Velocity Correlation Coefficient at $X = 2.64\delta_o$

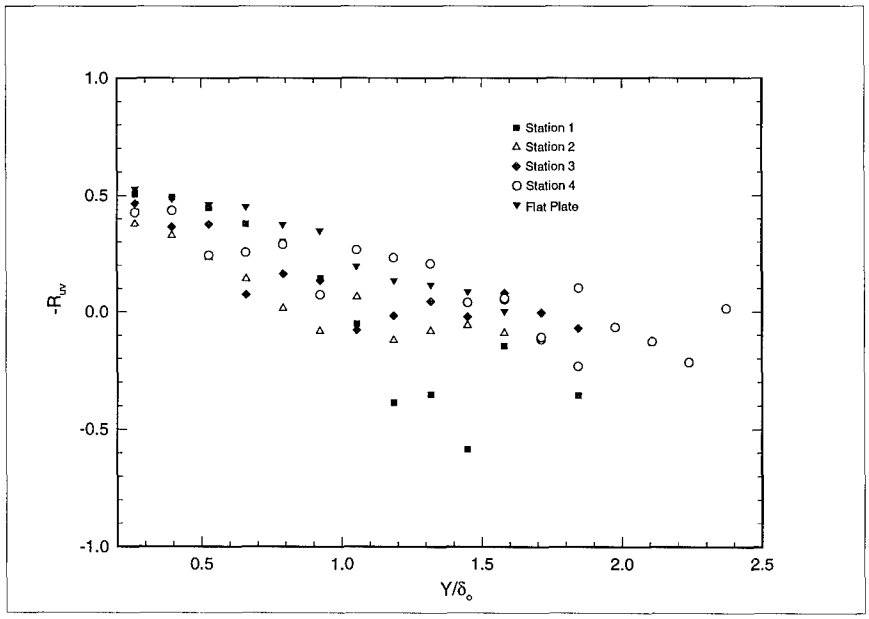

Figure C.44 5^o Wedge Correlation Coefficient

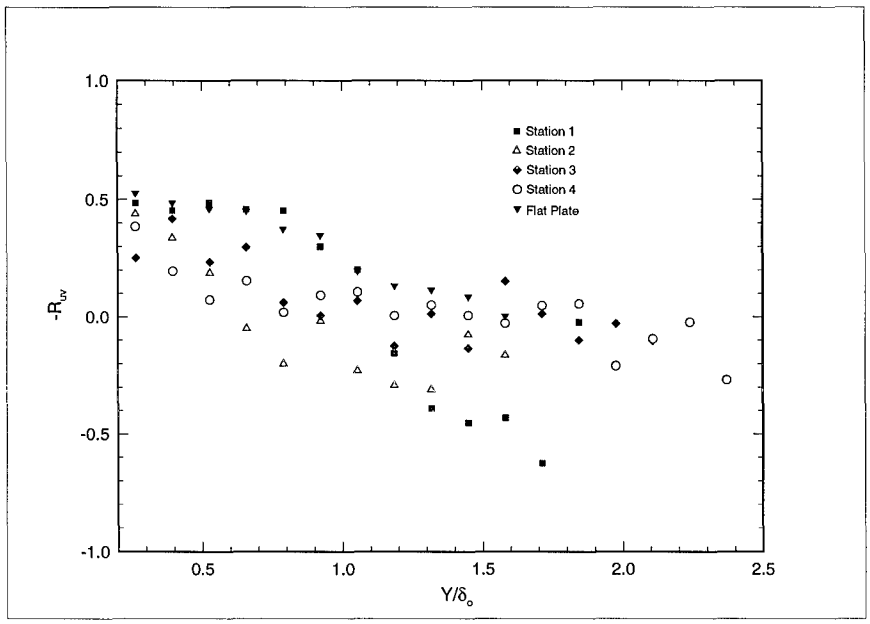

Figure C.45 7^o Wedge Correlation Coefficient

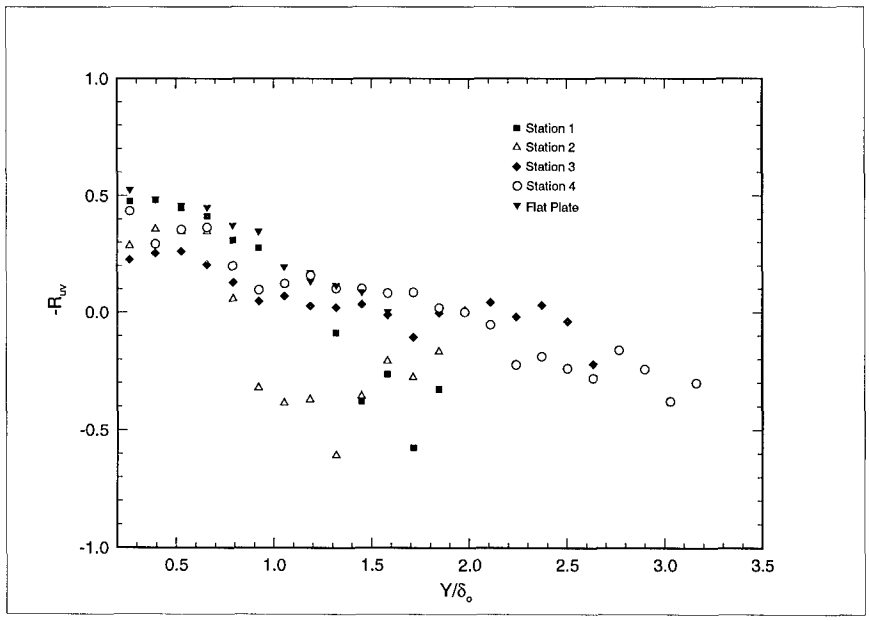

Figure C.46 10^o Wedge Correlation Coefficient

Appendix D. Tabulated Data

The tabulated data for all coincident data points is presented in Figures D.1 through D.24. The density, ρ, has units of $\frac{kg}{m^3}$ while the velocities have units of $\frac{m}{s}$. The temperature is in degrees Kelvin.

D.1 Flat Plate Tabulated Data

Y	Y/δ_u	Y/δ_M	ρ	T	M	M'	U
0.20000E+01	0.26353E+00	0.23726E+00	0.69895E+00	0.15992E+03	0.20651E+01	0.31831E+00	0.52322E+03
0.30000E+01	0.39529E+00	0.35589E+00	0.78662E+00	0.14210E+03	0.23236E+01	0.32062E+00	0.55500E+03
0.40000E+01	0.52706E+00	0.47452E+00	0.85933E+00	0.13008E+03	0.25220E+01	0.29720E+00	0.57640E+03
0.50000E+01	0.65882E+00	0.59315E+00	0.91476E+00	0.12220E+03	0.26642E+01	0.26048E+00	0.59020E+03
0.60000E+01	0.79058E+00	0.71178E+00	0.95510E+00	0.11703E+03	0.27642E+01	0.20616E+00	0.59933E+03
0.70000E+01	0.92235E+00	0.83041E+00	0.98247E+00	0.11377E+03	0.28286E+01	0.16022E+00	0.60470E+03
0.80000E+01	0.10541E+01	0.94904E+00	0.99873E+00	0.11192E+03	0.28668E+01	0.12672E+00	0.60786E+03
0.90000E+01	0.11859E+01	0.10677E+01	0.10012E+01	0.11164E+03	0.28738E+01	0.13699E+00	0.60860E+03
0.10000E+02	0.13176E+01	0.11863E+01	0.10092E+01	0.11076E+03	0.28926E+01	0.85648E-01	0.61018E+03
0.11000E+02	0.14494E+01	0.13049E+01	0.10087E+01	0.11082E+03	0.28918E+01	0.75619E-01	0.61016E+03
0.12000E+02	0.15812E+01	0.14236E+01	0.10048E+01	0.11125E+03	0.28842E+01	0.12443E+00	0.60973E+03

Y	U/U_e	U'/U	U'/U_e	SK_u	FL_u	γ_u	V
0.20000E+01	0.86033E+00	0.83268E-01	0.71638E-01	-0.45890E+00	0.27014E+01	0.11105E+01	0.28600E-01
0.30000E+01	0.91259E+00	0.66362E-01	0.60561E-01	-0.81140E+00	0.33291E+01	0.90114E+00	0.66600E+00
0.40000E+01	0.94777E+00	0.51824E-01	0.49117E-01	-0.12348E+01	0.44240E+01	0.67812E+00	0.16818E+01
0.50000E+01	0.97046E+00	0.40327E-01	0.39136E-01	-0.17185E+01	0.64578E+01	0.46455E+00	0.28439E+01
0.60000E+01	0.98547E+00	0.29431E-01	0.29004E-01	-0.25970E+01	0.12491E+02	0.24017E+00	0.26748E+01
0.70000E+01	0.99431E+00	0.21728E-01	0.21604E-01	-0.31115E+01	0.17634E+02	0.17013E+00	0.25860E+01
0.80000E+01	0.99952E+00	0.16662E-01	0.16654E-01	-0.48025E+01	0.56261E+02	0.53322E-01	0.27153E+01
0.90000E+01	0.10007E+01	0.17913E-01	0.17926E-01	-0.78776E+01	0.11491E+03	0.26108E-01	0.30132E+01
0.10000E+02	0.10033E+01	0.11039E-01	0.11076E-01	-0.78153E+01	0.18303E+03	0.16391E-01	0.22499E+01
0.11000E+02	0.10033E+01	0.97490E-02	0.97810E-02	-0.60488E+01	0.11377E+03	0.26370E-01	0.18630E+01
0.12000E+02	0.10026E+01	0.16164E-01	0.16206E-01	-0.12907E+02	0.24131E+03	0.12432E-01	0.16552E+01

Y	V/U_e	V'/U	V'/U_e	SK_v	FL_v	$\tau_{xy}/\rho U^2$	$\tau_{xy}/\rho_e U_e^2$
0.20000E+01	0.47027E-04	0.31638E-01	0.27220E-01	0.39080E+00	0.40740E+01	0.13859E-02	0.71698E-03
0.30000E+01	0.10951E-02	0.28759E-01	0.26245E-01	0.49870E+00	0.54416E+01	0.92662E-03	0.60704E-03
0.40000E+01	0.27654E-02	0.24409E-01	0.23134E-01	0.50840E+00	0.66261E+01	0.58153E-03	0.44889E-03
0.50000E+01	0.46762E-02	0.20790E-01	0.20176E-01	0.92780E+00	0.64238E+01	0.37800E-03	0.32566E-03
0.60000E+01	0.43982E-02	0.17393E-01	0.17140E-01	0.10518E+01	0.16192E+02	0.19150E-03	0.17763E-03
0.70000E+01	0.42522E-02	0.14574E-01	0.14491E-01	-0.39100E-01	0.22778E+02	0.11018E-03	0.10702E-03
0.80000E+01	0.44648E-02	0.13904E-01	0.13897E-01	-0.13710E+00	0.38591E+02	0.45249E-04	0.45147E-04
0.90000E+01	0.49546E-02	0.13400E-01	0.13409E-01	-0.10383E+01	0.44570E+02	0.32212E-04	0.32299E-04
0.10000E+02	0.36995E-02	0.10080E-01	0.10113E-01	-0.11090E+00	0.35446E+02	0.12913E-04	0.13119E-04
0.11000E+02	0.30633E-02	0.12159E-01	0.12199E-01	-0.12510E+00	0.69377E+02	0.10338E-04	0.10496E-04
0.12000E+02	0.27217E-02	0.12765E-01	0.12798E-01	-0.51488E+01	0.75345E+02	0.69802E-06	0.70499E-06

Y	τ_{xy}/τ_w	R_{uv}	TKE	U_{eff}/U^*	y^+
0.20000E+01	0.10000E+01	0.52606E+00	0.44678E-02	0.27134E+02	0.34822E+03
0.30000E+01	0.84667E+00	0.48553E+00	0.30290E-02	0.29230E+02	0.52233E+03
0.40000E+01	0.62609E+00	0.45971E+00	0.19387E-02	0.30711E+02	0.69645E+03
0.50000E+01	0.45421E+00	0.45086E+00	0.12454E-02	0.31702E+02	0.87056E+03
0.60000E+01	0.24775E+00	0.37411E+00	0.73561E-03	0.32375E+02	0.10447E+04
0.70000E+01	0.14927E+00	0.34796E+00	0.44844E-03	0.32777E+02	0.12188E+04
0.80000E+01	0.62969E-01	0.19531E+00	0.33213E-03	0.33017E+02	0.13929E+04
0.90000E+01	0.45048E-01	0.13420E+00	0.33998E-03	0.33074E+02	0.15670E+04
0.10000E+02	0.18298E-01	0.11605E+00	0.16253E-03	0.33194E+02	0.17411E+04
0.11000E+02	0.14639E-01	0.87208E-01	0.19537E-03	0.33192E+02	0.19152E+04
0.12000E+02	0.98328E-03	0.33830E-02	0.29358E-03	0.33159E+02	0.20893E+04

Figure D.1 Tabulated Data for Flat Plate at x = 48 cm

D.2 5° Wedge ($\theta_{eff} = 8.2°$) Tabulated Data

Y	ρ	T	M	M'	U	U/U_e
0.20000E+01	0.67237E+00	0.16737E+03	0.19729E+01	0.30990E+00	0.51131E+03	0.84074E+00
0.30000E+01	0.75450E+00	0.14915E+03	0.22313E+01	0.32684E+00	0.54596E+03	0.89773E+00
0.40000E+01	0.83719E+00	0.13442E+03	0.24642E+01	0.29982E+00	0.57248E+03	0.94132E+00
0.50000E+01	0.89741E+00	0.12540E+03	0.26217E+01	0.27056E+00	0.58833E+03	0.96740E+00
0.60000E+01	0.94140E+00	0.11954E+03	0.27308E+01	0.21386E+00	0.59839E+03	0.98393E+00
0.70000E+01	0.96168E+00	0.11702E+03	0.27795E+01	0.16683E+00	0.60263E+03	0.99091E+00
0.80000E+01	0.94593E+00	0.11897E+03	0.27418E+01	0.12785E+00	0.59914E+03	0.98517E+00
0.90000E+01	0.92155E+00	0.12211E+03	0.26827E+01	0.11438E+00	0.59342E+03	0.97576E+00
0.10000E+02	0.90851E+00	0.12387E+03	0.26508E+01	0.12360E+00	0.58992E+03	0.97000E+00
0.11000E+02	0.90517E+00	0.12432E+03	0.26424E+01	0.79900E-01	0.58875E+03	0.96808E+00
0.12000E+02	0.89353E+00	0.12594E+03	0.26135E+01	0.13342E+00	0.58581E+03	0.96326E+00
0.13000E+02	0.88525E+00	0.12712E+03	0.25925E+01	0.10551E+00	0.58356E+03	0.95956E+00
0.14000E+02	0.89303E+00	0.12601E+03	0.26127E+01	0.65691E-01	0.58587E+03	0.96335E+00

Y	U'/U	U'/U_e	SK_u	FL_u	γ_u	V
0.20000E+01	0.88409E-01	0.74329E-01	-0.36290E+00	0.26972E+01	0.11123E+01	0.30590E+00
0.30000E+01	0.73380E-01	0.65875E-01	-0.65570E+00	0.29860E+01	0.10047E+01	0.15251E+01
0.40000E+01	0.54919E-01	0.51697E-01	-0.10581E+01	0.39638E+01	0.75685E+00	0.13491E+01
0.50000E+01	0.43434E-01	0.42018E-01	-0.15863E+01	0.60092E+01	0.49923E+00	0.12729E+01
0.60000E+01	0.31436E-01	0.30931E-01	-0.20668E+01	0.86301E+01	0.34762E+00	0.18990E+00
0.70000E+01	0.23602E-01	0.23387E-01	-0.37264E+01	0.38925E+02	0.77071E-01	-0.54260E+00
0.80000E+01	0.19152E-01	0.18868E-01	-0.19338E+01	0.96959E+01	0.30941E+00	-0.13694E+02
0.90000E+01	0.18697E-01	0.18244E-01	-0.14820E+01	0.75852E+01	0.39551E+00	-0.27437E+02
0.10000E+02	0.21252E-01	0.20615E-01	-0.53164E+01	0.70473E+02	0.42570E-01	-0.38020E+02
0.11000E+02	0.14589E-01	0.14123E-01	-0.11552E+01	0.11356E+02	0.26417E+00	-0.44186E+02
0.12000E+02	0.23560E-01	0.22694E-01	-0.77760E+01	0.95624E+02	0.31373E-01	-0.47964E+02
0.13000E+02	0.19479E-01	0.18691E-01	-0.41341E+01	0.32354E+02	0.92725E-01	-0.50629E+02
0.14000E+02	0.12108E-01	0.11664E-01	-0.54063E+01	0.10818E+03	0.27731E-01	-0.47669E+02

Y	V/U_e	V'/U	V'/U_e	SK_v	FL_v	$\tau_{xy}/\rho U^2$
0.20000E+01	0.50299E-03	0.35048E-01	0.29466E-01	0.34490E+00	0.35181E+01	0.15677E-02
0.30000E+01	0.25077E-02	0.30890E-01	0.27731E-01	0.44770E+00	0.38879E+01	0.11162E-02
0.40000E+01	0.22183E-02	0.26256E-01	0.24716E-01	0.58340E+00	0.48127E+01	0.64361E-03
0.50000E+01	0.20930E-02	0.21743E-01	0.21034E-01	0.57010E+00	0.64466E+01	0.35559E-03
0.60000E+01	0.31225E-03	0.17959E-01	0.17670E-01	0.48320E+00	0.75967E+01	0.16949E-03
0.70000E+01	-0.89220E-03	0.15063E-01	0.14926E-01	0.12100E-01	0.68539E+01	0.51302E-04
0.80000E+01	-0.22518E-01	0.22180E-01	0.21851E-01	-0.18789E+01	0.14107E+02	-0.21816E-04
0.90000E+01	-0.45114E-01	0.25317E-01	0.24704E-01	-0.66280E+00	0.29690E+01	-0.18360E-03
0.10000E+02	-0.62516E-01	0.27487E-01	0.26662E-01	-0.31600E+00	0.47325E+01	-0.20655E-03
0.11000E+02	-0.72655E-01	0.25214E-01	0.24409E-01	-0.37170E+00	0.34797E+01	-0.21515E-03
0.12000E+02	-0.78868E-01	0.22336E-01	0.21515E-01	-0.71700E-01	0.30007E+01	-0.76536E-04
0.13000E+02	-0.83250E-01	0.22798E-01	0.21875E-01	0.85240E+00	0.63725E+01	-0.50672E-04
0.14000E+02	-0.78382E-01	0.17261E-01	0.16629E-01	-0.21060E+00	0.64373E+01	-0.74482E-04

Y	$\tau_{xy}/\rho_e U_e^2$	τ_{xy}/τ_w	R_{uv}	TKE	U_{eff}/U^*	y^+
0.20000E+01	0.49516E-02	0.10000E+01	0.50594E+00	0.51364E-02	0.23569E+02	0.31275E+03
0.30000E+01	0.40197E-02	0.91098E+00	0.49243E+00	0.36465E-02	0.25573E+02	0.46913E+03
0.40000E+01	0.25483E-02	0.64082E+00	0.44633E+00	0.21975E-02	0.27190E+02	0.62551E+03
0.50000E+01	0.14870E-02	0.40083E+00	0.37653E+00	0.14160E-02	0.28199E+02	0.78189E+03
0.60000E+01	0.73323E-03	0.20733E+00	0.30022E+00	0.81665E-03	0.28858E+02	0.93826E+03
0.70000E+01	0.22509E-03	0.65020E-01	0.14430E+00	0.50542E-03	0.29140E+02	0.10946E+04
0.80000E+01	-0.94616E-04	-0.26883E-01	-0.51358E-01	0.67536E-03	0.28907E+02	0.12510E+04
0.90000E+01	-0.78111E-03	-0.21621E+00	-0.38786E+00	0.81576E-03	0.28530E+02	0.14074E+04
0.10000E+02	-0.86841E-03	-0.23698E+00	-0.35359E+00	0.98134E-03	0.28302E+02	0.15638E+04
0.11000E+02	-0.90097E-03	-0.24496E+00	-0.58489E+00	0.74216E-03	0.28226E+02	0.17202E+04
0.12000E+02	-0.31733E-03	-0.85167E-01	-0.14544E+00	0.77643E-03	0.28037E+02	0.18765E+04
0.13000E+02	-0.20848E-03	-0.55436E-01	-0.11411E+00	0.70945E-03	0.27892E+02	0.20329E+04
0.14000E+02	-0.30887E-03	-0.82851E-01	-0.35636E+00	0.37126E-03	0.28040E+02	0.21893E+04

Figure D.2 5° Wedge ($\theta_{eff} = 8.2°$) Flow $X = -1.32\delta_o$ Coincident Data

Y	ρ	T	M	M'	U	U/U_e
0.20000E+01	0.59866E+00	0.18801E+03	0.17068E+01	0.30721E+00	0.46875E+03	0.77076E+00
0.30000E+01	0.67052E+00	0.16786E+03	0.19659E+01	0.32684E+00	0.51006E+03	0.83869E+00
0.40000E+01	0.72527E+00	0.15519E+03	0.21429E+01	0.31107E+00	0.53439E+03	0.87870E+00
0.50000E+01	0.78790E+00	0.14285E+03	0.23282E+01	0.27819E+00	0.55690E+03	0.91571E+00
0.60000E+01	0.83215E+00	0.13526E+03	0.24515E+01	0.22110E+00	0.56949E+03	0.93641E+00
0.70000E+01	0.87574E+00	0.12852E+03	0.25668E+01	0.14354E+00	0.58115E+03	0.95558E+00
0.80000E+01	0.89137E+00	0.12627E+03	0.26081E+01	0.11568E+00	0.58534E+03	0.96248E+00
0.90000E+01	0.89551E+00	0.12569E+03	0.26185E+01	0.85775E-01	0.58642E+03	0.96426E+00
0.10000E+02	0.89994E+00	0.12507E+03	0.26297E+01	0.86899E-01	0.58755E+03	0.96611E+00
0.11000E+02	0.90024E+00	0.12503E+03	0.26309E+01	0.94707E-01	0.58777E+03	0.96647E+00
0.12000E+02	0.90584E+00	0.12425E+03	0.26450E+01	0.63466E-01	0.58922E+03	0.96885E+00

Y	U'/U	U'/U_e	SK_u	FL_u	γ_u	V
0.20000E+01	0.11417E+00	0.88001E-01	-0.29540E+00	0.26043E+01	0.11519E+01	-0.32525E+01
0.30000E+01	0.94858E-01	0.79556E-01	-0.46290E+00	0.26752E+01	0.11214E+01	-0.12918E+02
0.40000E+01	0.77190E-01	0.67827E-01	-0.64370E+00	0.29119E+01	0.10303E+01	-0.21026E+02
0.50000E+01	0.58919E-01	0.53953E-01	-0.99370E+00	0.35823E+01	0.83745E+00	-0.26940E+02
0.60000E+01	0.43440E-01	0.40678E-01	-0.16466E+01	0.62927E+01	0.47674E+00	-0.45129E+02
0.70000E+01	0.26248E-01	0.25082E-01	-0.25703E+01	0.13158E+02	0.22801E+00	-0.48242E+02
0.80000E+01	0.21348E-01	0.20547E-01	-0.32061E+01	0.23207E+02	0.12927E+00	-0.46469E+02
0.90000E+01	0.15856E-01	0.15289E-01	-0.41410E+01	0.40883E+02	0.73380E-01	-0.46673E+02
0.10000E+02	0.15411E-01	0.14889E-01	-0.41942E+01	0.37289E+02	0.80454E-01	-0.46769E+02
0.11000E+02	0.16740E-01	0.16179E-01	-0.13750E+02	0.28183E+03	0.10645E-01	-0.45881E+02
0.12000E+02	0.11261E-01	0.10910E-01	-0.47412E+01	0.73245E+02	0.40959E-01	-0.44766E+02

Y	V/U_e	V'/U	V'/U_e	SK_v	FL_v	$\tau_{xy}/\rho U^2$
0.20000E+01	-0.53481E-02	0.38679E-01	0.29812E-01	0.45800E-01	0.49805E+01	0.16664E-02
0.30000E+01	-0.21241E-01	0.35595E-01	0.29853E-01	-0.13150E+00	0.41949E+01	0.11015E-02
0.40000E+01	-0.34573E-01	0.33535E-01	0.29467E-01	0.11930E+00	0.53959E+01	0.60416E-03
0.50000E+01	-0.44298E-01	0.28979E-01	0.26537E-01	0.52600E-01	0.64752E+01	0.24100E-03
0.60000E+01	-0.74206E-01	0.27651E-01	0.25893E-01	0.40020E+00	0.36470E+01	0.17609E-04
0.70000E+01	-0.79324E-01	0.23375E-01	0.22337E-01	-0.19070E+00	0.58287E+01	-0.50927E-04
0.80000E+01	-0.76409E-01	0.30494E-01	0.29350E-01	0.33937E+01	0.27439E+02	0.41899E-04
0.90000E+01	-0.76744E-01	0.24452E-01	0.23578E-01	0.30983E+01	0.32807E+02	-0.47015E-04
0.10000E+02	-0.76902E-01	0.18250E-01	0.17632E-01	0.13870E+00	0.11258E+02	-0.23177E-04
0.11000E+02	-0.75442E-01	0.19782E-01	0.19118E-01	0.35791E+01	0.59090E+02	-0.18928E-04
0.12000E+02	-0.73609E-01	0.15780E-01	0.15289E-01	0.28240E+00	0.17122E+02	-0.16079E-04

Y	$\tau_{xy}/\rho_e U_e^2$	τ_{xy}/τ_w	R_{uv}	TKE	U_{eff}/U^*	y^+
0.20000E+01	0.44235E-02	-0.52131E-01	0.37733E+00	0.80139E-02	0.21173E+02	0.31143E+03
0.30000E+01	0.34623E-02	-0.45700E-01	0.32624E+00	0.57659E-02	0.23421E+02	0.46715E+03
0.40000E+01	0.20845E-02	-0.29761E-01	0.23340E+00	0.41037E-02	0.24809E+02	0.62287E+03
0.50000E+01	0.90301E-03	-0.14006E-01	0.14115E+00	0.25755E-02	0.26143E+02	0.77858E+03
0.60000E+01	0.68995E-04	-0.11302E-02	0.14660E-01	0.17081E-02	0.26914E+02	0.93430E+03
0.70000E+01	-0.20780E-03	0.35824E-02	-0.83005E-01	0.89087E-03	0.27646E+02	0.10900E+04
0.80000E+01	0.17344E-03	-0.30433E-02	0.64363E-01	0.11577E-02	0.27913E+02	0.12457E+04
0.90000E+01	-0.19533E-03	0.34435E-02	-0.12127E+00	0.72362E-03	0.27983E+02	0.14015E+04
0.10000E+02	-0.96667E-04	0.17126E-02	-0.82406E-01	0.45182E-03	0.28055E+02	0.15572E+04
0.11000E+02	-0.79001E-04	0.14001E-02	-0.57159E-01	0.53142E-03	0.28070E+02	0.17129E+04
0.12000E+02	-0.67443E-04	0.12026E-02	-0.90486E-01	0.31242E-03	0.28163E+02	0.18686E+04

Figure D.3 5^o Wedge ($\theta_{eff} = 8.2^o$) Flow $X = 0\delta_o$ Coincident Data

Y	ρ	T	M	M'	U	U/U_e
0.20000E+01	0.12962E+00	0.19267E+03	0.16533E+01	0.28261E+00	0.45927E+03	0.75518E+00
0.30000E+01	0.14134E+00	0.17669E+03	0.18549E+01	0.29130E+00	0.49359E+03	0.81161E+00
0.40000E+01	0.15900E+00	0.15707E+03	0.21202E+01	0.29330E+00	0.53204E+03	0.87484E+00
0.50000E+01	0.17668E+00	0.14135E+03	0.23564E+01	0.22369E+00	0.56095E+03	0.92238E+00
0.60000E+01	0.18545E+00	0.13466E+03	0.24651E+01	0.16081E+00	0.57267E+03	0.94165E+00
0.70000E+01	0.19138E+00	0.13049E+03	0.25364E+01	0.14753E+00	0.57998E+03	0.95366E+00
0.80000E+01	0.20162E+00	0.12387E+03	0.26546E+01	0.59680E-01	0.59073E+03	0.97134E+00
0.90000E+01	0.20253E+00	0.12331E+03	0.26652E+01	0.12098E+00	0.59172E+03	0.97297E+00
0.10000E+02	0.20420E+00	0.12230E+03	0.26840E+01	0.59958E-01	0.59354E+03	0.97596E+00
0.11000E+02	0.20359E+00	0.12267E+03	0.26771E+01	0.11841E+00	0.59293E+03	0.97496E+00
0.12000E+02	0.20550E+00	0.12153E+03	0.26987E+01	0.54260E-01	0.59511E+03	0.97854E+00
0.13000E+02	0.20636E+00	0.12102E+03	0.27083E+01	0.84545E-01	0.59621E+03	0.98035E+00
0.14000E+02	0.20828E+00	0.11990E+03	0.27298E+01	0.55930E-01	0.59817E+03	0.98357E+00

Y	U'/U	U'/U_e	SK_u	FL_u	γ_u	V
0.20000E+01	0.11233E+00	0.84829E-01	-0.39220E+00	0.26698E+01	0.11237E+01	-0.14372E+02
0.30000E+01	0.94411E-01	0.76625E-01	-0.50130E+00	0.28072E+01	0.10687E+01	-0.12984E+02
0.40000E+01	0.74085E-01	0.64812E-01	-0.10148E+01	0.36562E+01	0.82052E+00	-0.16305E+02
0.50000E+01	0.46161E-01	0.42578E-01	-0.14098E+01	0.48671E+01	0.61638E+00	-0.20630E+02
0.60000E+01	0.30813E-01	0.29015E-01	-0.16684E+01	0.68282E+01	0.43935E+00	-0.21085E+02
0.70000E+01	0.26618E-01	0.25385E-01	-0.29619E+01	0.17649E+02	0.16998E+00	-0.27011E+02
0.80000E+01	0.10864E-01	0.10553E-01	-0.52530E+00	0.46089E+01	0.65091E+00	-0.39746E+02
0.90000E+01	0.19962E-01	0.19423E-01	-0.62481E+01	0.69415E+02	0.43218E-01	-0.41466E+02
0.10000E+02	0.10720E-01	0.10462E-01	-0.23170E+00	0.59540E+01	0.50386E+00	-0.38753E+02
0.11000E+02	0.19757E-01	0.19262E-01	-0.71158E+01	0.76312E+02	0.39312E-01	-0.38436E+02
0.12000E+02	0.98490E-02	0.96376E-02	-0.27350E+00	0.32223E+01	0.93101E+00	-0.34751E+02
0.13000E+02	0.14133E-01	0.13855E-01	-0.36153E+01	0.35460E+02	0.84602E-01	-0.30035E+02
0.14000E+02	0.99120E-02	0.97492E-02	0.12450E+00	0.29291E+01	0.10242E+01	-0.26601E+02

Y	V/U_e	V'/U	V'/U_e	SK_v	FL_v	$\tau_{xy}/\rho U^2$
0.20000E+01	-0.23632E-01	0.46596E-01	0.35189E-01	0.34330E+00	0.35497E+01	0.24325E-02
0.30000E+01	-0.21350E-01	0.43357E-01	0.35189E-01	0.22200E+00	0.44739E+01	0.14907E-02
0.40000E+01	-0.26811E-01	0.35197E-01	0.30791E-01	0.50790E+00	0.61403E+01	0.97653E-03
0.50000E+01	-0.33922E-01	0.29492E-01	0.27203E-01	-0.85660E+00	0.77919E+01	0.10052E-03
0.60000E+01	-0.34671E-01	0.35076E-01	0.33029E-01	0.55010E+00	0.11204E+02	0.17587E-03
0.70000E+01	-0.44414E-01	0.23878E-01	0.22772E-01	0.98370E+00	0.10202E+02	0.85335E-04
0.80000E+01	-0.65354E-01	0.22083E-01	0.21450E-01	-0.50000E+00	0.93841E+01	-0.18777E-04
0.90000E+01	-0.68183E-01	0.15890E-01	0.15461E-01	0.97490E+00	0.73069E+01	-0.53213E-05
0.10000E+02	-0.63722E-01	0.23336E-01	0.22775E-01	0.43410E+01	0.31584E+02	0.11224E-04
0.11000E+02	-0.63201E-01	0.23038E-01	0.22461E-01	0.69000E-01	0.28880E+02	-0.96064E-05
0.12000E+02	-0.57141E-01	0.27926E-01	0.27327E-01	0.46987E+01	0.47559E+02	0.22088E-04
0.13000E+02	-0.49387E-01	0.28525E-01	0.27965E-01	0.23649E+01	0.30690E+02	-0.11765E-05
0.14000E+02	-0.43741E-01	0.37257E-01	0.36645E-01	0.16325E+01	0.17897E+02	-0.26338E-04

Y	$\tau_{xy}/\rho_e U_e^2$	τ_{xy}/τ_w	R_{uv}	TKE	U_{cfl}/U^*	y^+
0.20000E+01	0.61988E-02	0.16982E+00	0.46473E+00	0.84802E-02	0.20734E+02	0.31271E+03
0.30000E+01	0.43877E-02	0.13107E+00	0.36417E+00	0.63365E-02	0.22574E+02	0.46907E+03
0.40000E+01	0.33396E-02	0.11223E+00	0.37450E+00	0.39831E-02	0.24742E+02	0.62543E+03
0.50000E+01	0.38215E-03	0.14270E-01	0.73836E-01	0.19352E-02	0.26464E+02	0.78179E+03
0.60000E+01	0.69684E-03	0.27314E-01	0.16272E+00	0.17051E-02	0.27188E+02	0.93814E+03
0.70000E+01	0.34680E-03	0.14028E-01	0.13426E+00	0.92444E-03	0.27649E+02	0.10945E+04
0.80000E+01	-0.79163E-04	-0.33734E-02	-0.78269E-01	0.54667E-03	0.28340E+02	0.12509E+04
0.90000E+01	-0.22510E-04	-0.96356E-03	-0.16776E-01	0.45173E-03	0.28404E+02	0.14072E+04
0.10000E+02	0.47773E-04	0.20619E-02	0.44867E-01	0.60203E-03	0.28523E+02	0.15636E+04
0.11000E+02	-0.40803E-04	-0.17557E-02	-0.21106E-01	0.72591E-03	0.28483E+02	0.17199E+04
0.12000E+02	0.94508E-04	0.41048E-02	0.80305E-01	0.82838E-03	0.28626E+02	0.18763E+04
0.13000E+02	-0.50525E-05	-0.22037E-03	-0.29181E-02	0.91357E-03	0.28698E+02	0.20326E+04
0.14000E+02	-0.11385E-03	-0.50120E-02	-0.71322E-01	0.14372E-02	0.28828E+02	0.21890E+04

Figure D.4 5^o Wedge ($\theta_{eff} = 8.2^o$) Flow $X = 1.32\delta_o$ Coincident Data

Y	ρ	T	M	M'	U	U/U_e
0.20000E+01	0.13079E+00	0.19259E+03	0.16516E+01	0.28223E+00	0.45877E+03	0.75435E+00
0.30000E+01	0.14776E+00	0.17047E+03	0.19324E+01	0.29460E+00	0.50526E+03	0.83080E+00
0.40000E+01	0.16425E+00	0.15336E+03	0.21711E+01	0.27316E+00	0.53855E+03	0.88553E+00
0.50000E+01	0.17760E+00	0.14183E+03	0.23459E+01	0.23542E+00	0.55976E+03	0.92042E+00
0.60000E+01	0.18597E+00	0.13544E+03	0.24492E+01	0.16265E+00	0.57117E+03	0.93918E+00
0.70000E+01	0.19022E+00	0.13241E+03	0.25005E+01	0.14890E+00	0.57654E+03	0.94800E+00
0.80000E+01	0.19515E+00	0.12907E+03	0.25593E+01	0.10472E+00	0.58268E+03	0.95811E+00
0.90000E+01	0.19869E+00	0.12677E+03	0.25999E+01	0.87471E-01	0.58661E+03	0.96457E+00
0.10000E+02	0.20157E+00	0.12496E+03	0.26325E+01	0.63833E-01	0.58962E+03	0.96952E+00
0.11000E+02	0.20427E+00	0.12331E+03	0.26631E+01	0.10678E+00	0.59252E+03	0.97428E+00
0.12000E+02	0.20846E+00	0.12083E+03	0.27097E+01	0.57955E-01	0.59661E+03	0.98102E+00
0.13000E+02	0.21245E+00	0.11856E+03	0.27538E+01	0.70419E-01	0.60060E+03	0.98757E+00
0.14000E+02	0.21413E+00	0.11763E+03	0.27719E+01	0.14666E+00	0.60216E+03	0.99013E+00
0.12000E+02	0.20940E+00	0.12029E+03	0.27213E+01	0.96553E-01	0.59797E+03	0.98324E+00
0.13000E+02	0.21394E+00	0.11774E+03	0.27697E+01	0.67077E-01	0.60210E+03	0.99003E+00
0.14000E+02	0.21491E+00	0.11720E+03	0.27806E+01	0.75307E-01	0.60314E+03	0.99175E+00
0.15000E+02	0.21808E+00	0.11550E+03	0.28145E+01	0.68614E-01	0.60613E+03	0.99666E+00
0.16000E+02	0.21852E+00	0.11527E+03	0.28196E+01	0.13776E+00	0.60660E+03	0.99743E+00
0.17000E+02	0.21996E+00	0.11451E+03	0.28351E+01	0.83407E-01	0.60801E+03	0.99976E+00
0.18000E+02	0.22309E+00	0.11291E+03	0.28685E+01	0.69944E-01	0.61067E+03	0.10041E+01

Y	U'/U	U'/U_e	SK_u	FL_u	γ_u	V
0.20000E+01	0.11195E+00	0.84446E-01	-0.39120E+00	0.26726E+01	0.11225E+01	-0.96799E+01
0.30000E+01	0.88048E-01	0.73151E-01	-0.63010E+00	0.29979E+01	0.10007E+01	-0.77240E+01
0.40000E+01	0.65256E-01	0.57786E-01	-0.11746E+01	0.45195E+01	0.66379E+00	-0.58386E+01
0.50000E+01	0.48033E-01	0.44210E-01	-0.18246E+01	0.71407E+01	0.42013E+00	-0.41419E+01
0.60000E+01	0.30381E-01	0.28533E-01	-0.20478E+01	0.84440E+01	0.35528E+00	-0.40091E+01
0.70000E+01	0.26553E-01	0.25172E-01	-0.37441E+01	0.28227E+02	0.10628E+00	-0.15487E+01
0.80000E+01	0.17859E-01	0.17111E-01	-0.37154E+01	0.34904E+02	0.85949E-01	-0.36912E+01
0.90000E+01	0.14532E-01	0.14017E-01	-0.43792E+01	0.53326E+02	0.56258E-01	-0.57335E+01
0.10000E+02	0.10499E-01	0.10179E-01	-0.96030E+00	0.64510E+01	0.46504E+00	-0.72431E+01
0.11000E+02	0.17033E-01	0.16595E-01	-0.78155E+01	0.95560E+02	0.31394E-01	-0.11434E+02
0.12000E+02	0.94150E-02	0.92363E-02	-0.69000E-02	0.32781E+01	0.91516E+00	-0.15832E+02
0.13000E+02	0.10766E-01	0.10632E-01	-0.50873E+01	0.90834E+02	0.33027E-01	-0.20904E+02
0.14000E+02	0.21635E-01	0.21421E-01	-0.10216E+02	0.13383E+03	0.22417E-01	-0.17005E+02
0.12000E+02	0.14782E-01	0.14534E-01	-0.32013E+01	0.30814E+02	0.97359E-01	-0.12265E+02
0.13000E+02	0.99850E-02	0.98854E-02	0.17410E+00	0.39983E+01	0.75032E+00	-0.17958E+02
0.14000E+02	0.11028E-01	0.10937E-01	-0.38411E+01	0.73999E+02	0.40541E-01	-0.15361E+02
0.15000E+02	0.97530E-02	0.97204E-02	0.67300E-01	0.27839E+01	0.10776E+01	-0.11647E+02
0.16000E+02	0.19198E-01	0.19149E-01	-0.71293E+01	0.78967E+02	0.37990E-01	-0.94179E+01
0.17000E+02	0.11475E-01	0.11472E-01	-0.54683E+01	0.10199E+03	0.29415E-01	-0.64258E+01
0.18000E+02	0.93970E-02	0.94357E-02	0.14180E+00	0.32385E+01	0.92635E+00	-0.33643E+01

Figure D.5 5^o Wedge ($\theta_{eff} = 8.2°$) Flow $X = 2.64\delta_o$ Coincident Data

Y	V/U_e	V'/U	V'/U_e	SK_v	FL_v	$\tau_{xy}/\rho U^2$
0.20000E+01	-0.15917E-01	0.50073E-01	0.37773E-01	0.20040E+00	0.34606E+01	0.23890E-02
0.30000E+01	-0.12701E-01	0.39990E-01	0.33224E-01	0.39750E+00	0.40030E+01	0.15298E-02
0.40000E+01	-0.96004E-02	0.36898E-01	0.32674E-01	0.77300E-01	0.74147E+01	0.58340E-03
0.50000E+01	-0.68105E-02	0.29360E-01	0.27024E-01	-0.16450E+00	0.10441E+02	0.35917E-03
0.60000E+01	-0.65922E-02	0.24526E-01	0.23035E-01	-0.73880E+00	0.16628E+02	0.21571E-03
0.70000E+01	-0.25465E-02	0.27323E-01	0.25903E-01	-0.13398E+01	0.14417E+02	0.53409E-04
0.80000E+01	-0.60695E-02	0.21734E-01	0.20823E-01	-0.34270E+00	0.93745E+01	0.10334E-03
0.90000E+01	-0.94276E-02	0.22367E-01	0.21574E-01	-0.25360E+00	0.12749E+02	0.75429E-04
0.10000E+02	-0.11910E-01	0.26700E-01	0.25886E-01	-0.96710E+00	0.15145E+02	0.57869E-04
0.11000E+02	-0.18802E-01	0.22762E-01	0.22176E-01	-0.53110E+00	0.65407E+01	0.15587E-04
0.12000E+02	-0.26033E-01	0.27789E-01	0.27261E-01	-0.13172E+01	0.10029E+02	0.13904E-04
0.13000E+02	-0.34372E-01	0.16943E-01	0.16733E-01	0.31577E+01	0.36984E+02	-0.21416E-04
0.14000E+02	-0.27962E-01	0.26388E-01	0.26128E-01	0.23060E+01	0.37166E+02	0.58545E-04
0.12000E+02	-0.20168E-01	0.22814E-01	0.22432E-01	0.41480E+00	0.14523E+02	0.19750E-04
0.13000E+02	-0.29528E-01	0.14032E-01	0.13892E-01	0.20710E+00	0.37028E+01	-0.15047E-04
0.14000E+02	-0.25258E-01	0.15036E-01	0.14912E-01	-0.91250E+00	0.14734E+02	-0.38477E-04
0.15000E+02	-0.19152E-01	0.16287E-01	0.16233E-01	-0.53910E+00	0.78877E+01	-0.10374E-04
0.16000E+02	-0.15486E-01	0.20689E-01	0.20636E-01	-0.36454E+01	0.29696E+02	-0.50325E-04
0.17000E+02	-0.10566E-01	0.17803E-01	0.17799E-01	-0.20350E+01	0.22761E+02	-0.43921E-04
0.18000E+02	-0.55319E-02	0.30963E-01	0.31091E-01	-0.67380E+00	0.15880E+02	0.44273E-05

Y	$\tau_{xy}/\rho_c U_e^2$	τ_{xy}/τ_w	R_{uv}	TKE	U_{eff}/U^*	y^+
0.20000E+01	0.79479E-03	0.16821E+00	0.42619E+00	0.87732E-02	0.20715E+02	0.31487E+03
0.30000E+01	0.69744E-03	0.14761E+00	0.43446E+00	0.54754E-02	0.23228E+02	0.47231E+03
0.40000E+01	0.33588E-03	0.71088E-01	0.24229E+00	0.34906E-02	0.25132E+02	0.62975E+03
0.50000E+01	0.24156E-03	0.51125E-01	0.25468E+00	0.20156E-02	0.26402E+02	0.78718E+03
0.60000E+01	0.15817E-03	0.33477E-01	0.28950E+00	0.10630E-02	0.27106E+02	0.94462E+03
0.70000E+01	0.40815E-04	0.86383E-02	0.73613E-01	0.10991E-02	0.27443E+02	0.11021E+04
0.80000E+01	0.82753E-04	0.17514E-01	0.26623E+00	0.63183E-03	0.27833E+02	0.12595E+04
0.90000E+01	0.62331E-04	0.13192E-01	0.23207E+00	0.60585E-03	0.28085E+02	0.14169E+04
0.10000E+02	0.49013E-04	0.10373E-01	0.20643E+00	0.76801E-03	0.28280E+02	0.15744E+04
0.11000E+02	0.13510E-04	0.28593E-02	0.40202E-01	0.66317E-03	0.28469E+02	0.17318E+04
0.12000E+02	0.12469E-04	0.26390E-02	0.53146E-01	0.81654E-03	0.28738E+02	0.18892E+04
0.13000E+02	-0.19836E-04	-0.41982E-02	-0.11741E+00	0.34503E-03	0.29002E+02	0.20467E+04
0.14000E+02	0.54939E-04	0.11628E-01	0.10255E+00	0.93037E-03	0.29105E+02	0.22041E+04
0.12000E+02	0.17873E-04	0.37828E-02	0.58564E-01	0.62974E-03	0.28827E+02	0.18892E+04
0.13000E+02	-0.14104E-04	-0.29851E-02	-0.10740E+00	0.24674E-03	0.29101E+02	0.20467E+04
0.14000E+02	-0.36357E-04	-0.76948E-02	-0.23204E+00	0.28689E-03	0.29172E+02	0.22041E+04
0.15000E+02	-0.10046E-04	-0.21261E-02	-0.65313E-01	0.31282E-03	0.29372E+02	0.23615E+04
0.16000E+02	-0.48906E-04	-0.10351E-01	-0.12670E+00	0.61232E-03	0.29404E+02	0.25190E+04
0.17000E+02	-0.43164E-04	-0.91355E-02	-0.21499E+00	0.38279E-03	0.29500E+02	0.26764E+04
0.18000E+02	0.44515E-05	0.94213E-03	0.15217E-01	0.10029E-02	0.29681E+02	0.28339E+04

Figure D.6 5^o Wedge ($\theta_{eff} = 8.2^o$) Flow $X = 2.64\delta_o$ Coincident Data (Cont.)

X/δ	ρ	T	M	M'	U	U/U$_e$
-0.20000E+01	0.30677E+00	0.12521E+03	0.26322E+01	0.26118E+00	0.59022E+03	0.97049E+00
-0.17500E+01	0.30886E+00	0.12323E+03	0.26684E+01	0.24077E+00	0.59362E+03	0.97610E+00
-0.15000E+01	0.30594E+00	0.12325E+03	0.26675E+01	0.25526E+00	0.59346E+03	0.97582E+00
-0.12500E+01	0.30182E+00	0.12378E+03	0.26579E+01	0.23929E+00	0.59259E+03	0.97440E+00
-0.10000E+01	0.29943E+00	0.12359E+03	0.26617E+01	0.23831E+00	0.59302E+03	0.97510E+00
-0.75000E+00	0.29183E+00	0.12560E+03	0.26247E+01	0.25667E+00	0.58949E+03	0.96931E+00
-0.50000E+00	0.28040E+00	0.12948E+03	0.25560E+01	0.28645E+00	0.58280E+03	0.95829E+00
-0.25000E+00	0.26640E+00	0.13496E+03	0.24630E+01	0.26975E+00	0.57272E+03	0.94173E+00
0.00000E+00	0.25853E+00	0.13771E+03	0.24177E+01	0.25523E+00	0.56722E+03	0.93267E+00
0.25000E+00	0.26008E+00	0.13554E+03	0.24534E+01	0.22844E+00	0.57084E+03	0.93863E+00
0.50000E+00	0.25542E+00	0.13664E+03	0.24357E+01	0.19718E+00	0.56953E+03	0.93648E+00
0.75000E+00	0.24942E+00	0.13852E+03	0.24059E+01	0.20137E+00	0.56678E+03	0.93196E+00
0.10000E+01	0.24882E+00	0.13744E+03	0.24238E+01	0.17520E+00	0.56889E+03	0.93543E+00
0.12500E+01	0.24653E+00	0.13730E+03	0.24258E+01	0.19910E+00	0.56927E+03	0.93605E+00
0.15000E+01	0.24223E+00	0.13829E+03	0.24101E+01	0.19318E+00	0.56772E+03	0.93350E+00
0.17500E+01	0.24029E+00	0.13794E+03	0.24157E+01	0.18954E+00	0.56830E+03	0.93446E+00
0.20000E+01	0.23370E+00	0.14033E+03	0.23776E+01	0.19094E+00	0.56430E+03	0.92789E+00
0.22500E+01	0.23529E+00	0.13789E+03	0.24165E+01	0.22442E+00	0.56861E+03	0.93497E+00
0.25000E+01	0.22895E+00	0.14018E+03	0.23813E+01	0.23453E+00	0.56486E+03	0.92881E+00
0.27500E+01	0.22800E+00	0.13922E+03	0.23967E+01	0.22896E+00	0.56663E+03	0.93170E+00
0.30000E+01	0.22906E+00	0.13704E+03	0.24320E+01	0.23412E+00	0.57042E+03	0.93795E+00

X/δ	U'/U	U'/U$_e$	SK$_u$	FL$_u$	γ$_u$	V
-0.20000E+01	0.41592E-01	0.40365E-01	-0.17080E+01	0.60167E+01	0.49861E+00	0.58940E+00
-0.17500E+01	0.37187E-01	0.36298E-01	-0.18650E+01	0.73975E+01	0.40554E+00	0.14470E+01
-0.15000E+01	0.39429E-01	0.38476E-01	-0.21219E+01	0.92168E+01	0.32549E+00	0.20995E+01
-0.12500E+01	0.37264E-01	0.36310E-01	-0.15752E+01	0.56524E+01	0.53075E+00	0.17436E+01
-0.10000E+01	0.37015E-01	0.36093E-01	-0.17691E+01	0.70975E+01	0.42268E+00	0.12671E+01
-0.75000E+00	0.41110E-01	0.39848E-01	-0.15192E+01	0.55740E+01	0.53821E+00	0.97520E+00
-0.50000E+00	0.48844E-01	0.46807E-01	-0.15739E+01	0.56406E+01	0.53186E+00	-0.52925E+01
-0.25000E+00	0.51022E-01	0.48049E-01	-0.15942E+01	0.64445E+01	0.46551E+00	-0.25479E+02
0.00000E+00	0.50950E-01	0.47520E-01	-0.14345E+01	0.52615E+01	0.57018E+00	-0.37697E+02
0.25000E+00	0.44704E-01	0.41961E-01	-0.17151E+01	0.62240E+01	0.48201E+00	-0.40550E+02
0.50000E+00	0.38786E-01	0.36322E-01	-0.16629E+01	0.67022E+01	0.44761E+00	-0.33421E+02
0.75000E+00	0.40117E-01	0.37387E-01	-0.18275E+01	0.73802E+01	0.40649E+00	-0.26803E+02
0.10000E+01	0.34471E-01	0.32245E-01	-0.17301E+01	0.68097E+01	0.44055E+00	-0.23354E+02
0.12500E+01	0.38563E-01	0.36097E-01	-0.20845E+01	0.80088E+01	0.37459E+00	-0.19408E+02
0.15000E+01	0.37817E-01	0.35302E-01	-0.18137E+01	0.70229E+01	0.42717E+00	-0.14288E+02
0.17500E+01	0.36928E-01	0.34508E-01	-0.20743E+01	0.83688E+01	0.35847E+00	-0.11822E+02
0.20000E+01	0.38036E-01	0.35293E-01	-0.15314E+01	0.51765E+01	0.57954E+00	-0.58801E+01
0.22500E+01	0.43120E-01	0.40316E-01	-0.34770E+01	0.22106E+02	0.13571E+00	-0.59990E+01
0.25000E+01	0.46301E-01	0.43005E-01	-0.16914E+01	0.59457E+01	0.50457E+00	-0.18881E+01
0.27500E+01	0.44620E-01	0.41573E-01	-0.17912E+01	0.67579E+01	0.44392E+00	-0.25736E+01
0.30000E+01	0.44244E-01	0.41499E-01	-0.23226E+01	0.10268E+02	0.29216E+00	-0.19289E+01

Figure D.7 5^o Wedge ($\theta_{eff} = 8.2^o$) Flow $Y = 0.66\delta_o$ Coincident Data

X/δ	V/U$_e$	V'/U	V'/U$_e$	SK$_v$	FL$_v$	$\tau_{xy}/\rho U^2$
-0.20000E+01	0.96915E-03	0.24893E-01	0.24158E-01	-0.26900E+00	0.16206E+02	0.30915E-03
-0.17500E+01	0.23793E-02	0.21698E-01	0.21180E-01	0.37520E+00	0.13601E+02	0.32486E-03
-0.15000E+01	0.34522E-02	0.23668E-01	0.23096E-01	-0.84910E+00	0.19064E+02	0.31234E-03
-0.12500E+01	0.28670E-02	0.22222E-01	0.21653E-01	-0.43590E+00	0.12656E+02	0.28436E-03
-0.10000E+01	0.20835E-02	0.20820E-01	0.20302E-01	-0.60500E-01	0.12636E+02	0.28292E-03
-0.75000E+00	0.16035E-02	0.21751E-01	0.21083E-01	0.33800E+00	0.53691E+01	0.29943E-03
-0.50000E+00	-0.87025E-02	0.24833E-01	0.23798E-01	0.95200E-01	0.71314E+01	0.17659E-03
-0.25000E+00	-0.41895E-01	0.31331E-01	0.29505E-01	-0.37120E+00	0.44301E+01	-0.16003E-03
0.00000E+00	-0.61986E-01	0.30427E-01	0.28379E-01	-0.28070E+00	0.35430E+01	-0.11043E-03
0.25000E+00	-0.66677E-01	0.30989E-01	0.29088E-01	0.32420E+00	0.82248E+01	0.66959E-04
0.50000E+00	-0.54955E-01	0.27394E-01	0.25654E-01	0.44850E+00	0.53801E+01	0.24839E-03
0.75000E+00	-0.44073E-01	0.25657E-01	0.23912E-01	0.13697E+01	0.13914E+02	0.25661E-03
0.10000E+01	-0.38402E-01	0.28137E-01	0.26321E-01	-0.41980E+00	0.96705E+01	0.16862E-03
0.12500E+01	-0.31912E-01	0.23298E-01	0.21808E-01	0.64190E+00	0.38740E+01	0.25905E-03
0.15000E+01	-0.23494E-01	0.27234E-01	0.25423E-01	-0.28680E+00	0.80049E+01	0.13316E-03
0.17500E+01	-0.19438E-01	0.32224E-01	0.30112E-01	-0.13871E+01	0.89116E+01	0.37748E-04
0.20000E+01	-0.96687E-02	0.29371E-01	0.27253E-01	-0.10891E+01	0.11547E+02	0.33794E-03
0.22500E+01	-0.98642E-02	0.23929E-01	0.22373E-01	0.72820E+00	0.10753E+02	0.14025E-03
0.25000E+01	-0.31046E-02	0.31664E-01	0.29410E-01	0.76900E+00	0.12567E+02	0.26226E-03
0.27500E+01	-0.42318E-02	0.27864E-01	0.25961E-01	-0.42350E+00	0.12493E+02	0.42876E-03
0.30000E+01	-0.31717E-02	0.30468E-01	0.28577E-01	-0.69810E+00	0.15943E+02	0.35574E-03

X/δ	$\tau_{xy}/\rho_e U_e^2$	R_{uv}	TKE	y^+
-0.20000E+01	0.33037E+02	0.29859E+00	0.14846E-02	-0.13194E+02
-0.17500E+01	0.35358E+02	0.40261E+00	0.11622E-02	-0.11545E+02
-0.15000E+01	0.33655E+02	0.33470E+00	0.13375E-02	-0.98959E+01
-0.12500E+01	0.30139E+02	0.34340E+00	0.11881E-02	-0.82466E+01
-0.10000E+01	0.29791E+02	0.36711E+00	0.11185E-02	-0.65972E+01
-0.75000E+00	0.30367E+02	0.33487E+00	0.13181E-02	-0.49479E+01
-0.50000E+00	0.16818E+02	0.14559E+00	0.18096E-02	-0.32986E+01
-0.25000E+00	-0.13984E+02	-0.10011E+00	0.22832E-02	-0.16493E+01
0.00000E+00	-0.91856E+01	-0.71236E-01	0.22238E-02	0.00000E+00
0.25000E+00	0.56747E+01	0.48334E-01	0.19596E-02	0.16493E+01
0.50000E+00	0.20579E+02	0.23378E+00	0.15026E-02	0.32986E+01
0.75000E+00	0.20560E+02	0.24930E+00	0.14630E-02	0.49479E+01
0.10000E+01	0.13578E+02	0.17385E+00	0.13858E-02	0.65972E+01
0.12500E+01	0.20696E+02	0.28834E+00	0.12863E-02	0.82466E+01
0.15000E+01	0.10396E+02	0.12930E+00	0.14567E-02	0.98959E+01
0.17500E+01	0.29295E+01	0.31723E-01	0.17202E-02	0.11545E+02
0.20000E+01	0.25149E+02	0.30250E+00	0.15860E-02	0.13194E+02
0.22500E+01	0.10670E+02	0.13593E+00	0.15023E-02	0.14844E+02
0.25000E+01	0.19158E+02	0.17888E+00	0.20745E-02	0.16493E+02
0.27500E+01	0.31387E+02	0.34487E+00	0.17718E-02	0.18142E+02
0.30000E+01	0.26514E+02	0.26390E+00	0.19070E-02	0.19792E+02

Figure D.8 5^o Wedge ($\theta_{eff} = 8.2^o$) Flow $Y = 0.66\delta_o$ Coincident Data (Cont.)

D.3 7° Wedge ($\theta_{eff} = 10.4°$) Flow Tabulated Data

Y	ρ	T	M	M'	U	U/U_c
0.20000E+01	0.14663E+00	0.17103E+03	0.19279E+01	0.30794E+00	0.50505E+03	0.83045E+00
0.30000E+01	0.16173E+00	0.15505E+03	0.21486E+01	0.32081E+00	0.53598E+03	0.88131E+00
0.40000E+01	0.18229E+00	0.13757E+03	0.24168E+01	0.31986E+00	0.56799E+03	0.93394E+00
0.50000E+01	0.19239E+00	0.13034E+03	0.25389E+01	0.28779E+00	0.58084E+03	0.95507E+00
0.60000E+01	0.20334E+00	0.12332E+03	0.26641E+01	0.24891E+00	0.59287E+03	0.97486E+00
0.70000E+01	0.21140E+00	0.11863E+03	0.27534E+01	0.20467E+00	0.60101E+03	0.98824E+00
0.80000E+01	0.21372E+00	0.11733E+03	0.27789E+01	0.18807E+00	0.60327E+03	0.99196E+00
0.90000E+01	0.20965E+00	0.11962E+03	0.27353E+01	0.15194E+00	0.59941E+03	0.98561E+00
0.10000E+02	0.19906E+00	0.12598E+03	0.26180E+01	0.16461E+00	0.58787E+03	0.96663E+00
0.11000E+02	0.19448E+00	0.12895E+03	0.25657E+01	0.13063E+00	0.58205E+03	0.95707E+00
0.12000E+02	0.19116E+00	0.13118E+03	0.25273E+01	0.12233E+00	0.57751E+03	0.94960E+00
0.13000E+02	0.19027E+00	0.13180E+03	0.25176E+01	0.85672E-01	0.57633E+03	0.94767E+00
0.14000E+02	0.18601E+00	0.13482E+03	0.24667E+01	0.81090E-01	0.57016E+03	0.93751E+00

Y	U'/U	U'/U_c	SK_u	Fl_u	γ_u	V
0.20000E+01	0.91721E-01	0.76170E-01	-0.30120E+00	0.26392E+01	0.11367E+01	0.32800E+00
0.30000E+01	0.77593E-01	0.68384E-01	-0.48450E+00	0.27207E+01	0.11027E+01	0.20513E+01
0.40000E+01	0.61007E-01	0.56977E-01	-0.10488E+01	0.37350E+01	0.80321E+00	0.16627E+01
0.50000E+01	0.49475E-01	0.47252E-01	-0.13634E+01	0.49812E+01	0.60226E+00	0.16667E+01
0.60000E+01	0.38571E-01	0.37601E-01	-0.17619E+01	0.64182E+01	0.46742E+00	0.16655E+01
0.70000E+01	0.29510E-01	0.29163E-01	-0.33923E+01	0.27541E+02	0.10893E+00	0.12823E+01
0.80000E+01	0.26549E-01	0.26335E-01	-0.31615E+01	0.18389E+02	0.16314E+00	0.18760E+01
0.90000E+01	0.22660E-01	0.22334E-01	-0.28894E+01	0.17222E+02	0.17419E+00	-0.99679E+01
0.10000E+02	0.28367E-01	0.27420E-01	-0.40276E+01	0.37125E+02	0.80809E-01	-0.30907E+02
0.11000E+02	0.24744E-01	0.23682E-01	-0.21621E+01	0.18282E+02	0.16409E+00	-0.43110E+02
0.12000E+02	0.24769E-01	0.23521E-01	-0.36762E+01	0.45340E+02	0.66167E-01	-0.52121E+02
0.13000E+02	0.18496E-01	0.17528E-01	0.22560E+00	0.30406E+01	0.98665E+00	-0.55820E+02
0.14000E+02	0.20509E-01	0.19227E-01	-0.19495E+01	0.15649E+02	0.19171E+00	-0.60497E+02

Y	V/U_e	V'/U	V'/U_c	SK_v	Fl_v	$\tau_{xy}/\rho U^2$
0.20000E+01	0.53933E-03	0.36277E-01	0.30126E-01	0.22280E+00	0.40768E+01	0.16144E-02
0.30000E+01	0.33730E-02	0.34205E-01	0.30146E-01	0.12410E+00	0.55207E+01	0.12044E-02
0.40000E+01	0.27340E-02	0.27464E-01	0.25650E-01	0.33800E+00	0.70670E+01	0.81282E-03
0.50000E+01	0.27406E-02	0.25372E-01	0.24232E-01	0.60900E+00	0.80774E+01	0.57494E-03
0.60000E+01	0.27386E-02	0.23454E-01	0.22865E-01	-0.18900E+00	0.17667E+02	0.40959E-03
0.70000E+01	0.21085E-02	0.19856E-01	0.19623E-01	-0.14554E+01	0.23266E+02	0.17543E-03
0.80000E+01	0.30847E-02	0.18555E-01	0.18406E-01	0.43800E-01	0.26131E+02	0.99046E-04
0.90000E+01	-0.16390E-01	0.23518E-01	0.23180E-01	-0.88750E+00	0.19499E+02	-0.83020E-04
0.10000E+02	-0.50820E-01	0.33137E-01	0.32031E-01	-0.67320E+00	0.50112E+01	-0.36611E-03
0.11000E+02	-0.70886E-01	0.35353E-01	0.33835E-01	-0.34070E+00	0.35933E+01	-0.39466E-03
0.12000E+02	-0.85703E-01	0.36723E-01	0.34872E-01	0.52410E+00	0.72211E+01	-0.39232E-03
0.13000E+02	-0.91785E-01	0.34393E-01	0.32593E-01	0.60020E+00	0.61455E+01	-0.39763E-03
0.14000E+02	-0.99476E-01	0.51589E-01	0.48365E-01	0.34641E+01	0.18870E+02	-0.23851E-04

Y	$\tau_{xy}/\rho_e U_e^2$	τ_{xy}/τ_w	R_{uv}	TKE	U_{eff}/U^*	y^+
0.20000E+01	0.49751E-02	0.10000E+01	0.48520E+00	0.55224E-02	0.23318E+02	0.31553E+03
0.30000E+01	0.41801E-02	0.92675E+00	0.45378E+00	0.41804E-02	0.25090E+02	0.47329E+03
0.40000E+01	0.31681E-02	0.79167E+00	0.48512E+00	0.26152E-02	0.27024E+02	0.63105E+03
0.50000E+01	0.23435E-02	0.61806E+00	0.45802E+00	0.18676E-02	0.27835E+02	0.78881E+03
0.60000E+01	0.17394E-02	0.48485E+00	0.45276E+00	0.12940E-02	0.28614E+02	0.94658E+03
0.70000E+01	0.76558E-03	0.22186E+00	0.29939E+00	0.82968E-03	0.29153E+02	0.11043E+04
0.80000E+01	0.43549E-03	0.12759E+00	0.20106E+00	0.69672E-03	0.29305E+02	0.12621E+04
0.90000E+01	-0.36037E-03	-0.10357E+00	-0.15578E+00	0.80986E-03	0.29047E+02	0.14199E+04
0.10000E+02	-0.15286E-02	-0.41712E+00	-0.38947E+00	0.15004E-02	0.28287E+02	0.15776E+04
0.11000E+02	-0.16153E-02	-0.43064E+00	-0.45116E+00	0.15559E-02	0.27912E+02	0.17354E+04
0.12000E+02	-0.15808E-02	-0.41424E+00	-0.43130E+00	0.16554E-02	0.27623E+02	0.18932E+04
0.13000E+02	-0.15957E-02	-0.41619E+00	-0.62509E+00	0.13539E-02	0.27548E+02	0.20509E+04
0.14000E+02	-0.93673E-04	-0.23885E-01	-0.22543E-01	0.28717E-02	0.27160E+02	0.22087E+04

Figure D.9 $7°$ Wedge ($\theta_{eff} = 10.4°$) Flow $X = -1.32\delta_o$ Coincident Data

Y	ρ	T	M	M'	U	U/U_e
0.20000E+01	0.13567E+00	0.18436E+03	0.17640E+01	0.34390E+00	0.47952E+03	0.78848E+00
0.30000E+01	0.14883E+00	0.16807E+03	0.19749E+01	0.37971E+00	0.51277E+03	0.84315E+00
0.40000E+01	0.16895E+00	0.14805E+03	0.22599E+01	0.33624E+00	0.55042E+03	0.90505E+00
0.50000E+01	0.18136E+00	0.13792E+03	0.24194E+01	0.23709E+00	0.56803E+03	0.93402E+00
0.60000E+01	0.18770E+00	0.13327E+03	0.24965E+01	0.18104E+00	0.57562E+03	0.94649E+00
0.70000E+01	0.18887E+00	0.13243E+03	0.25110E+01	0.12253E+00	0.57651E+03	0.94796E+00
0.80000E+01	0.19032E+00	0.13143E+03	0.25286E+01	0.11368E+00	0.57826E+03	0.95083E+00
0.90000E+01	0.19108E+00	0.13091E+03	0.25375E+01	0.95677E-01	0.57888E+03	0.95186E+00
0.10000E+02	0.19164E+00	0.13052E+03	0.25446E+01	0.72477E-01	0.57954E+03	0.95294E+00
0.11000E+02	0.19105E+00	0.13092E+03	0.25381E+01	0.86744E-01	0.57888E+03	0.95185E+00
0.12000E+02	0.19068E+00	0.13118E+03	0.25337E+01	0.10885E+00	0.57850E+03	0.95124E+00

Y	U'/U	U'/U_e	SK_u	FL_u	γ_u	V
0.20000E+01	0.11945E+00	0.94182E-01	-0.16340E+00	0.22666E+01	0.13236E+01	0.11017E+02
0.30000E+01	0.10851E+00	0.91492E-01	-0.56310E+00	0.25881E+01	0.11592E+01	-0.40500E+01
0.40000E+01	0.75198E-01	0.68058E-01	-0.11269E+01	0.38758E+01	0.77403E+00	-0.22026E+02
0.50000E+01	0.47740E-01	0.44590E-01	-0.14555E+01	0.54713E+01	0.54832E+00	-0.35411E+02
0.60000E+01	0.35064E-01	0.33188E-01	-0.24067E+01	0.12398E+02	0.24198E+00	-0.45238E+02
0.70000E+01	0.24920E-01	0.23623E-01	-0.21352E+01	0.11124E+02	0.26969E+00	-0.52442E+02
0.80000E+01	0.22883E-01	0.21758E-01	-0.36989E+01	0.28703E+02	0.10452E+00	-0.54155E+02
0.90000E+01	0.19494E-01	0.18556E-01	-0.59316E+01	0.81343E+02	0.36881E-01	-0.57538E+02
0.10000E+02	0.15255E-01	0.14537E-01	-0.41455E+01	0.56805E+02	0.52812E-01	-0.58905E+02
0.11000E+02	0.17905E-01	0.17043E-01	-0.50427E+01	0.48807E+02	0.61467E-01	-0.59436E+02
0.12000E+02	0.21279E-01	0.20241E-01	-0.95645E+01	0.13426E+03	0.22345E-01	-0.59499E+02

Y	V/U_e	V'/U	V'/U_e	SK_v	FL_v	$\tau_{xy}/\rho U^2$
0.20000E+01	0.18115E-01	0.44289E-01	0.34921E-01	-0.93300E-01	0.60670E+01	0.23190E-02
0.30000E+01	-0.66594E-02	0.39808E-01	0.33564E-01	0.13580E+00	0.60488E+01	0.14533E-02
0.40000E+01	-0.36218E-01	0.34682E-01	0.31389E-01	0.12310E+00	0.55566E+01	0.49087E-03
0.50000E+01	-0.58227E-01	0.37792E-01	0.35299E-01	0.57610E+00	0.88570E+01	-0.87941E-04
0.60000E+01	-0.74385E-01	0.32454E-01	0.30717E-01	0.64340E+00	0.76201E+01	-0.22852E-03
0.70000E+01	-0.86231E-01	0.34452E-01	0.32659E-01	0.18815E+01	0.14387E+02	-0.14084E-04
0.80000E+01	-0.89048E-01	0.31614E-01	0.30060E-01	0.24767E+01	0.18314E+02	-0.16583E-03
0.90000E+01	-0.94610E-01	0.28547E-01	0.27173E-01	0.30427E+01	0.25672E+02	-0.16237E-03
0.10000E+02	-0.96858E-01	0.26633E-01	0.25380E-01	0.33893E+01	0.30963E+02	-0.12561E-03
0.11000E+02	-0.97731E-01	0.27287E-01	0.25973E-01	0.30396E+01	0.30568E+02	-0.37130E-04
0.12000E+02	-0.97834E-01	0.21996E-01	0.20924E-01	0.18896E+01	0.13761E+02	-0.76563E-04

Y	$\tau_{xy}/\rho_e U_e^2$	τ_{xy}/τ_w	R_{uv}	TKE	U_{eff}/U^*	y^+
0.20000E+01	0.64422E-02	-0.59569E-01	0.43835E+00	0.90953E-02	0.21873E+02	0.31489E+03
0.30000E+01	0.46167E-02	-0.46829E-01	0.33645E+00	0.74721E-02	0.23707E+02	0.47233E+03
0.40000E+01	0.17967E-02	-0.20689E-01	0.18821E+00	0.40302E-02	0.25898E+02	0.62977E+03
0.50000E+01	-0.34282E-03	0.42374E-02	-0.48742E-01	0.25678E-02	0.26974E+02	0.78722E+03
0.60000E+01	-0.91478E-03	0.11702E-01	-0.20082E+00	0.16680E-02	0.27448E+02	0.94466E+03
0.70000E+01	-0.56556E-04	0.72803E-03	-0.16405E-01	0.14974E-02	0.27505E+02	0.11021E+04
0.80000E+01	-0.66994E-03	0.86900E-02	-0.22924E+00	0.12613E-02	0.27615E+02	0.12595E+04
0.90000E+01	-0.65738E-03	0.85609E-02	-0.29177E+00	0.10050E-02	0.27655E+02	0.14170E+04
0.10000E+02	-0.50970E-03	0.66572E-02	-0.30916E+00	0.82569E-03	0.27696E+02	0.15744E+04
0.11000E+02	-0.15032E-03	0.19574E-02	-0.75998E-01	0.90485E-03	0.27654E+02	0.17319E+04
0.12000E+02	-0.30957E-03	0.40231E-02	-0.16357E+00	0.71024E-03	0.27631E+02	0.18893E+04

Figure D.10 7^o Wedge ($\theta_{eff} = 10.4^o$) Flow $X = 0\delta_o$ Coincident Data

Y	ρ	T	M	M'	U	U/U_e
0.20000E+01	0.12708E+00	0.19539E+03	0.16265E+01	0.25628E+00	0.45458E+03	0.74746E+00
0.30000E+01	0.14117E+00	0.17589E+03	0.18699E+01	0.27938E+00	0.49604E+03	0.81563E+00
0.40000E+01	0.16415E+00	0.15127E+03	0.22110E+01	0.25496E+00	0.54392E+03	0.89438E+00
0.50000E+01	0.17452E+00	0.14228E+03	0.23484E+01	0.17332E+00	0.56021E+03	0.92116E+00
0.60000E+01	0.17918E+00	0.13858E+03	0.24079E+01	0.14020E+00	0.56685E+03	0.93207E+00
0.70000E+01	0.18220E+00	0.13628E+03	0.24458E+01	0.10802E+00	0.57061E+03	0.93825E+00
0.80000E+01	0.18759E+00	0.13237E+03	0.25109E+01	0.10510E+00	0.57681E+03	0.94846E+00
0.90000E+01	0.19291E+00	0.12872E+03	0.25748E+01	0.65122E-01	0.58285E+03	0.95839E+00
0.10000E+02	0.19446E+00	0.12769E+03	0.25938E+01	0.87522E-01	0.58491E+03	0.96176E+00
0.11000E+02	0.19577E+00	0.12683E+03	0.26089E+01	0.11203E+00	0.58656E+03	0.96448E+00
0.12000E+02	0.19649E+00	0.12637E+03	0.26172E+01	0.11559E+00	0.58752E+03	0.96607E+00
0.13000E+02	0.19592E+00	0.12674E+03	0.26106E+01	0.22332E+00	0.58705E+03	0.96528E+00
0.14000E+02	0.19998E+00	0.12416E+03	0.26575E+01	0.67407E-01	0.59181E+03	0.97312E+00
0.15000E+02	0.19999E+00	0.12415E+03	0.26582E+01	0.98618E-01	0.59202E+03	0.97347E+00
0.16000E+02	0.20069E+00	0.12372E+03	0.26660E+01	0.86878E-01	0.59299E+03	0.97506E+00

Y	U'/U	U'/U_e	SK_u	FL_u	γ_u	V
0.20000E+01	0.10607E+00	0.79282E-01	-0.26120E+00	0.27098E+01	0.11071E+01	-0.20674E+02
0.30000E+01	0.90411E-01	0.73742E-01	-0.51450E+00	0.27994E+01	0.10717E+01	-0.23918E+02
0.40000E+01	0.60361E-01	0.53985E-01	-0.13482E+01	0.42073E+01	0.71305E+00	-0.31076E+02
0.50000E+01	0.37041E-01	0.34121E-01	-0.22211E+01	0.85476E+01	0.35098E+00	-0.34422E+02
0.60000E+01	0.28632E-01	0.26687E-01	-0.28472E+01	0.19089E+02	0.15716E+00	-0.36487E+02
0.70000E+01	0.22618E-01	0.21221E-01	-0.26493E+01	0.15115E+02	0.19848E+00	-0.39826E+02
0.80000E+01	0.21819E-01	0.20694E-01	-0.66130E+01	0.69839E+02	0.42956E-01	-0.45453E+02
0.90000E+01	0.13593E-01	0.13027E-01	-0.12228E+01	0.96745E+01	0.31009E+00	-0.53637E+02
0.10000E+02	0.17338E-01	0.16675E-01	-0.47770E+01	0.43381E+02	0.69155E-01	-0.51988E+02
0.11000E+02	0.21636E-01	0.20867E-01	-0.41642E+01	0.31201E+02	0.96149E-01	-0.47449E+02
0.12000E+02	0.20775E-01	0.20070E-01	-0.83745E+01	0.97553E+02	0.30753E-01	-0.49252E+02
0.13000E+02	0.38440E-01	0.37105E-01	-0.53789E+01	0.38251E+02	0.78430E-01	-0.47253E+02
0.14000E+02	0.12066E-01	0.11742E-01	-0.54120E+00	0.44915E+01	0.66793E+00	-0.44339E+02
0.15000E+02	0.17764E-01	0.17293E-01	-0.50254E+01	0.45741E+02	0.65587E-01	-0.39662E+02
0.16000E+02	0.14575E-01	0.14211E-01	-0.65684E+01	0.81650E+02	0.36742E-01	-0.40265E+02

Figure D.11 7^o Wedge ($\theta_{eff} = 10.4^o$) Flow $X = 1.32\delta_o$ Coincident Data

Y	V/U_e	V'/U	V'/U_e	SK_v	FL_v	$\tau_{xy}/\rho U^2$
0.20000E+01	-0.33994E-01	0.54947E-01	0.41071E-01	0.23720E+00	0.41416E+01	0.14683E-02
0.30000E+01	-0.39328E-01	0.43810E-01	0.35733E-01	0.51750E+00	0.44715E+01	0.16540E-02
0.40000E+01	-0.51098E-01	0.31567E-01	0.28233E-01	0.37700E-01	0.52031E+01	0.44653E-03
0.50000E+01	-0.56600E-01	0.29047E-01	0.26756E-01	0.56720E+00	0.77046E+01	0.31931E-03
0.60000E+01	-0.59996E-01	0.23982E-01	0.22353E-01	0.57750E+00	0.13238E+02	0.43223E-04
0.70000E+01	-0.65486E-01	0.34218E-01	0.32105E-01	0.39680E+00	0.13668E+02	0.52216E-05
0.80000E+01	-0.74738E-01	0.40118E-01	0.38050E-01	0.26147E+01	0.18411E+02	0.60798E-04
0.90000E+01	-0.88195E-01	0.28446E-01	0.27263E-01	0.21654E+01	0.20299E+02	-0.48205E-04
0.10000E+02	-0.85484E-01	0.31776E-01	0.30561E-01	0.30226E+01	0.18403E+02	0.77208E-05
0.11000E+02	-0.78020E-01	0.40804E-01	0.39354E-01	0.21981E+01	0.11999E+02	-0.11820E-03
0.12000E+02	-0.80986E-01	0.23838E-01	0.23029E-01	0.14902E+01	0.17122E+02	0.75476E-04
0.13000E+02	-0.77699E-01	0.24657E-01	0.23801E-01	0.22790E+01	0.17513E+02	0.12859E-04
0.14000E+02	-0.72906E-01	0.19883E-01	0.19349E-01	0.11289E+01	0.10772E+02	-0.23747E-04
0.15000E+02	-0.65216E-01	0.34370E-01	0.33458E-01	0.53074E+01	0.34782E+02	-0.17574E-04
0.16000E+02	-0.66208E-01	0.15505E-01	0.15119E-01	-0.12571E+01	0.14922E+02	-0.23061E-04

Y	$\tau_{xy}/\rho_e U_e^2$	τ_{xy}/τ_w	R_{uv}	TKE	U_{eff}/U^*	y^+
0.20000E+01	0.36657E-02	0.15212E+00	0.25194E+00	0.86444E-02	0.20467E+02	0.31190E+03
0.30000E+01	0.49169E-02	0.22666E+00	0.41758E+00	0.60064E-02	0.22684E+02	0.46785E+03
0.40000E+01	0.15961E-02	0.85549E-01	0.23435E+00	0.28182E-02	0.25410E+02	0.62380E+03
0.50000E+01	0.12107E-02	0.68995E-01	0.29678E+00	0.15297E-02	0.26387E+02	0.77975E+03
0.60000E+01	0.16779E-03	0.98172E-02	0.62946E-01	0.98504E-03	0.26794E+02	0.93570E+03
0.70000E+01	0.20540E-04	0.12220E-02	0.67468E-02	0.14266E-02	0.27027E+02	0.10916E+04
0.80000E+01	0.24439E-03	0.14970E-01	0.69457E-01	0.18475E-02	0.27415E+02	0.12476E+04
0.90000E+01	-0.19785E-03	-0.12463E-01	-0.12467E+00	0.90158E-03	0.27798E+02	0.14035E+04
0.10000E+02	0.31912E-04	0.20265E-02	0.14014E-01	0.11600E-02	0.27929E+02	0.15595E+04
0.11000E+02	-0.49132E-03	-0.31409E-01	-0.13389E+00	0.18990E-02	0.28035E+02	0.17154E+04
0.12000E+02	0.31476E-03	0.20196E-01	0.15241E+00	0.78402E-03	0.28097E+02	0.18714E+04
0.13000E+02	0.53540E-04	0.34252E-02	0.13567E-01	0.13468E-02	0.28067E+02	0.20273E+04
0.14000E+02	-0.10049E-03	-0.65618E-02	-0.98981E-01	0.46813E-03	0.28375E+02	0.21833E+04
0.15000E+02	-0.74418E-04	-0.48600E-02	-0.28784E-01	0.13391E-02	0.28389E+02	0.23392E+04
0.16000E+02	-0.97970E-04	-0.64203E-02	-0.10204E+00	0.34663E-03	0.28452E+02	0.24952E+04

Figure D.12 7^o Wedge ($\theta_{eff} = 10.4^o$) Flow $X = 1.32\delta_o$ Coincident Data (Cont.)

Y	ρ	T	M	M'	U	U/U$_e$
0.20000E+01	0.13277E+00	0.18762E+03	0.17198E+01	0.28135E+00	0.47149E+03	0.77527E+00
0.30000E+01	0.15361E+00	0.16216E+03	0.20516E+01	0.26741E+00	0.52311E+03	0.86015E+00
0.40000E+01	0.16854E+00	0.14780E+03	0.22596E+01	0.19190E+00	0.55015E+03	0.90462E+00
0.50000E+01	0.17790E+00	0.14002E+03	0.23805E+01	0.14461E+00	0.56414E+03	0.92761E+00
0.60000E+01	0.18219E+00	0.13672E+03	0.24348E+01	0.12643E+00	0.57024E+03	0.93764E+00
0.70000E+01	0.18609E+00	0.13386E+03	0.24827E+01	0.97025E-01	0.57519E+03	0.94579E+00
0.80000E+01	0.18922E+00	0.13165E+03	0.25207E+01	0.66030E-01	0.57917E+03	0.95233E+00
0.90000E+01	0.19221E+00	0.12959E+03	0.25561E+01	0.88704E-01	0.58271E+03	0.95815E+00
0.10000E+02	0.19199E+00	0.12975E+03	0.25543E+01	0.15145E+00	0.58268E+03	0.95811E+00
0.11000E+02	0.19420E+00	0.12827E+03	0.25801E+01	0.78607E-01	0.58518E+03	0.96221E+00
0.12000E+02	0.19929E+00	0.12499E+03	0.26387E+01	0.53338E-01	0.59076E+03	0.97138E+00
0.13000E+02	0.20456E+00	0.12177E+03	0.26980E+01	0.78676E-01	0.59586E+03	0.97978E+00
0.14000E+02	0.20800E+00	0.11976E+03	0.27373E+01	0.64404E-01	0.59930E+03	0.98542E+00
0.15000E+02	0.20630E+00	0.12075E+03	0.27189E+01	0.73424E-01	0.59810E+03	0.98345E+00
0.16000E+02	0.21011E+00	0.11856E+03	0.27611E+01	0.71521E-01	0.60181E+03	0.98956E+00
0.17000E+02	0.21101E+00	0.11805E+03	0.27705E+01	0.15423E+00	0.60267E+03	0.99097E+00
0.18000E+02	0.21201E+00	0.11749E+03	0.27817E+01	0.88576E-01	0.60396E+03	0.99309E+00

Y	U'/U	U'/U$_e$	SK$_u$	FL$_u$	γ$_u$	V
0.20000E+01	0.10423E+00	0.80805E-01	-0.35670E+00	0.26763E+01	0.11210E+01	-0.10670E+02
0.30000E+01	0.71905E-01	0.61849E-01	-0.93170E+00	0.37467E+01	0.80070E+00	-0.13200E+02
0.40000E+01	0.42919E-01	0.38825E-01	-0.15898E+01	0.66885E+01	0.44853E+00	-0.13320E+02
0.50000E+01	0.29410E-01	0.27281E-01	-0.17947E+01	0.74333E+01	0.40359E+00	-0.15372E+02
0.60000E+01	0.24544E-01	0.23013E-01	-0.30077E+01	0.20213E+02	0.14842E+00	-0.14114E+02
0.70000E+01	0.18542E-01	0.17537E-01	-0.35052E+01	0.34663E+02	0.86547E-01	-0.20618E+02
0.80000E+01	0.12502E-01	0.11906E-01	-0.65100E-01	0.41490E+01	0.72307E+00	-0.15678E+02
0.90000E+01	0.16026E-01	0.15355E-01	-0.21485E+01	0.19302E+02	0.15542E+00	-0.20319E+02
0.10000E+02	0.26655E-01	0.25538E-01	-0.10883E+02	0.14193E+03	0.21137E-01	-0.15888E+02
0.11000E+02	0.14051E-01	0.13520E-01	-0.47752E+01	0.57123E+02	0.52518E-01	-0.16757E+02
0.12000E+02	0.94430E-02	0.91728E-02	0.43500E-01	0.31039E+01	0.96653E+00	-0.19903E+02
0.13000E+02	0.13335E-01	0.13065E-01	-0.13776E+01	0.11697E+02	0.25647E+00	-0.27658E+02
0.14000E+02	0.11342E-01	0.11177E-01	-0.53210E+00	0.52967E+01	0.56639E+00	-0.28333E+02
0.15000E+02	0.11956E-01	0.11758E-01	-0.55530E+00	0.94234E+01	0.31836E+00	-0.27570E+02
0.16000E+02	0.11640E-01	0.11519E-01	-0.11400E-01	0.31711E+01	0.94604E+00	-0.23553E+02
0.17000E+02	0.23197E-01	0.22987E-01	-0.75439E+01	0.78159E+02	0.38383E-01	-0.22413E+02
0.18000E+02	0.13189E-01	0.13098E-01	-0.35810E+00	0.61292E+01	0.48946E+00	-0.19640E+02

Figure D.13 7^o Wedge ($\theta_{eff} = 10.4^o$) Flow $X = 2.64\delta_o$ Coincident Data

Y	V/U_e	V'/U	V'/U_e	SK_v	FL_v	$\tau_{xy}/\rho U^2$
0.20000E+01	-0.17545E-01	0.49912E-01	0.38695E-01	0.11870E+00	0.44369E+01	0.20022E-02
0.30000E+01	-0.21705E-01	0.38961E-01	0.33512E-01	-0.36260E+00	0.59103E+01	0.54858E-03
0.40000E+01	-0.21903E-01	0.34041E-01	0.30794E-01	0.10100E+00	0.80000E+01	0.10858E-03
0.50000E+01	-0.25276E-01	0.32431E-01	0.30083E-01	-0.13040E+00	0.12540E+02	0.14788E-03
0.60000E+01	-0.23208E-01	0.30265E-01	0.28377E-01	-0.12984E+01	0.96714E+01	0.15026E-04
0.70000E+01	-0.33902E-01	0.27987E-01	0.26469E-01	-0.21800E+01	0.13865E+02	0.48585E-04
0.80000E+01	-0.25780E-01	0.34882E-01	0.33219E-01	0.28862E+01	0.18601E+02	0.46696E-04
0.90000E+01	-0.33410E-01	0.27306E-01	0.26163E-01	-0.10556E+01	0.10229E+02	0.23920E-05
0.10000E+02	-0.26125E-01	0.32427E-01	0.31069E-01	-0.16178E+01	0.10190E+02	0.45168E-04
0.11000E+02	-0.27554E-01	0.33452E-01	0.32187E-01	0.14538E+01	0.10165E+02	0.34074E-05
0.12000E+02	-0.32727E-01	0.29033E-01	0.28202E-01	-0.24680E+00	0.43137E+01	-0.73328E-05
0.13000E+02	-0.45478E-01	0.30668E-01	0.30048E-01	0.91550E+00	0.99938E+01	0.20353E-04
0.14000E+02	-0.46588E-01	0.39962E-01	0.39379E-01	0.92550E+00	0.16277E+02	0.26080E-04
0.15000E+02	-0.45334E-01	0.22393E-01	0.22023E-01	0.21049E+01	0.21741E+02	-0.55893E-04
0.16000E+02	-0.38728E-01	0.34561E-01	0.34201E-01	0.50690E+00	0.16485E+02	-0.37744E-04
0.17000E+02	-0.36854E-01	0.31911E-01	0.31623E-01	-0.17970E+01	0.13306E+02	-0.16415E-04
0.18000E+02	-0.32294E-01	0.20657E-01	0.20515E-01	-0.10453E+01	0.90092E+01	-0.73112E-04

Y	$\tau_{xy}/\rho_e U_e^2$	τ_{xy}/τ_w	R_{uv}	TKE	U_{eff}/U^*	y^+
0.20000E+01	0.54559E-02	0.14619E+00	0.38488E+00	0.79231E-02	0.20884E+02	0.30533E+03
0.30000E+01	0.18401E-02	0.57045E-01	0.19582E+00	0.41031E-02	0.23665E+02	0.45800E+03
0.40000E+01	0.40284E-03	0.13702E-01	0.74321E-01	0.20798E-02	0.25210E+02	0.61066E+03
0.50000E+01	0.57687E-03	0.20712E-01	0.15504E+00	0.14842E-02	0.26039E+02	0.76333E+03
0.60000E+01	0.59890E-04	0.22021E-02	0.20228E-01	0.12172E-02	0.26408E+02	0.91600E+03
0.70000E+01	0.19703E-03	0.73995E-02	0.93624E-01	0.95516E-03	0.26710E+02	0.10687E+04
0.80000E+01	0.19200E-03	0.73321E-02	0.10708E+00	0.12949E-02	0.26955E+02	0.12213E+04
0.90000E+01	0.99557E-05	0.38620E-03	0.54663E-02	0.87402E-03	0.27175E+02	0.13740E+04
0.10000E+02	0.18798E-03	0.72834E-02	0.52256E-01	0.14068E-02	0.27174E+02	0.15267E+04
0.11000E+02	0.14302E-04	0.56054E-03	0.72494E-02	0.12177E-02	0.27330E+02	0.16793E+04
0.12000E+02	-0.31369E-04	-0.12617E-02	-0.26746E-01	0.88748E-03	0.27682E+02	0.18320E+04
0.13000E+02	0.88578E-04	0.36569E-02	0.49769E-01	0.10295E-02	0.28008E+02	0.19847E+04
0.14000E+02	0.11482E-03	0.48198E-02	0.57539E-01	0.16613E-02	0.28229E+02	0.21373E+04
0.15000E+02	-0.24508E-03	-0.10204E-01	-0.20876E+00	0.57294E-03	0.28152E+02	0.22900E+04
0.16000E+02	-0.16756E-03	-0.71052E-02	-0.93820E-01	0.12622E-02	0.28393E+02	0.24427E+04
0.17000E+02	-0.73083E-04	-0.31123E-02	-0.22175E-01	0.12874E-02	0.28448E+02	0.25953E+04
0.18000E+02	-0.32690E-03	-0.13987E-01	-0.26835E+00	0.51371E-03	0.28533E+02	0.27480E+04

Figure D.14 7^o Wedge ($\theta_{eff} = 10.4^o$) Flow $X = 2.64\delta_o$ Coincident Data (Cont.)

X/δ	ρ	T	M	M'	U	U/U$_e$
-0.20000E+01	0.29360E+00	0.12619E+03	0.26053E+01	0.26236E+00	0.58652E+03	0.96442E+00
-0.17500E+01	0.29252E+00	0.12557E+03	0.26155E+01	0.25283E+00	0.58738E+03	0.96583E+00
-0.15000E+01	0.29121E+00	0.12506E+03	0.26283E+01	0.24938E+00	0.58903E+03	0.96854E+00
-0.12500E+01	0.28762E+00	0.12552E+03	0.26212E+01	0.25792E+00	0.58852E+03	0.96771E+00
-0.10000E+01	0.28602E+00	0.12512E+03	0.26293E+01	0.25228E+00	0.58939E+03	0.96914E+00
-0.75000E+00	0.28072E+00	0.12635E+03	0.26074E+01	0.25939E+00	0.58736E+03	0.96580E+00
-0.50000E+00	0.27663E+00	0.12708E+03	0.25954E+01	0.25906E+00	0.58633E+03	0.96410E+00
-0.25000E+00	0.26206E+00	0.13294E+03	0.24945E+01	0.26448E+00	0.57620E+03	0.94745E+00
0.00000E+00	0.24826E+00	0.13905E+03	0.23944E+01	0.25408E+00	0.56508E+03	0.92916E+00
0.25000E+00	0.23715E+00	0.14424E+03	0.23129E+01	0.24912E+00	0.55554E+03	0.91348E+00
0.50000E+00	0.23027E+00	0.14718E+03	0.22681E+01	0.23219E+00	0.55053E+03	0.90524E+00
0.75000E+00	0.23026E+00	0.14581E+03	0.22906E+01	0.20857E+00	0.55351E+03	0.91014E+00
0.10000E+01	0.23260E+00	0.14299E+03	0.23344E+01	0.18415E+00	0.55859E+03	0.91849E+00
0.12500E+01	0.22485E+00	0.14651E+03	0.22808E+01	0.20339E+00	0.55257E+03	0.90859E+00
0.15000E+01	0.22886E+00	0.14256E+03	0.23419E+01	0.16518E+00	0.55983E+03	0.92054E+00
0.17500E+01	0.22461E+00	0.14386E+03	0.23225E+01	0.18006E+00	0.55789E+03	0.91734E+00
0.20000E+01	0.22316E+00	0.14337E+03	0.23305E+01	0.17059E+00	0.55896E+03	0.91909E+00
0.22500E+01	0.22241E+00	0.14243E+03	0.23456E+01	0.16114E+00	0.56081E+03	0.92214E+00
0.25000E+01	0.22285E+00	0.14074E+03	0.23724E+01	0.15164E+00	0.56393E+03	0.92727E+00
0.27500E+01	0.22089E+00	0.14056E+03	0.23753E+01	0.16015E+00	0.56429E+03	0.92786E+00
0.30000E+01	0.21832E+00	0.14077E+03	0.23720E+01	0.17350E+00	0.56392E+03	0.92726E+00

X/δ	U'/U	U'/U$_e$	SK$_u$	FL$_u$	γ$_u$	V
-0.20000E+01	0.42805E-01	0.41282E-01	-0.17051E+01	0.63333E+01	0.47369E+00	-0.21045E+01
-0.17500E+01	0.40902E-01	0.39505E-01	-0.17336E+01	0.64607E+01	0.46435E+00	-0.19199E+01
-0.15000E+01	0.39901E-01	0.38646E-01	-0.17419E+01	0.64134E+01	0.46777E+00	-0.12944E+01
-0.12500E+01	0.41473E-01	0.40134E-01	-0.16584E+01	0.58914E+01	0.50922E+00	-0.30550E+00
-0.10000E+01	0.40272E-01	0.39029E-01	-0.17997E+01	0.69276E+01	0.43305E+00	0.46780E+00
-0.75000E+00	0.42125E-01	0.40684E-01	-0.16373E+01	0.59608E+01	0.50329E+00	0.14254E+01
-0.50000E+00	0.42545E-01	0.41018E-01	-0.18043E+01	0.69098E+01	0.43417E+00	0.20000E-03
-0.25000E+00	0.47847E-01	0.45333E-01	-0.16609E+01	0.62682E+01	0.47861E+00	-0.13699E+02
0.00000E+00	0.50907E-01	0.47301E-01	-0.14816E+01	0.54243E+01	0.55307E+00	-0.27786E+02
0.25000E+00	0.54032E-01	0.49357E-01	-0.13335E+01	0.48788E+01	0.61491E+00	-0.33609E+02
0.50000E+00	0.52115E-01	0.47177E-01	-0.12645E+01	0.46489E+01	0.64531E+00	-0.30250E+02
0.75000E+00	0.45854E-01	0.41734E-01	-0.15545E+01	0.58339E+01	0.51424E+00	-0.29168E+02
0.10000E+01	0.39103E-01	0.35916E-01	-0.18905E+01	0.74802E+01	0.40106E+00	-0.29966E+02
0.12500E+01	0.45093E-01	0.40971E-01	-0.16454E+01	0.61584E+01	0.48714E+00	-0.25904E+02
0.15000E+01	0.34761E-01	0.31999E-01	-0.21234E+01	0.94649E+01	0.31696E+00	-0.23456E+02
0.17500E+01	0.38176E-01	0.35020E-01	-0.21367E+01	0.89064E+01	0.33684E+00	-0.18979E+02
0.20000E+01	0.35836E-01	0.32937E-01	-0.22301E+01	0.10115E+02	0.29660E+00	-0.14862E+02
0.22500E+01	0.33300E-01	0.30707E-01	-0.21373E+01	0.92296E+01	0.32504E+00	-0.11819E+02
0.25000E+01	0.30476E-01	0.28260E-01	-0.24365E+01	0.11609E+02	0.25842E+00	-0.97944E+01
0.27500E+01	0.31991E-01	0.29683E-01	-0.23566E+01	0.10947E+02	0.27405E+00	-0.73453E+01
0.30000E+01	0.34651E-01	0.32130E-01	-0.20694E+01	0.91257E+01	0.32874E+00	-0.49509E+01

Figure D.15 7^o Wedge ($\theta_{eff} = 10.4^o$) Flow $Y = 0.66\delta_o$ Coincident Data

X/δ	V'/U_e	V'/U	V'/U_e	SK_v	FL_v	$\tau_{xy}/\rho U^2$
-0.20000E+01	-0.34604E-02	0.20076E-01	0.19361E-01	0.93500E+00	0.83845E+01	0.39592E-03
-0.17500E+01	-0.31569E-02	0.20290E-01	0.19596E-01	0.52630E+00	0.10466E+02	0.36651E-03
-0.15000E+01	-0.21284E-02	0.20214E-01	0.19578E-01	0.47620E+00	0.10393E+02	0.37532E-03
-0.12500E+01	-0.50233E-03	0.20647E-01	0.19981E-01	0.53420E+00	0.86365E+01	0.39679E-03
-0.10000E+01	0.76921E-03	0.20584E-01	0.19949E-01	0.45750E+00	0.11756E+02	0.36915E-03
-0.75000E+00	0.23438E-02	0.21735E-01	0.20992E-01	-0.55700E-01	0.14161E+02	0.38454E-03
-0.50000E+00	0.32886E-06	0.20848E-01	0.20100E-01	0.12500E-01	0.11435E+02	0.33775E-03
-0.25000E+00	-0.22525E-01	0.23483E-01	0.22249E-01	-0.26360E+00	0.78065E+01	0.16814E-03
0.00000E+00	-0.45689E-01	0.26816E-01	0.24916E-01	0.38420E+00	0.98131E+01	0.12004E-03
0.25000E+00	-0.55263E-01	0.29103E-01	0.26585E-01	0.49320E+00	0.70498E+01	0.44287E-03
0.50000E+00	-0.49741E-01	0.26764E-01	0.24228E-01	0.58120E+00	0.72639E+01	0.38677E-03
0.75000E+00	-0.47962E-01	0.24181E-01	0.22008E-01	0.10933E+01	0.11415E+02	0.30591E-03
0.10000E+01	-0.49274E-01	0.22905E-01	0.21038E-01	0.82590E+00	0.10729E+02	0.25552E-03
0.12500E+01	-0.42594E-01	0.26849E-01	0.24394E-01	0.80240E+00	0.80199E+01	0.54440E-03
0.15000E+01	-0.38568E-01	0.24920E-01	0.22940E-01	0.11464E+01	0.14724E+02	0.32408E-03
0.17500E+01	-0.31207E-01	0.24007E-01	0.22022E-01	0.82470E+00	0.95535E+01	0.43281E-03
0.20000E+01	-0.24438E-01	0.26357E-01	0.24224E-01	0.45550E+00	0.15355E+02	0.34802E-03
0.22500E+01	-0.19435E-01	0.26324E-01	0.24274E-01	0.47800E-01	0.16932E+02	0.28395E-03
0.25000E+01	-0.16105E-01	0.21908E-01	0.20315E-01	0.14410E+00	0.13975E+02	0.26383E-03
0.27500E+01	-0.12078E-01	0.22369E-01	0.20755E-01	0.46770E+00	0.14683E+02	0.29245E-03
0.30000E+01	-0.81408E-02	0.24047E-01	0.22298E-01	0.15550E+00	0.14321E+02	0.29084E-03

X/δ	$\tau_{xy}/\rho_e U_e^2$	R_{uv}	TKE	y^+
-0.20000E+01	0.16455E-02	0.46073E+00	0.13192E-02	-0.12794E+02
-0.17500E+01	0.15277E-02	0.44164E+00	0.12482E-02	-0.11195E+02
-0.15000E+01	0.15732E-02	0.46533E+00	0.12047E-02	-0.95954E+01
-0.12500E+01	0.16604E-02	0.46338E+00	0.12863E-02	-0.79962E+01
-0.10000E+01	0.15493E-02	0.44532E+00	0.12346E-02	-0.63969E+01
-0.75000E+00	0.16028E-02	0.42000E+00	0.13597E-02	-0.47977E+01
-0.50000E+00	0.14028E-02	0.38079E+00	0.13397E-02	-0.31985E+01
-0.25000E+00	0.67443E-03	0.14964E+00	0.16961E-02	-0.15992E+01
0.00000E+00	0.46308E-03	0.87933E-01	0.20149E-02	0.00000E+00
0.25000E+00	0.16513E-02	0.28163E+00	0.23067E-02	0.15992E+01
0.50000E+00	0.14163E-02	0.27729E+00	0.20743E-02	0.31985E+01
0.75000E+00	0.11323E-02	0.27590E+00	0.16360E-02	0.47977E+01
0.10000E+01	0.96322E-03	0.28529E+00	0.12892E-02	0.63969E+01
0.12500E+01	0.20082E-02	0.44967E+00	0.17375E-02	0.79962E+01
0.15000E+01	0.12272E-02	0.37412E+00	0.12252E-02	0.95954E+01
0.17500E+01	0.16275E-02	0.47225E+00	0.13050E-02	0.11195E+02
0.20000E+01	0.13137E-02	0.36846E+00	0.13368E-02	0.12794E+02
0.22500E+01	0.10789E-02	0.32392E+00	0.12474E-02	0.14393E+02
0.25000E+01	0.10137E-02	0.39516E+00	0.94435E-03	0.15992E+02
0.27500E+01	0.11250E-02	0.40867E+00	0.10121E-02	0.17592E+02
0.30000E+01	0.11174E-02	0.34904E+00	0.11786E-02	0.19191E+02

Figure D.16 7^o Wedge ($\theta_{eff} = 10.4^o$) Flow $Y = 0.66\delta_o$ Coincident Data (Cont.)

D.4 10° Wedge ($\theta_{eff} = 13.5°$) Flow Tabulated Data

Y	ρ	T	M	M'	U	U/U_e
0.20000E+01	0.15240E+00	0.16314E+03	0.20389E+01	0.30129E+00	0.52173E+03	0.85788E+00
0.30000E+01	0.17388E+00	0.14298E+03	0.23345E+01	0.31486E+00	0.55935E+03	0.91974E+00
0.40000E+01	0.18958E+00	0.13114E+03	0.25284E+01	0.28418E+00	0.58025E+03	0.95411E+00
0.50000E+01	0.19677E+00	0.12635E+03	0.26130E+01	0.24597E+00	0.58861E+03	0.96786E+00
0.60000E+01	0.20688E+00	0.12017E+03	0.27272E+01	0.18678E+00	0.59917E+03	0.98521E+00
0.70000E+01	0.21157E+00	0.11751E+03	0.27788E+01	0.14439E+00	0.60374E+03	0.99274E+00
0.80000E+01	0.21335E+00	0.11653E+03	0.27984E+01	0.13736E+00	0.60545E+03	0.99555E+00
0.90000E+01	0.21552E+00	0.11536E+03	0.28220E+01	0.10192E+00	0.60752E+03	0.99895E+00
0.10000E+02	0.21276E+00	0.11686E+03	0.27925E+01	0.10145E+00	0.60494E+03	0.99471E+00
0.11000E+02	0.19919E+00	0.12482E+03	0.26427E+01	0.89015E-01	0.59082E+03	0.97150E+00
0.12000E+02	0.19020E+00	0.13072E+03	0.25388E+01	0.10983E+00	0.57947E+03	0.95283E+00
0.13000E+02	0.18652E+00	0.13329E+03	0.24948E+01	0.82462E-01	0.57407E+03	0.94394E+00
0.14000E+02	0.18280E+00	0.13600E+03	0.24500E+01	0.71185E-01	0.56859E+03	0.93493E+00

Y	U'/U	U'/U_e	SK_u	FL_u	γ_u	V
0.20000E+01	0.80775E-01	0.69295E-01	-0.35660E+00	0.26791E+01	0.11198E+01	-0.31100E-01
0.30000E+01	0.64640E-01	0.59452E-01	-0.88070E+00	0.34397E+01	0.87217E+00	-0.12675E+01
0.40000E+01	0.49450E-01	0.47181E-01	-0.14678E+01	0.54135E+01	0.55417E+00	-0.25050E+01
0.50000E+01	0.39904E-01	0.38621E-01	-0.16833E+01	0.61854E+01	0.48501E+00	-0.26113E+01
0.60000E+01	0.27644E-01	0.27235E-01	-0.25121E+01	0.11617E+02	0.25825E+00	-0.32614E+01
0.70000E+01	0.20508E-01	0.20359E-01	-0.31638E+01	0.19060E+02	0.15740E+00	-0.32904E+01
0.80000E+01	0.19210E-01	0.19125E-01	-0.57288E+01	0.68932E+02	0.43521E-01	-0.29417E+01
0.90000E+01	0.13975E-01	0.13960E-01	-0.56482E+01	0.89198E+02	0.33633E-01	-0.21271E+01
0.10000E+02	0.14440E-01	0.14364E-01	-0.56127E+01	0.80238E+02	0.37389E-01	-0.83827E+01
0.11000E+02	0.15405E-01	0.14966E-01	-0.22606E+01	0.15066E+02	0.19913E+00	-0.31105E+02
0.12000E+02	0.21899E-01	0.20866E-01	-0.31791E+01	0.30824E+02	0.97327E-01	-0.48345E+02
0.13000E+02	0.17862E-01	0.16861E-01	-0.22280E+01	0.31287E+02	0.95888E-01	-0.59282E+02
0.14000E+02	0.17059E-01	0.15949E-01	-0.19680E+00	0.34314E+01	0.87428E+00	-0.66307E+02

Y	V/U_e	V'/U	V'/U_e	SK_v	FL_v	$\tau_{xy}/\rho U^2$
0.20000E+01	-0.51138E-04	0.32255E-01	0.27671E-01	0.20650E+00	0.61034E+01	0.12430E-02
0.30000E+01	-0.20842E-02	0.26752E-01	0.24605E-01	0.23830E+00	0.64680E+01	0.83378E-03
0.40000E+01	-0.41190E-02	0.22650E-01	0.21611E-01	0.33120E+00	0.81335E+01	0.50151E-03
0.50000E+01	-0.42938E-02	0.20594E-01	0.19932E-01	0.29830E+00	0.11624E+02	0.33867E-03
0.60000E+01	-0.53627E-02	0.18675E-01	0.18398E-01	-0.83690E+00	0.28266E+02	0.15944E-03
0.70000E+01	-0.54104E-02	0.15022E-01	0.14913E-01	-0.21960E+00	0.28282E+02	0.85315E-04
0.80000E+01	-0.48370E-02	0.15860E-01	0.15790E-01	-0.27998E+01	0.53694E+02	0.37070E-04
0.90000E+01	-0.34976E-02	0.12352E-01	0.12339E-01	-0.23151E+01	0.37406E+02	0.29184E-04
0.10000E+02	-0.13784E-01	0.17285E-01	0.17194E-01	-0.27741E+01	0.37619E+02	-0.21692E-04
0.11000E+02	-0.51146E-01	0.24767E-01	0.24061E-01	0.49880E+00	0.21979E+02	-0.14413E-03
0.12000E+02	-0.79494E-01	0.34124E-01	0.32514E-01	0.12930E+01	0.16418E+02	-0.19576E-03
0.13000E+02	-0.97477E-01	0.28747E-01	0.27136E-01	0.99020E+00	0.12456E+02	-0.29505E-03
0.14000E+02	-0.10903E+00	0.31402E-01	0.29359E-01	0.22564E+01	0.21509E+02	-0.17480E-03

Y	$\tau_{xy}/\rho_e U_e^2$	τ_{xy}/τ_w	R_{uv}	TKE	U_{eff}/U^*	y^+
0.20000E+01	0.40877E-02	0.10000E+01	0.47708E+00	0.43027E-02	0.24199E+02	0.31266E+03
0.30000E+01	0.31517E-02	0.87972E+00	0.48217E+00	0.28048E-02	0.26420E+02	0.46899E+03
0.40000E+01	0.20400E-02	0.62082E+00	0.44775E+00	0.17357E-02	0.27722E+02	0.62532E+03
0.50000E+01	0.14176E-02	0.44779E+00	0.41213E+00	0.12203E-02	0.28259E+02	0.78165E+03
0.60000E+01	0.69154E-03	0.22966E+00	0.30885E+00	0.73082E-03	0.28952E+02	0.93799E+03
0.70000E+01	0.37571E-03	0.12760E+00	0.27693E+00	0.43595E-03	0.29257E+02	0.10943E+04
0.80000E+01	0.16418E-03	0.56227E-01	0.12167E+00	0.43606E-03	0.29372E+02	0.12506E+04
0.90000E+01	0.13013E-03	0.45021E-01	0.16906E+00	0.25023E-03	0.29512E+02	0.14070E+04
0.10000E+02	-0.95908E-04	-0.32756E-01	-0.86907E-01	0.40304E-03	0.29338E+02	0.15633E+04
0.11000E+02	-0.60786E-03	-0.19436E+00	-0.37778E+00	0.73204E-03	0.28403E+02	0.17196E+04
0.12000E+02	-0.79418E-03	-0.24248E+00	-0.26196E+00	0.14042E-02	0.27673E+02	0.18760E+04
0.13000E+02	-0.11747E-02	-0.35174E+00	-0.57459E+00	0.98594E-03	0.27331E+02	0.20323E+04
0.14000E+02	-0.68276E-03	-0.20035E+00	-0.32632E+00	0.11316E-02	0.26989E+02	0.21886E+04

Figure D.17 10° Wedge ($\theta_{eff} = 13.5°$) Flow $X = -1.32\delta_o$ Coincident Data

Y	ρ	T	M	M'	U	U/U_e
0.20000E+01	0.12190E+00	0.20519E+03	0.15024E+01	0.34007E+00	0.42991E+03	0.70690E+00
0.30000E+01	0.13486E+00	0.18548E+03	0.17403E+01	0.39290E+00	0.47374E+03	0.77897E+00
0.40000E+01	0.14752E+00	0.16956E+03	0.19453E+01	0.38644E+00	0.50729E+03	0.83413E+00
0.50000E+01	0.16109E+00	0.15527E+03	0.21433E+01	0.35551E+00	0.53444E+03	0.87878E+00
0.60000E+01	0.17466E+00	0.14321E+03	0.23247E+01	0.23720E+00	0.55493E+03	0.91248E+00
0.70000E+01	0.18026E+00	0.13876E+03	0.23957E+01	0.12651E+00	0.56171E+03	0.92363E+00
0.80000E+01	0.17990E+00	0.13904E+03	0.23920E+01	0.88814E-01	0.56047E+03	0.92158E+00
0.90000E+01	0.17981E+00	0.13911E+03	0.23910E+01	0.69629E-01	0.55980E+03	0.92048E+00
0.10000E+02	0.18064E+00	0.13847E+03	0.24018E+01	0.56273E-01	0.56119E+03	0.92277E+00
0.11000E+02	0.17983E+00	0.13909E+03	0.23921E+01	0.53230E-01	0.55975E+03	0.92040E+00
0.12000E+02	0.18008E+00	0.13890E+03	0.23952E+01	0.67814E-01	0.55992E+03	0.92068E+00
0.13000E+02	0.18081E+00	0.13834E+03	0.24051E+01	0.69169E-01	0.56129E+03	0.92293E+00
0.14000E+02	0.18105E+00	0.13816E+03	0.24076E+01	0.42634E-01	0.56148E+03	0.92325E+00

Y	U'/U	U'/U_e	SK_u	FL_u	γ_u	V
0.20000E+01	0.15369E+00	0.10864E+00	-0.14590E+00	0.22540E+01	0.13310E+01	0.28386E+02
0.30000E+01	0.13861E+00	0.10797E+00	-0.34070E+00	0.22883E+01	0.13110E+01	0.27411E+02
0.40000E+01	0.11277E+00	0.94064E-01	-0.61660E+00	0.25777E+01	0.11638E+01	0.64155E+01
0.50000E+01	0.88465E-01	0.77741E-01	-0.11520E+01	0.38841E+01	0.77238E+00	-0.22098E+02
0.60000E+01	0.53027E-01	0.48386E-01	-0.18107E+01	0.72044E+01	0.41641E+00	-0.50513E+02
0.70000E+01	0.28768E-01	0.26571E-01	-0.17769E+01	0.94296E+01	0.31815E+00	-0.64219E+02
0.80000E+01	0.21767E-01	0.20060E-01	-0.38120E+00	0.42547E+01	0.70510E+00	-0.72238E+02
0.90000E+01	0.17993E-01	0.16562E-01	-0.50150E+00	0.72393E+01	0.41440E+00	-0.76636E+02
0.10000E+02	0.14364E-01	0.13255E-01	0.88400E+00	0.55344E+01	0.54206E+00	-0.76254E+02
0.11000E+02	0.14549E-01	0.13391E-01	0.96740E+00	0.61871E+01	0.48488E+00	-0.78873E+02
0.12000E+02	0.17263E-01	0.15894E-01	-0.51383E+01	0.53763E+02	0.55800E-01	-0.80309E+02
0.13000E+02	0.16494E-01	0.15223E-01	-0.89452E+01	0.19687E+03	0.15238E-01	-0.79721E+02
0.14000E+02	0.11715E-01	0.10816E-01	-0.21426E+01	0.33013E+02	0.90872E-01	-0.79602E+02

Y	V/U_e	V'/U	V'/U_e	SK_v	FL_v	$\tau_{xy}/\rho U^2$
0.20000E+01	0.46675E-01	0.50589E-01	0.35761E-01	0.86800E-01	0.45123E+01	0.22237E-02
0.30000E+01	0.45072E-01	0.48401E-01	0.37703E-01	0.28360E+00	0.44416E+01	0.23928E-02
0.40000E+01	0.10549E-01	0.40504E-01	0.33786E-01	0.18560E+00	0.46727E+01	0.15925E-02
0.50000E+01	-0.36336E-01	0.41686E-01	0.36633E-01	0.17420E+00	0.54666E+01	0.12764E-02
0.60000E+01	-0.83058E-01	0.38566E-01	0.35190E-01	0.45000E-01	0.53499E+01	0.11994E-03
0.70000E+01	-0.10559E+00	0.33534E-01	0.30973E-01	-0.14600E-01	0.57771E+01	-0.30921E-03
0.80000E+01	-0.11878E+00	0.32177E-01	0.29654E-01	0.13887E+01	0.15627E+02	-0.26947E-03
0.90000E+01	-0.12601E+00	0.30236E-01	0.27831E-01	0.32300E+00	0.11413E+02	-0.20128E-03
0.10000E+02	-0.12538E+00	0.24126E-01	0.22263E-01	0.88880E+00	0.10952E+02	-0.21059E-03
0.11000E+02	-0.12969E+00	0.28089E-01	0.25853E-01	0.18040E+00	0.92164E+01	-0.14535E-03
0.12000E+02	-0.13205E+00	0.26478E-01	0.24378E-01	0.56480E+00	0.17139E+02	-0.94558E-04
0.13000E+02	-0.13108E+00	0.20322E-01	0.18756E-01	0.10628E+01	0.20233E+02	-0.92553E-04
0.14000E+02	-0.13089E+00	0.23591E-01	0.21780E-01	0.10182E+01	0.26992E+02	-0.45939E-04

Y	$\tau_{xy}/\rho_e U_e^2$	τ_{xy}/τ_w	R_{uv}	TKE	U_{eff}/U^*	y^+
0.20000E+01	0.49653E-02	-0.53853E-01	0.28600E+00	0.14370E-01	0.19227E+02	0.31332E+03
0.30000E+01	0.64880E-02	-0.77847E-01	0.35668E+00	0.11948E-01	0.21511E+02	0.46998E+03
0.40000E+01	0.49511E-02	-0.64986E-01	0.34865E+00	0.79990E-02	0.23345E+02	0.62665E+03
0.50000E+01	0.44047E-02	-0.63132E-01	0.34613E+00	0.56508E-02	0.24896E+02	0.78331E+03
0.60000E+01	0.44624E-03	-0.69346E-02	0.58650E-01	0.28932E-02	0.26113E+02	0.93997E+03
0.70000E+01	-0.11787E-02	0.18904E-01	-0.32051E+00	0.15384E-02	0.26526E+02	0.10966E+04
0.80000E+01	-0.10227E-02	0.16369E-01	-0.38472E+00	0.12723E-02	0.26449E+02	0.12533E+04
0.90000E+01	-0.76205E-03	0.12191E-01	-0.36997E+00	0.10761E-02	0.26408E+02	0.14100E+04
0.10000E+02	-0.80128E-03	0.12879E-01	-0.60766E+00	0.68525E-03	0.26494E+02	0.15666E+04
0.11000E+02	-0.55020E-03	0.88034E-02	-0.35566E+00	0.89482E-03	0.26406E+02	0.17233E+04
0.12000E+02	-0.35816E-03	0.57387E-02	-0.20687E+00	0.85009E-03	0.26416E+02	0.18799E+04
0.13000E+02	-0.35228E-03	0.56674E-02	-0.27612E+00	0.54901E-03	0.26499E+02	0.20366E+04
0.14000E+02	-0.17498E-03	0.28186E-02	-0.16623E+00	0.62515E-03	0.26511E+02	0.21933E+04

Figure D.18 10^o Wedge ($\theta_{eff} = 13.5^o$) Flow $X = 0\delta_o$ Coincident Data

Y	ρ	T	M	M'	U	U/U_e
0.20000E+01	0.12057E+00	0.20661E+03	0.14926E+01	0.24336E+00	0.42801E+03	0.70377E+00
0.30000E+01	0.13705E+00	0.18175E+03	0.17938E+01	0.24470E+00	0.48250E+03	0.79337E+00
0.40000E+01	0.15168E+00	0.16423E+03	0.20235E+01	0.21714E+00	0.51723E+03	0.85048E+00
0.50000E+01	0.16123E+00	0.15450E+03	0.21603E+01	0.17033E+00	0.53556E+03	0.88062E+00
0.60000E+01	0.16597E+00	0.15009E+03	0.22260E+01	0.11002E+00	0.54431E+03	0.89501E+00
0.70000E+01	0.16894E+00	0.14745E+03	0.22648E+01	0.78401E-01	0.54892E+03	0.90259E+00
0.80000E+01	0.17113E+00	0.14556E+03	0.22941E+01	0.72149E-01	0.55215E+03	0.90791E+00
0.90000E+01	0.17450E+00	0.14275E+03	0.23373E+01	0.67694E-01	0.55636E+03	0.91482E+00
0.10000E+02	0.17970E+00	0.13862E+03	0.24039E+01	0.62940E-01	0.56308E+03	0.92588E+00
0.11000E+02	0.18317E+00	0.13599E+03	0.24468E+01	0.57620E-01	0.56691E+03	0.93217E+00
0.12000E+02	0.18433E+00	0.13514E+03	0.24610E+01	0.43908E-01	0.56884E+03	0.93535E+00
0.13000E+02	0.18470E+00	0.13486E+03	0.24655E+01	0.44585E-01	0.56968E+03	0.93673E+00
0.14000E+02	0.18650E+00	0.13356E+03	0.24873E+01	0.55420E-01	0.57216E+03	0.94080E+00
0.15000E+02	0.18739E+00	0.13293E+03	0.24980E+01	0.68721E-01	0.57340E+03	0.94285E+00
0.16000E+02	0.18855E+00	0.13211E+03	0.25118E+01	0.34961E-01	0.57523E+03	0.94585E+00
0.17000E+02	0.19011E+00	0.13103E+03	0.25304E+01	0.39846E-01	0.57754E+03	0.94965E+00
0.18000E+02	0.19094E+00	0.13046E+03	0.25411E+01	0.42813E-01	0.57896E+03	0.95198E+00
0.19000E+02	0.19339E+00	0.12881E+03	0.25694E+01	0.42512E-01	0.58183E+03	0.95671E+00
0.20000E+02	0.19230E+00	0.12953E+03	0.25572E+01	0.36885E-01	0.58122E+03	0.95570E+00

Y	U'/U	U'/U_e	SK_u	FL_u	γ_u	V
0.20000E+01	0.11844E+00	0.83356E-01	-0.30680E+00	0.26989E+01	0.11116E+01	-0.33445E+02
0.30000E+01	0.87462E-01	0.69390E-01	-0.69630E+00	0.32367E+01	0.92687E+00	-0.41834E+02
0.40000E+01	0.62765E-01	0.53380E-01	-0.11614E+01	0.43124E+01	0.69567E+00	-0.48527E+02
0.50000E+01	0.44084E-01	0.38821E-01	-0.18845E+01	0.72440E+01	0.41414E+00	-0.51405E+02
0.60000E+01	0.27018E-01	0.24181E-01	-0.20894E+01	0.12622E+02	0.23767E+00	-0.49016E+02
0.70000E+01	0.19350E-01	0.17465E-01	-0.14369E+01	0.13156E+02	0.22803E+00	-0.49071E+02
0.80000E+01	0.18269E-01	0.16587E-01	-0.24100E+01	0.38698E+02	0.77524E-01	-0.51482E+02
0.90000E+01	0.18038E-01	0.16501E-01	-0.36580E+01	0.46493E+02	0.64526E-01	-0.57789E+02
0.10000E+02	0.15428E-01	0.14284E-01	-0.77557E+01	0.12951E+03	0.23164E-01	-0.67673E+02
0.11000E+02	0.14579E-01	0.13590E-01	-0.58413E+01	0.64403E+02	0.46582E-01	-0.74163E+02
0.12000E+02	0.10711E-01	0.10019E-01	-0.62916E+01	0.11992E+03	0.25016E-01	-0.71692E+02
0.13000E+02	0.98160E-02	0.91950E-02	-0.42268E+01	0.87816E+02	0.34162E-01	-0.69368E+02
0.14000E+02	0.13114E-01	0.12338E-01	-0.43026E+01	0.51045E+02	0.58772E-01	-0.66582E+02
0.15000E+02	0.15600E-01	0.14708E-01	-0.95131E+01	0.16649E+03	0.18019E-01	-0.65091E+02
0.16000E+02	0.87030E-02	0.82317E-02	0.46760E+00	0.52773E+01	0.56847E+00	-0.62181E+02
0.17000E+02	0.84700E-02	0.80435E-02	0.50220E+00	0.39291E+01	0.76353E+00	-0.59018E+02
0.18000E+02	0.91990E-02	0.87573E-02	-0.93120E+00	0.18285E+02	0.16407E+00	-0.56325E+02
0.19000E+02	0.98000E-02	0.93757E-02	0.46990E+00	0.46836E+01	0.64053E+00	-0.53726E+02
0.20000E+02	0.75780E-02	0.72423E-02	0.22380E+00	0.34623E+01	0.86648E+00	-0.49447E+02

Figure D.19 10^o Wedge ($\theta_{eff} = 13.5^o$) Flow $X = 1.32\delta_o$ Coincident Data

Y	V/U_e	V'/U	V'/U_e	SK_v	FL_v	$\tau_{xy}/\rho U^2$
0.20000E+01	-0.54994E-01	0.58523E-01	0.41187E-01	0.32790E+00	0.40975E+01	0.15658E-02
0.30000E+01	-0.68788E-01	0.42479E-01	0.33701E-01	0.47660E+00	0.54781E+01	0.94190E-03
0.40000E+01	-0.79793E-01	0.33925E-01	0.28853E-01	-0.22670E+00	0.73522E+01	0.55749E-03
0.50000E+01	-0.84526E-01	0.30109E-01	0.26515E-01	-0.55040E+00	0.14775E+02	0.27112E-03
0.60000E+01	-0.80597E-01	0.21986E-01	0.19678E-01	-0.11336E+01	0.21762E+02	0.76365E-04
0.70000E+01	-0.80688E-01	0.23675E-01	0.21369E-01	-0.32013E+01	0.37001E+02	0.22266E-04
0.80000E+01	-0.84652E-01	0.30019E-01	0.27254E-01	-0.28076E+01	0.26028E+02	0.38618E-04
0.90000E+01	-0.95023E-01	0.38769E-01	0.35466E-01	-0.10465E+01	0.14778E+02	0.19530E-04
0.10000E+02	-0.11127E+00	0.25781E-01	0.23870E-01	-0.20036E+01	0.22127E+02	0.87257E-05
0.11000E+02	-0.12195E+00	0.28061E-01	0.26157E-01	-0.40548E+01	0.24804E+02	0.14382E-04
0.12000E+02	-0.11788E+00	0.19925E-01	0.18637E-01	0.12697E+01	0.49668E+02	-0.20839E-05
0.13000E+02	-0.11406E+00	0.12582E-01	0.11786E-01	-0.66080E+00	0.66802E+02	-0.13086E-04
0.14000E+02	-0.10948E+00	0.25898E-01	0.24365E-01	-0.25889E+01	0.32141E+02	-0.63355E-06
0.15000E+02	-0.10703E+00	0.28151E-01	0.26542E-01	-0.26869E+01	0.29583E+02	0.46808E-05
0.16000E+02	-0.10225E+00	0.22895E-01	0.21655E-01	-0.93150E+00	0.43708E+02	0.87617E-05
0.17000E+02	-0.97044E-01	0.14596E-01	0.13861E-01	-0.46237E+01	0.46460E+02	-0.23421E-05
0.18000E+02	-0.92615E-01	0.18242E-01	0.17366E-01	-0.56660E+01	0.77192E+02	0.51968E-05
0.19000E+02	-0.88341E-01	0.28194E-01	0.26973E-01	-0.42363E+01	0.33213E+02	-0.10495E-04
0.20000E+02	-0.81306E-01	0.15059E-01	0.14392E-01	0.64264E+01	0.79630E+02	-0.25117E-04

Y	$\tau_{xy}/\rho_e U_e^2$	τ_{xy}/τ_w	R_{uv}	TKE	U_{eff}/U^*	y^+
0.20000E+01	0.34655E-02	-0.40004E-01	0.22589E+00	0.10439E-01	0.19146E+02	0.31296E+03
0.30000E+01	0.26492E-02	-0.34763E-01	0.25352E+00	0.56292E-02	0.21999E+02	0.46944E+03
0.40000E+01	0.18019E-02	-0.26168E-01	0.26182E+00	0.31206E-02	0.23923E+02	0.62592E+03
0.50000E+01	0.93950E-03	-0.14503E-01	0.20426E+00	0.18783E-02	0.24979E+02	0.78241E+03
0.60000E+01	0.27334E-03	-0.43436E-02	0.12856E+00	0.84838E-03	0.25495E+02	0.93889E+03
0.70000E+01	0.81058E-04	-0.13111E-02	0.48604E-01	0.74773E-03	0.25770E+02	0.10954E+04
0.80000E+01	0.14224E-03	-0.23306E-02	0.70419E-01	0.10680E-02	0.25964E+02	0.12518E+04
0.90000E+01	0.73033E-04	-0.12202E-02	0.27927E-01	0.16657E-02	0.26217E+02	0.14083E+04
0.10000E+02	0.33425E-04	-0.57508E-03	0.21938E-01	0.78368E-03	0.26628E+02	0.15648E+04
0.11000E+02	0.55843E-04	-0.97937E-03	0.35155E-01	0.89369E-03	0.26864E+02	0.17213E+04
0.12000E+02	-0.81466E-05	0.14378E-03	-0.97641E-02	0.45438E-03	0.26984E+02	0.18778E+04
0.13000E+02	-0.51310E-04	0.90740E-03	-0.10597E+00	0.20647E-03	0.27036E+02	0.20343E+04
0.14000E+02	-0.25057E-05	0.44744E-04	-0.18654E-02	0.75671E-03	0.27191E+02	0.21907E+04
0.15000E+02	0.18594E-04	-0.33360E-03	0.10658E-01	0.91417E-03	0.27269E+02	0.23472E+04
0.16000E+02	0.35026E-04	-0.63230E-03	0.43970E-01	0.56205E-03	0.27383E+02	0.25037E+04
0.17000E+02	-0.94381E-05	0.17179E-03	-0.18945E-01	0.24891E-03	0.27529E+02	0.26602E+04
0.18000E+02	0.21045E-04	-0.38473E-03	0.30966E-01	0.37510E-03	0.27619E+02	0.28167E+04
0.19000E+02	-0.42923E-04	0.79478E-03	-0.37983E-01	0.84293E-03	0.27802E+02	0.29731E+04
0.20000E+02	-0.10251E-03	0.18874E-02	-0.22010E+00	0.25548E-03	0.27763E+02	0.31296E+04

Figure D.20 10^o Wedge ($\theta_{eff} = 13.5^o$) Flow $X = 1.32\delta_o$ Coincident Data (Cont.)

Y	ρ	T	M	M'	U	U/U_e
0.20000E+01	0.12934E+00	0.19289E+03	0.16571E+01	0.24461E+00	0.46007E+03	0.75649E+00
0.30000E+01	0.14400E+00	0.17326E+03	0.19035E+01	0.23289E+00	0.50099E+03	0.82378E+00
0.40000E+01	0.15877E+00	0.15714E+03	0.21232E+01	0.19196E+00	0.53220E+03	0.87510E+00
0.50000E+01	0.16776E+00	0.14872E+03	0.22468E+01	0.10928E+00	0.54786E+03	0.90085E+00
0.60000E+01	0.17130E+00	0.14565E+03	0.22935E+01	0.78646E-01	0.55340E+03	0.90996E+00
0.70000E+01	0.17486E+00	0.14269E+03	0.23391E+01	0.51247E-01	0.55857E+03	0.91846E+00
0.80000E+01	0.17704E+00	0.14093E+03	0.23673E+01	0.49417E-01	0.56185E+03	0.92386E+00
0.90000E+01	0.17907E+00	0.13933E+03	0.23929E+01	0.41284E-01	0.56482E+03	0.92874E+00
0.10000E+02	0.18030E+00	0.13837E+03	0.24079E+01	0.45570E-01	0.56661E+03	0.93167E+00
0.11000E+02	0.18158E+00	0.13740E+03	0.24237E+01	0.37808E-01	0.56845E+03	0.93470E+00
0.12000E+02	0.18345E+00	0.13600E+03	0.24471E+01	0.41678E-01	0.57088E+03	0.93870E+00
0.13000E+02	0.18641E+00	0.13385E+03	0.24826E+01	0.45504E-01	0.57455E+03	0.94474E+00
0.14000E+02	0.19084E+00	0.13074E+03	0.25363E+01	0.44679E-01	0.57988E+03	0.95350E+00
0.15000E+02	0.19471E+00	0.12814E+03	0.25812E+01	0.69152E-01	0.58381E+03	0.95996E+00
0.16000E+02	0.19725E+00	0.12649E+03	0.26109E+01	0.42291E-01	0.58679E+03	0.96487E+00
0.17000E+02	0.19873E+00	0.12555E+03	0.26274E+01	0.51322E-01	0.58869E+03	0.96799E+00
0.18000E+02	0.19975E+00	0.12490E+03	0.26394E+01	0.56261E-01	0.59011E+03	0.97032E+00
0.19000E+02	0.20155E+00	0.12379E+03	0.26598E+01	0.58707E-01	0.59219E+03	0.97374E+00
0.20000E+02	0.20263E+00	0.12313E+03	0.26719E+01	0.66739E-01	0.59341E+03	0.97575E+00
0.21000E+02	0.20439E+00	0.12207E+03	0.26920E+01	0.70865E-01	0.59539E+03	0.97900E+00
0.22000E+02	0.20559E+00	0.12136E+03	0.27049E+01	0.57647E-01	0.59669E+03	0.98115E+00
0.23000E+02	0.20802E+00	0.11994E+03	0.27316E+01	0.53045E-01	0.59932E+03	0.98547E+00
0.24000E+02	0.20998E+00	0.11882E+03	0.27531E+01	0.56959E-01	0.60136E+03	0.98882E+00

Y	U'/U	U'/U_e	SK_u	FL_u	γ_u	V
0.20000E+01	0.98533E-01	0.74539E-01	-0.52410E+00	0.28197E+01	0.10639E+01	-0.25381E+02
0.30000E+01	0.73748E-01	0.60752E-01	-0.84160E+00	0.38612E+01	0.77696E+00	-0.27905E+02
0.40000E+01	0.49745E-01	0.43532E-01	-0.19307E+01	0.74937E+01	0.40034E+00	-0.33612E+02
0.50000E+01	0.25780E-01	0.23224E-01	-0.28605E+01	0.17505E+02	0.17138E+00	-0.37107E+02
0.60000E+01	0.18353E-01	0.16701E-01	-0.28352E+01	0.26932E+02	0.11139E+00	-0.37778E+02
0.70000E+01	0.11926E-01	0.10954E-01	-0.24270E+00	0.97111E+01	0.30892E+00	-0.39493E+02
0.80000E+01	0.11018E-01	0.10179E-01	-0.35949E+01	0.64121E+02	0.46787E-01	-0.39620E+02
0.90000E+01	0.90540E-02	0.84088E-02	-0.59920E+00	0.13104E+02	0.22894E+00	-0.38088E+02
0.10000E+02	0.98250E-02	0.91537E-02	-0.41772E+01	0.71560E+02	0.41923E-01	-0.34873E+02
0.11000E+02	0.83390E-02	0.77945E-02	-0.14944E+01	0.27408E+02	0.10946E+00	-0.32186E+02
0.12000E+02	0.94220E-02	0.88445E-02	0.10072E+01	0.10926E+02	0.27458E+00	-0.32314E+02
0.13000E+02	0.94150E-02	0.88947E-02	-0.49032E+01	0.88156E+02	0.34031E-01	-0.34863E+02
0.14000E+02	0.91310E-02	0.87065E-02	-0.11923E+01	0.11496E+02	0.26096E+00	-0.38790E+02
0.15000E+02	0.12995E-01	0.12475E-01	-0.67324E+01	0.10353E+03	0.28978E-01	-0.45547E+02
0.16000E+02	0.83770E-02	0.80827E-02	-0.43700E-01	0.44072E+01	0.68070E+00	-0.44669E+02
0.17000E+02	0.92220E-02	0.89268E-02	-0.46407E+01	0.11485E+03	0.26122E-01	-0.39995E+02
0.18000E+02	0.97650E-02	0.94752E-02	-0.57025E+01	0.10445E+03	0.28723E-01	-0.36597E+02
0.19000E+02	0.99210E-02	0.96604E-02	-0.47114E+01	0.66332E+02	0.45227E-01	-0.33572E+02
0.20000E+02	0.11024E-01	0.10757E-01	-0.64172E+01	0.10094E+03	0.29720E-01	-0.31603E+02
0.21000E+02	0.11689E-01	0.11444E-01	-0.72166E+01	0.11239E+03	0.26693E-01	-0.28816E+02
0.22000E+02	0.93000E-02	0.91247E-02	-0.50670E+00	0.40039E+01	0.74927E+00	-0.25243E+02
0.23000E+02	0.82120E-02	0.80927E-02	-0.42500E+00	0.31809E+01	0.94313E+00	-0.18844E+02
0.24000E+02	0.84810E-02	0.83862E-02	-0.11857E+01	0.91574E+01	0.32760E+00	-0.12949E+02

Figure D.21 10^o Wedge ($\theta_{eff} = 13.5^o$) Flow $X = 2.64\delta_o$ Coincident Data

Y	V/U_e	$\overline{V'}/U$	$\overline{V'}/U_e$	SK_v	FL_v	$\tau_{xy}/\rho U^2$
0.20000E+01	-0.41735E-01	0.49445E-01	0.37404E-01	0.43370E+00	0.45163E+01	0.21178E-02
0.30000E+01	-0.45884E-01	0.44042E-01	0.36281E-01	0.93330E+00	0.64682E+01	0.95407E-03
0.40000E+01	-0.55268E-01	0.31142E-01	0.27252E-01	-0.33420E+00	0.13095E+02	0.55101E-03
0.50000E+01	-0.61016E-01	0.21477E-01	0.19347E-01	0.29820E+00	0.22843E+02	0.20188E-03
0.60000E+01	-0.62119E-01	0.22789E-01	0.20737E-01	-0.37400E+00	0.27366E+02	0.83282E-04
0.70000E+01	-0.64939E-01	0.19924E-01	0.18299E-01	0.26500E-01	0.36604E+02	0.22887E-04
0.80000E+01	-0.65147E-01	0.15934E-01	0.14720E-01	-0.12267E+01	0.32501E+02	0.21791E-04
0.90000E+01	-0.62628E-01	0.14426E-01	0.13398E-01	-0.93580E+00	0.41072E+02	0.20811E-04
0.10000E+02	-0.57341E-01	0.16661E-01	0.15522E-01	-0.91410E+00	0.39505E+02	0.16839E-04
0.11000E+02	-0.52924E-01	0.20135E-01	0.18820E-01	-0.30790E+01	0.36886E+02	0.17104E-04
0.12000E+02	-0.53135E-01	0.28975E-01	0.27199E-01	-0.14492E+01	0.20767E+02	0.22595E-04
0.13000E+02	-0.57325E-01	0.19311E-01	0.18244E-01	-0.58230E+00	0.24273E+02	0.15700E-04
0.14000E+02	-0.63783E-01	0.20760E-01	0.19794E-01	0.25239E+01	0.22597E+02	0.38098E-05
0.15000E+02	-0.74893E-01	0.18401E-01	0.17664E-01	0.66730E+00	0.40749E+02	0.55804E-06
0.16000E+02	-0.73450E-01	0.19459E-01	0.18776E-01	-0.43289E+01	0.43020E+02	-0.84379E-05
0.17000E+02	-0.65764E-01	0.14383E-01	0.13922E-01	0.23325E+01	0.68596E+02	-0.29497E-04
0.18000E+02	-0.60176E-01	0.13264E-01	0.12870E-01	0.23522E+01	0.48100E+02	-0.24239E-04
0.19000E+02	-0.55202E-01	0.13239E-01	0.12892E-01	-0.29631E+01	0.39555E+02	-0.31237E-04
0.20000E+02	-0.51965E-01	0.13244E-01	0.12923E-01	-0.46897E+01	0.59301E+02	-0.40874E-04
0.21000E+02	-0.47382E-01	0.18867E-01	0.18471E-01	-0.66504E+01	0.63459E+02	-0.35320E-04
0.22000E+02	-0.41507E-01	0.14905E-01	0.14624E-01	-0.43761E+01	0.83599E+02	-0.33481E-04
0.23000E+02	-0.30985E-01	0.13106E-01	0.12916E-01	-0.34496E+01	0.45544E+02	-0.40700E-04
0.24000E+02	-0.21292E-01	0.11714E-01	0.11583E-01	-0.39750E+00	0.46878E+01	-0.29837E-04

Y	$\tau_{xy}/\rho_e U_e^2$	τ_{xy}/τ_w	R_{uv}	TKE	U_{eff}/U^*	y^+
0.20000E+01	0.54155E-02	0.16986E+00	0.43468E+00	0.72992E-02	0.20785E+02	0.31321E+03
0.30000E+01	0.28931E-02	0.10102E+00	0.29374E+00	0.46591E-02	0.22992E+02	0.46982E+03
0.40000E+01	0.18855E-02	0.72593E-01	0.35569E+00	0.22071E-02	0.24762E+02	0.62642E+03
0.50000E+01	0.73207E-03	0.29780E-01	0.36462E+00	0.79355E-03	0.25684E+02	0.78303E+03
0.60000E+01	0.30815E-03	0.12800E-01	0.19913E+00	0.68775E-03	0.26016E+02	0.93964E+03
0.70000E+01	0.86273E-04	0.36580E-02	0.96318E-01	0.46808E-03	0.26329E+02	0.10962E+04
0.80000E+01	0.83109E-04	0.35678E-02	0.12413E+00	0.31458E-03	0.26529E+02	0.12528E+04
0.90000E+01	0.80213E-04	0.34831E-02	0.15934E+00	0.24909E-03	0.26712E+02	0.14095E+04
0.10000E+02	0.65314E-04	0.28557E-02	0.10287E+00	0.32584E-03	0.26822E+02	0.15661E+04
0.11000E+02	0.66775E-04	0.29402E-02	0.10187E+00	0.44018E-03	0.26936E+02	0.17227E+04
0.12000E+02	0.88968E-04	0.39577E-02	0.82768E-01	0.88395E-03	0.27087E+02	0.18793E+04
0.13000E+02	0.62614E-04	0.28303E-02	0.86350E-01	0.41725E-03	0.27317E+02	0.20359E+04
0.14000E+02	0.15478E-04	0.71625E-03	0.20099E-01	0.47265E-03	0.27653E+02	0.21925E+04
0.15000E+02	0.22979E-05	0.10850E-03	0.23336E-02	0.42304E-03	0.27904E+02	0.23491E+04
0.16000E+02	-0.35102E-04	-0.16790E-02	-0.51761E-01	0.41376E-03	0.28096E+02	0.25057E+04
0.17000E+02	-0.12351E-03	-0.59516E-02	-0.22240E+00	0.24938E-03	0.28218E+02	0.26623E+04
0.18000E+02	-0.10198E-03	-0.49395E-02	-0.18715E+00	0.22360E-03	0.28310E+02	0.28189E+04
0.19000E+02	-0.13235E-03	-0.64683E-02	-0.23781E+00	0.22450E-03	0.28445E+02	0.29755E+04
0.20000E+02	-0.17390E-03	-0.85445E-02	-0.27994E+00	0.23618E-03	0.28525E+02	0.31321E+04
0.21000E+02	-0.15126E-03	-0.74971E-02	-0.16015E+00	0.42429E-03	0.28655E+02	0.32887E+04
0.22000E+02	-0.14402E-03	-0.71798E-02	-0.24153E+00	0.26542E-03	0.28741E+02	0.34453E+04
0.23000E+02	-0.17662E-03	-0.89090E-02	-0.37813E+00	0.20550E-03	0.28915E+02	0.36019E+04
0.24000E+02	-0.13036E-03	-0.66378E-02	-0.30034E+00	0.17318E-03	0.29050E+02	0.37585E+04

Figure D.22 10^o Wedge ($\theta_{eff} = 13.5^o$) Flow $X = 2.64\delta_o$ Coincident Data (Cont.)

X/δ	ρ	T	M	M'	U	U/U$_e$
-0.15000E+01	0.28510E+00	0.12546E+03	0.26158E+01	0.25791E+00	0.58719E+03	0.96551E+00
-0.12500E+01	0.28086E+00	0.12625E+03	0.26017E+01	0.26181E+00	0.58583E+03	0.96329E+00
-0.10000E+01	0.27845E+00	0.12622E+03	0.26026E+01	0.26454E+00	0.58598E+03	0.96353E+00
-0.75000E+00	0.27810E+00	0.12525E+03	0.26204E+01	0.24693E+00	0.58773E+03	0.96641E+00
-0.50000E+00	0.27224E+00	0.12680E+03	0.25926E+01	0.26884E+00	0.58507E+03	0.96202E+00
-0.25000E+00	0.25718E+00	0.13301E+03	0.24857E+01	0.37078E+00	0.57439E+03	0.94448E+00
0.00000E+00	0.21049E+00	0.16104E+03	0.20575E+01	0.34454E+00	0.52251E+03	0.85916E+00
0.25000E+00	0.20229E+00	0.16603E+03	0.19894E+01	0.26638E+00	0.51301E+03	0.84355E+00
0.50000E+00	0.20377E+00	0.16329E+03	0.20272E+01	0.21602E+00	0.51795E+03	0.85167E+00
0.75000E+00	0.20931E+00	0.15747E+03	0.21089E+01	0.17700E+00	0.52842E+03	0.86889E+00
0.10000E+01	0.21214E+00	0.15391E+03	0.21607E+01	0.16811E+00	0.53458E+03	0.87901E+00
0.12500E+01	0.21412E+00	0.15102E+03	0.22034E+01	0.13721E+00	0.54011E+03	0.88811E+00
0.15000E+01	0.21346E+00	0.15003E+03	0.22181E+01	0.11844E+00	0.54247E+03	0.89198E+00
0.17500E+01	0.21153E+00	0.14992E+03	0.22202E+01	0.12618E+00	0.54329E+03	0.89334E+00
0.20000E+01	0.21074E+00	0.14900E+03	0.22344E+01	0.11179E+00	0.54540E+03	0.89680E+00
0.22500E+01	0.20747E+00	0.14985E+03	0.22221E+01	0.12769E+00	0.54431E+03	0.89500E+00
0.25000E+01	0.20864E+00	0.14751E+03	0.22573E+01	0.10646E+00	0.54888E+03	0.90253E+00
0.27500E+01	0.20742E+00	0.14688E+03	0.22673E+01	0.10913E+00	0.55029E+03	0.90484E+00
0.30000E+01	0.20616E+00	0.14626E+03	0.22767E+01	0.12001E+00	0.55149E+03	0.90682E+00

X/δ	U'/U	U'/U$_e$	SK$_u$	FL$_u$	γ$_u$	V
-0.15000E+01	0.41659E-01	0.40222E-01	-0.15915E+01	0.56453E+01	0.53142E+00	-0.35190E+00
-0.12500E+01	0.42821E-01	0.41249E-01	-0.15441E+01	0.53005E+01	0.56598E+00	-0.13186E+01
-0.10000E+01	0.43277E-01	0.41699E-01	-0.17423E+01	0.71820E+01	0.41771E+00	-0.25504E+01
-0.75000E+00	0.39810E-01	0.38473E-01	-0.17194E+01	0.64945E+01	0.46193E+00	-0.25444E+01
-0.50000E+00	0.44310E-01	0.42627E-01	-0.16431E+01	0.60627E+01	0.49483E+00	-0.15008E+01
-0.25000E+00	0.66851E-01	0.63139E-01	-0.17796E+01	0.64329E+01	0.46635E+00	-0.14063E+01
0.00000E+00	0.92611E-01	0.79568E-01	-0.85980E+00	0.31645E+01	0.94802E+00	-0.19758E+02
0.25000E+00	0.76487E-01	0.64520E-01	-0.83800E+00	0.33917E+01	0.88451E+00	-0.22816E+02
0.50000E+00	0.60758E-01	0.51746E-01	-0.11606E+01	0.45150E+01	0.66445E+00	-0.32824E+02
0.75000E+00	0.47248E-01	0.41053E-01	-0.16713E+01	0.66756E+01	0.44940E+00	-0.43906E+02
0.10000E+01	0.43370E-01	0.38122E-01	-0.17700E+01	0.70556E+01	0.42519E+00	-0.51920E+02
0.12500E+01	0.34348E-01	0.30505E-01	-0.19621E+01	0.82359E+01	0.36426E+00	-0.51837E+02
0.15000E+01	0.29170E-01	0.26019E-01	-0.21233E+01	0.10414E+02	0.28807E+00	-0.46377E+02
0.17500E+01	0.30726E-01	0.27449E-01	-0.24163E+01	0.14491E+02	0.20702E+00	-0.39283E+02
0.20000E+01	0.26946E-01	0.24165E-01	-0.25286E+01	0.14575E+02	0.20583E+00	-0.34422E+02
0.22500E+01	0.30297E-01	0.27116E-01	-0.24263E+01	0.12377E+02	0.24239E+00	-0.29187E+02
0.25000E+01	0.24403E-01	0.22024E-01	-0.31786E+01	0.22807E+02	0.13154E+00	-0.23800E+02
0.27500E+01	0.24650E-01	0.22304E-01	-0.25770E+01	0.14066E+02	0.21328E+00	-0.19071E+02
0.30000E+01	0.26696E-01	0.24208E-01	-0.23309E+01	0.11825E+02	0.25369E+00	-0.16011E+02

Figure D.23 10^o Wedge ($\theta_{eff} = 13.5^o$) Flow $Y = 0.66\delta_o$ Coincident Data

X/δ	V/U$_e$	V'/U	V'/U$_e$	SK$_v$	FL$_v$	$\tau_{xy}/\rho U^2$
-0.15000E+01	-0.57863E-03	0.20743E-01	0.20028E-01	0.11020E+00	0.10762E+02	0.40383E-03
-0.12500E+01	-0.21682E-02	0.21602E-01	0.20809E-01	0.47140E+00	0.11659E+02	0.40471E-03
-0.10000E+01	-0.41936E-02	0.21094E-01	0.20325E-01	0.48030E+00	0.81770E+01	0.39879E-03
-0.75000E+00	-0.41838E-02	0.20376E-01	0.19691E-01	0.26940E+00	0.11642E+02	0.34375E-03
-0.50000E+00	-0.24678E-02	0.21837E-01	0.21007E-01	0.62350E+00	0.10744E+02	0.45746E-03
-0.25000E+00	-0.23124E-02	0.29433E-01	0.27799E-01	0.70330E+00	0.87214E+01	0.68638E-03
0.00000E+00	-0.32488E-01	0.43155E-01	0.37077E-01	0.53300E-01	0.46598E+01	0.13510E-02
0.25000E+00	-0.37516E-01	0.33968E-01	0.28654E-01	0.36430E+00	0.70078E+01	0.40657E-03
0.50000E+00	-0.53973E-01	0.31175E-01	0.26551E-01	0.11910E+00	0.63744E+01	0.87210E-04
0.75000E+00	-0.72195E-01	0.29889E-01	0.25970E-01	0.71380E+00	0.10434E+02	0.13509E-03
0.10000E+01	-0.85372E-01	0.28017E-01	0.24627E-01	0.12433E+01	0.13117E+02	0.26650E-03
0.12500E+01	-0.85235E-01	0.25444E-01	0.22597E-01	0.98560E+00	0.83910E+01	0.26784E-03
0.15000E+01	-0.76259E-01	0.23920E-01	0.21336E-01	0.15382E+01	0.10770E+02	0.16853E-03
0.17500E+01	-0.64594E-01	0.26805E-01	0.23946E-01	0.18766E+01	0.15392E+02	0.23197E-03
0.20000E+01	-0.56599E-01	0.28361E-01	0.25435E-01	0.26954E+01	0.24355E+02	0.16570E-03
0.22500E+01	-0.47993E-01	0.23941E-01	0.21427E-01	0.14306E+01	0.12525E+02	0.32070E-03
0.25000E+01	-0.39135E-01	0.22792E-01	0.20571E-01	0.15333E+01	0.20874E+02	0.18401E-03
0.27500E+01	-0.31358E-01	0.25179E-01	0.22783E-01	0.57900E+00	0.17980E+02	0.17015E-03
0.30000E+01	-0.26327E-01	0.26702E-01	0.24214E-01	0.21770E+00	0.15025E+02	0.20687E-03

X/δ	$\tau_{xy}/\rho_e U_e^2$	R$_{uv}$	TKE	y$^+$
-0.15000E+01	0.16822E-02	0.46732E+00	0.12980E-02	-0.94218E+01
-0.12500E+01	0.16781E-02	0.43751E+00	0.13835E-02	-0.78515E+01
-0.10000E+01	0.16544E-02	0.43684E+00	0.13814E-02	-0.62812E+01
-0.75000E+00	0.14346E-02	0.42378E+00	0.12076E-02	-0.47109E+01
-0.50000E+00	0.18919E-02	0.47279E+00	0.14585E-02	-0.31406E+01
-0.25000E+00	0.27359E-02	0.34883E+00	0.31008E-02	-0.15703E+01
0.00000E+00	0.44561E-02	0.33803E+00	0.61508E-02	0.00000E+00
0.25000E+00	0.12927E-02	0.15648E+00	0.40790E-02	0.15703E+01
0.50000E+00	0.28267E-03	0.46042E-01	0.28177E-02	0.31406E+01
0.75000E+00	0.45574E-03	0.95661E-01	0.20095E-02	0.47109E+01
0.10000E+01	0.92011E-03	0.21932E+00	0.17254E-02	0.62812E+01
0.12500E+01	0.94399E-03	0.30647E+00	0.12373E-02	0.78515E+01
0.15000E+01	0.59917E-03	0.24154E+00	0.99759E-03	0.94218E+01
0.17500E+01	0.82724E-03	0.28165E+00	0.11906E-02	0.10992E+02
0.20000E+01	0.59548E-03	0.21682E+00	0.11674E-02	0.12562E+02
0.22500E+01	0.11479E-02	0.44214E+00	0.10321E-02	0.14133E+02
0.25000E+01	0.66975E-03	0.33083E+00	0.81723E-03	0.15703E+02
0.27500E+01	0.62250E-03	0.27415E+00	0.93780E-03	0.17273E+02
0.30000E+01	0.76014E-03	0.29021E+00	0.10693E-02	0.18844E+02

Figure D.24 10^o Wedge ($\theta_{eff} = 13.5^o$) Flow $Y = 0.66\delta_o$ Coincident Data (Cont.)

Bibliography

1. *TSI Six Jet Atomizer MODEL 9306 Operating Manual.* Operating Manual Model 9306. TSI, USA, undated.
2. Anderson, John A. *Modern Compressible Flow with Historical Perspective..* McGraw Hill Book Company, 1982.
3. Bowersox, Rodney D.W. Class Notes AERO 827., Wright-Patterson AFB OH, 1995.
4. Dale A. Anderson, John C. Tannehill and Richard H. Pletcher. *Computational Fluid Mechanics and Heat Transfer.* Taylor and Francis, 1984.
5. Dantec Measurement Technology A/S. *Burstware 3.0 User's Manual.* Technical Report. Skovlunde, Denmark: Dantec, Inc.
6. Driest, E.R. Van. "Turbulent Boundary Layer in Compressible Fluids.," *Journal of the Aeronautical Sciences*, *18*(3) (1951).
7. Elena, M. and J. LaCharme. "Experimental Study of a Supersonic Turbulent Boundary Layer Using a Laser Doppler Anemometer.," *Journal of Theoretical and Applied Mechanics*, *7*(2) (1988).
8. Fick, Eric Thomas. *Numerical Simulation of Supersonic Turbulent Boundary Layer Flow Under the Influence of Mild Pressure Gradients.* MS thesis, Air Force Institute of Technology, 1995.
9. Hale, Chad S. *Experimental Investigation of a Supersonic Turbulent Boundary Layer with Adverse Pressure Gradient.* MS thesis, Air Force Institute of Technology, 1995.
10. John D. Anderson, Jr. *Hypersonic and High Temperature Gas Dynamics.* McGraw Hill Book Company, 1989.
11. Kays, W.M. and M.E. Crawford. *Convective Heat and Mass Transfer..* McGraw Hill Book Company, 1993.
12. Kistler., Alan L. "Fluctuation Measurements in a Supersonic Turbulent Boundary Layer.," *The Physics of Fluids*, *2*(3) (1959).
13. Luker, Joel J. *Compressible Turbulence Measurements in a Boundary Layer including Favorable Pressure Gradient Effects.* MS thesis, Air Force Institute of Technology, 1995.
14. Marvin, Joseph G. "Turbulence Modeling for Computational Aerodynamics," *AIAA Journal*, *21*(7) (1983).
15. Robinson, S., et al. "Hot-Wire and Laser Doppler Anemometer Measurements in a Supersonic Boundary Layer.." *AIAA Paper 83-1723*. 1983.
16. Rose, William C. and Dennis A. Johnson. "Turbulence in a Shock-Wave Boundary-Layer Interaction.," *AIAA Journal*, *13*(7) (1975).
17. Settles, Gary S. and Lori J. Dodson. "Supersonic and Hypersonic Shock/Boundary-Layer Interaction Database," *AIAA Journal*, *32*(7) (1994).
18. Spina, Eric F., Smits Alexander J. and Stephen K. Robinson. "The Physics of Turbulent Boundary Layers," *Annual Review of Fluid Mechanics 1994*, *26* (1994).
19. White, Frank M. *Viscous Fluid Flow.* McGraw Hill Book Company, 1991.

Vita

First Lieutenant Michael J. Meyer [redacted]. He graduated from Eldorado High School in Albuquerque, New Mexico, in 1987, and entered undergraduate studies at the Arizona State University in Tempe, Arizona. He graduated with a Bachelor of Science in Engineering in Aerospace Engineering in December 1991. He was commissioned by his father, Lieutenant Colonel John A. Meyer (Retired) on 20 December 1991. His first assignment in the United States Air Force is at Wright-Patterson AFB, Ohio, as an Aircrew Escape Systems Engineer with Wright Laboratory. He completed his Master of Science Degree in Aeronautical Engineering part-time while assigned to Wright Laboratory. His follow-on assignment is with the 31st Test and Evaluation Squadron at Edwards AFB, CA.

[redacted]